

IntechOpen

Geodetic Sciences

Theory, Applications and Recent Developments

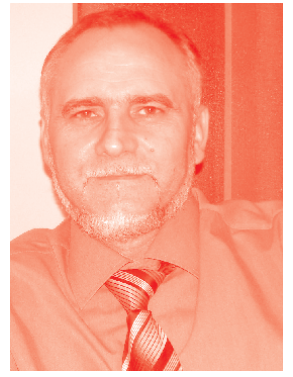
Edited by Bihter Erol and Serdar Erol



Geodetic Sciences - Theory, Applications and Recent Developments

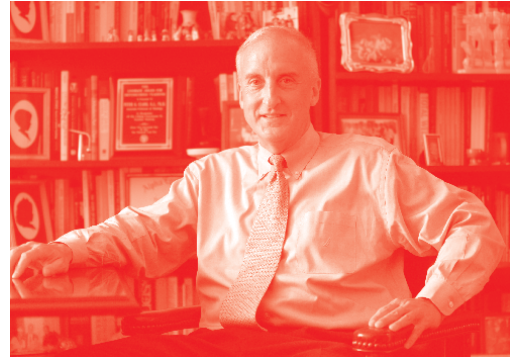
Edited by Bihter Erol and Serdar Erol

Published in London, United Kingdom



IntechOpen





Supporting open minds since 2005



Geodetic Sciences – Theory, Applications and Recent Developments

<http://dx.doi.org/10.5772/intechopen.87679>

Edited by Bihter Erol and Serdar Erol

Contributors

Héctor Mora-Páez, Franck Audemard, Guillaume Ramillien, Lucia Seoane, Mehdi Eshagh, Lars Sjöberg, Majid Abrehdary, Jean-Pierre Barriot, Peng Feng, Riccardo Barzaghi, Carlo Iapige De Gaetani, Anna Maria Marotta, Mirko Reguzzoni, Lorenzo Rossi, Marijan Grgic, Tomislav Bašić, Stefano Vignudelli, Francesco De Biasio

© The Editor(s) and the Author(s) 2021

The rights of the editor(s) and the author(s) have been asserted in accordance with the Copyright, Designs and Patents Act 1988. All rights to the book as a whole are reserved by INTECHOPEN LIMITED. The book as a whole (compilation) cannot be reproduced, distributed or used for commercial or non-commercial purposes without INTECHOPEN LIMITED's written permission. Enquiries concerning the use of the book should be directed to INTECHOPEN LIMITED rights and permissions department (permissions@intechopen.com).

Violations are liable to prosecution under the governing Copyright Law.



Individual chapters of this publication are distributed under the terms of the Creative Commons Attribution 3.0 Unported License which permits commercial use, distribution and reproduction of the individual chapters, provided the original author(s) and source publication are appropriately acknowledged. If so indicated, certain images may not be included under the Creative Commons license. In such cases users will need to obtain permission from the license holder to reproduce the material. More details and guidelines concerning content reuse and adaptation can be found at <http://www.intechopen.com/copyright-policy.html>.

Notice

Statements and opinions expressed in the chapters are these of the individual contributors and not necessarily those of the editors or publisher. No responsibility is accepted for the accuracy of information contained in the published chapters. The publisher assumes no responsibility for any damage or injury to persons or property arising out of the use of any materials, instructions, methods or ideas contained in the book.

First published in London, United Kingdom, 2021 by IntechOpen

IntechOpen is the global imprint of INTECHOPEN LIMITED, registered in England and Wales, registration number: 11086078, 5 Princes Gate Court, London, SW7 2QJ, United Kingdom

Printed in Croatia

British Library Cataloguing-in-Publication Data

A catalogue record for this book is available from the British Library

Additional hard and PDF copies can be obtained from orders@intechopen.com

Geodetic Sciences – Theory, Applications and Recent Developments

Edited by Bihter Erol and Serdar Erol

p. cm.

Print ISBN 978-1-83962-763-7

Online ISBN 978-1-83962-767-5

eBook (PDF) ISBN 978-1-83962-768-2

We are IntechOpen, the world's leading publisher of Open Access books Built by scientists, for scientists

5,300+

Open access books available

131,000+

International authors and editors

155M+

Downloads

156

Countries delivered to

Our authors are among the
Top 1%

most cited scientists

12.2%

Contributors from top 500 universities



WEB OF SCIENCE™

Selection of our books indexed in the Book Citation Index
in Web of Science™ Core Collection (BKCI)

Interested in publishing with us?
Contact book.department@intechopen.com

Numbers displayed above are based on latest data collected.
For more information visit www.intechopen.com



Meet the editors



Dr. Bihter Erol received her Ph.D. degree in geodesy from Istanbul Technical University (ITU), Turkey, in 2007, and she still works as a full-time associate professor at ITU Geomatics Department. Her research interests in the field of physical geodesy include static and temporal determination of the Earth's gravity field, regional geoid modeling with terrestrial and airborne gravimetry, and structural deformation analyses. Dr. Erol has research experience in her major at different departments and institutes in Canada, Germany, and the Netherlands. She has published many scientific journal articles and proceedings and has made contributions as editor and reviewer in geodetic journals and proceedings. She takes a role in various international symposia organizations and scientific committees. She is a member of the International Association of Geodesy (IAG) working groups; leads the ITU Gravity Research Group; supervises the thesis studies, and carries out research projects at the ITU Geomatics Department.



Dr. Serdar Erol is a full-time professor at the Istanbul Technical University (ITU), Turkey. He received his Ph.D. degree in Geodesy and Photogrammetry Engineering at the ITU in 2008. His main research areas include satellite geodesy, monitoring and analyzing deformations using geodetic methods, sea level monitoring and satellite altimeter, engineering surveying and applications, statistical data analyses and modeling, and spectral data evaluation methods. He was a research associate at the University of Calgary-Geomatics Engineering Department, Canada, in 2004/2005. He currently contributes to study groups of the International Association of Geodesy (IAG) and Turkey National Geodesy Commission (TUJK). He is a member of the ITU Gravity Research Group. He gives lectures, supervises thesis studies, and owns administrative responsibilities in Geomatics Department at ITU.

Contents

Preface	XIII
Chapter 1 The Earth's Gravity Field Role in Geodesy and Large-Scale Geophysics <i>by Mehdi Eshagh</i>	1
Chapter 2 On Moho Determination by the Vening Meinesz-Moritz Technique <i>by Lars Erik Sjöberg and Majid Abrehdary</i>	23
Chapter 3 The Gravity Effect of Topography: A Comparison among Three Different Methods <i>by Carlo Iapige De Gaetani, Anna Maria Marotta, Riccardo Barzaghi, Mirko Reguzzoni and Lorenzo Rossi</i>	43
Chapter 4 Continental Water Storage Changes Sensed by GRACE Satellite Gravimetry <i>by Guillaume Ramillien and Lucía Seoane</i>	59
Chapter 5 Radar Satellite Altimetry in Geodesy - Theory, Applications and Recent Developments <i>by Marijan Grgić and Tomislav Bašić</i>	77
Chapter 6 Coastal Sea Level Trends from a Joint Use of Satellite Radar Altimetry, GPS and Tide Gauges: Case Study of the Northern Adriatic Sea <i>by Stefano Vignudelli and Francesco De Biasio</i>	95
Chapter 7 Beyond Mapping Functions and Gradients <i>by Jean-Pierre Barriot and Peng Feng</i>	125
Chapter 8 GNSS Networks for Geodynamics in the Caribbean, Northwestern South America, and Central America <i>by Héctor Mora-Páez and Franck Audemard</i>	143

Preface

Geodesy covers a broad range of applications related to the Earth and its dynamic phenomena, and it relies on well-established theories with mathematical formulations for generating solutions and models in analyzing and explaining the Earth phenomena. According to this perspective, geodesy is an applied science based on strong theoretical foundations that serves many other science and engineering disciplines for a better and sustainable future in the world. In the twenty-first century, technological developments, in particular the artificial satellites, have led the unprecedented progress in observation techniques and have expanded the possibilities in the fields of geodesy for observing and analyzing the Earth as a whole in detail with much higher precision. These developments in technology not only led to the advancement of measurement and data acquisition techniques but also to the more rigorous application of the theory through powerful computers and processors. All these developments in theory and practice influenced each field of Geodesy, and it began to provide improved outputs that would serve humanity's future.

In this collection, eight chapters provide a detailed overview of the recent developments lived in the Geodetic Science and its theory and applications, through the selected case studies and their investigation fields. In this way, a picture was depicted from the last point reached in the main fields of Geodetic Science including Earth gravity field, sea level investigations, navigation satellites' data evaluations, and continental-scale tectonic investigations. The following paragraphs refer to some of the research issues that are currently under investigation in Geodesy. The research topics mentioned are those that have been investigated and exemplified in the chapters of this book.

Gravity inversion provides a useful tool for investigating the Earth's interior, and static gravity observations are mainly used to determine the lithosphere density distribution or the Moho depth. In this manner, global geopotential models derived from the Earth gravity field satellite missions' data contribute to these investigations on a global scale, and in the regions without terrestrial data such as the polar areas. The satellite missions Gravity Recovery and Climate Experiment (GRACE) and GRACE Follow-On also provide gravity observations with a high temporal resolution, which are being used to model the geophysical phenomena such as the glacial isostatic adjustment and seismic and volcanic events, and for carrying out hydrological research such as drought monitoring. However, since the gravity inversion includes numerical instability, independent data such as seismic data or GNSS-derived vertical deformations are additionally required to constrain the solutions, and the methodological contributions are essentially required for the modeling and better understanding of the Earth's interior and related processes.

Precise modeling of the regional and global static gravity field and the geoid with the high-spatial-resolution is another research issue and essential for a broad range of scientific and engineering applications. For this purpose, terrestrial, marine, and airborne gravity data, in addition to the satellite-based data, are used. In this field, the launch of dedicated satellite missions such as GRACE and GOCE and

the improvements in satellite radar altimetry are breakthrough accomplishments, and they have an essential role in the unprecedented improvement in accuracy and spatial resolutions of the calculated models. Also crucial is the information coming from digital topography/bathymetry models. The improvements of the elevation and bathymetry models make an important contribution to the precise gravity field and geoid determination, as well as the use of forward modeling techniques for estimating the realistic densities and unknown sub-ice terrains in polar areas. Although the methodologies of use and computations of the terrain effects have already been well-formulated so far, there is still a need for justifications to explain differences between the approximations and their consequences for precise cm-level geoid determination, and the computation of the high-resolution global models of the topographic or topographic-isostatic potential.

Besides the progress in the modeling of the static gravity field, it has become possible to determine its temporal variations with high accuracy and resolution related to the mass transport and the physical processes within the Earth's system such as ocean circulation, hydrological cycle, postglacial rebound, and gravity change as a result of a strong earthquake. Although the dedicated satellite gravimetry missions on estimating the time-varying gravity field continue to evolve with the successors, temporal and spatial resolutions of their observations are still currently insufficient to meet the demand of the hydrological studies. Therefore, new data evaluation strategies and algorithms are required to investigate the hydrological signals. Besides more developed algorithms, other space techniques including altimeter, GNSS, and interferometric synthetic-aperture radar are used to complement the satellite gravimetry for more detailed analyses of the consequences that stem from the hydrological mass loading or groundwater depletion, etc. Thus, the combination of various geodetic observation techniques at different spatiotemporal scales yields further opportunities for deeper and more detailed analyses of global and regional water cycling and climate change.

In addition to the satellite gravimetry, the developments in satellite altimeter techniques lead possibilities to perform more detailed investigations with improved products at global seas as well as at coastal areas and inland water bodies (SAR/SARIn altimetry). Satellite altimetry with the complementary data makes an essential contribution to monitoring the near-global ocean surface topography, thus improving the knowledge of oceanography, marine geodesy, and geophysics, as well as their roles in climate. The evaluation results of satellite altimetry data are used to clarify regional (even in very small water bodies and areas very close to the shore) and global sea-level changes, surface currents, mesoscale circulation and variability, wind speeds and wave heights, marine gravity field, geoid, mean sea surface, mean dynamic topography, seafloor topography, vertical height datum, as well as the land vertical deformations.

The experienced developments have not only been in the Earth gravity field investigations branch of geodesy but also the global navigation satellite systems and their related applications have noticeable improvements. As a consequence of the developments, new fields such as GNSS meteorology are constituted where the navigation signal has benefited different purposes. In these fields, rather than considering the atmosphere as an error source for the GNSS signals, the geodetic measurements including the GNSS, satellite altimetry, VLBI, SLR, and DORIS are considered valuable data sources for understanding and analyzing the state and dynamics of the atmosphere. From this point of view, real-time observations

have the potential to evolve for monitoring and forecasting the ionospheric state and to optimize ultrafast tropospheric products. All the developments in this area lead to improvements in all application areas where the GNSS position is used.

These are the highlights of the topics, which are currently studied in the field of geodesy. Regarding these highlights and pointed research topics, this book aims to provide a useful reference for the researchers and practitioners who are working in the field of geodesy and its multidisciplinary fields.

Bihter Erol and Serdar Erol
Istanbul Technical University,
Istanbul, Turkey

The Earth's Gravity Field Role in Geodesy and Large-Scale Geophysics

Mehdi Eshagh

Abstract

The Earth gravity field is a signature of the Earth's mass heterogeneities and structures and applied in Geodesy and Geophysics for different purposes. One of the main goals of Geodesy is to determine the physical shape of the Earth, geoid, as a reference for heights, but Geophysics aims to understand the Earth's interior. In this chapter, the general principles of geoid determination using the well-known methods of Remove-Compute-Restore, Stokes-Helmert and least-squares modification of Stokes' formula with additive corrections are shortly discussed. Later, some Geophysical applications like modelling the Mohorovičić discontinuity and density contrast between crust and uppermantle, elastic thickness, ocean depth, sediment and ice thicknesses, sub-lithospheric and lithospheric stress, Earthquakes and epicentres, post-glacial rebound, groundwater storage are discussed. The goal of this chapter is to briefly present the roll of gravity in these subjects.

Keywords: bathymetry, earthquake, geoid height, groundwater, ice thickness, Moho discontinuity, post-glacial rebound, sediment basement, stress, sea level change, viscosity

1. Introduction

The Earth's gravity field reflects of the Earth's interior and is an interesting subject in Geodesy and Geophysics with various applications. Geodesy aims to determine three types of the shape and size of the Earth, the Earth's surface, geoid as the physical shape, reference ellipsoid as the mathematical one. Physical Geodesy deals with determination of the physical shape of the Earth or the geoid, which is a reference for heights, from gravimetric data. In this chapter, short descriptions of three known methods of geoid determination such as Remove-Compute-Restore (RCR) [1], Stokes-Helmert (SH) [2] and least-squares modification of the Stokes formula with addition corrections (LSMSF) [3] are presented.

In Geophysics, understanding the Earth's physics, dynamics and interior geometry is of interest using such data. Gravity measurements can be analysed over small or large area depending on the geophysical purpose. For instance, in exploration Geophysics they are used to detect or discover near surface resources and for such a goal precision and accuracy of these data should be high. Here, such applications are named small-scale Geophysics. However, understanding or studying the deep Earth's interior physics, dynamics or geometry does not require high spatial

resolutions and long wavelength portions of the gravity data are more suitable. In addition, large areas are considered for such purpose and therefore, here, such subjects are called large-scale Geophysics. Some of these large-scale phenomena are modelling the Mohorovičić discontinuity, elastic thickness of the lithosphere, sub-lithospheric/lithospheric stress, and thickness of ocean water, sediments, and ice; land uplift, mantle viscosity and groundwater storage; and post-seismic studies of Earthquakes, detecting the epicentre points of shallow Earthquakes, which are briefly presented in this chapter.

2. Geoid determination as a purpose in Geodesy

The geoid is a reference surface for heights and if this reference is not enough precise and accurate, all determined heights from it will be unreliable. Having a precise geoid model simplifies the lengthy and costly work of levelling by simply using a global navigation satellite systems (GNSS) receiver, the height above the geoid can be determined. However, to reach to this goal, deep knowledge about the Earth's gravity field and the Physical Geodesy theories, skills in numerical modelling and precise data in all frequency bands are required.

The main task of Physical Geodesy is to develop theories and methods to model a precise geoid. Different approaches have been developed toward this goal. As known, the surface terrestrial gravity data are sensitive to high frequencies and near surface mass variations, but their low frequencies of the signal are weak unlike satellite-only Earth gravity models (EGMs) having better qualities only in the low frequency band. In geoid modelling approaches the terrestrial gravity data are used for recovering the high frequencies of the geoid and the satellite EGMs for the lower. Generally, in geoid modelling the following issues should also be considered:

1. The effects of topographic and atmospheric masses.
2. Downward continuation of gravity data.
3. Conversion of gravity anomalies to geoid/co-geoid.

The differences between the geoid modelling methods are related to how mathematically these issues are handled. In the following the three methods of RCR, SH and LSMSF are shortly presented.

2.1 Remove-compute-restore approach

In the RCR scheme, the low and high frequencies of terrestrial gravity data are removed by an EGM and topographic heights. Because the low frequencies are global and for converting of the gravity data with a regional coverage to the geoid, the low frequencies of geoid cannot be recovered well. In addition, removing the effect of topographic terrain makes the gravity data smoother, and simplifies the computations. After computing the geoid excluding the low and high frequencies, the removed frequencies are restored to it to complete all frequencies of the geoid. Mathematically, the idea is presented by:

$$N = \frac{R}{4\pi\gamma} \iint_{\sigma} S(\psi) \left((\Delta g - \Delta g^{\text{RTM}})^* - \sum_{n=2}^L \Delta g_n^{\text{EGM}} \right) d\sigma + \sum_{n=2}^L N_n^{\text{EGM}} + N^{\text{RTM}} \quad (1)$$

where

$$\left. \begin{array}{l} \Delta g_n^{\text{EGM}} \\ N_n^{\text{EGM}} \end{array} \right\} = \sum_{m=-n}^n \left. \begin{array}{l} \Delta g_{nm}^{\text{EGM}} \\ N_{nm}^{\text{EGM}} \end{array} \right\} Y_{nm}(\theta, \lambda) \quad (2)$$

N is the geoid height, $S(\psi)$ the Stokes function [4] converting gravity to geoid, Δg the gravity anomaly, Δg^{RTM} the residual terrain effect (RTM) on the anomaly, $(\Delta g - \Delta g^{\text{RTM}})^*$ means the downward continued $\Delta g - \Delta g^{\text{RTM}}$, σ_0 the integration domain, $d\sigma$ the surface integration element, $\Delta g_{nm}^{\text{EGM}}$ and N_{nm}^{EGM} are, respectively, the spherical harmonic coefficients of Δg and N of degree n and order m , derived from an EGM, limited to the maximum degree L , $Y_{nm}(\theta, \lambda)$ the spherical harmonic with arguments of co-latitude θ and longitude λ , N^{RTM} the restored RTM effect on the computed geoid.

The first term on the right-hand side (rhs) of Eq. (1), is the Stokes integral, which converts the gravity anomalies to geoid height, and since the long and short frequencies of the anomalies are removed, the solution of this integral is the geoid height excluding these frequencies. In fact, the addition of the second and third terms of Eq. (1) is to restore these frequencies back to the computed geoid height. In the following, some issues regarding the RCR method is presented and discussed:

1. Three types of data are used in Eq. (1), terrestrial gravity data, EGM and RTM with own error properties. According to the error propagation law, the error of the reduced gravity anomalies is the square root of summation of variances of the terrestrial data, EGM and RTM, which is surely larger than the error of gravity data. If the discretisation error of the Stokes integral is assumed small, in the restoring step, the errors of the EGM and RTM will be propagated to the final solution again.
2. Most portion of the geoid signal comes from its low frequencies, and by removing it by an EGM, this part of signal is assumed as known. By increasing the maximum degree of it, more portion of the geoid signal removed and restored. This means that the sensitivity to the terrestrial data will be reduced. The high frequencies of the geoid comes from topographic masses, and by considering it known as well, the main task will be to recover the medium wavelengths from gravity data.
3. After the removal step, gravity data are converted to a medium frequency geoid height, using Stokes formula, least-squares collocation (LSC) [5] or Fast Fourier Transform (FFT); see e.g. [1]. The low frequencies are restored by the same EGM applied limited to the same maximum degree, and the high frequencies from the RTM effect.
4. Downward continuation (DWC) of the gravity data should be performed before applying the Stokes formula or FFT. However, by using LSC, the conversion of the gravity data to the geoid heights and DWC can be done in one-step simultaneously.

2.2 Stokes-Helmert approach

The Stokes-Helmert (SH) method was proposed by Vanicek and Martinec [2] and developed further by Martinec [6]. Theoretically, the gravity data on a spherical surface are needed to numerically solve the Stokes integral for computing a

geoid height. In addition, this integral is the solution of the gravimetric boundary-problem, the Laplace equation, with gravity anomalies at the boundary, the geoid. This means that this solution is theoretically valid where there is no mass outside the boundary surface. However, in practice, the gravity data are collected at the Earth's surface, on topographic and under atmospheric masses. The presence of such masses violates the theory. Therefore, the gravitational effects on the gravity data should be removed to fulfil the Laplace equation. The result will be a no-topography and no-atmosphere computational space, or the Helmert space. After removing these effects the gravity data still remain above the boundary and need to be continued downward. By solving the Stokes integral numerically, these continued data are converted to a surface similar to geoid, known as co-geoid. The next step will be to convert this co-geoid by restoring the effects of topographic and atmospheric masses. The principle of SH method is:

$$N = \frac{R}{4\pi\gamma} \iint_{\sigma_0} S^L(\psi) (\Delta g^L - \Delta g_{\text{dir}}^{\text{TAe}}) d\sigma + \frac{R}{2\gamma} \sum_{n=2}^L \frac{2}{n-1} \Delta g_n^{\text{EGM}} + N_{\text{Ind}}^{\text{TAe}} \quad (3)$$

where $S^L(\psi)$ is the modified Stokes function, $\Delta g_{\text{dir}}^{\text{TAe}}$ the joint direct effect of topographic and atmospheric masses as well as the ellipticity of the Earth, which should be removed from the gravity data. Δg^L means the gravity anomalies excluding the frequencies to degree L . $N_{\text{Ind}}^{\text{TAe}}$ is the joint indirect effect of the removed masses and ellipticity.

The SH method has the following properties:

1. The topographic and atmospheric effects are removed from the gravity anomalies directly. The topographic effect (TE) over mountainous areas is considerably larger than the gravity anomalies, then a compensation/condensation mechanism is required to reduce their values to the order of the terrestrial ones. The anomalies will be smoother and the Stokes integral can be solved numerically with a better precision. The same mechanism is used for restoring the TE as Indirect TE. This means that it has no effect on the resulted geoid height, because of being added and subtracted during the process.
2. The TE and atmospheric effect (AE) are computed by taking the radial derivative of their respective gravitational potentials. This means the effect on the gravity, and not the gravity anomaly which is used in the Stokes formula. There are two terms in the fundamental equation of Physical Geodesy as the definition of gravity anomaly. The first term is the radial derivative of the disturbing potential and the second is $2/R$ times of the potential. Considering the TE and AE on the gravity solely by taking the radial derivatives of their potentials, means ignorance of the second term. Therefore, the restoration is done in two step, primary indirect effects, in which the removed effected are restored, and the secondary indirect effect when the effect of the missing second term is restored. If the fundamental equation of Physical Geodesy is applied for computing the direct and indirect TE and AE, this secondary effect will not be needed.
3. The Stokes-integral is modified meaning that its kernel function is changed in such a way that the contribution of the anomalies outside the integration cap is minimised. The effect of the truncation of the integration domain will be restored after integrating the reduced anomalies.

4. The TE and AE have their own error properties, in addition by removing the long wavelengths of the anomalies by an EGM, Therefore, the reduced anomalies contaminate larger stochastic error than the measured ones. The errors of the gravity anomalies and EGMs are not considered in the solution.
5. The reduced gravity anomalies in the Helmert space need to be continued downward to see level prior to integrating them. To do so, inverse solution of the Poisson integral is applied; see [6], which is an ill-posed problem and complicated when the resolution of the anomalies is high.

2.3 Least-squares modification of stokes formula with additive corrections

Unlike the RCR and SH methods, neither the TE and AE nor the long wavelength portion of the anomalies are removed from the gravity anomalies. Instead, the terrestrial anomalies and EGM are spectrally weighted which means that the Stokes integral is modified in such a way their errors and the truncation error of the Stokes integral outside the integration cap are minimised in a least-squares sense. This method is called least-squares modification of Stokes formula [3]. In this method, the terrestrial anomalies are integrated directly by the modified Stokes formula to estimate a geoid model. Later the total TE and AE, DWC and ellipsoidal corrections will be added to the modelled geoid to make it precise. This method can be mathematically presented by:

$$N = \frac{R}{4\pi\gamma} \iint_{\sigma_0} S^L(\psi) \Delta g d\sigma + \frac{R}{2\gamma} \sum_{n=2}^L b_n \Delta g_n^{\text{EGM}} + N^T + N^A + N^e + N^{\text{DWC}} \quad (4)$$

where b_n is a parameter depending on type of modification, N^T and N^A are, respectively, the total TE and AE. N^e is the ellipsoidal correction, N^{DWC} the DWC effect on the geoid.

The properties of this method are:

1. The measured gravity anomalies are used in the modified Stokes integral. However, gridded anomalies are not at the boundary surface, which is not theoretically corrected, also no mass should exist outside the geoid when applying the stokes formula.
2. This method considers the errors of the terrestrial data, EGM and truncation of the integral formula and modify the integral in an optimal way, meaning that the quality of the data play important role in geoid modelling. The data contributes to solution according to their precision.
3. Because of neglecting the TE and AE on the gravity data, results of the modified Stokes integral will contain biases. However, the total TE and AE will be removed. In fact, the gravitational potential of these masses are computed for points at the surface of the Earth. Later they are continued downward to the boundary, and subtracted from the indirect gravitational potential of the points under the masses at the boundary. Such a potential will be converted simply to correction to geoid using the Bruns formula. Note that no compensation or condensation mechanism is required in this method
4. The DWC process is done directly on the potential, the gravity data converted to the potential and continued downward analytically. Therefore, no integral equation needs to be solved numerically.

5. The effect of ignoring the ellipticity of the Earth will be considered as an extra correction to the geoid directly.

3. Gravity field and large-scale Geophysics

In Geophysics, the gravimetric data are used for different purposes; e.g. in exploration and prospecting for detecting near surface sources, or studying the Earth's deep interior, which are named here the large-scale Geophysics. The Earth gravity field is determined in two ways. If the temporal variations of the gravity is considered the time-variable gravity field can be determined, otherwise, the static field. In this section, some of the well-known applications of static and time-variable gravity data in large-scale Geophysics are presented and discussed.

3.1 Static gravity field and large-scale Geophysics

A static gravity field reflects the physics of the Earth's interior, which is not fully known. Therefore, different assumptions are used to extract the desired information from the gravity field. Here, the use of the static gravity data and modelling of crustal structure, elastic thickness and rigidity, ice thickness, bathymetry, sediment basement, lithospheric and sub-lithospheric stresses due to mantle convection are presented briefly.

3.1.1 Determination of Moho depth

One the assumptions about the Earth's interior is Isostasy, which is a state of equilibrium between the crust and upper mantle. Aity-Heiskanen, in which the mountains have roots beneath to keep them in isostatic balance, and Pratt-Hayford theory, which states that the mountains loads are compensated by density variations inside the crust are two known models of Isostasy. The gravimetric isostasy mean that the isostatic gravity anomaly (Δg^I) should be zero to have the crust in isostatic equilibrium. The mathematical description of the gravimetric isostasy is [4]:

$$\Delta g^I = \Delta g - \Delta g^{\text{TBSCI}} + \Delta g^{\text{CMP}} = 0 \quad (5)$$

where Δg is gravity anomaly, Δg^{TBSCI} total effect of the topographic and bathymetric masses, sediments, crustal crystalline and ice on Δg and finally, Δg^{CMP} the compensation effect on Δg . Eq. (5) means that there are some compensation attraction, which is equal to the gravitational difference between the effect of loads on the crust and gravity.

In Eq. (5), when $\Delta g = 0$, then $\Delta g^{\text{TBSCI}} = \Delta g^{\text{CMP}}$, meaning that the gravimetric isostasy becomes the Airy-Heiskanen model having a local compensation property. The presence of Δg in Eq. (5), makes the compensation mechanism regional and Δg acts as a smoother or regularisation factor of the compensation [7].

Two factors are important for modelling the compensation depth, so-called the Mohorovic discontinuity (Moho), a) the mean compensation depth (\tilde{D}_0) and b) the density contrast ($\Delta\rho$) between the crust and upper-mantle. If either of $\Delta\rho$ or \tilde{D}_0 is known the other one can be estimated from the model. The variation of Moho depth around \tilde{D}_0 can be determined by; see [7]:

$$\Delta\tilde{D} = \frac{1}{4\pi GR\Delta\rho} \sum_{\substack{n=0 \\ n \neq 1}}^{\infty} \frac{2n+1}{n-1} \beta_n^* \Gamma_n \sum_{m=-n}^n (\Delta g_{nm}^{\text{TBSCI}} - \Delta g_{nm}) Y_{nm}(\theta, \lambda) \quad (6)$$

where G is the Newtonian gravitational constant and

$$\beta_n^* = \begin{cases} 1 & \text{over oceans} \\ \left(1 + (n+2) \frac{\tilde{D}_0}{2R}\right)^{-1} & \text{over continents} \end{cases} \quad (7)$$

$$\Gamma_n = \left(\frac{R}{R - \tilde{D}_0}\right)^{n+2}. \quad (8)$$

The factor Γ_n is a signal amplifier, and when n increases this factor grows. For large values of \tilde{D}_0 , this amplification starts from lower frequencies, therefore, the series in Eq. (6) should be truncated at lower degrees [7].

$\Delta\rho$ can also be determined from $\Delta\tilde{D}$, if its available or even the product $\Delta\rho \Delta\tilde{D}$; e.g. see [7] in which the GOCE data are constrained to seismic data for determination of $\Delta\rho \Delta\tilde{D}$.

CRUST1.0 [8] is a global model having information about the thicknesses and densities of sediments, crustal crystalline, topographic heights and bathymetric depths, and the Moho depths with a spatial resolution of $1^\circ \times 1^\circ$. This means that $\Delta g_{nm}^{\text{TBSCI}}$ can be generated from CRUST1.0. In addition, numerous EGMs have been provided, which applicable for computing Δg_{nm} . **Figure 1a** shows the Moho flexure/variation computed based on Eq. (6) the CRUST1.0 model, and EGM08 [9] limited to degree and order 180, corresponding to the resolution $1^\circ \times 1^\circ$. **Figure 1b** showed the contribution of Δg ranging from -15 to 15 km to the estimated Moho depth.

3.1.2 Elastic thickness and rigidity

In flexural isostasy [10] the lithospheric is considered as an elastic shell, being flexes under loads. This shell bends based on its own mechanical properties and pressure of the loads. Elastic thickness (T_e) is one of the properties of this shell. Admittance and coherence analyses between the topography and gravity anomalies; see [11] are known methods for estimating this elastic thickness. By combining the gravimetric and flexure isostasy models the elastic thickness or rigidity of the lithosphere can be estimated as well [7]. The main assumption of this approach is that the Moho variations derived from the gravimetric and flexural isostasy theories are equal. Therefore, the elastic thickness is estimated such a way that the Moho variation estimated from the gravimetric isostasy becomes closer to that from the

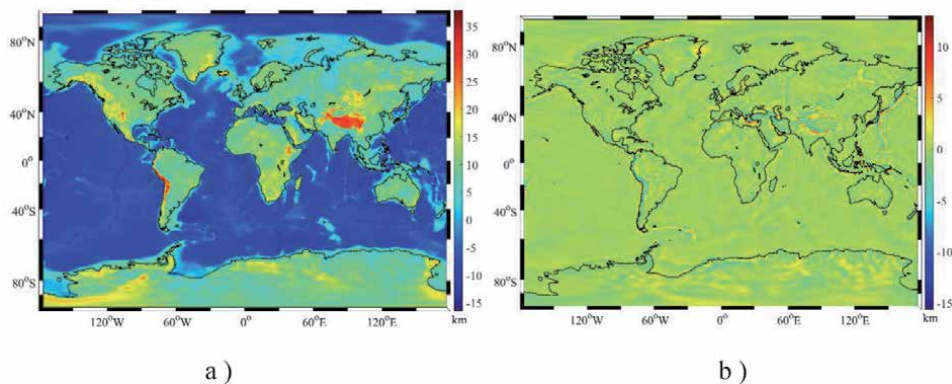


Figure 1.
 (a) Global Moho flexure, and (b) the contribution of the gravity data to the Moho flexure.

flexural isostasy, by this assumption the resulted Δg from the lithospheric properties will be [7]:

$$\Delta g = \Delta g^{\text{TBSCL}} - 4\pi GR\Delta\rho \sum_{n=0}^{\infty} \Gamma_n^{-1} \frac{n-1}{2n+1} \beta_n^* C_n^{-1} \sum_{m=-n}^n \bar{K}_{nm} Y_{nm}(\theta, \lambda) \quad (9)$$

with

$$\bar{K}_{nm} = (\bar{\rho}d)_{nm} + (\rho^S d_S)_{nm} + (\rho^C d_C)_{nm} + (\rho^I d_I)_{nm} \quad (10)$$

where $\bar{\rho}$ is the density of the topographic masses when the computation point is in continents and the density contrast between the water and topographic masses when it is over ocean, d stands for the topography height or bathymetric depth based on the position of the computation point. ρ^S and d_S are, respectively the density and the thickness of sediment layers, ρ^C and d_C the corresponding one for crustal crystalline, and ρ^I and d_I those of the ice. $(\bullet)_{nm}$ means the spherical harmonic coefficients. C_n is the compensation degree, which is derived from the flexure isostasy model:

$$C_n = \frac{n^2(n+1)^2}{R^4 g} \tilde{\Theta} + \Delta\rho \text{ and } \tilde{\Theta} = \begin{cases} D^{\text{Rig}} & \text{if flexural rigidity is desired} \\ \frac{ET_e^3}{12(1-\nu^2)} & \text{if elastic thickness is desired} \end{cases} \quad (11)$$

g is the gravity attraction, E stands for the Young modulus and ν the Poisson ratio. In fact, C_n carries the mechanical information of lithosphere including the elastic thickness.

The gravity anomaly on the left-hand side of Eq. (9), is generated from the lithosphere's mass and density structures excluding the signal from sub-lithosphere. By comparison of this gravity anomaly and the observed ones excluding the lower degrees, coming from sub-lithosphere say to degree 15 [12] elastic thickness is determined in a trial and error process.

Figure 2 is the map of elastic thickness determined from GOCE gradiometric data over Africa in [13] the same procedure as explained for Eq. (9). The large elastic thickness over the tectonic border in the ocean is not realistic.

3.1.3 Bathymetry

Determining the ocean depths using gravity data is an old subject. Over offshore areas, hydrographic surveying methods are applicable by boats and Echo-sounders, known as traditional methods, modernised today by being equipped by GNSS technologies. However, they are costly and not practicable over oceans. Satellite altimetry data cover oceans sufficiently well and bathymetry can be done with acceptable precision, but the shortcoming is the low quality of them over shallow water. In this section, the focus will be on application of gravimetry over oceans for bathymetry purpose, based on isostasy. The theory and mathematical developments are available in [7], but they are not applied so far. Then the strengths and weaknesses of the method is still unknown.

Satellite altimetry data are the distance between the satellite and the sea surface, which is not fully-coincidence to the geoid. The departure of the sea surface from geoid is called sea surface topography. For determining the geoid from satellite altimetry, the sea surface topography should be known; and for determining the sea

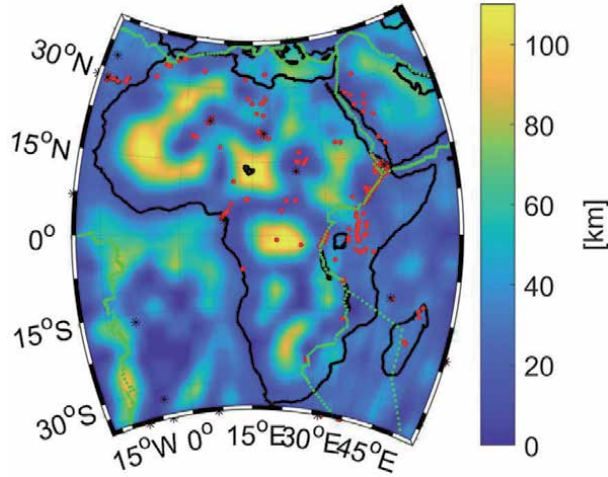


Figure 2.
 Elastic thickness determined from GOCE data over Africa [13].

surface topography, the geoid is needed. The satellite gravimetry data or gravity models can be used without any involvement with the sea surface topography, but they have low resolutions. If the average depth of ocean d_0 is available, the variations of the seafloor topography around it will be [7]:

$$\Delta d = -\frac{1}{4\pi G\rho} \sum_{n=0}^{\infty} \frac{2n+1}{B_n} \sum_{m=-n}^n (t_{nm} - v_{nm}^{B/Iso}) Y_{nm}(\theta, \lambda) - \left(\frac{R^2 A \delta_{n0}}{B_0} \right) \quad (12)$$

where δ_{n0} stands for the Kronecker delta and

$$v_{nm}^{B/Iso} = -(v_{nm}^S + v_{nm}^C) + 4\pi G R \Delta \rho \Gamma_n^{-1} \beta_n^* C_n^{-1} \left((\rho^S d_S)_{nm} + (\rho^C d_C)_{nm} \right) \quad (13)$$

$$A = \frac{1}{3R} \left(1 - \left(1 - \frac{d_0}{R} \right)^3 \right) - \Delta \rho \frac{1}{R} \Gamma_0^{-1} \beta_0^* C_0^{-1} d_0 \quad (14)$$

$$B_n = R \left(\frac{R - d_0}{R} \right)^{n+2} + R \Delta \rho \Gamma_n^{-1} \beta_n^* C_n^{-1} \quad (15)$$

v_{nm}^S and v_{nm}^C are gravitational potential of the sediment and crustal crystalline masses. Eq. (13) means the compensated gravitational potentials of sediment and crustal crystalline by the flexure isostasy. A and B_n are the contribution of the mean depth and its flexural compensation.

The important factor in bathymetry using this method is the elastic thickness of the lithosphere over oceans, which can be independently determined with a proper approximation from the age of the oceanic lithosphere by [14]:

$$T_e = 2.7\sqrt{t} \quad (16)$$

where t is the age of oceanic lithosphere in Ma.

3.1.4 Ice thickness

Determination the thickness of continental ice and its changes is important these days because of global warming. The continental ice is melted and water flow enters

oceans and causes the sea level to rise. This is an issue which affect the Earth climate and may have risk of entering water to low land areas. Some satellite missions have been designed and developed for measuring the ice thickness using radar signals directly. This thickness can also be determined indirectly using gravimetry data. By assuming that the ice mass covers the surface of the Earth and it is part of the Earth's solid topography, its thickness can be determined using the following spherical harmonic expansion [7]:

$$d_I = \frac{1}{4\pi GR} \sum_{n=0}^{\infty} \left(-\frac{\Delta\rho^I}{2n+1} + \Delta\rho\rho^I\Gamma_n^{-1}\beta_n^* C_n^{-1} \right)^{-1} \sum_{m=-n}^n \left(t_{nm} - v_{nm}^{TSC/Iso} \right) Y_{nm}(\theta, \lambda) \quad (17)$$

where $\Delta\rho^I$ is the density contrast between the upper crust and ice, ρ^I stands for the density of ice, and

$$v_{nm}^{TSC/Iso} = -(v_{nm}^T + v_{nm}^S + v_{nm}^C) + 4\pi Gr\Delta\rho\Gamma_n^{-1}\beta_n^* C_n^{-1} \left((\rho^T H)_{nm} + (\rho^S d_S)_{nm} + (\rho^C d_C)_{nm} \right). \quad (18)$$

Note that Eq. (17) is based on the linear approximation of the involved binomial terms related to the topographic heights. Such an approximation is good as long as the heights are not large and the maximum degree of the expansion is not high. For example, for a height of 10 km and maximum degree 360, the relative error of this approximation will be 11%, for degree 180 is 4% and when the height is 5 km for the maximum degree of 360 it will be 4% and less than 1% for 180. Since we have applied isostasy principle to obtain this equation, higher resolution than 180 is not needed, then approximation should be rather fine. One issue is the elastic thickness of lithosphere which is needed to determine the compensation degrees, which should be known from independent sources.

3.1.5 Sediment basement determination

Sediments are located at the surface of the upper-crust resulted from erosion during a long period of time. They are compacted by time meaning that their density will be high at their bottom and low at the surface. Therefore, the process of determining their thickness is not simple because the sediment density is an exponential function increasing by depth. In [7] some of the density contrast models have been presented and the gravitational potential of sediments have been modelled in spherical harmonics series. If we assume an average density for sediments the following approximate formula can be used to determine its thickness

$$d_S = \frac{\rho^S}{-4\pi GR} \sum_{n=0}^{\infty} \left(-\frac{1}{2n+1} + \Delta\rho\Gamma_n^{-1}\beta_n^* C_n^{-1} \right)^{-1} \sum_{m=-n}^n \left(t_{nm} - v_{nm}^{BC/Iso} \right) Y_{nm}(\theta, \lambda) \quad (19)$$

where $\Delta\rho^I$ is the density contrast between the upper crust and ice, ρ^I stands for the density of ice, and

$$v_{nm}^{BC/Iso} = -(v_{nm}^B + v_{nm}^C) + 4\pi GR\Delta\rho\Gamma_n^{-1}\beta_n^* C_n^{-1} \left((\rho^B H)_{nm} + (\rho^C d_C)_{nm} \right). \quad (20)$$

One important parameter which should be known for sediment thickness determination using Eq. (19) is the elastic thickness of lithosphere, needed for computing

the compensation degree. Over ocean there is a known relation between the lithospheric plate age and its elastic thickness see Eq. (16), but not over continents.

3.1.6 Runcorn's theory and sub-lithospheric shear stresses

Mantle convection can also be studied by the long wavelength structure of the Earth gravity field. The Navier–Stokes equations of convection can be solved and simplified it in such a way that simple formula for shear stress at the base of lithosphere is obtained see [15]:

$$\begin{pmatrix} \tau_{zx} \\ \tau_{zy} \end{pmatrix} = \frac{g}{4\pi G(R - D_{\text{Lith}})} \sum_{n=2}^{\infty} \frac{2n+1}{n+1} \left(\frac{R}{R - D_{\text{Lith}}} \right)^{n+1} \sum_{m=-n}^n t_{nm} \begin{pmatrix} \frac{\partial Y_{nm}(\theta, \lambda)}{\partial \theta} \\ \frac{\partial Y_{nm}(\theta, \lambda)}{\sin \theta \partial \lambda} \end{pmatrix} \quad (21)$$

where τ_{zx} and τ_{zy} are the shear-stresses at the base of the lithosphere toward north and east, respectively. D_{Lith} is the depth of boundary between lithosphere and mantle.

Eq. (21) is known as Runcorn's formulae. He assumed that the mantle convection creates only the shear stresses at the base of the lithosphere. Most importantly, he assumed that:

- a. the viscosity of mantle is constant.
- b. the toroidal flow in the mantle is negligible.
- c. the mantle is Newtonian.

Only by these assumptions the simple formula having a direct relation with the gravity data can be obtained. Many believe that the Runcorn simple solution is not realistic and successful, in spite of different efforts for justifying the applicability of this theory [16–18].

In Eq. (21), the maximum degree of expansion should not be infinity as the mantle convection contributes mainly in low frequencies of the gravity field. In [16] degrees between 13 to 25 are suggested to reduce the contributions from the core and lithosphere. However, in [12] the degrees below 15 are considered as contributions from sub-lithosphere.

Figure 3a and **b** show the map of the sub-lithospheric shear stresses τ_{zx} and τ_{zy} , respectively, using Eq. (21) at the lithospheric depths of Conrad and Lithgow-Bertelloni model [19] over Iran. One issue in applying Eq. (21) is the choice of the maximum degree of expansion based on the lithospheric depth. When the base of the lithosphere is deeper, this degree should be lower and vice versa.

In [20] a better theory was developed for modelling the mantle convection using the displacement vectors of and tectonic movement. They also use the long wavelength portion of a geoid model in their solution, but the contribution of geoid is not very significant. This could be the reason that Runcorn has simplified the same mathematical models by ignoring the significant parameters and emphasising on the weakest one.

3.1.7 Stress propagation through the lithosphere from its base

By assuming that the lithosphere is an elastic shell, solution of the spherical boundary-value problem of elasticity can be applied for presenting the stress status inside the lithosphere. The stresses at base and top of the lithosphere is considered

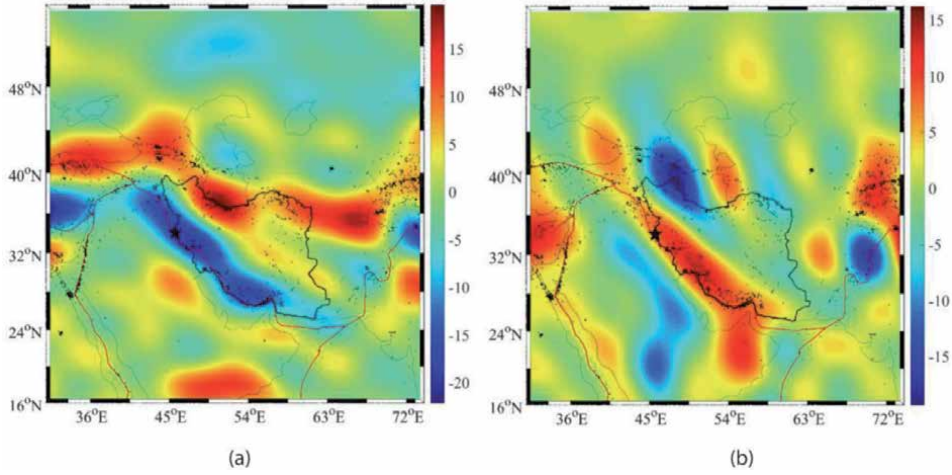


Figure 3.
 (a) τ_{zz} and (b) τ_{yz} , [MPa], [18] with permission from the publisher.

as the boundary-values. This subject was investigated by in [21] based on the solution of this problem by [22], and developed further by Fu and Huang [17]. The general solution of the boundary-value problem of elasticity is a displacement vector with four constants, which should be determined from the boundary-values. To do so this vector should be converted to general solutions for stress by the known relation between displacement and strain; and strain and stress [7]. The general solutions for stress include also those four constants. The Runcorn formula (21) can be considered as the low boundary-values of stresses, and it is assumed that the stress will disappear at the upper boundary, meaning that there is no stress. By selecting these boundary-values, a system of four equations is constructed and its solution will be those constants. By inserting these constants into the general solutions the stresses at a geocentric distance of r inside the lithospheric shell can be estimated. Also, they can be used in the general solutions of the strain and displacement to determine the strain tensor and displacement vector; for details see [7]. The elements of the stress tensor are:

$$\tau_{zz} = \frac{1}{r} \sum_{n=2}^{\infty} (\tilde{\lambda}K_n^1 + 2\tilde{\mu}K_n^2) \sum_{m=-n}^n t_{nm} Y_{nm}(\theta, \lambda) \quad (22)$$

$$\tau_{xx} = \frac{1}{r} \sum_{n=2}^{\infty} \sum_{m=-n}^n t_{nm} \left\{ (\tilde{\lambda}K_n^1 + 2\tilde{\mu}K_n^3) Y_{nm}(\theta, \lambda) + 2\tilde{\mu}K_n^5 \frac{\partial^2 Y_{nm}(\theta, \lambda)}{\partial \theta^2} \right\}, \quad (23)$$

$$\tau_{yy} = \frac{1}{r} \sum_{n=2}^{\infty} \sum_{m=-n}^n t_{nm} \left\{ (\tilde{\lambda}K_n^1 + 2\tilde{\mu}K_n^3) Y_{nm}(\theta, \lambda) + 2\tilde{\mu}K_n^5 \left[\frac{1}{\sin^2 \theta} \frac{\partial^2 Y_{nm}(\theta, \lambda)}{\partial \lambda^2} + \cot \theta \frac{\partial Y_{nm}(\theta, \lambda)}{\partial \theta} \right] \right\} \quad (24)$$

$$\tau_{xz} = \frac{\tilde{\mu}}{r} \sum_{n=2}^{\infty} \sum_{m=-n}^n t_{nm} K_n^4 \frac{\partial Y_{nm}(\theta, \lambda)}{\partial \theta} \quad (25)$$

$$\tau_{yz} = \frac{\tilde{\mu}}{r \sin \theta} \sum_{n=2}^{\infty} \sum_{m=-n}^n t_{nm} K_n^4 \frac{\partial Y_{nm}(\theta, \lambda)}{\partial \lambda}, \quad (26)$$

$$\tau_{xy} = \frac{\tilde{\mu}}{r \sin \theta} \sum_{n=2}^{\infty} \sum_{m=-n}^n t_{nm} K_n^5 \left(\frac{\partial^2 Y_{nm}(\theta, \lambda)}{\partial \theta \partial \lambda} - \cot \theta \frac{\partial Y_{nm}(\theta, \lambda)}{\partial \lambda} \right) \quad (27)$$

where $\tilde{\mu}$ and $\tilde{\lambda}$ are the elasticity coefficients, which can be determined from seismic data. For the coefficients K_n^i , $i = 1, 2, \dots, 5$, which are derived from the constants see [7].

Figure 4 shows the elements of the stress tensor for an earthquake at the depth of 10 km occurred in 25th of November 2018 with the magnitude of 6.3. The earthquake epicentre (34.361° N, 45.744° E) was located near the town Sar-e-Pol Zahab in West Iran close to the border with Iraq. The stress tensor has been determined by the Gravity field and Climate Experiment follow-on (GRACE-FO) [24] gravity model in October 2018.

3.2 Time-variable gravity field

The gravity field of the Earth varies in time due to different Geodynamical phenomena. This means that time-variable gravity data can be used for studying them. For example, the satellite missions Gravity Recovery and Climate Experiment (GRACE) [23] and GRACE-FO [24] have been designed and developed for determining temporal variations of the gravity field. Here, some of the phenomena causing such variations like Earthquakes, post-glacial rebound, ground water variations.

3.2.1 Earthquakes

Earthquakes are the result of energy extractions in the solid Earth based on different reasons. Whether an Earthquake is detectable by time-variable gravity

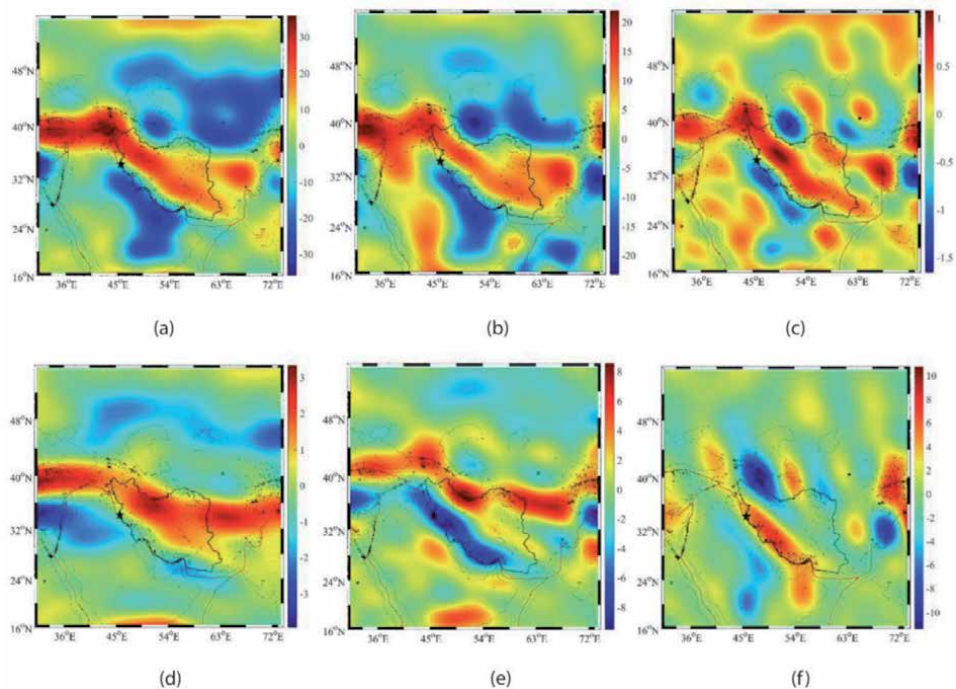


Figure 4. (a) τ_{xx} (b) τ_{yy} (c) τ_{zz} (d) τ_{xz} (e) τ_{yz} and (f) τ_{xy} [MPa], the star is the earthquake epicentre and the small dots are the distribution of seismic points, [18] with permission from the publisher.

data depends on the magnitude of the Earthquake, resolution and sensitivity of gravimetry. The GRACE and GRACE-FO monthly gravity models are applicable for studying the large Earthquakes. Geoid, gravity anomalies/disturbances, gravity gradients, stress, strain and even displacements can be computed from such gravity models before and after the Earthquakes. Changes of each quantities before and after the Earthquake provides information about the effect of the Earthquake on the gravity regime of area. However, one important issue is that the changes due to the non-Earthquake variations, like hydrological signals, should be removed or reduced from the gravity data/models prior to analysing any Earthquake.

Figure 5 shows the map of changes of gravity anomaly before and after the Zar-e-Pol Zahab Earthquake. Positive values are seen over the area and around the Earthquake's epicentre illustrates by a circle, meaning increase of gravity, whilst the negative values are seen in eastern part of the area or gravity reduction. The black dot are earthquake points.

3.2.2 Determination of epicentre of shallow earthquakes

In [25] a connection between the maximum shear strain of the gravity strain tensor and epicentre of shallow Earthquakes were presented. A theory was presented in [26] for determining gravity strain tensor. In order to explain this type of strain, consider the geoid as a deforming surface. The changes of the geoid surface are regarded as a displacement field, and accordingly, this field is converted to a strain tensor, named gravity strain tensor with the following mathematical definition [26]:

$$\mathbf{S} = \frac{1}{2} (\mathbf{B}^{-1} \mathbf{b} \mathbf{b} \mathbf{B}^{-1} - \mathbf{I}) \quad (28)$$

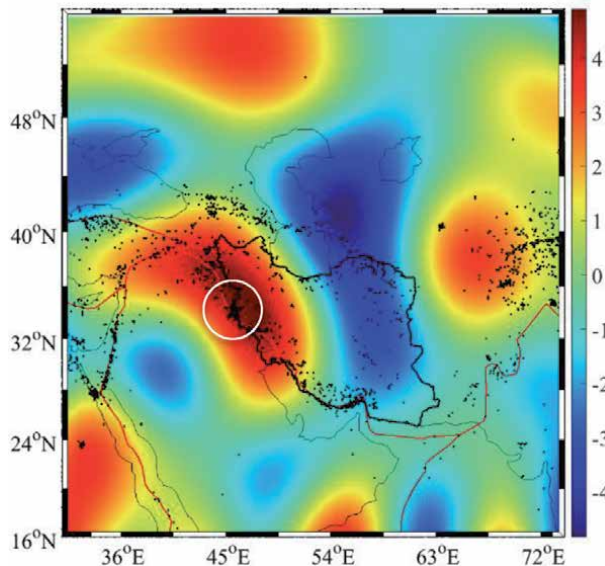


Figure 5. Changes of the gravity anomalies before and after the Sar-e-pol Zahab earthquake on 25th November 2018, determined by the GRACE-FO gravity models in December 2018 and January 2019, [μGal]. Black dots are active seismic points and the start the earthquake epicentre. [18] With permission from publisher.

where.

$$\mathbf{B} = \begin{bmatrix} V_{xx}(t_1) & V_{xy}(t_1) & V_{xz}(t_1) \\ V_{xy}(t_1) & V_{yy}(t_1) & V_{yz}(t_1) \\ V_{xz}(t_1) & V_{yz}(t_1) & V_{zz}(t_1) \end{bmatrix} \text{ and } \mathbf{b} = \begin{bmatrix} V_{xx}(t_2) & V_{xy}(t_2) & V_{xz}(t_2) \\ V_{xy}(t_2) & V_{yy}(t_2) & V_{yz}(t_2) \\ V_{xz}(t_2) & V_{yz}(t_2) & V_{zz}(t_2) \end{bmatrix}. \quad (29)$$

In fact, \mathbf{B} and \mathbf{b} are the gravitational tensor in the local north-oriented frame at two epochs of t_1 before and t_2 after deformation.

Dilatation and maximum shear strain of the gravity strain tensor are, respectively

$$\Delta = \lambda_{\max}^{\text{eig}} + \lambda_{\min}^{\text{eig}} \quad (30)$$

$$\gamma = \lambda_{\max}^{\text{eig}} - \lambda_{\min}^{\text{eig}} \quad (31)$$

where $\lambda_{\max}^{\text{eig}}$ and $\lambda_{\min}^{\text{eig}}$ the largest and smaller eigenvalue of the gravity strain tensor.

The map of the maximum shear strain over the area experiencing a shallow Earthquake will show a high value at the Earthquake epicentre; see [25].

In order to represent an example about the application of this theory, the eastern Turkey Earthquake occurred on 2010-2103-08 at 7:41:41 UTC and depth of 10 km is considered. The position of the earthquake epicentre is 38.709°N and 40.051°E according to the United States Geological Survey (USGS); see **Figure 6**. In this figure, the map of the maximum shear strain determined from the GRACE monthly gravity models are over the area. The maximum shear strain have been computed from two years of gravity models before and after the Earthquake, and the yellow rectangle shows the approximate position of the Earthquake epicentre. Note that the colour of the circle was chosen for better visualisation of the epicentre reported by the USGS, and is not related to the colourbar present for the map.

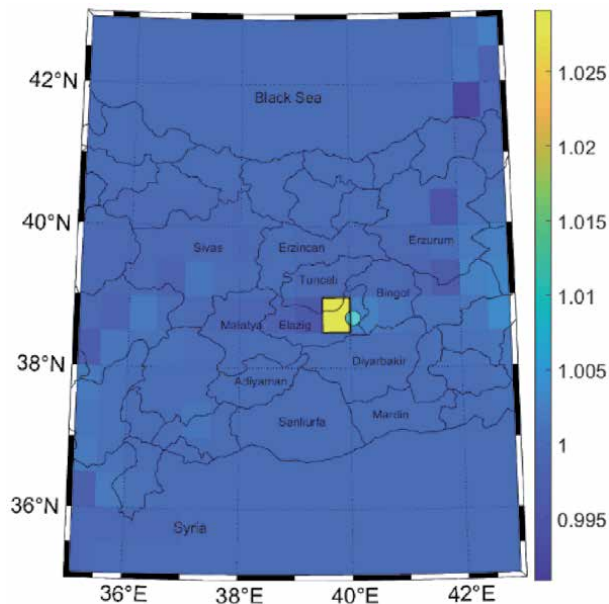


Figure 6.
 The position of the eastern Turkey earthquake epicentre detected by the gravity strain approach and USGS, [27].

3.2.3 Post-glacial rebound and mantle viscosity

Mantle is a viscous medium and its viscosity creates an upward force at the base of the lithosphere against bending due to loads. The lithosphere would bend more if it was buoyant over a less viscous medium. In addition, the age of load is an important factor in the lithosphere thrusting into the mantle; older lithosphere is more inside the mantle than the younger one. Both of the lithospheric strength and the mantle's viscosity keep the lithosphere in an isostatic equilibrium against loads pushing the lithosphere downwards. If these loads are removed, this balance is destroyed and the mantle pushes the lithosphere upwards causing the land rise or uplift.

In the ice age period, huge ice masses existed at the surface of the lithosphere, and by the increase of the Earth's temperature, they were melted and the lithospheric rebound began toward the isostatic equilibrium. This phenomena is called post-glacial rebound, or glacial isostatic adjustment, causing land uplift, which can be monitored by the temporal changes of gravity data. For example, if the geoid rate is determined using time-variable gravity models, the land uplift rate due to this rebound can be computed by [7, 28]:

$$\dot{h}(\theta, \lambda) = \frac{\gamma}{4\pi GR} \sum_{n=0}^{\infty} \frac{2n+1}{\kappa_n''} \sum_{m=-n}^n \Delta \dot{N}_{nm} Y_{nm}(\theta, \lambda) \quad (32)$$

where $\Delta \dot{N}_{nm}$ the spherical harmonic coefficients of the geoid rate and

$$\kappa_n'' = \rho^C + \Gamma_n^{-1} \Delta \rho. \quad (33)$$

The effect of hydrological signals should be removed from the time-variable gravity models prior to applying them for determining the geoid rate by a linear regression. **Figure 7a** is the map of this rate showing variation from -0.6 to 0.4 mm/yr., determined from the GRACE time-variable gravity models during the of the GRACE mission and after removing the hydrological signals using Global Land data Assimilation System (GLDAS) [29] model over Fennoscandia, which is experiencing the post-glacial rebound after the ice age. The geoid rate of change has been computed globally and after performing a spherical harmonic analysis its

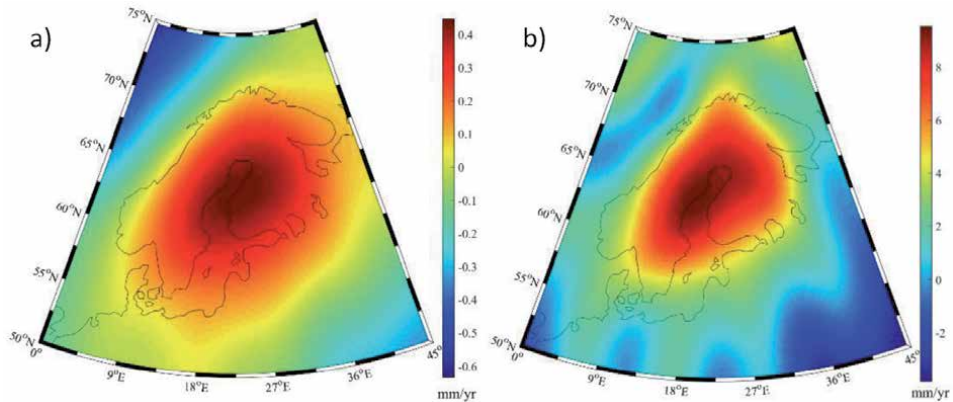


Figure 7. (a) Geoid trend during 15 years of GRACE mission, (b) land uplift model determined from geoid rate of change.

harmonics have been computed and inserted into Eq. (32) for estimating the land uplift rate; see **Figure 7b**. The uplift rate varies from -4 to 9 mm/yr. with the maximum around the centre of Gulf of Bohemia.

In [30] methods for determining the mantle viscosity were presented, but the geodetic approach was proposed in [31] and shown that the highest correlation between the land uplift data and geoid is achieved when the geoid is computed from degree 10 to 70. In [29, 32] used the spherical harmonic degrees to 23 instead of 70. In fact, degree 23 is obtained by performing a correlation analysis between the geoid derived to different maximum degrees and the land uplift model determined by the GNSS measurements. In [33] there is a discussion about some frequencies window of the geoid signal affected by the post-glacial rebound and later investigation in [33] it is shown that this frequency window is limited between degrees 10 to 23. If we accept this theory the viscosity of the upper mantle can be determined by [7]:

$$\tilde{\eta} = -\frac{\gamma^2 \rho_m}{4\pi G h(\theta, \lambda)} \sum_{n=10}^{23} \frac{2n+1}{\kappa_n''(2n+4+3/n)} \sum_{m=-n}^n N_{nm} Y_{nm}(\theta, \lambda) \quad (34)$$

where ρ_m is density of the upper mantle.

The mean viscosity of the upper mantle will be $(5.0 \pm 0.2) \times 10^{21}$ Pa, and in the case of using Eq. (34), it will be $(6.0 \pm 0.3) \times 10^{21}$ Pa over Fennoscandia [7].

3.2.4 Monitoring hydrological signals

Hydrological signals are the main surfaces of fast temporal changes of the gravity field. They come from ground water storage (GWS), snow water equivalent (SWE), solid moisture (SM) and Canopy (CAN). Different models have been presented these signals except for the GWS and the most known one is the GLDAS model [29] which has had good agreement with the temporal variations of the gravity field determined by GRACE. However, the GRACE models provide information about the total water, or equivalent water height, or a summations of SM, SWE, CAN and GWS. Therefore, if one of these hydrological signals is required, it

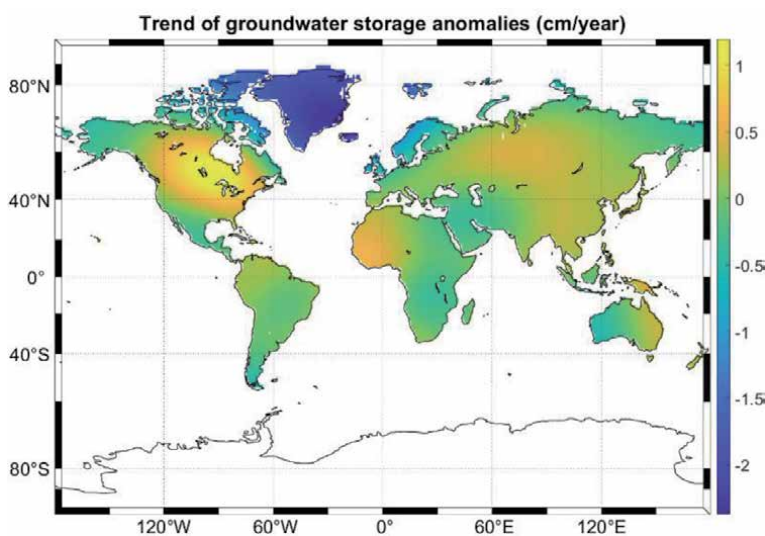


Figure 8.
 The global ground water storage (WGS) rate determined from 15 years of GRACE gravity models and GLDAS [27].

can be determined from a combination of the GRACE and hydrological models; see [7, 34]. In the case where the GWS is needed, it can be computed by:

$$\delta h_{nm}^{GWS} = \sum_{n=2}^{\infty} \sum_{m=-n}^n \left(\frac{1}{4\pi GR\gamma} \frac{2n+1}{1+k_n} \delta v_{nm} - \frac{1}{\rho_w} (\delta \rho_{nm}^{SM} + \delta \rho_{nm}^{SWE} + \delta \rho_{nm}^{CAN}) \right) Y_{nm}(\theta, \lambda) \quad (35)$$

where ρ_w is the density of water, δv_{nm} is the changes of the gravitational potential, k_n is the Love numbers, $\delta \rho_{nm}^{SM}$, $\delta \rho_{nm}^{SWE}$ and $\delta \rho_{nm}^{CAN}$ are the spherical harmonic coefficients of the densities of SM, SWE and CAN, respectively.

Figure 8 is the global map of the GWS all over the globe computed by the GRACE gravity models during 15 years, 2002 to 2017. Note that the post-glacial rebound and earthquake signals have not be excluded in the computations.

The largest GWS is seen over Hudson Bay in Canada, and the green land. Both of these places are known as active areas for post-glacial rebound. Reduction of GWS is seen in the Middle East and eastern Africa, and Western Australia and increase in Russia, western Africa, eastern Australia.

4. Concluding remarks

The goal of this chapter was to demonstrate applications of the Earth's gravity field in Geodesy and Global Geophysics. In Geodesy, the main goal is to determine the physical shape of the Earth, or the geoid, and its importance in levelling and height systems were discussed. Philosophies behind three well-known methods of geoid determination, such as Remove-Compute-Restore, Stokes-Helmert and Least-squares modification of the Stokes formula with additive corrections, were discussed.

When the temporal variation of the gravity field is disregarded and the field is considered static, some geophysical subjects can be studied by them to understand the Earth's interior such as the crustal structure, density contrast between the crust and mantle, sediment basement, ice thickness, and depth of ocean water determination. In addition, the sub-lithospheric stress induced by mantle convection and its propagation through the lithosphere can also be determined using gravity data.

By studying the temporal variations of the gravity field, Geodynamic phenomena can be studied. Post-glacial rebound, determining the land uplift rate and mantle viscosity, studying the earthquakes and their epicentre and also ground water storage mapping are the subject which can be studied by these variations.

One distinction between the application of the gravity field in Geodesy and global geophysics is the resolution of gravity field. The main purpose of Geodesy is to determine the shape of the Earth as precise and accurate as possible, and focus is on recovering the high frequencies of the gravity field, by combining satellite and terrestrial data with mathematical tools with the least approximations. However, in Geophysics due to lack our knowledge about the Earth's interior structure and dynamic, different assumptions have been made and also the mathematical models are developed based on them. In addition high resolution gravity data do not play a significant role in global Geophysics.

Acknowledgements

The author is thankful to Farzam Fatolazadeh for generating maps of the maximum shear gravity strain and global ground water storage.

Author details

Mehdi Eshagh
University West, Trollhättan, Sweden

*Address all correspondence to: mehdi.eshagh@hv.se

IntechOpen

© 2021 The Author(s). Licensee IntechOpen. This chapter is distributed under the terms of the Creative Commons Attribution License (<http://creativecommons.org/licenses/by/3.0>), which permits unrestricted use, distribution, and reproduction in any medium, provided the original work is properly cited. 

References

- [1] Forsberg R. and Sideris M.G. Geoid computations by the multi-band spherical FFT approach. *Manuscripta Geodaetica*. 1993, 18, 82–90
- [2] Vaníček P. and Martinec Z. Stokes-Helmert scheme for the evaluation of a precise geoid. *Manuscripta Geodaetica*, 1994, 19, 119–128.
- [3] Sjöberg, L. E. Least-Squares modification of Stokes' and Vening-Meinesz' formula by accounting for truncation and potential coefficients errors, *Manuscripta Geodaetica*, 1984, 9, 209–229.
- [4] Heiskanen W. and Moritz H. *Physical Geodesy*, W.H. Freeman and Co., 1967, San Francisco-London.
- [5] Tscherning C.C. Geoid Determination for the Nordic Countries Using Collocation, *Proceedings of the General Meeting of IAG*, Tokyo, 1982, May 7–15.
- [6] Martinec Z. *Boundary-Value Problems for Gravimetric Determination of a Precise Geoid*, Springer. 1998.
- [7] Eshagh M. *Satellite gravimetry and the solid Earth*, Elsevier, 2020.
- [8] Laske G., Masters, G., Ma, Z. and Pasyanos, M.E. Update on CRUST1.0—a 1-degree global model of Earth's crust. *Geophysical Research Abstracts* 15, 2013 (Abstract EGU2013–2658).
- [9] Pavlis, N. K., Holmes S.A: Kenyon S. C. and Factor J. K. *Gravitational Model 2008 (EGM2008)*, *J. Geophys. Res.*, 2010, 117, B04406.
- [10] Vening Meinesz, F.A., Une nouvelle methode pour la reduction isostatique regionale de l'intensite de la pesanteur. *Bull. Geod.* 1931 29 (1), 33–51.
- [11] Watts AB., *Isostasy and flexure of the lithosphere*. Cambridge University Press, Cambridge, 2001.
- [12] Stewart, J. & Watts, A.B., Gravity anomalies and spatial variations of flexural rigidity at mountain ranges, *J. Geophys. Res.* 1997, 102(B3), 5327–5352
- [13] Eshagh M. and Pitoňák M. Elastic thickness determination from on-orbit GOCE data and CRUST1.0, *Pure Appl. Geophys.*, 2018, 176, 2, 685–696.
- [14] Calmant S., Francheteau J. and Cazenave A. Elastic Layer Thickening with Age of the Oceanic Lithosphere: A Tool for Prediction of the Age of Volcanoes or Oceanic Crust, *Geophysical Journal International*, Volume 100, Issue 1, January 1990, Pages 59–67,
- [15] Runcorn S.K. Flow in the mantle inferred from the low degree harmonics of the geopotential, *Geophys. J. Int.*, 1967, 14(1–4), 375–384.
- [16] Liu H.S. Mantle convection pattern and subcrustal stress under Asia, *Phys. Earth Planet. Inter.*, 1978, 16(3), 247–256.
- [17] Fu R. and Huang P. Global stress pattern constrained on deep mantle flow and tectonic features, *Phys. Earth Planet. Inter.*, 1990, 60(1–4), 314–323.
- [18] Eshagh M., Fatolazadeh F. and Tenzer R. Lithospheric stress, strain and displacement changes from GRACE-FO time-variable gravity: case study for Sar-e-Pol Zahab Earthquake 2018, *Geophysical Journal International*, 2020, 223, 379–397.
- [19] Conrad C.P. & Lithgow-Bertelloni C. Influence of continental roots and asthenosphere on plate-mantle coupling, *Geophys. Res. Lett.*, 2006, 33 (5), L05312, doi.org/10.1029/2005GL025621.

- [20] Hager B.H. and O'Connell, R.J. A simple global model of plate dynamics and mantle convection, *J. Geophys. Res.*, 1981, 86(B6), 4843–4867.
- [21] Liu H.S. A dynamical basis for crustal deformation and seismotectonic block movements in central Europe, *Phys. Earth Planet. Inter.*, 1983, 32, 146–159.
- [22] Love A.E.H. *A Treatise on the Mathematical Theory of Elasticity*, Dover Publication, New York, 1944, p. 249
- [23] Tapley B. D., Bettadpur S., Ries J., Thompson P. F., and Watkins M. M. GRACE measurements of mass variability in the Earth system. *Science* 2004, 305, 503–505, DOI: 10.1126/science.1099192.
- [24] Kornfeld R.P., Arnold, B.W., Gross, M.A., Dahya, N.T., Klipstein, W.M., Gath, P.F. & Bettadpur, S. GRACE-FO: the gravity recovery and climate experiment follow-on mission, *J. Spacecr. Rockets*, 2019, 56(3), doi.org/10.2514/1.A34326.
- [25] Fatolazadeh F., Kalifa G., and Javadi Azar R. Determination of earthquake epicenter based on invariant quantities of GRACE strain gravity tensor, *Scientific Reports*, 2019, 10, 7636.
- [26] Dermanis A., and Livireratos E. Applications of deformation analysis in geodesy and geodynamics. *Reviews of Geophysics and Space Physics*, 1983, 21, 41–50.
- [27] Fatolazadeh F. Personal communication, 2021
- [28] Sjöberg L.E and Bagherbandi M. A study on the Fennoscandian post-glacial rebound as observed by present-day uplift rates and gravity field model GOCO02S, *Acta Geodetica et Geophysica Hungarica*, 2013, 48, 3, 317–331.
- [29] Rodell M., Houser P. R., Jambor U., Gottschalck J., Mitchell K., Meng C. J., Arsenault K., Cosgrove B., Radakovich J., Bosilovich M., Entin J. K., Walker J. P., Lohmann D., and Toll D. The Global Land Data Assimilation System. *Bulletin of the American Meteorological Society*, 2004, 85, 381–394.
- [30] Fjeldskaar W. and Cathles L. The present rate of uplift of Fennoscandia implies a low-viscosity asthenosphere. *Terra Nova*, 1991, 3, 393–400.
- [31] Bjerhammar A., Stocki S., Svensson L. A geodetic determination of viscosity. The Royal Institute of Technology, Stockholm, 1980.
- [32] Sjöberg LE Land uplift and its implications on the geoid in Fennoscandia. *Tectonophysics*, 1983, 97,97–101.
- [33] Shafiei Joud M.S., Sjöberg L.E. and Bagherbandi M. Use of GRACE data to detect the present land uplift rate in Fennoscandia, 2017, 209, 2, 909–922.
- [34] Wahr J., Molenaar M., and Bryan F. Time variability of the Earth's gravity field: Hydrological and oceanic effects and their possible detection using GRACE. *Journal of Geophysical Research*, 1998, 103, 30,229–32,205.

On Moho Determination by the Vening Meinesz-Moritz Technique

Lars Erik Sjöberg and Majid Abrehdary

Abstract

This chapter describes a theory and application of satellite gravity and altimetry data for determining Moho constituents (i.e. Moho depth and density contrast) with support from a seismic Moho model in a least-squares adjustment. It presents and applies the Vening Meinesz-Moritz gravimetric-isostatic model in recovering the global Moho features. Internal and external uncertainty estimates are also determined. Special emphasis is devoted to presenting methods for eliminating the so-called non-isostatic effects, i.e. the gravimetric signals from the Earth both below the crust and from partly unknown density variations in the crust and effects due to delayed Glacial Isostatic Adjustment as well as for capturing Moho features not related with isostatic balance. The global means of the computed Moho depths and density contrasts are 23.8 ± 0.05 km and 340.5 ± 0.37 kg/m³, respectively. The two Moho features vary between 7.6 and 70.3 km as well as between 21.0 and 650.0 kg/m³. Validation checks were performed for our modeled crustal depths using a recently published seismic model, yielding an RMS difference of 4 km.

Keywords: crustal depth, Moho density contrast, Moho depth, Vening Meinesz-Moritz method

1. Introduction

Traditionally, the structure of the Earth's interior is divided according to its chemical and physical properties into crust, mantle, outer core and inner core. The oceanic crust ranges from 5 to 10 km depth, while the continental crust ranges from 35 to 70 km depth. The layer below the crust is the mantle, which is the thickest layer of the Earth. It can be divided into the upper (extending down to 660 km from the Earth's surface) and lower mantle (down to 2900 km beneath the surface). The innermost layer of the Earth is the core, which can be decomposed into the outer and inner core. (A modern decomposition of the Earth's interior is based on its main mechanical properties: the lithosphere and asthenosphere, of main interest in global geodynamics, plate tectonics and motion, but not for this study).

The geoscientist typically uses three sources of information to figure out the interior of the Earth's structure:

The first source is understood by direct evidence from rock samples by drilling projects. In this way, the scientist attempts to drill holes in the Earth's surface, to a maximum depth of about 12 km, and explode rocks for inferring the conditions within the Earth's interior. The drilling method is severely limited, because it is difficult to drill a deep hole due to the high pressure and temperature, and it is also a very time-consuming and expensive technology (see [1]).

The second source includes the records of seismic waves, which are generated, for example, by earthquakes, explosions, volcanoes and other natural sources. Accordingly, specialists can detect information about the Earth's interior, e.g. depth to density discontinuities, through detailed analysis of seismic data. Also, by studying the velocity of the wave, it can to some extent be used for estimating the density of the medium. At this point it deserves to be mentioned that the seismic data are also expensive to collect and therefore sparse and in-homogeneously distributed around the Earth (see [2]).

The third set of information in modeling the Earth's interior is the recent gravity field models, generated through modern satellite gravity missions such as Challenging Mini-satellite Payload (CHAMP), Gravity Recovery and Climate Experiment (GRACE) and Gravity field and steady state Ocean Circulation Explorer (GOCE), which can provide a global and homogeneous coverage of data. An improvement can also be obtained in the accuracy and spatial resolution of these models by combining them with airborne and ground-based gravity data as well as satellite altimetry data over the oceans. Other important sources for studying Earth's interior are its magnetic field and meteorites.

1.1 Background of Moho modeling

The primary interface of the Earth's interior is the boundary between the Earth's crust and mantle, which is called the Mohorovičić discontinuity (or Moho). This discontinuity was first discovered in 1909 by the Croatian seismologist Andrija Mohorovičić, when analyzing seismograph records of an earthquake in the Kapula valley, namely *P*-waves (compressional waves) and *S*-waves (shear waves). He noticed that the *P*-waves, which travel deeper into the Earth, moved faster than those that travel nearer the surface. Accordingly, he concluded that the Earth is not homogeneous, and at a specific depth there must be a boundary surface, which distinguishes two media with different compositions, and by which the seismic waves propagate with different velocities (see [3]).

Currently the Moho interface can be studied using two main methods: the gravimetric and seismic ones. These methods cannot provide exactly the same results, as they are based on different hypotheses, different types, qualities and spatial distributions of data (see, e.g. [4, 5]).

The seismic methods are the major traditional techniques in modeling the thickness of the Earth's crust (the Moho depth, MD), where the base of the crust is defined as the Moho. Another Moho constituent is the Moho Density Contrast (MDC), which can be estimated from the change of velocity of a seismic wave passing through the Moho boundary. Models based on seismic data can be locally very accurate but useless in areas without adequate seismic observations, particularly over large portions of the oceans. In addition, the seismic data acquisition is costly with lack of global coverage [6].

In contrast, while using satellite gravity data, information on the Moho can be inferred from a uniform and global data set. However, Moho models based on gravity data are in general characterized by simplified hypotheses to guarantee the uniqueness of the solution of the inverse gravitational problem (see, e.g. [7]). As we will show in Section 2.1, gravity data alone cannot separate the MD from the MDC, but additional information is needed to solve this problem. In any case, due to the complementary information described above, a combined gravimetric-seismic method could be fruitful in modeling the Moho.

Much research using seismic surveys for recovering the Moho interface has been performed in the last decades. For instance, [8, 9] compiled global Moho models based on seismic data analysis, and [10] estimated the MD using seismic surface

waves. For global studies the most frequently used crustal models are the CRUST2.0 [11] and CRUST1.0 models [12], compiled with $2^\circ \times 2^\circ$ and $1^\circ \times 1^\circ$ resolutions, respectively. More recently, [13] developed a global crustal thickness model and velocity structure from geostatistical analysis of seismic data, and we hereafter call this model CRUST19.

Over large areas of the world with a sparse coverage of seismic data, in particular at sea, a gravimetric-isostatic or combined gravimetric/seismic method can be prosperous. For example, [14] modified the Airy/Heiskanen theory ([15], Section 3.4) by introducing a regional isostatic compensation model based on a thin plate lithospheric flexure model [16, p. 114]. [17, Section 8] generalized the Vening Meinesz hypothesis from a regional to global compensation. [7] expressed the Vening Meinesz-Moritz (VMM) problem as that of solving a non-linear Fredholm integral equation, and presented some solutions for recovering the MD. The VMM method was also followed up by some additional theoretical studies, such as methods for estimating the MDC [6] and for reducing the Bouguer gravity anomaly for non-isostatic effects [18, 19]. [20] demonstrated that the MD estimated from the isostatic gravity disturbance based on solving the VMM model has a better agreement with the CRUST2.0 seismic model than those computed by the isostatic gravity anomaly. Their argument was also theoretically explained by [21]. [22] estimated the MD and MDC using a combination of the CRUST2.0 and a GOCE global gravity models. [23] showed that the application of the Bouguer gravity disturbance and the no-topography correction in the VMM model to determine the MD provides very similar results, suggesting the preference of the gravity disturbance to the traditional Bouguer gravity anomaly for gravity inversion. [4, 5] computed combined Moho constituent model according to the VMM method. [24] estimated a new MDC model named MDC2018, using the marine gravity field from satellite altimetry in combination with a seismic-based crustal model and Earth's topographic/bathymetric data. Finally, [25] estimated a combined Moho model for marine areas via satellite altimetric - gravity and seismic crustal models.

1.2 Gravimetric-isostatic Moho models

Isostasy is an important concept in Earth sciences describing the state of equilibrium (or mass balance) to which the mantle tends to balance the mass of the crust in the absence of external disturbing forces. *“When a certain area of the crust reaches the state of isostasy, it is said to be in isostatic equilibrium (or balance), and the depth at which isostatic equilibrium prevails is called the depth of compensation”* [26].

However, the transport of material over the Earth's surface, such as glaciers, volcanism, and sedimentation, etc., are factors that disturb isostasy, yielding so-called non-isostatic effects (NIEs).

Four principle models of isostasy related with the crustal depth and/or density can briefly be listed as those of (a) Airy/Heiskanen (A/H; [27–29]), (b) Pratt/Hayford (P/H; [30, 31]), (c) Vening Meinesz (VM; [14]), and (d) the Vening Meinesz-Moritz (VMM; [7, 17]). Common for the isostatic models is that the Bouguer gravity anomaly Δg^b (or disturbance δg^b) is fully compensated by a compensation attraction below the crust such that the isostatic gravity anomaly and disturbance vanish:

$$\Delta g^I = \delta g^I = 0. \quad (1)$$

A/H and P/H are local models, implying that the compensation attraction operates along the vertical of the observation point, implying that the sum of the

masses of the crust and its compensation along each vertical is assumed to be constant from place to place.

The A/H model assumes a constant crustal density, and variations in topographic height is compensated by variations in the depth of the crust. That is, the mass excess of topography is compensated by the mass deficit of mountain roots in the upper mantle. In ocean areas anti-roots of mantle material compensates for the light mass of the ocean.

The P/H model assumes a constant depth of compensation of the solid Earth topography (including negative topography over oceans), while the density of the topography varies with topographic height.

Due to the elasticity of the Earth's crust these local models are not very realistic. Hence, [14] modified the A/H model by introducing a model with a regional compensation in which mass loads and unloads are balanced by a gentle bending or flexure of the crust over a regional area. [17] generalized the VM model from a regional to a global compensation with a spherical sea level approximation. [7] and, finally, [6] generalized the VMM model to allow for variations both in crustal density and depth. In this way the VMM can be seen as a generalization of both the A/H and P/H models with global isostatic compensations by variations of both mountain root and crustal density.

Below we will present the least-squares theory for determining a combined VMM-seismic model for both MD and MDC. The theory is finally applied in a new global model.

2. The VMM theory

2.1 Solution for the product of Moho depth and density contrast ($D\Delta\rho$)

In H. Moritz' original publication [17] the problem is to determine the MD (D) such that the compensation attraction (A_C) fully compensates the Bouguer gravity anomaly. Here we employ this condition in the last part of Eq. (1), which can be written (cf. [7, 21])

$$\delta g^I = \delta g^B + A_C = 0, \quad (2)$$

where δg^B is the Bouguer gravity disturbance (i.e., the free-air gravity disturbance after removal of the topographic attraction).

The VMM technique uses both gravimetric and seismic data in a least squares combination to determine the MD (D) and/or MDC ($\Delta\rho$). The method assumes that the crust is in isostatic balance, implying that the isostatic gravity anomaly (Δg^I) and disturbance (δg^I) vanish at each point on the Earth's surface as in Eq. (1) above. Note that the compensation attraction is a function of both MD and MDC. Approximating the Earth's surface by a sphere of radius R , one obtains after several manipulations of Eq. (2) the following equation in D for a constant $\Delta\rho$:

$$RG\Delta\rho \iint_{\sigma} K(\psi, s) d\sigma = f, \quad (3)$$

where G is the gravitational constant, $K(\psi, s)$ is an integral kernel function with arguments ψ = geocentric angle between integration and computation points and $s = 1 - D/R$, and $f = -(\delta g^b + A_{C0})/G$. Here A_{C0} is zero-degree harmonic of the compensation attraction (which does not affect the Moho undulation). Eq. (3) is a

non-linear Fredholm integral equation of the first kind, which has the following first- and second-order solutions:

$$D_1 = \frac{1}{4\pi\Delta\rho} \sum_{n=0}^{\infty} \frac{2n+1}{n+1} \sum_{m=-n}^n f_{nm} Y_{nm} \quad (4)$$

where Y_{nm} is a fully-normalized spherical harmonic, f_{nm} is the corresponding coefficient given by the Bouguer gravity disturbance f , and

$$(D_2)_P = (D_1)_P + \frac{(D_1^2)_P}{R} - \frac{1}{32R\pi} \iint_{\sigma} \left[\frac{(D_1^2)_Q - (D_1^2)_P}{\sin^3 \psi_{PQ}} \right] d\sigma_Q. \quad (5)$$

Here subscripts P and Q denote computation and integration points, respectively, f_{nm} is the spherical harmonic coefficient of f . Note that the integral contributes significantly only locally around the computation point. The formula can be improved by a few steps of iteration:

$$D_P^{k+1} = D_P^k + \frac{(D_P^k)^2}{R} - \frac{1}{32R\pi} \iint_{\sigma} \left[\frac{(D_Q^k)^2 - (D_P^k)^2}{\sin^3 \psi_{PQ}} \right] d\sigma_Q; k = 0, 1, 2, \dots, \quad (6)$$

where $D_P^0 = D_1$ at point P determined by Eq. (4).

As the isostatic balance of the crust is hardly valid for crustal blocks of diameter smaller than, say, 100 km ([32], p.195), the upper limit of the series in Eq. (4) of should not exceed $n_2 = 180$. Also, as we shall see later, the low-degree harmonics in D_1 , say, below $n_1 = 10$, are not contributing to the isostatic balance but are due to mass anomalies in the Earth's interior below the crust.

The integrals in Eqs. (5) and (6) are local, as the integrand quickly vanishes with distance away from the computation point. Hence a flat earth approximation may be relevant (See [6]).

If the MDC varies laterally, the following 2nd-order approximation of Eq. (3) can be found in the spectral domain (cf. [6]) when introducing the notation $\chi = D\Delta\rho$

$$f_{nm} = 4\pi \frac{n+1}{2n+1} \left[\chi_{nm} + \frac{n+2}{2R} (\chi D)_{nm} \right] \quad (7)$$

and, after summing up, one obtains:

$$\chi = \sum_{n=n_1}^{n_2} \left[\frac{2n+1}{n+1} \frac{f_n}{4\pi} - \frac{n+2}{2R} (\chi D)_n \right], \quad (8)$$

where f_n and $(\chi D)_n$ are the Laplace harmonics

$$\begin{pmatrix} f_n \\ (\chi D)_n \end{pmatrix} = \sum_{m=-n}^n \begin{pmatrix} f_{nm} \\ (\chi D)_{nm} \end{pmatrix} Y_{nm}. \quad (9)$$

Using the approximation

$$\chi D \approx \chi^2 / \Delta\rho_P, \quad (10)$$

one obtains from (8) the iterative formula

$$\chi_P^{k+1} = \sum_{n=n_1}^{n_2} \left[\frac{2n+1}{n+1} \frac{f_n}{4\pi} - \sum_{m=-n}^n \frac{n+2}{2R\Delta\rho_P} (\chi^2)_n^k \right], ; k = 0, 1, 2, \dots \quad (11)$$

where χ_P^0 is the first-order solution:

$$\chi^0 = \frac{1}{4\pi} \sum_{n=n_1}^{n_2} \frac{2n+1}{n+1} f_n. \quad (12)$$

Alternatively, we may present Eq. (11) by the iterative formula:

$$\chi_P^{k+1} = \chi_P^0 + I_P^k, ; k = 0, 1, 2, \dots, \quad (13)$$

where

$$I_P^k = \frac{1}{R\Delta\rho_P} \iint_{\sigma} \frac{(\chi_P^k)^2 - (\chi_Q^k)^2}{\sin^3\psi} d\sigma_Q. \quad (14)$$

Again, this integral is very local, which suggests the use of a flat-Earth approximation. Also, assuming that $(n_2 + 2)D_0/(2R) < 1$, Eq. (7) leads to the approximate solution:

$$\chi_P \approx \frac{1}{4\pi} \sum_{n=n_1}^{n_2} \frac{2n+1}{n+1} \frac{f_n}{1 + (n+2)D_0/(2R)}. \quad (15)$$

Note that the solution χ_P is the product of the MD and MDC. If one of the parameters is known, the other can be determined by the equation. Hence, gravity data alone cannot be used to distinguish between the two Moho constituents. Hence, additional information, e.g., from seismic and/or geological data, is needed to separate the two. However, as we shall see later, usually such data is not taken for granted in the VMM technique, but the gravity data used in Eq. (8) is typically applied to improve a priori Moho constituents in a least-squares procedure.

The solution (8) can be derived from Eq. (1), and from the inversion of a 3-D Newton integral. See Appendix A.

2.2 A least-squares solution for both the Moho depth and the Moho density contrast

The Moho component χ , the product of D and $\Delta\rho$, can be estimated from Eq. (11) or (12) and applied as an observation together with seismic data for solving both the MD and the MDC in a least-squares adjustment. Then a linear set of equations including gravimetric data (l_1), and seismic data for MD (l_2) and MDC (l_3) can be written for each pixel (P):

$$\Delta\rho_P dD + D_P d\Delta\rho = l_1 - \varepsilon_1 \quad (16)$$

$$dD = l_2 - \varepsilon_2 \quad (17)$$

$$d\Delta\rho = l_3 - \varepsilon_3, \quad (18)$$

Where dD and $d\Delta\rho$ are the (unknown) corrections to the initial values D_P and $\Delta\rho_P$, $l_1 = \chi - \chi_P - I_P^k$, where $I_P^0 = 0$, and ε_i are the errors of the observations. In matrix form the adjustment system can be written

$$\mathbf{A} \mathbf{X} = \mathbf{L} - \boldsymbol{\varepsilon}, \quad (19)$$

where

$$\mathbf{A} = \begin{bmatrix} \Delta\rho_P & D_P \\ 1 & 0 \\ 0 & 1 \end{bmatrix}, \quad \mathbf{X} = \begin{bmatrix} dD \\ d\Delta\rho \end{bmatrix} \quad \text{and} \quad \mathbf{L} = \begin{bmatrix} l_1 \\ l_2 \\ l_3 \end{bmatrix}. \quad (20)$$

Assuming that the observation errors are random with expectation zero and covariance matrix \mathbf{Q} , the weighted least squares solution of this system becomes:

$$\hat{\mathbf{X}} = (\mathbf{A}^T \mathbf{Q}^{-1} \mathbf{A})^{-1} \mathbf{A}^T \mathbf{Q}^{-1} \mathbf{L}. \quad (21)$$

From this result, the adjusted MD and MDC for point P are obtained by:

$$\hat{D} = D_P + d\hat{D} \quad \text{and} \quad \Delta\hat{\rho} = \Delta\rho_P + d\Delta\hat{\rho}. \quad (22)$$

As the first equation (l_1) is a linearization, it could make sense to iterate the adjustment procedure by replacing the previous initial values D_P and $\Delta\rho_P$ in Eq. (16) by their adjusted values $\hat{D}, \Delta\hat{\rho}$ and repeat the above computation procedure until sufficient convergence.

3. Uncertainty estimations

First, the result of the least-squares procedure depends on the quality and weighting of the gravity and seismic observations. The weights should be selected as proportional to the inverse standard errors (STEs) of the observations squared. The STEs of seismic data is, hopefully, provided along with the data files. For the gravity data we derive the global mean STE in Section 3.1. In Section 3.2 we propagate the data errors to error estimates in the VMM least-squares results of Moho constituents. Finally, in Section 3.3 a method for validating the modeled Moho undulations is presented.

3.1 The uncertainty in the gravimetric-isostatic observation equation

Assuming that there are no systematic errors and disregarding 2nd –order terms in Eq. (8), one obtains the error in χ by simple error propagation from Eq. (12):

$$\varepsilon_\chi = \frac{1}{4\pi} \sum_{n=n_1}^{n_2} \frac{2n+1}{n+1} df_n, \quad (23)$$

where df_n is the error in f_n . Then it follows that the global Root Mean Square Error (RMSE) of χ becomes

$$RMSE(\chi) = \frac{1}{4\pi} E \left\{ \iint_{\sigma} (\varepsilon_\chi^2) d\sigma \right\} = \frac{1}{4\pi} \sqrt{\sum_{n_1}^{n_2} \left(\frac{2n+1}{n+1} \right)^2 dc_n}, \quad (24)$$

where $E\{\}$ denotes the statistical expectation of the term in the bracket, and dc_n are the error degree variances of the gravity disturbances. Using this formula with harmonics between 10 and 180 of the XGM2019e gravity field model (see [33]), the RMSE value becomes $1.17 \times 10^4 \text{ kg/m}^2$.

3.2 The uncertainties in VMM Moho depth and density contrast

Assuming that all observation errors are stochastic with expectation zero, an error propagation of the least squares solution in Eq. (21) yields that the covariance matrix of $\hat{\mathbf{X}}$ becomes

$$\mathbf{Q}_{\mathbf{XX}} = \sigma_0^2 (\mathbf{A}^T \mathbf{Q}^{-1} \mathbf{A})^{-1} \quad (25)$$

where σ_0^2 is the variance of unit weight, which can be unbiasedly estimated by

$$s_0^2 = \mathbf{L}^T \mathbf{Q}^{-1} (\mathbf{L} - \mathbf{A} \hat{\mathbf{X}}). \quad (26)$$

Note that there is no denominator in Eq. (26), because in the present adjustment example with 3 observations and 2 unknowns per pixel there is only 1 degree of freedom.

3.3 Verification of the solutions

First, we will find an estimate of the variance σ_x^2 of the solution x for the MD or MDC by assuming that we know another solution y with variance σ_y^2 . If both solutions have vanishing expected errors, the solution becomes

$$\sigma_x^2 = \sigma_y^2 + E\{x^2 - y^2\}. \quad (27)$$

The correlation coefficient between x and y follows from

$$k = \left[\sigma_x^2 + \sigma_y^2 - E\{(x - y)^2\} \right] / (2\sigma_x \sigma_y) \quad (28)$$

One can also plot the t-test parameter of the normalized (and unitless) difference between x and y :

$$T = \frac{x - y}{\sqrt{\sigma_x^2 + \sigma_y^2 - 2k\sigma_x \sigma_y}} \quad (29)$$

to study the expected difference.

To verify Eqs. (27)–(29), one may start from the substitutions that the true value for x and y is given by

$$\bar{x} = x - e_x = y - e_y, \quad (30)$$

where e_x and e_y are random errors with zero-expectations.

In practice, x and y are the Moho quantities at a pixel estimated from two models, and the expectation operator should be replaced by the (weighted) mean value over the central and surrounding pixels. Note that the solution in Eq. (27) is independent on whether x and y are correlated or not. Eq. (29) can be used in an

approximate t-test to judge whether the estimates x and y from the two models are statistically equal or not, if they are (weighted) mean values.

4. Corrections to gravimetric data

Nowadays, the Earth's gravity field has been recognized as an important source of information about the Earth's structure. Such data contain both short- and long-wavelength features, i.e., signals from the topographic and bathymetry geometries and density heterogeneities in the topography, ice caps, sediment basins and also in the mantle and core/mantle topography variations.

The long-wavelength contribution to the gravity field, say to spherical harmonic degree and order 10, may be assumed to be related to the mantle and below located heterogeneities.

To isolate the gravity data caused only by the geometry and density contrast of the Moho interface, all aforementioned signal contributors to the gravity data must be removed by applying the so-called stripping corrections and NIEs [34] and NIEs (see section 4.2). Another gravity correction corresponds to the gravimetric effect of filling-up all oceans with masses to a standard density of 2670 kg/m^3 . Finally, by removing also normal gravity from the resulting stripped free-air gravity observation, one obtains the refined Bouguer gravity disturbance. As a result, the ideal stripped Bouguer gravity disturbance can be explained as caused by a spherical Earth without solid Earth topography and mass anomalies below the crust.

4.1 Crustal density corrections

In order to compute the stripped refined Bouguer gravity disturbance, i.e. free-air gravity disturbance corrected for topography, bathymetry, ice thickness and sediment basins (i.e. stripping corrections), [34] developed and applied a uniform mathematical formalism of computing the gravity corrections of the density variations within the Earth's crust. This operation can be summarized as the correction

$$\delta g^{TBIS} = \delta g^t + \delta g^b + \delta g^i + \delta g^s \quad (31)$$

where δg^t is the topographic gravity correction, and δg^b , δg^i and δg^s are the stripping gravity corrections due to the ocean (bathymetry), ice and sediment density variations, respectively.

Applying a spherical approximation of the Earth, each gravity correction on the right-hand side of Eq. (31) can be computed using the following spherical harmonic series:

$$\delta g^q(P) = \frac{GM}{R^2} \sum_{n=0}^{n_{\max}} (n+1) \sum_{m=-n}^n c_{nm}^q Y_{nm}(P), \quad (32)$$

with superscript q being one of t , b , i or s , and $GM = 3986005 \times 10^8 \text{ m}^3 \text{ s}^{-2}$ is the geocentric gravitational constant. The coefficient c_{nm}^q of a particular volumetric mass density (or density contrast) layer q (i.e., topography, bathymetry, glacial ice and sediments) is defined by:

$$c_{nm}^q = \frac{2}{(2n+1)\rho_e} \left[\frac{(\rho^q L_q)_{nm}}{R} + \frac{n+2}{2} \frac{(\rho^q L_q^2)_{nm}}{R^2} + \dots \right] \quad (33)$$

where ρ^q is the Earth's mean mass density, and the coefficients $(\rho^q L_q^i)$ are evaluated (from discrete data of density ρ^q and thickness L_q) by applying a discretization to the following integral convolution

$$(\rho^q L_q)_{nm} = \frac{1}{4\pi} \iint_{\sigma} \rho^q L_q^j Y_{nm} d\sigma, j = 1, 2, \dots, n \quad (34)$$

4.2 Non-isostatic effects

It is important to remind the reader that in general the crust is not in complete isostatic equilibrium, and the observed gravity data are not only generated by the topographic/isostatic masses, but also from those in the deep Earth interior, that leads to non-isostatic effects (NIEs) (see [18, 19, 35]).

According to [7], the major part of the long-wavelengths of the geopotential undulation is caused by density variations in the Earth's mantle and core/mantle topography variations. Such NIEs could be the contribution of different factors, such as crustal thickening/thinning, thermal expansion of mass of the mantle [36], Glacial Isostatic Adjustment (GIA), plate flexure ([16], p. 114), and effect of other phenomena. This implies that this contribution to gravity will lead to systematic errors/NIEs of the computed Moho topography. Hence the NIEs should also be corrected on the isostatic gravity disturbance.

Assuming that the seismic Moho model CRUST1.0 is known and correct, the gravity effect of the NIEs can be determined by:

$$\delta g^{NIE} = \frac{GM}{R^2} \sum_{n=0}^{n_{\max}} (n+1) \sum_{m=-n}^n c_{nm}^{NIE} Y_{nm}(P) \quad (35)$$

where

$$c_{nm}^{NIE} = c_{nm}^{CRUST1.0} - c_{nm}^{VMM} \quad (36)$$

Here c_{nm}^{NIE} , c_{nm}^{VMM} , $c_{nm}^{CRUST1.0}$ are the spherical harmonic coefficients of the gravity disturbances of the NIE, VMM and CRUST1.0, respectively.

The isostatic equilibrium equation in Eq. (2) is then rewritten as:

$$\delta g^I(P) = \delta g_B^{TBISN}(P) + A_C(P) = 0. \quad (37)$$

Here δg_B^{TBISN} is the refined Bouguer gravity disturbance corrected for the gravitational contributions of topography and density variations of the oceans, ice, sediments and NIEs, i.e. by Eq. (31).

4.3 Glacial isostatic adjustment (GIA)

Delayed GIA (DGIA) expresses the delayed adjustment process of the Earth to an equilibrium state when former ice sheet loads have vanished. The ongoing adjustment of the Earth's body to the redistribution of ice and water masses is evident in various phenomena, which have been studied to infer the extent and amount of the former ice masses, to reconstruct the sea level during a glacial cycle and to constrain rheological properties of the Earth's interior. Here we aim at answering the question whether the effect of the gravimetric DGIA correction is significant for Moho determination in Fennoscandia. Usually, this effect is part of

and reduced by the general NIE correction, but one may also estimate the DGIA effect on gravity as a separate correction by the harmonic window:

$$\delta g^{DGIA} = \gamma \sum_{n=10}^{23} (n+1) \sum_{m=-n}^n A_{nm} Y_{nm}, \quad (38)$$

where γ is normal gravity, Y_{nm} and A_{nm} are spherical harmonics and coefficients of the gravitational potential (see [37]). Here the limits of the series are based on the optimum correlation between the present land uplift and the gravity field in the region.

5. A global VMM solution

The main gravimetric input data to be used in the following VMM Moho model is the global Earth gravitational field model (e.g. XGM2019e) in the harmonic window from $n_1 = 10$ to $n_2 = 180$. The gravity disturbance data were corrected for the gravitational signals of mass density variations due in different layers of the Earth's crust (i.e. stripping gravity corrections) and for the gravity contribution from deeper masses below the crust (i.e. non-isostatic effects). The NIEs were computed using the seismic crustal model CRUST1.0, and the stripping corrections for different crustal heterogeneous data utilized the global topographic models DTM2006 and Earth2014. The preliminary gravimetric Moho solution was combined with the CRUST1.0 model in a least-squares procedure (see Section 2.2). The adjustment was performed globally for each $1^\circ \times 1^\circ$ -block.

The statistics of the stripping gravity corrections and refined Bouguer gravity disturbance are presented in **Table 1**. It shows the largest corrections for bathymetry and NIE, but also ice cap corrections have some extreme values. The sum of the corrections varies roughly within ± 600 mGal with the STD of 178 mGal.

Figure 1 depicts the Bouguer gravity disturbances corrected for the ocean (bathymetry), ice, sediment variations and the NIEs, respectively. As one can see from the figure, these features can drastically change the Bouguer gravity disturbance from the free-air disturbance over oceans due to the application of the bathymetric stripping gravity correction. It also changes in central Greenland and Antarctica due to the applied ice density variation stripping gravity correction

Quantities δg (mGal)	Max	Mean	Min	STD
δg	285.85	-0.44	-281.40	23.84
δg^t	255.13	-71.06	-647.61	105.98
δg^b	721.60	332.91	110.28	165.02
δg^I	325.78	21.84	-2.61	56.57
δg^S	185.31	45.48	-0.02	32.47
δg^{NIE}	248.70	-134.65	-497.98	69.98
δg^{TBISN}	562.82	128.87	-620.54	178.10

Table 1.

Statistics of global estimates of the gravity disturbances, stripping gravity corrections and NIEs. STD is the standard deviation of the estimated quantity over the blocks. δg is the gravity disturbance computed by the XGM2019e coefficients. δg^t , δg^b , δg^I and δg^S are the topographic/bathymetric, ice and sediment stripping gravity corrections derived from the CRUST1.0, respectively. δg^{NIE} is the non-isostatic effect. δg^{TBISN} is the refined Bouguer gravity disturbance after applying the topographic and stripping gravity corrections due to the ocean, ice and sediment density variations.

(Figure 1d). In Figure 1e one can see large stripping corrections in sediment basins, and the NIEs are also very significant (Figure 1f).

Figure 1g shows the refined Bouguer gravity disturbance after applying the above corrections. This disturbance has a span of about ± 500 mGal, to be compared with the approximate span of ± 250 mGal of the free-air disturbance. Notable is the large positive disturbances on the oceans corresponding to the effect of filling the oceans with topographic masses. The DGIA effect, demonstrated for Fennoscandia and, depicted in Figure 1h, is very small compared to other corrections.

In the least-squares procedure of the combined VMM solution the weights of the two types of data were chosen as follows. The weights of the gravity disturbances were estimated from their inverse variances by Eq. (23), while the weights for CRUST1.0 data were those published in [12]. Figures 2 and 3 depict the results of the MD and density contrast undulations and their estimated standard errors. Their extreme values for continental and oceanic crusts and mean values are reported in Table 2.

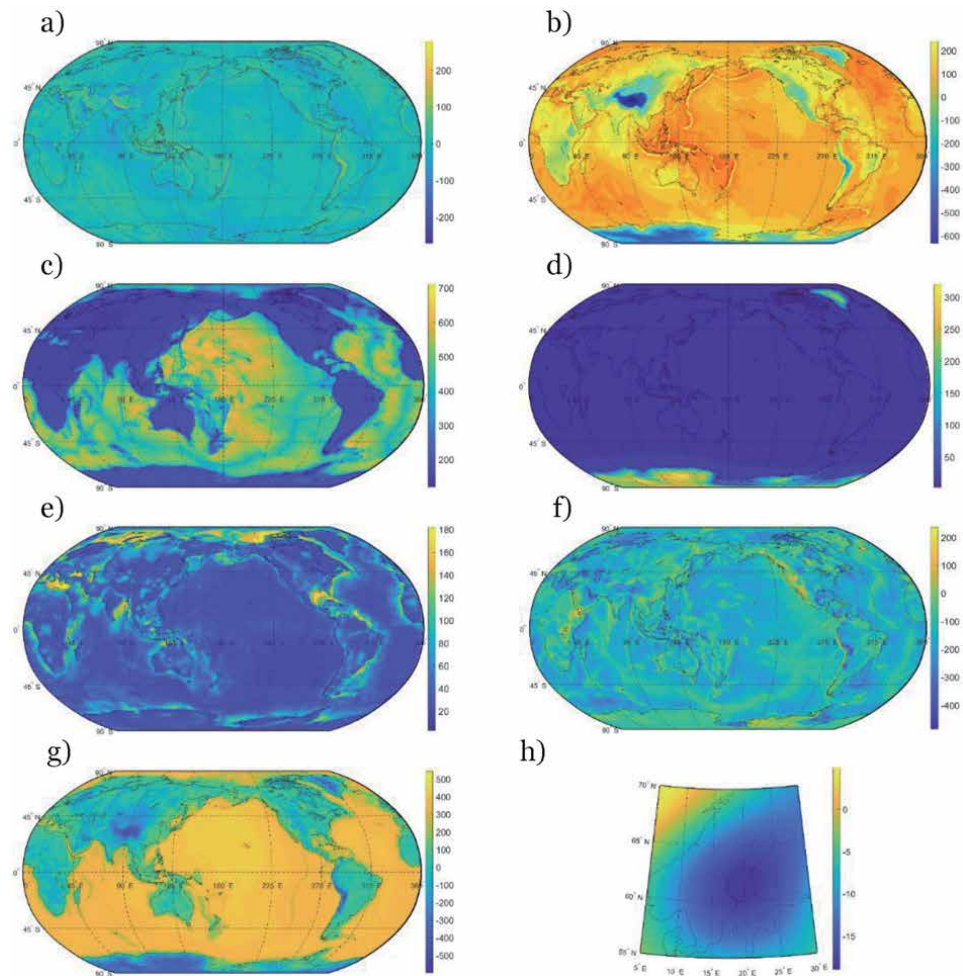


Figure 1. (a) The free-air gravity disturbance computed using the XGM2019e coefficients complete to degree 180 of spherical harmonics, (b) the topographic gravity correction, (c) the bathymetric stripping gravity correction, (d) the ice density variation stripping gravity correction, (e) the sediments density variation stripping gravity corrections, (f) non-isostatic effects and (g) refined Bouguer gravity disturbances after applying the above corrections. (h) the DGIA effect in Fennoscandia. Unit: mGal.

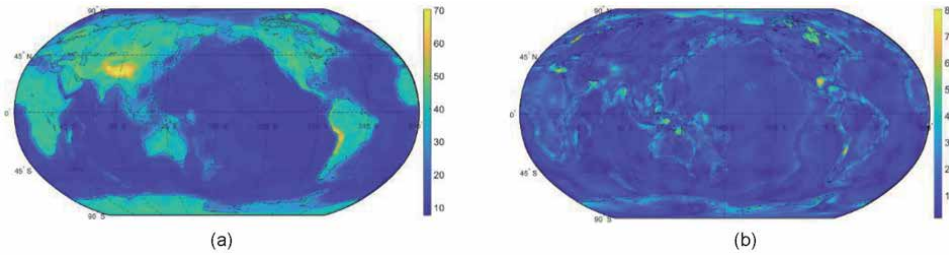


Figure 2.
 (a) The MD estimated from combined approach, and (b) its standard error. (unit km).

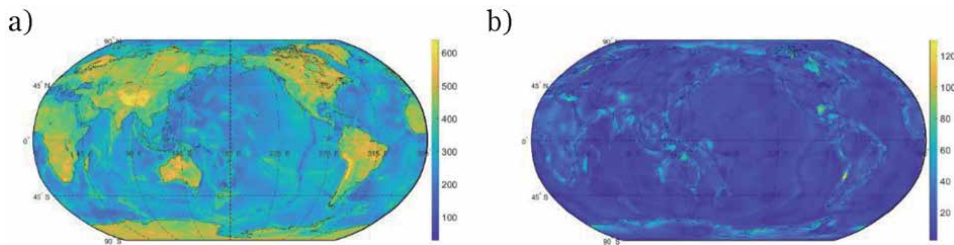


Figure 3.
 (a) The MDC estimated by combined approach, and (b) its standard error. (unit kg/m^3).

To validate the STE of the VMM solution for crustal depth, we determined the global mean of it by Eq. (27) using the seismic model CRUST19. The result is 1.73 km, which is in fair agreement with the 1.20 km given in **Table 2**. Also, as one can see from **Figure 4** the test parameter in Eq. (29) for validating the VMM solution of MD from the seismic model CRUST19 is mainly in the range ± 1 , which suggest rather close agreements of estimated MDs and their error estimates.

Quantities		Max.	Mean	Min.	STD
MD (km)	Global	70.26	23.78	7.55	13.17
	Ocean	43.19	14.98	7.55	
	Land	70.26	40.03	18.37	
STE MD (km)	Global	8.15	1.20	0.05	0.94
	Ocean	7.34	2.06	0.05	
	Land	8.15	2.49	1.05	
MDC (kg/m^3)	Global	649.99	340.49	20.98	100.90
	Ocean	637.36	281.01	20.98	
	Land	649.99	440.01	69.34	
STE MDC (kg/m^3)	Global	132.26	17.44	0.09	14.17
	Ocean	99.98	35.21	0.09	
	Land	132.26	38.65	19.09	

Table 2.
 Statistics of global estimates of MD and MDC in the VMM approach for $1^\circ \times 1^\circ$ block data. STD is the standard deviation. STE is the standard error obtained in the least-squares adjustment. Units for MD and MDC are km and kg/m^3 , respectively.

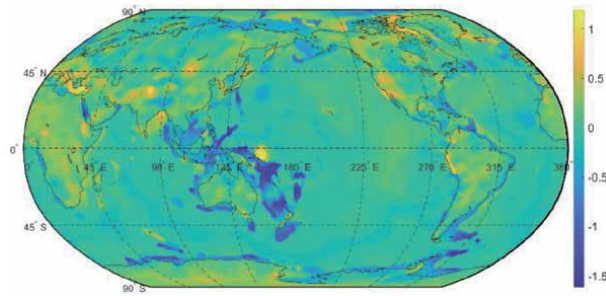


Figure 4. Validation of the VMM MD solution by Eq. (29) and CRUST19 model. (the scale is unitless).

(Note that $E\{T^2\} = 1$, implies that assumed variance components are correct and the expected MDs of the two models are the same).

6. Discussion and final remarks

The study of the Moho discontinuity has been a crucial topic in inferring the dynamics of the Earth's interior for a long time. In general, the Moho can be studied with profitable results through seismic data. However, due to the sparsity of seismic data in parts of the world, it has not been well determined. With the advent of satellite missions, it has been possible to recover the Moho constituents via satellite gravity observations based on an isostatic model.

So far, various isostatic models have been presented for recovering the Moho constituents, but it was not clarified which one is most appropriate to employ for geophysical and geodynamical purposes. The preliminary and simplest isostatic models proposed are the classical ones with local or regional compensation. However, those models cannot realistically image the actual Moho undulation. This is because they assume a uniform crustal density, disregarding the density irregularities distributed within the crust and sub-crust. Understanding this important role of Moho recovery has been in the center of the discussions by many geoscientists during the last decades.

Here we have determined the Moho constituents and their uncertainties based on the VMM technique using both gravimetric and seismic data on a global scale to a resolution of $1^\circ \times 1^\circ$. The combination of the gravimetric and seismic data in one approach as well as the joint adjustment of MD and density contrast are expected to significantly improve the total result.

The basic VMM method is based on the hypothesis that the isostatic gravity disturbance vanish. However, this is the case only if the gravity component is reduced such that there are no signals from the Earth's interior below the crust. The major problem in this reduction is therefore to distinguish and remove those signals, which we utilize by estimating and removing the NIEs with the help from CRUST1.0 seismic model.

The second step is to combine the gravimetric data, propagated in the VMM technique to a linear equation (with MD and MDC as the unknowns), with a seismic model, CRUST1.0. This is performed by a weighted least-squares adjustment, block by block, which has the advantage that the standard error of the unknowns can also be estimated block-wise. The weights of the gravity disturbances were based on the error estimates by Eq. (23), while the weights for CRUST1.0 data were those published in [12].

Our estimated results can be summarized as follows. The global means of MD and MDC are 23.8 ± 0.05 km and 340.5 ± 0.37 kg/m³, respectively, ranging between 7.6–70.3 km and 21.0–650.0 kg/m³. The MD results were validated by the recent CRUST19 seismic model, showing that the differences between the models vary within the extremes -23.4 and 32.9 km, with a global average of 0.91 km and an RMS fit of 4 km. The normalized differences were generally within the limits ± 1 , which should be regarded as acceptable.

Acknowledgements

This study was supported by project no. 187/18 of the Swedish National Space Agency (SNSA).

Appendix A

Let us assume that the compensation attraction in Eq. (2) is generated by a density contrast $\Delta\rho$ between the constant reference depth D_0 and the actual depth D . Assuming that the density contrast may change only laterally, it follows from the Newton integral in 3D, that the compensation potential becomes:

$$(Vc)_P = G \iint_{\sigma} \Delta\rho \int_{R-D}^{R-D_0} \frac{r^2 dr}{l_P} d\sigma = G \iint_{\sigma} \Delta\rho \int_{R-D}^R \frac{r^2 dr}{l_P} d\sigma + G \iint_{\sigma} \Delta\rho \int_R^{R-D_0} \frac{r^2 dr}{l_P} d\sigma, \quad (\text{A.1})$$

where the last integral term is a constant, global mean value. Disregarding this term (which does not contribute to the Moho undulation) the integral can be written in the spectral domain after integration with respect to r and setting $r_P = R$ (sea level radius):

$$(Vc)_P = GR^2 \sum_{n=0}^{\infty} \frac{1}{n+3} \iint_{\sigma} \frac{\Delta\rho}{n+3} \left[1 - \left(1 - \frac{D}{R} \right)^{n+3} \right] P_n(\cos\psi) d\sigma \quad (\text{A.2})$$

Considering the addition theorem of fully normalized spherical harmonics (Heiskanen and Moritz 1967, p. 33):

$$P_n(\cos\psi_{PQ}) = \frac{1}{2n+1} \sum_{m=-n}^n Y_{nm}(P) Y_{nm}(Q),$$

one obtains

$$\delta T_P = GR^2 \sum_{n=0}^{\infty} \frac{1}{(2n+1)(n+3)} \sum_{m=-n}^n Y_{nm}(P) \iint_{\sigma} \Delta\rho \left[1 - \left(1 - \frac{D}{R} \right)^{n+3} \right] Y_{nm} d\sigma. \quad (\text{A.3})$$

As D is small vs. R , one may expand the last bracket in this equation a la Taylor as

$$\frac{1}{n+3} \left[1 - \left(1 - \frac{D}{R} \right)^{n+3} \right] = \frac{D}{R} - \frac{n+2}{2} \left(\frac{D}{R} \right)^2 + \frac{(n+2)(n+1)}{6} \left(\frac{D}{R} \right)^3 + \dots, \quad (\text{A.4})$$

and by inserting this series in Eq. (A.3) one obtains after integration

$$(Vc)_P = 4\pi GR \sum_{n=0}^{\infty} \frac{1}{2n+1} \times \sum_{m=-n}^n \left[(D\Delta\rho)_{nm} - \frac{n+2}{2R} (D^2\Delta\rho)_{nm} + \frac{(n+2)(n+1)}{6R^2} (D^3\Delta\rho)_{nm} - \dots \right] Y_{nm}(P) \quad (A.5)$$

where $(\)_{nm}$ are spherical harmonic coefficients. As the compensation potential coefficients are related to those of the compensation attraction Ac by

$$(Vc)_{nm} = \frac{R}{n+1} (Ac)_{nm}, \quad (A.6)$$

one obtains the spectral equation from (A.5):

$$\frac{R}{n+1} (Ac)_{nm} = \frac{4\pi GR}{2n+1} \left[(D\Delta\rho)_{nm} - \frac{n+2}{2R} (D^2\Delta\rho)_{nm} + \frac{(n+2)(n+1)}{6R^2} (D^3\Delta\rho)_{nm} - \dots \right] \quad (A.7)$$

By comparing the spectra of both sides and summing up all harmonics and considering Eq. (2),

$$D\Delta\rho = \frac{1}{4\pi} \sum_{n=0}^{\infty} \frac{2n+1}{n+1} \sum_{m=-n}^n f_{nm} Y_{nm} + \Delta, \quad (A.8)$$

where $f_{nm} = -\delta g_{nm}^B/G$ and

$$\Delta = \sum_{n=0}^{\infty} \sum_{m=-n}^n \left[\frac{n+2}{2R} (D^2\Delta\rho)_{nm} - \frac{(n+2)(n+1)}{6R^2} (D^3\Delta\rho)_{nm} + \dots \right] Y_{nm} \quad (A.9)$$

accounts for higher order terms in the series.

In practical application for Moho feature determination the lower limit for the summation is found to be about 10 (as the lower harmonics are related with deep Earth gravity anomalies) and the upper limit should not exceed about 180.

Author details

Lars Erik Sjöberg^{1,2*} and Majid Abrehdary²

1 Division of Geodesy and Satellite Positioning, Royal Institute of Technology (KTH), Stockholm, Sweden

2 Division of Mathematics, Computer and Surveying Engineering, University West (HV), Trollhättan, Sweden

*Address all correspondence to: lsjo@kth.se

IntechOpen

© 2021 The Author(s). Licensee IntechOpen. This chapter is distributed under the terms of the Creative Commons Attribution License (<http://creativecommons.org/licenses/by/3.0>), which permits unrestricted use, distribution, and reproduction in any medium, provided the original work is properly cited. 

References

- [1] Kearey P, Brooks M, Hill I. An introduction to geophysical exploration. John Wiley & Sons; 2002 Apr 26.
- [2] Anderson DL. Theory of the Earth. Blackwell scientific publications; 1989 Jan 1.
- [3] Abrehdary M. *Recovering Moho parameters using gravimetric and seismic data*. KTH (Doctoral dissertation, Ph. D. thesis, TRITA SoM 2016–02, 56 pp., Stockholm, Sweden).
- [4] Abrehdary M, Sjöberg LE, Bagherbandi M. Combined Moho parameters determination using CRUST1. 0 and Vening Meinesz-Moritz model. *Journal of Earth Science*. 2015 Aug;26(4):607–16.
- [5] Abrehdary M, Sjöberg LE, Bagherbandi M, Sampietro D. Towards the Moho depth and Moho density contrast along with their uncertainties from seismic and satellite gravity observations. *Journal of Applied Geodesy*. 2017 Dec 1;11(4):231–47.
- [6] Sjöberg LE, Bagherbandi M. A method of estimating the Moho density contrast with a tentative application of EGM08 and CRUST2. 0. *Acta Geophysica*. 2011 Jun;59(3):502–25.
- [7] Sjöberg LE. Solving Vening Meinesz-Moritz inverse problem in isostasy. *Geophysical Journal International*. 2009 Dec 1;179(3):1527–36.
- [8] Meier U, Curtis A, Trampert J. Global crustal thickness from neural network inversion of surface wave data. *Geophysical Journal International*. 2007 May 1;169(2):706–22.
- [9] Shapiro NM, Ritzwoller MH. Monte-Carlo inversion for a global shear-velocity model of the crust and upper mantle. *Geophysical Journal International*. 2002 Oct 1;151(1):88–105.
- [10] Lebedev S, Adam JM, Meier T. Mapping the Moho with seismic surface waves: a review, resolution analysis, and recommended inversion strategies. *Tectonophysics*. 2013 Dec 8;609:377–94.
- [11] Bassin C. The current limits of resolution for surface wave tomography in North America. *EOS Trans. AGU*. 81: Fall Meet. Suppl., Abstract. 2000.
- [12] Laske G, Masters G, Ma Z, Pasyanos M. Update on CRUST1. 0—A 1-degree global model of Earth's crust. In *Geophys. res. abstr* 2013 Apr (Vol. 15, p. 2658).
- [13] Szwillus W, Afonso JC, Ebbing J, Mooney WD. Global crustal thickness and velocity structure from geostatistical analysis of seismic data. *Journal of Geophysical Research: Solid Earth*. 2019 Feb;124(2):1626–52.
- [14] Meinesz FV. Une nouvelle methode pour la reduction isostatique regionale de l'intensite de la pesanteur. *Bulletin geodesique*. 1931 Jan 1;29(1):33–51.
- [15] Heiskanen WA, Moritz H, Physical Geodesy WH. Freeman and Company. San Francisco. 1967.
- [16] Watts AB. *Isostasy and Flexure of the Lithosphere* Cambridge Univ. Press, Cambridge. 2001.
- [17] Moritz H. *The figure of the Earth: theoretical geodesy and the Earth's interior*. Karlsruhe: Wichmann. 1990.
- [18] Bagherbandi M, Sjöberg LE. Non-isostatic effects on crustal thickness: A study using CRUST2. 0 in Fennoscandia. *Physics of the Earth and Planetary Interiors*. 2012 Jun 1;200: 37–44.
- [19] Bagherbandi M, Sjöberg LE. Improving gravimetric–isostatic models of crustal depth by correcting for non-isostatic effects and using CRUST2. 0.

Earth-Science Reviews. 2013 Feb 1;117: 29–39.

[20] Tenzer R, Bagherbandi M. Reformulation of the Vening–Meinesz Moritz inverse problem of isostasy for isostatic gravity disturbances. *International Journal of Geosciences*. 2012;3(5A):918–29.

[21] Sjöberg LE. On the isostatic gravity anomaly and disturbance and their applications to Vening Meinesz–Moritz gravimetric inverse problem. *Geophysical Journal International*. 2013 Jun 1;193(3):1277–82.

[22] Reguzzoni M, Sampietro D, Sansò F. Global Moho from the combination of the CRUST2. 0 model and GOCE data. *Geophysical Journal International*. 2013 Oct 1;195(1):222–37.

[23] Sjöberg LE, Bagherbandi M, Tenzer R. On gravity inversion by no-topography and rigorous isostatic gravity anomalies. *Pure and Applied Geophysics*. 2015 Oct;172(10):2669–80.

[24] Abrehdary M, Sjöberg LE, Sampietro D. Contribution of satellite altimetry in modelling Moho density contrast in oceanic areas. *Journal of Applied Geodesy*. 2019 Jan 28;13(1): 33–40.

[25] Abrehdary M, Sjöberg LE. Estimating a combined Moho model for marine areas via satellite altimetric-gravity and seismic crustal models. *Studia Geophysica et Geodaetica*. 2020 Jan;64(1):1–25.

[26] Sjöberg, L. E. and Bagherbandi, M. *Isostasy–Geodesy*. In *Encyclopedia of Geodesy*. Springer International Publishing Switzerland 2014.

[27] Airy GB. III. On the computation of the effect of the attraction of mountain-masses, as disturbing the apparent astronomical latitude of stations in geodetic surveys. *Philosophical Transactions of the Royal Society of London*. 1855 Dec 31(145):101–4.

[28] Heiskanen WA. *Untersuchungen über Schwerkraft und Isostasie*. Buchdruckerei-aktiengesellschaft Sana; 1924.

[29] Heiskanen WA, Airy SG. *New Isostatic Tables for the Reduction of Gravity Values Calculated on the Basis of Airy’s Hypothesis*. Suomalainen Tiedeakatemia; 1938.

[30] Hayford JF. *Geodesy: The Figure of the Earth and Isostasy from Measurements in the United States*. US Government Printing Office; 1909.

[31] Pratt JH. I. On the attraction of the Himalaya Mountains, and of the elevated regions beyond them, upon the plumb-line in India. *Philosophical Transactions of the Royal Society of London*. 1855 Dec 31(145):53–100.

[32] Turcotte DL, Schubert G. *Geodynamics*. Cambridge university press; 2002 Mar 25.

[33] Zingerle P, Pail R, Gruber T, Oikonomidou X. The combined global gravity field model XGM2019e. *Journal of Geodesy*. 2020 Jul;94(7):1-2.

[34] Tenzer R, Chen W, Tsoulis D, Bagherbandi M, Sjöberg LE, Novák P, Jin S. Analysis of the refined CRUST1. 0 crustal model and its gravity field. *Surveys in geophysics*. 2015 Jan;36(1):139–65.

[35] Abrehdary M, Sjöberg LE, Bagherbandi M. The spherical terrain correction and its effect on the gravimetric-isostatic Moho determination. *Geophysical Journal International*. 2016 Jan 1;204(1):262–73.

[36] Kaban MK, Schwintzer P, Reigber C. A new isostatic model of the lithosphere and gravity field. *Journal of Geodesy*. 2004 Dec 1;78(6):368–85.

[37] Abrehdary M, Sjöberg LE. A New Moho Depth Model for Fennoscandia with Special Correction for the Glacial Isostatic Effect. *Pure and Applied Geophysics*. 2021 Feb 15:1-2.

The Gravity Effect of Topography: A Comparison among Three Different Methods

*Carlo Iapige De Gaetani, Anna Maria Marotta,
Riccardo Barzaghi, Mirko Reguzzoni and Lorenzo Rossi*

Abstract

In this paper, three different methods for computing the terrain correction have been compared. The terrain effect has been accounted for by using the standard right parallelepiped closed formula, the spherical tesseroid and the flat tesseroid formulas. Particularly, the flat tesseroid approximation is obtained by flattening the top and the bottom sides of the spherical tesseroid. Its gravitational effect can be computed as the gravitational effect of a polyhedron, i.e. a three-dimensional body with flat polygonal faces, straight edges and sharp corners or vertices. These three methods have been applied in the context of a Bouguer reduction scheme. Two tests were devised in the Alpine area in order to quantify possible discrepancies. In the first test, the terrain correction has been evaluated on a grid of points on the DTM. In the second test, Bouguer gravity anomalies were computed on sparse observed gravity data points. The results prove that the three methods are practically equivalent even in an area of rough topography though, in the second test, the Bouguer anomalies obtained by using the tesseroid and the flat tesseroid formulas have slightly smaller RMSs than the one obtained by applying the standard right parallelepiped formula.

Keywords: Gravitational Terrain Effect, Bouguer reduction, Terrain Correction, Parallelepiped, Tesseroid, Polyhedron

1. Introduction

The gravity effect of topography has been always intensively analyzed and modeled. In all the classical books of Geodesy and Geophysics there are sections devoted to this topic. Among the standard methods for modeling the gravity effect of topography one can enumerate the Bouguer reduction, the Helmert reduction and the isostasy reduction according to Airy-Heiskanen and Pratt-Hayford models (see e.g. [1]). In more recent years, the Residual Terrain Correction (RTC) has been devised as a method to be used in geodetic applications for gravity field and geoid estimation (see e.g. [2]).

In all these approaches, the gravity effect of topography is computed by using a Digital Terrain Model (DTM) at a given resolution, which is assumed to represent the actual shape of the Earth surface. Thus, the topography is discretized at the DTM resolution and the gravitational effect of each topography element is

computed. In doing so, different formulas can be applied. Usually, the single terrain element is modeled as a right parallelepiped (see e.g. [2]) or as a spherical or ellipsoidal tesseroid [3]. In this study, we compare the two aforementioned approach with that introduced by Tsoulis [4] in which the bottom and the top sides of the tesseroid are flat surfaces (flat tesseroid). This is done for the computation of the terrain correction in the framework of the Bouguer reduction.

The formulas giving the gravitational effect of a right parallelepiped, a spherical tesseroid and a flat tesseroid are given in Section 2. In Section 3, the Bouguer reduction is computed using these three different approaches in an area of the Alps, both on a grid of points and on a set of observed gravity values, and comments on the obtained results are given. Conclusions are then stated in Section 4.

2. The terrain correction and its computation

The terrain correction is commonly applied in the computation of the Bouguer gravity anomalies. The gravity observation in a point P on the Earth surface is strongly influenced by gravitational effect of the topographic masses. In order to use gravity in geophysical analyses, e.g. for estimating the Moho depth or intra-crustal mass anomalies, the topographic gravity signal is removed from the observed data. In this context, the most frequently used reduction is the Bouguer reduction (see e.g. [1]).

From the observed gravity value $g(P)$ one removes the gravity effect of a plate of height H_P equal to the height of point P , the so-called Bouguer plate. This plate is usually considered as an infinite horizontal slab of known constant density ρ even though spherical plate models have been proposed [5]. If the infinite horizontal slab model is assumed, the gravitational effect A_B is given by the well-known formula (see e.g. [1]):

$$A_B = 2\pi G\rho H_P \quad (1)$$

Where $G = 6.67 \times 10^{-11} \text{ m}^3/\text{kg s}^2$ is the universal gravitational constant. The topography signal reduction is then refined through the so-called Terrain Correction (TC). This is computed accounting for the masses that are above or below the plate of height H_P (see **Figure 1**). This is a quantity always positive that must be summed to the observed gravity reduced by the effect of the plate. Thus, one has:

$$g(P) - A_B + TC(P) \quad (2)$$

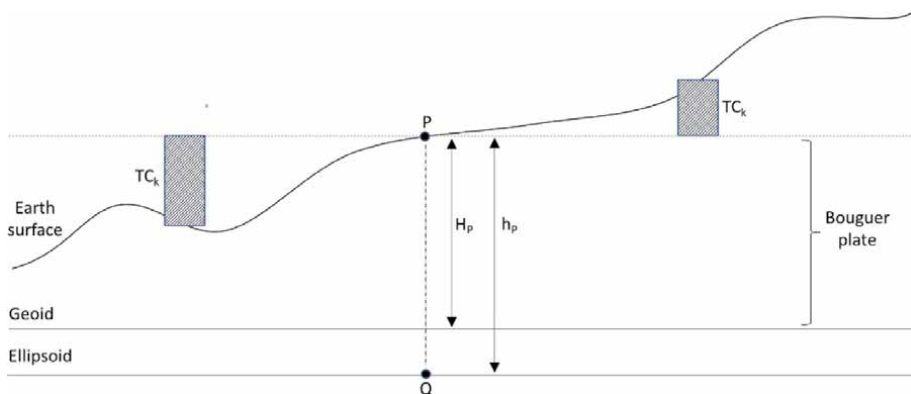


Figure 1. The plate and the terrain correction (H_P = orthometric height, h_P = ellipsoidal height).

It must be underlined that both the plate and the TC effects are usually computed at constant density ρ set at 2670 kg/m^3 . This means that residual effects coming from masses having density different from the standard value given above may still affect the reduced gravity values. However, it is assumed that, in this way, the topography effect is substantially removed from the observed gravity values $g(P)$.

The reduced gravity data are then moved to the geoid by considering the gravity gradient, which is approximated by the free-air normal gravity gradient $\partial\gamma/\partial h$:

$$g(P) - A_B + TC(P) - \frac{\partial g}{\partial H} H_P \cong g(P) - A_B + TC(P) - \frac{\partial \gamma}{\partial h} H_P \quad (3)$$

Finally, the normal gravity at point Q (see **Figure 1**) on the ellipsoid is subtracted and the standard Bouguer anomaly is obtained as:

$$\Delta g_B = g(P) - A_B + TC(P) - \frac{\partial \gamma}{\partial h} H_P - \gamma(Q) \quad (4)$$

While the Bouguer plate effect can be easily computed via e.g. Eq. (1), the computation of the terrain effect is more complex. In planar approximation, this effect is given by the integral formula:

$$TC(P) = G\rho \iiint_{-\infty}^{+\infty} \int_{z_P}^z \frac{\zeta - z_P}{l^3} d\xi d\eta d\zeta \quad (5)$$

where $l = \sqrt{(x_P - \xi)^2 + (y_P - \eta)^2 + (z_P - \zeta)^2}$, (x_P, y_P, z_P) are the coordinates of the computational point P and (ξ, η, ζ) are the coordinates of the integration point. The integral is numerically evaluated by using a Digital Terrain Model (DTM). This can be done using FFT methods in planar approximation as described in e.g. [6, 7].

Alternatively, the TC is computed by quadrature of the integral formula using the DTM in the area S having a radius that depends on the topography roughness (in high mountain range this radius can be 200 km). The TC effect can be thus evaluated as:

$$TC(P) \cong \sum_{k=1}^n TC_k \quad (6)$$

where TC_k is the volume integral giving the gravitational effect of the k -th DTM element in S and n is the total number of DTM elements (see **Figure 1**). Different mathematical models for the computation of TC_k have been proposed. In this paper three of them have been considered and compared, namely the formula of the gravitational effect of a right parallelepiped, a spherical tesseroid and a flat tesseroid.

Given the gravitational potential V of a body B of constant density ρ as the integral:

$$V(P) = G\rho \iiint_B \frac{1}{l} dv(Q) \quad (7)$$

$$l = |\underline{r}(P) - \underline{r}(Q)|$$

$\underline{r}(P)$ = position vector of the computation point;

$\underline{r}(Q)$ = position vector of the integration point;

one can compute the gravitational effect of a right parallelepiped assuming the computational point P at the origin of a Cartesian reference system as the closed formula [2]:

$$\frac{\partial V}{\partial z} = G\rho \left\| x \ln(y+r) + y \ln(x+r) - z \arctan\left(\frac{xy}{zr}\right) \right|_{x_2}^{x_1} \Big|_{y_2}^{y_1} \Big|_{z_2}^{z_1} \quad (8)$$

where $r = \sqrt{x^2 + y^2 + z^2}$ and $(x_1, x_2), (y_1, y_2), (z_1, z_2)$ are the coordinates of the parallelepiped edges.

This formula is implemented in e.g. the TC program of the GRAVSOFT package [8] that will be used in the computations described in the next section.

The gravitational effect of spherical tesseroid has been studied in several papers. Relevant studies on this topic have been carried out by [3, 9–12]. In this study the approach presented in [11], hereinafter referred to as UNIPOL, is used.

The UNIPOL approach grounds on the result that a closed formula of the volume Newtonian integral (Eq. (8)) exists when the observation point P is located along the polar axis (see e.g. [13]) and the tesseroids coincide with sectors of a spherical zonal band of a spherical cap.

In this case the gravitational contribution of spherical tesseroid of height h can be expressed as:

$$\frac{\partial V}{\partial r} = \frac{G\rho}{r^2} \Delta\lambda(I_1 + I_2 + I_3 + I_4 + I_5) \quad (9)$$

with

$$\begin{aligned} I_1 &= \frac{1}{3} \left[(R+h)^2 + r^2(3 \cos^2 \varphi_2 - 2) + r(R+h) \cos \varphi_2 \right] \\ &\quad \times \sqrt{(R+h)^2 + r^2 - 2r(R+h) \cos \varphi_2} \\ I_2 &= \frac{1}{3} \left[R^2 + r^2(3 \cos^2 \varphi_2 - 2) + rR \cos \varphi_2 \right] \times \sqrt{R^2 + r^2 - 2r(R+h) \cos \varphi_2} \\ I_3 &= -\frac{1}{3} \left[(R+h)^2 + r^2(3 \cos^2 \varphi_1 - 2) + r(R+h) \cos \varphi_1 \right] \\ &\quad \times \sqrt{(R+h)^2 + r^2 - 2r(R+h) \cos \varphi_1} \\ I_4 &= \frac{1}{3} \left[R^2 + r^2(3 \cos^2 \varphi_1 - 2) + rR \cos \varphi_1 \right] \times \sqrt{R^2 + r^2 - 2r(R+h) \cos \varphi_1} \\ I_5 &= -\cos \varphi_2 \sin^2 \varphi_2 r^3 \\ &\quad \times \ln \left(\frac{\sqrt{(R+h)^2 + r^2 - 2r(R+h) \cos \varphi_2} + (R+h) - r \cos \varphi_2}{\sqrt{R^2 + r^2 - 2r(R+h) \cos \varphi_2} + R - r \cos \varphi_2} \right) \end{aligned}$$

In Eq. (9), R is the radius of the Earth and φ and λ colatitude and longitude, respectively. When the observation point P is not located along the polar axis, the UNIPOL approach maps each tesseroid defined in the Earth-Centered Rotational reference frame (ECR_{Tesseroid}) into a sector of a spherical zonal band of a spherical cap in the Earth-Centered P -Rotational reference frame, having the same origin O

and polar axis coinciding with the line connecting O to the observation point P ($ECP_{\text{Tesseroid}}$), for which it is possible to use the exact solution in Eq. (9) (**Figure 2**).

Mapping can be done by means of two procedures, depending on the spherical distance of the tesseroid from the observation point (**Figure 3a**).

The first procedure (ST procedure) involves a local second-order decomposition of each tesseroid into a number N_S of small equal-area sectors of a spherical band, which develop along the local ECP meridians (dashed black lines) and parallels (dashed blue lines in **Figure 3b**). Sensitivity tests [11] show that the *optimum* value of N_S for which the ST procedure converges varies only with the latitude and decreases from the equator to the North Pole. In the present study we use $N_S = 4$, in agreement with [11].

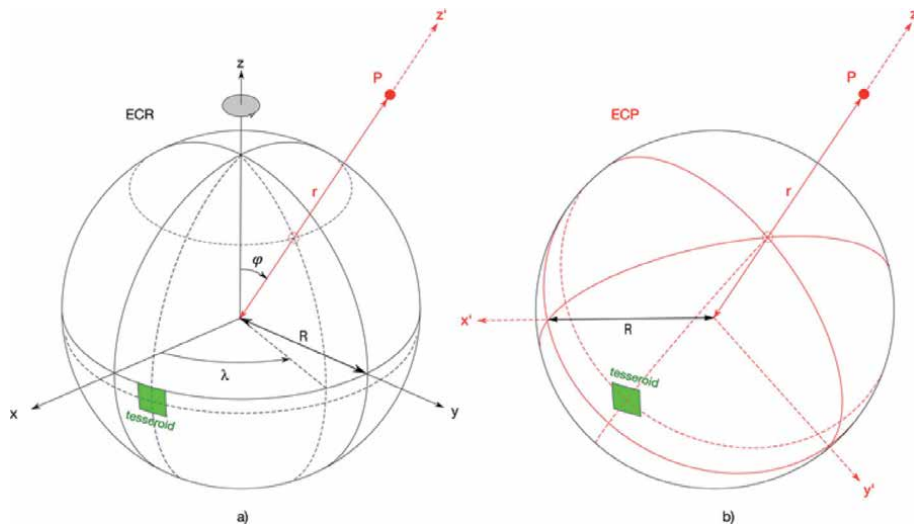


Figure 2. Geometry used to calculate the contribution of a spherical tesseroid (green rectangle) to the gravitational acceleration at a point P outside a spherically symmetric earth. a) Representation in the earth-Centered rotational reference frame (ECR). b) Representation in the earth-Centered P-rotational reference frame (ECP), defined with respect to the observation point P . R stands for the mean radius of the spherical earth; φ and λ stand for colatitude and longitude, respectively.

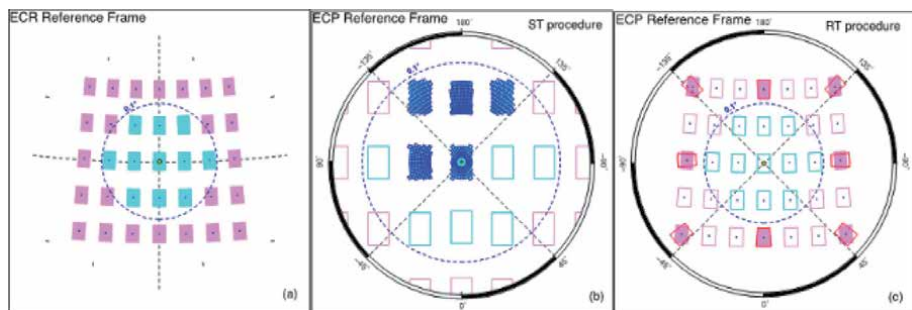


Figure 3. Scheme of the UNIPOL approach. a) Set of tesseroids in the earth-centred rotational (ECR) reference frame. The yellow circllet indicates the observation point. The blue dashed circle around the observation point marks the area where tesseroids are at a distance $\leq 0.1^\circ$ from the observation point and the ST procedure is required. Cyan and pink colors are used to indicate the tesseroids that require the application of the ST (cyan) and the RT (pink) procedure. b) Tesseroids mapped in the earth-Centered P-rotational (ECP) reference frame ECP and decomposition of some of them into sectors of a spherical band (light blue-colored tesseroids) in the local ECP reference frame. c) Tesseroids mapped in the earth-Centered P-rotational (ECP) reference frame ECP (pink areas) and re-orientation of some of them in the local ECP reference frame (red sectors). Modified from Marotta and Barzaghi [11].

The second procedure (RT procedure) is based on the rotation of an $ECR_{Tesseractoid}$ (pink areas in **Figure 3c**) around its center and on its resizing to form a sector of a spherical band (red lines in **Figure 3c**) that develops along the local ECP-meridian and has the ECP-longitudinal dimension such that the $ECP_{Tesseractoid}$ maintains the same area of the original $ECR_{Tesseractoid}$.

In agreement with [11], in the present study we use the ST procedure for angular distance between the observational point and the center of the tesseractoid less than 0.1° . For angular distance greater than 0.1° we use the RT procedure.

Finally, the Flat Tesseractoid (FT) approximation is considered. In this case, the bottom and the top of the tesseractoid are flattened thus obtaining a particular polyhedron. A polyhedron is by definition a three-dimensional body with flat polygonal faces, straight edges and sharp corners or vertices and, through proper determination of its vertices, it can realize volumes approximating both right and spherical prisms.

By assuming the FT approximation, one can apply the linear integral algorithm for the computation of the gravitational effect implied by the topographic masses as proved in [4]. The implementation of such approach is based on the double application of the divergence theorem of Gauss to volume integrals of the general expressions for the gravity field resulting from a polyhedral constant density mass and evaluated at an arbitrary point in space. Given the potential of the body B in Eq. (7), the three components of the attraction of this body in a Cartesian orthogonal frame (x, y, z) can be expressed as

$$V_{x_i}(P) = G\rho \iiint_B \frac{\partial}{\partial x_i} \left(\frac{1}{l} \right) dv(Q) \quad i = 1, 2, 3 \quad (10)$$

where $V_{x_i}(P)$ is the partial derivative of the potential $V(P)$ along the x_i direction.

The double application of the divergence theorem transforms these expressions first into an equal set of surface integrals (of the same number of faces of the polyhedral source) and subsequently each of them into a set of line integrals defined for each individual segment belonging on that face of the polyhedron. The solution of each line integral produces the final analytical formulas that, in terms of first-derivatives of the potential, are given by [4]:

$$V_{x_i}(P) = G\rho \sum_{p=1}^n \cos(N_p, e_i) \left[\sum_{q=1}^m \sigma_{pq} h_{pq} LN_{pq} + h_p \sum_{q=1}^m \sigma_{pq} AN_{pq} + \sin(g_{A_p}) \right] \quad (11)$$

In Eq. (11), p defines one of the polygonal surfaces S_p , q defines one of the segments delimitating the p polygonal surface, N_p is the outer unit normal of the polyhedral plane p , e_i is the unit vector situated in the computation point P , σ_{pq} is equal to -1 when the normal of segment q lying on the plane of polygon S_p points to the half-plane that contains the projection P' of P on S_p , σ_{pq} is equal to $+1$ otherwise, h_{pq} is the distance between P' and the segment q , h_p is the distance between P and the plane p . LN_{pq} and AN_{pq} are transcendental expressions:

$$LN_{pq} = \ln \frac{s_{2pq} + l_{2pq}}{s_{1pq} + l_{1pq}} \quad (12)$$

$$AN_{pq} = \arctan \frac{h_p s_{2pq}}{h_{pq} l_{2pq}} - \arctan \frac{h_p s_{1pq}}{h_{pq} l_{1pq}} \quad (13)$$

The l_{1pq} and l_{2pq} terms are the three-dimensional distances between P and the end points of the segment pq , while s_{1pq} and s_{2pq} are the one-dimensional distances between the origin P'' of a 1D local coordinate system defined on the segment pq and its two end points. Last term of Eq. (11), $\sin(g_{Ap})$, is the singularity term that appears for specific locations of P' with respect to the closed polygonal line G_p . It expresses the analytical solutions of the corresponding limiting values of the line integrals that are obtained from the partial application of the divergence theorem for a small circle containing the singularity point when its radius tends toward zero. This singularity terms yield finally the values $-2\pi h_p$ when P' lies inside S_p , $-\pi h_p$ when P' is located on G_p but not at any of its vertices, $-\vartheta h_p$ when P' is located at one of the vertices of G_p and ϑ is the angle defined by two subsequent segments that meet at the corresponding vertex, and 0 when P' is located outside S_p . In Eq. (11), the two coordinate transformations occurring in every face of the polyhedron are given by two nested summations, firstly over faces and secondly over segments, of the same transcendental expressions depending on the vertices of the polyhedron. This means properly managing the relative position of points P , P' and P'' with respect to every surface S_p that can be done algorithmically by standard tools of vector calculus. **Figure 4** presents a sketch of their relative positions.

Once clarified that the linear integral approach requires the control of the relative position of the vertices of a polyhedral mass with respect to the computation point, in the following a brief description of the implementation of such approach in the framework of residual terrain correction algorithms assessment is provided. Let us consider a set of n points in space P_i ($i = 1$ to n) on which the gravitational effect of the terrain must be computed and a set of m gridded points Q_j ($j = 1$ to m) with grid spacings $\Delta\varphi_j$ in latitude and $\Delta\lambda_j$ in longitude describing the DTM considered to compute this effect. The coordinates of P_i and Q_j are expressed in terms of spherical coordinates (φ, λ, r) referring to the same reference system, as well as the angular grid spacings $\Delta\varphi_j$ and $\Delta\lambda_j$. On the basis of the spherical coordinates of Q_j $(\varphi_j, \lambda_j, r_j)$, the grid spacings $\Delta\varphi_j, \Delta\lambda_j$ and the radius of the computation point r_i , a six-facet polyhedron can be defined. In particular, the eight vertices of this polyhedron will be: A $(\varphi_j, \lambda_j, r_i)$, B $(\varphi_j, \lambda_j + \Delta\lambda_j, r_i)$, C $(\varphi_j + \Delta\varphi_j, \lambda_j + \Delta\lambda_j, r_i)$, D $(\varphi_j + \Delta\varphi_j, \lambda_j, r_i)$, E $(\varphi_j, \lambda_j, r_j)$, F $(\varphi_j, \lambda_j + \Delta\lambda_j, r_j)$, G $(\varphi_j + \Delta\varphi_j, \lambda_j + \Delta\lambda_j, r_j)$,

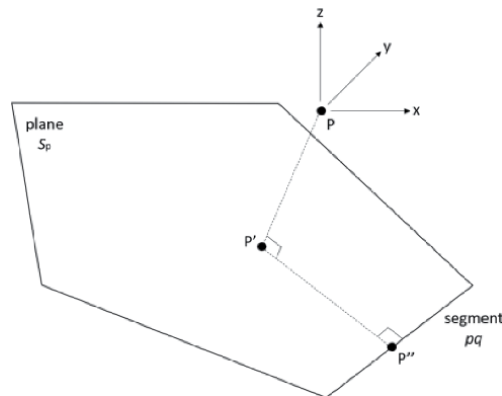


Figure 4. Sketch of the relative position of points P , P' and P'' and of the local reference system defined in the computation point P .

$H(\varphi_j + \Delta\varphi_j, \lambda_j, r_j)$. Note that the two planar surfaces identified by the closed polygons $ABCD$ and $EFGH$ have their vertices whose radiuses depend in the first case on the radius of the computation point P_i while in the second case on the radius of the DTM point Q_j . **Figure 5** illustrates in graphical form how the single polyhedron is built.

This procedure defines the spherical coordinates of the vertices of the polyhedron that are at the height of the terrain and at the height of the computation point, i.e. the level at which the Bouguer plate is computed. The computation of the first-order derivative along the direction of r_i of the gravitational effect of such polyhedron corresponds to the terrain correction to be applied at P_i as contribute of Q_j . Such value is obtained by running the code *polyhedron.f* made available by the author [4] implementing the linear integral approach. As input, the relative cartesian coordinates of the polyhedron vertices with respect to the computation point and their topological relationships are required. These are obtained applying a change of reference system to the polyhedron vertices. In particular, their coordinates were roto-translated into a local reference system having the origin at the computation point P_i , the z axis pointing up along the direction of r_i and the x and y axes parallel to the local East and North directions, respectively. Regarding the topological relationships defining the outer normal direction of the six planes of the polyhedron, they are defined by a topology matrix containing the counterclockwise sequence of the vertices as seen from outside. As output, the absolute value of the computed V_r is taken. This procedure contemplates two nested loops over all the m DTM points Q_j and the n computation points P_i . Within the loop over the computation points, different local reference systems are defined. This leads to slight changes in the directions of the x and y axes but not on the z axis, always normal and pointing outside the reference sphere defined on P_i , then maintaining

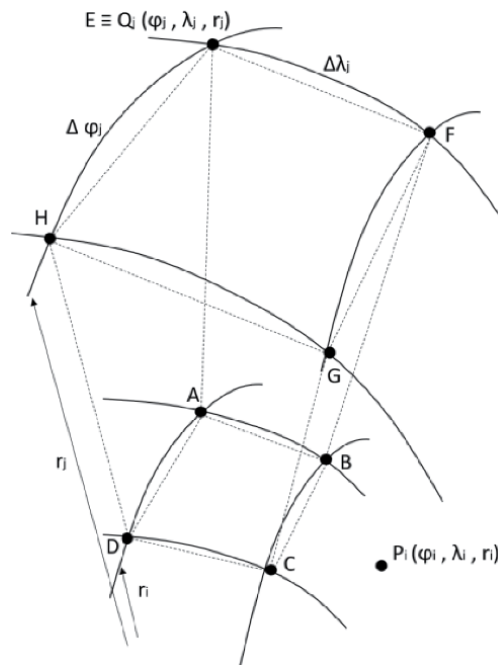


Figure 5. Sketch of the polyhedron vertices building procedure on the basis of the DTM point Q_j and the computation point P_i .

consistency between the different V_r computed by the same DTM point Q_j with respect to the different computation points P_i .

The three different models adopted in computing the TC account for a different geometry of the single terrain element. The spheroid formula (Eq. (9)) considers the radial convergence component of the vertical edges of each terrain element and, besides that, gives a spherical approximation of the top and the bottom of this element. The flat spheroid has the same geometry in the radial component but top and bottom are planar surfaces. Thus, its geometry is, in principle, less accurate than the one of the spheroid. Finally, the computation based on the right parallelepiped disregards also the radial convergence of the vertical edges. Hence, this model describes the topography geometry of each element in a way that does not adhere properly the two main features of the given DTM element. However, since in computing the TC effect only the differences between the height of the computation point and the heights of the DTM needs to be considered, the above-mentioned differences between the geometries of the elements used in computing the TC should have a limited impact on the computed values. To prove this, we have devised a test in the Alpine area where the largest discrepancies are expected in the TC effect evaluated with the three different geometries of each single DTM element.

3. The numerical tests on the three proposed approaches

The three different mathematical models presented in Section 2 have been applied in two TC computation tests. Both tests have been carried out in the Alpine area.

In the first test, the SRTM3 DTM (see [14]) have been selected in the area (called AREA_1):

$$46^\circ \leq \varphi \leq 47^\circ \quad 11^\circ \leq \lambda \leq 12^\circ$$

The statistics of the height data in this area (see **Figure 6**) are given in **Table 1**.

Points for the TC computation have been selected on a $3' \times 3'$ regular grid in the inner area:

$$46.25^\circ \leq \varphi \leq 46.75^\circ \quad 11.25^\circ \leq \lambda \leq 11.75^\circ$$

The computation points are thus in an inner area which have 0.25° from the extents of the outer one containing the DTM. So, the terrain correction in points

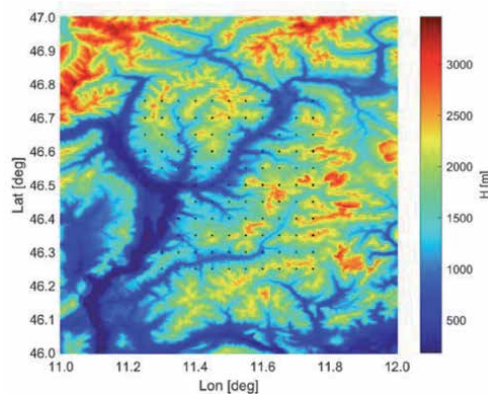


Figure 6.
 The DTM (AREA_1) and the points for TC computation.

Number of points	μ [m]	σ [m]	Min [m]	Max [m]
1442401	1502.0	644.1	160.0	3460.0

Table 1.
The statistics of the DTM data in AREA_1.

close to the DTM boundaries is not computed according to the standard. However, in the relative comparison between methods, this should not affect the results.

The heights of these 121 prediction points have been assumed coincident with those of the SRTM3 DTM and their statistics are listed in **Table 2**.

Given the geometry of tesseroids and flat tesseroids, SRTM3 orthometric heights were transformed into ellipsoidal heights via the EGM96 geoid undulation [15].

Based on the ellipsoidal coordinates $(\varphi_{ellipsoidal}, \lambda, h)$ of both DTM and prediction points were converted into spherical coordinates (φ, λ, r) and used in the terrain effect computation with tesseroids and flat tesseroids.

The statistics of the differences among the three methods are given in **Table 3**.

As a first overall comment, it can be stated that the results are in good agreement even in such a rough mountain area with sharp height variations (see **Tables 1** and **2**). By inspecting in more detail the statistics, one can see that values computed by the TC-GRAVSOF and the UNIPOL approaches are in better agreement than those computed by the TC-GRAVSOF and the Flat Tesseroid (FT) approaches. The mean of the differences in the first case is nearly 60% of that of the second comparison and the standard deviation is the 86%. This is quite an unexpected result as the geometry of the FT tesseroid is closer to that of the TC prism than to the geometry of the UNIPOL tesseroid. Further investigations will be performed in order to understand this behavior.

On the other hands, the terrain correction values based on the UNIPOL tesseroid procedure and the ones obtained with the FT approach agree very well.

The mean and the standard deviation of the differences between these terrain corrections are of the order of some hundredth of mGal and the maximum difference is of the order of one third of mGal. Although in principle this is quite foreseen, it is important to quantify the differences in view of practical applications.

Larger differences can be seen when comparing these two methods with the one based on prism effect. In these cases, the maximum differences are of the order of 1

Number of points	μ [m]	σ [m]	Min [m]	Max [m]
121	1471.3	611.7	212.0	2577.0

Table 2.
The statistics of the heights of the computation points in AREA_1.

	μ [mGal]	σ [mGal]	Min [mGal]	Max [mGal]
TC (GRAVSOF)	13.686	5.194	5.185	35.526
TESSEROID (UNIPOL)	13.553	5.111	5.313	35.065
FLAT TESSEROID (FT)	13.472	5.077	5.275	34.883
TC (GRAVSOF) - UNIPOL	0.133	0.175	-0.246	0.782
TC (GRAVSOF) - FT	0.214	0.203	-0.156	1.050
UNIPOL - FT	0.081	0.056	0.006	0.306

Table 3.
The statistics of the TC computations in AREA_1.

mGal. Even though this value is high if compared with the precision of the gravity observations (which can reach few μGals), one has to consider that other error sources in the topography reduction process can have a larger impact. As an example, the discrepancy between the heights of the point associated with the gravity observations as compared with those obtained by the DTM in the same points can amount to ten meters (or even more) in mountain areas. Given that the absolute value of the free-air gradient is 0.30877 mGal/m , this implies 3 mGal in 10 m due to this mismatch. Also, biases can occur due to the assumption of constant density. In view of that, even the maximum difference between the GRAVSOFT terrain correction and the spherical tesseroid/flat tesseroid values are not so significant.

A second test was then devised. Observed gravity data were selected in the area (AREA_2):

$$46^\circ \leq \varphi \leq 47^\circ \quad 11^\circ \leq \lambda \leq 12^\circ$$

Gravity point coordinates were surveyed with GNSS and framed to ITRF94. Statistics of the ellipsoidal heights of these gravity points are listed in **Table 4**.

Gravity values have been measured with a Lacoste&Romberg G-367 relative gravimeter. The standard deviation of the observed values is of the order of 0.02 mGal . Gravity data are referred to IGSN71 and their statistics are summarized in **Table 5**.

For the computation of the terrain component, the SRTM3 DTM have been selected in the $3^\circ \times 3^\circ$ area centered on the one containing the gravity data area (AREA_2)

$$45^\circ \leq \varphi \leq 48^\circ \quad 10^\circ \leq \lambda \leq 13^\circ$$

The statistics of the SRTM3 in AREA_2 are described in **Table 6**.

Figure 7 shows the DTM features of AREA_2 and the position of the gravity points.

Similarly to what has been done in the first test, SRTM3 and gravity point coordinates were transformed into spherical coordinates for the computation of the terrain correction with the UNIPOL and FT approaches. On the other hands, ellipsoidal heights of gravity points have been converted into orthometric heights via

Number of points	μ [m]	σ [m]	Min [m]	Max [m]
116	1161.74	384.22	312.67	2217.08

Table 4.
The statistics of the heights of the computation points in AREA_2.

Number of points	μ [mGal]	σ [mGal]	Min [mGal]	Max [mGal]
116	980404.459	71.605	980208.060	980545.806

Table 5.
The statistics of the observed gravity values.

Number of points	μ [m]	σ [m]	Min [m]	Max [m]
12967201	1054.4	853.2	-35.0	3865.0

Table 6.
The statistics of the DTM data in AREA_2.

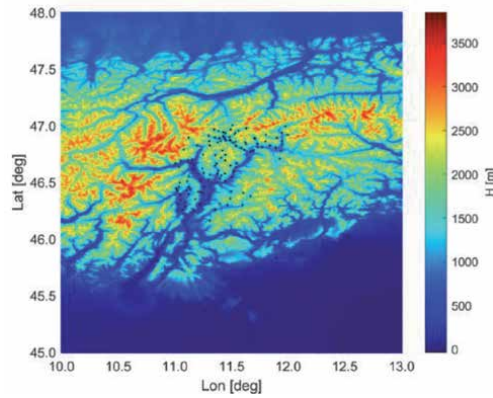


Figure 7.
The DTM (AREA_2) and the points for TC computation.

the EGM96 geoid undulations when computing the terrain correction with the TC software of the GRAVSOFTE package.

Given the three different terrain corrections, by applying Eq. (4), three different sets of Bouguer anomalies have been derived.

In Eq. (4), as previously stated, the orthometric height H is derived via the EGM96 geoid undulation and the Bouguer plate is accounted for by using Eq. (1). We further assumed that

$$\frac{\partial \gamma}{\partial h} = -0.30877 \text{ mGal/m} \quad (14)$$

and the normal gravity in a point Q of latitude φ_Q on the ellipsoid is given by the GRS80 normal gravity formula [16]:

$$\gamma(Q) = 978032.7(1 + 0.0053024 \sin^2 \varphi_Q - 0.0000058 \sin^2 2\varphi_Q) \text{ mGal} \quad (15)$$

Although this formula has an accuracy of 0.1 mGal (see [16]), it can be used in the context of this relative comparison among different terrain correction computation methods.

Table 7 summarizes the statistics of the Bouguer anomalies obtained with the three terrain correction methods.

Comments similar to those given on **Table 3** hold for the Bouguer values in **Table 7**. The Bouguer anomalies obtained by applying the three methods have quite similar statistics. Those computed via TC-GRAVSOFTE software have the smallest standard deviation and the highest mean while those obtained with the other two methods have smaller mean and higher standard deviations. If the RMSs are considered, one can see that the Bouguer anomalies based on the flat tesseroid have the smallest value. However, as pointed out before, even the largest difference among

Δg_B	μ [mGal]	σ [mGal]	RMS [mGal]	Min [mGal]	Max [mGal]
TC (GRAVSOFTE)	-137.846	16.131	138.786	-168.873	-90.511
TESSEROID (UNIPOL)	-137.074	16.205	138.028	-166.337	-90.299
FLAT TESSEROID (FT)	-136.894	16.221	137.852	-166.262	-90.069

Table 7.
The statistics of the Bouguer anomalies.

the maximum values (around 2.6 mGal) is not so significant if compared with other biases occurring in the Bouguer reduction.

Thus, the statistics of **Tables 3** and **7** prove the substantial equivalence of the three approaches used for the *TC* computation.

4. Conclusions

Three different methods for terrain correction have been compared in two areas over the Alps. The standard computation given by the TC-GRAVSOFTE program has been compared with the terrain corrections evaluated via spherical tesseroid and flat tesseroid formulas. In the first test, the SRTM DTM was clipped in a $1^\circ \times 1^\circ$ window and *TC* effect was computed in a set of gridded points in the same area. In the second test, observed gravity values in a $1^\circ \times 1^\circ$ area have been used in the computation of Bouguer anomalies considering the $3^\circ \times 3^\circ$ SRTM DTM values centered on the area containing the gravity data. Despite the fact that the topography in the two selected DTM windows is quite rough, no significant differences among the methods have been revealed. The statistics of the values obtained by modeling in different ways the shape of the discretized topography elements are practically equivalent. Differences among *TC* effects and Bouguer anomalies computed with parallelepiped, spherical tesseroid and flat tesseroid amount to maximum values that are around 1 and 3 mGal respectively. As a matter of fact, there are other error sources (e.g., density heterogeneities, DTM and gravity point heights mismatch) that can have impacts on the terrain correction computation larger than 3 mGal. However, if in the second test on Bouguer computation we consider the values *per se*, spherical tesseroid and flat tesseroid models perform slightly better when RMS values are compared, i.e. the spherical tesseroid and flat tesseroid based Bouguer anomalies are smoother.

Finally, we remark that the concept applied in the flat tesseroid modeling can be adapted to the terrain effect computation when shaping the topography according to the Triangulated Irregular Network model [17]. In this way, a more detailed terrain effect evaluation will be possible, particularly in the neighbor of the computational points, by better modeling the terrain slopes.

Acknowledgements

We thank DTU Space for providing us with the *TC* program of the GRAVSOFTE package.

Conflict of interest

The authors declare no conflict of interest.

Author details

Carlo Iapige De Gaetani¹, Anna Maria Marotta², Riccardo Barzaghi^{1*},
Mirko Reguzzoni¹ and Lorenzo Rossi¹

1 Department of Civil and Environmental Engineering, Politecnico di Milano,
Milan, Italy

2 Department of Earth Sciences “Ardito Desio”, Università degli Studi di Milano,
Milan, Italy

*Address all correspondence to: riccardo.barzaghi@polimi.it

IntechOpen

© 2021 The Author(s). Licensee IntechOpen. This chapter is distributed under the terms of the Creative Commons Attribution License (<http://creativecommons.org/licenses/by/3.0>), which permits unrestricted use, distribution, and reproduction in any medium, provided the original work is properly cited. 

References

- [1] Heiskanen WA, Moritz H. *Physical Geodesy*. San Francisco: Freeman; 1967.
- [2] Forsberg R. *A Study of Terrain Reduction, Density Anomalies and Geophysical Inversion Methods in Gravity Field Modelling [report]*. Ohio: Department of Geodetic Science and Surveying, The Ohio State University; 1984.
- [3] Heck B, Seitz K. A comparison of the tesseroid, prism and point-mass approaches for mass reductions in gravity field modelling. *Journal of Geodesy*. 2007; 81: 121-136.
- [4] Tsoulis D. Analytical computation of the full gravity tensor of a homogeneous arbitrarily shaped polyhedral source using line integrals. *Geophysics*. 2012; 77(2).
- [5] Vaníček R, Tenzer R, Sjöberg L, Martinec Z, Featherstone W. New views of the spherical Bouguer gravity anomaly. *Geophysical Journal International*. 2004; 159(2): 460-472.
- [6] Sideris MG. A fast Fourier Transform Method for computing terrain correction. *Manuscripta Geodaetica*. 1985; 10: 66-73.
- [7] Forsberg R. Gravity Field Terrain Effect Computation by FFT. *Bulletin Geodesique*. 1985; 59: 342-360.
- [8] Tscherning CC, Forsberg R, Knudsen P. The GRAVSOFTE package for geoid determination. In: *Proceedings of the 1st continental workshop on the geoid in Europe; 11-14 May 1992; Prague*. 1992.
- [9] Grombein T, Seitz K, Heck B. Optimized formulas for the gravitational field of a tesseroid. *Journal of Geodesy*. 2013; 87: 645-660.
- [10] Uieda L, Barbosa VCF, Braitenberg C. Tesseroids: Forward-modeling gravitational fields in spherical coordinates. *Geophysics*. 2015; 81(5): F41-F48.
- [11] Marotta AM, Barzaghi R. A new methodology to compute the gravitational contribution of a spherical tesseroid based on the analytical solution of a sector of a spherical zonal band. *Journal of Geodesy*. 2017; 91(10): 1207-1224.
- [12] Lin M and Denker H. On the computation of gravitational effects for tesseroids with constant and linear varying density. *Journal of Geodesy*. 2019; 93:723-747.
- [13] La Fehr TR. An exact solution for the gravity curvature (Bullard B) correction. *Geophysics*. 1991; 56: 1179-1184.
- [14] U.S. Releases Enhanced Shuttle Land Elevation Data [internet]. Available from: <https://www2.jpl.nasa.gov/srtm/> [Accessed: 2021-02-02]
- [15] Lemoine FG, Kenyon SC, Factor JK, Trimmer RG, Pavlis NK, Chinn DS, Cox CM, Klosko SM, Luthcke SB, Torrence MH, Wang YM, Williamson RG, Pavlis EC, Rapp RH, Olson TR. *The Development of the Joint NASA GSFC and the National Imagery and Mapping Agency (NIMA) Geopotential Model EGM96 [report]*. Greenbelt, USA: NASA Technical Paper NASA/TP1998206861, Goddard Space Flight Center; 1998.
- [16] Moritz H. Geodetic Reference System 1980. *Bulletin Géodésique*. 1988; 62(3).
- [17] Lee J. Comparison of existing methods for building triangular irregular network, models of terrain from grid digital elevation models. *International Journal of Geographical Information Systems*. 1991; 5(3): 267-285.

Continental Water Storage Changes Sensed by GRACE Satellite Gravimetry

Guillaume Ramillien and Lucía Seoane

Abstract

Since its launch in March 2002, the Gravity Recovery And Climate Experiment (GRACE) mission has been mapping the time variations of the Earth's gravity field with a precision of 2–3 cm in terms of geoid height at the surface resolution of 300–400 km. The unprecedented precision of this twin satellite system enables to detect tiny changes of gravity that are due to the water mass variations inside the fluid envelopes of our planet. Once they are corrected from known gravitational contributions of the atmosphere and the oceans, the monthly and (bi)weekly GRACE solutions reveal the continental water storage redistributions, and mainly the dominant seasonal cycle in the largest drainage river basins such as Amazon, Congo, Mississippi. The potential differences measured between the twin GRACE satellites represent the sum of integrated surface waters (lakes and rivers), soil moisture, snow, ice and groundwater. Once they are inverted for estimating surface water mass densities, GRACE solutions are also used to establish the long-term mass balance of the ice sheets impacted by global warming, for quantifying the interannual variations of the major aquifers, as well as for surveying the hydrological signatures of intense meteorological events lasting a few days such as tropical hurricanes. This chapter describes GRACE gravity products and the different data processings used for mapping continental water storage variations, it also presents the most remarkable results concerning global continental hydrology and climate changes.

Keywords: satellite gravimetry, geodesy, global hydrology, gravity field, continental water storage

1. Introduction

Water that is present in different forms in the Earth's system ensures the global transport of the solar heat in the oceans and atmosphere, and thus maintains life development. As it represents a precious resource, in particular for human activities, monitoring the water cycle from space remains important for its management and understanding climate change. Observation of the Earth from space, and the determination of its gravity fields in particular, provide precious information on the mass transfers in any part of the globe.

Global gravity field models are based on the theoretical expression of the variations of the geopotential V :

$$V(\lambda, \theta, r) = \frac{GM}{a_e} \sum_{n=0}^{\infty} \left(\frac{a_e}{r}\right)^{n+1} \sum_{m=0}^n P_{nm}(\sin \theta) (C_{nm} \cos m\lambda + S_{nm} \sin m\lambda) \quad (1)$$

where λ and θ are the longitude and the latitude of the observation point respectively, r is the radial distance from the Earth's center to the point of observation, P_{nm} is the associate Legendre function of degree n and order m , a_e is the equatorial Earth's radius and the gravitational parameter is the product of the gravitational constant G with the total mass of the Earth M , so that $GM = 3.986004410 \cdot 10^{14} \pm 8 \cdot 10^5 \text{ m}^3/\text{s}^2$, according to IERS Standard. Space geodesy consists of determining the dimensionless Stokes coefficients C_{nm} and S_{nm} of the gravity field model as precisely as possible using combined satellite data and terrestrial gravity measurements on lands. As the satellite motion depends mainly on the gravitational field according to the Newton's law of attraction (~99% of the sensed gravity signal is from the solid Earth part), the only remote sensing technique to measure variations of water mass quantity is based on inversion of very precise satellite positions - with an accuracy of at least a few cm for detecting long wavelengths of the continental hydrology -, and/or satellite velocities [1].

Historically, long wavelengths of the gravity field time variations were determined using very precise Satellite Laser Ranging (SLR) data of 5900-km altitude LAGEOS 1–2 trajectories that reveal the movements of the center of mass of the Earth (or “geocenter”) representing a few thousands of mm, and Earth's flatness due to seasonal mass exchange between the two hemispheres and the regular decrease due to post-glacial rebound occurring since 20 000 years [2] (Figure 1).

Since the beginning of the 21st century, a new generation of passive and quasi-polar Low-Earth-Orbit (LEO) satellites has been launched to improve the spatial resolution of global gravity field models: the CHALLENGING Mini-satellite Payload (CHAMP, 2000–2010) mission operated by the DLR in Germany, and the Gravity field and steady-state Ocean Circulation Explorer (GOCE, 2009–2013) of ESA.

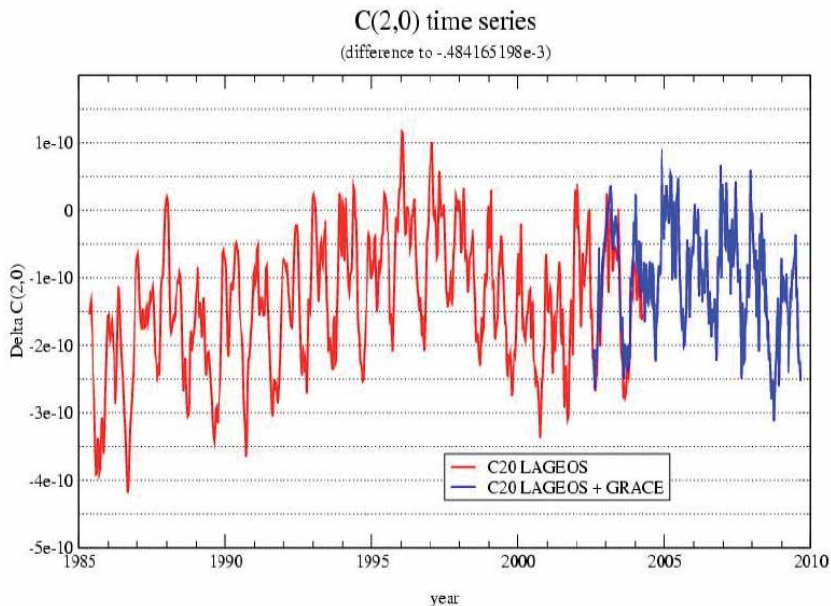


Figure 1. Time variations of the C_{20} coefficient (representing Earth's flatness) determined by analysis of the LAGEOS 1 & 2 satellite telemetry (source: GRGS, Toulouse).

As the CHAMP mission represents its precursor, the main scientific objective of the Gravity Recovery And Climate Experiment (GRACE, 2002–2017) mission proposed by the American National Aeronautics and Space Administration (NASA) and the German Aerospace Center Deutsches Zentrum für Luft- und Raumfahrt (DLR), was to measure both static and time-varying gravity field acting in different regions of the world.

GRACE was the first mission to use the principle of two co-orbital identical satellites in pursuit, as initially proposed by [3] for estimating the spatial and temporal variations of the gravitational field which reflect mass changes in the Earth system over time scales ranging from months to a ten of years [4], so that GRACE observation represents the sum of the effects of all changes in mass which are radially integrated. In fact, GRACE observations are used to successfully survey the continental hydrology at different time scales (decadal, seasonal, rapid events) allowing to measure the climate change impacts in the Earth system, as for example, ice mass lost in Polar regions as a consequence of global warming [5].

2. GRACE mission orbit and its on-board instruments

The GRACE mission consists of two 0.5 ton satellites that followed each other at a distance of ~220 km, which were placed at a relatively low average altitude of around 450 km with a quasi-polar orbit inclination of 89.5 degrees to ensure a quasi-global coverage (**Figure 2**). The relative distance between the two satellites was measured with an accuracy of $1 \mu\text{m}\cdot\text{s}^{-1}$ by a radar telemeter operating at K-Band microwave Ranging (KBR) [4]. The inter-satellite distance depends of the gravitational acceleration changes that affect each GRACE satellite [6]. The A three-axis accelerometer that senses the dynamical effects as non-dissipative forces (the mean solar and Earth's radiation pressure, the atmospheric drag) is also placed on-board. Afterwards the non-gravitational effects are removed from the raw accelerations, the geopotential change along the track of the GRACE satellites is estimated from the residual perturbations in distance and inter-satellite distance changing rate. Changes of the observed inter-satellite distances reflect the variations of the Earth's gravity field related to topography and density heterogeneities.

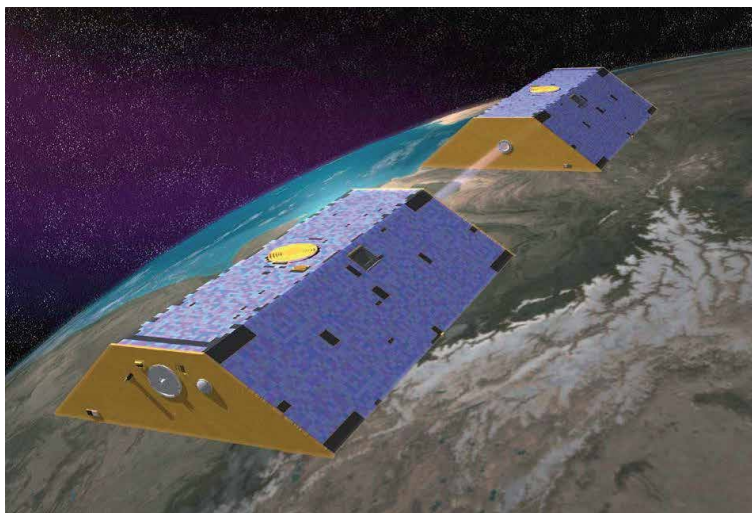


Figure 2. Artistic view of the twin GRACE vehicles orbiting around the earth (source: NASA [7]).

The payload was composed of five instruments on-board, the satellite components of the GRACE mission are listed below [3]:

- The K-band ranging system (KBR) for inter-satellite distance an accuracy of 10 μm . It uses the phases of carrier electromagnetic waves in the K and Ka bands at frequencies of 26 and 32 GHz.
- The Ultra-Stable Oscillator (USO) for generating electromagnetic waves in the K-band for the KBR system at the desired frequency.
- The SuperSTAR accelerometers (ACC) for accurate measurement of the forces acting on each satellite along three axis.
- The Stellar Camera ASSEMBLY (SCA) for determining the orientation of the satellite relatively to the positions of fixed stars.
- The Black-Jack GPS receivers and Instrument Processing Unit for providing three coordinate components of the position and the ones of the velocity of each GRACE satellite in the geocentric reference frame.

3. GRACE data products

The three official processing centers forming the GRACE Science Data Center (GSDC), i.e. the Center for Space Research (CSR) in Austin, Texas, United States; the GeoForschungsZentrum (GFZ) in Potsdam, Germany; the Jet Propulsion Laboratory (JPL) in Pasadena, California, United States, produce the Level-1B parameter products and the Level-2 solutions derived from measurements of the GRACE mission. Level-1B products are constituted by the processed positions and velocities, which were measured by the on-board GPS receivers, accelerometers and the accurate K-band measurements of the variations in distance between the two vehicles. Using these measurements, the monthly gravity field models or Level-2 products for continental hydrology are computed. These products are expressed by means of geoid heights and Equivalent-Water Heights (EWH). The latter products are distributed by the GFZ's Integrated System Data Center (ISDC, [8]), and the JPL's Physical Oceanography Distributive Active Data Center (PODAAC, [9]).

3.1 Spherical harmonics solutions

The Level-2 products are obtained using a dynamic approach, which relies on the Newtonian formulation of the satellite motion equation evaluated in an inertial reference frame having the origin at the Earth's center. The formulated solution is combined with a dedicated modeling of the gravitational and non-conservative forces, which act on the spacecrafts [6]. During the process of data reduction, the known gravitational contributions are removed from observations using a priori information from meteorological and global ocean circulation models as well as the non-gravitational forces that were measured by the on-board accelerometers [10, 11]. The residual values represent mainly the contribution of the continental hydrology and errors of the correcting models in the measured gravity field. More details about the pre-treatment of the GRACE data reduction can be found in [12]. These solutions are provided as monthly or weekly lists of Stokes coefficients, i.e. dimensionless Spherical Harmonic (SH) coefficients of the geopotential [13], up to degree and order 96 or less that correspond to a spatial resolution of 200–300 km [14–17]. The range

of an ideal resolution for GRACE products for hydrology is discussed in [18]. While the correcting models represent a reasonable dealiasing of high-frequency changes, the errors due to tide modeling remain in the GRACE solutions, especially for diurnal S2 tides [18–22]. These SH solutions are affected by north–south striping, especially dominant in the tropical band where the coverage of the satellite is insufficient mainly because of three reasons including the sparsity of GRACE track sampling in the longitudinal direction due to the polar orbit plane; propagation of systematic errors from the correcting model acceleration [19–21]; and the numerical correlations generated by solving the underdetermined systems of normal equations for the high-degree Stokes coefficients [23]. Average of each Stokes coefficient C_{nm} and S_{nm} versus time is computed and removed to estimate the time anomalies for each monthly or weekly period. It is necessary to eliminate this noisy effect on the GRACE solutions, which are impacted by short North–South wavelength components. The monthly Stokes coefficients ΔC_{nm} and ΔS_{nm} that have been destriped by filtering have been used in very numerous studies on the evaluation of water storage on lands and the oceans [4, 24–32]. A simple strategy to attenuate the short-wavelength striping of the GRACE solutions consists of computing the weighted average of the solutions taken from the official centers for each period of time, and by considering the a posteriori uncertainty levels of the fitted Stokes coefficients to define these weights for combination [33].

Maps of water storage anomalies over lands directly based on [34] are:

$$\Delta\sigma(\lambda, \theta, t) = a_e \rho_w \sum_{n=0}^{\infty} \sum_{m=0}^n P_{nm}(\sin\theta) \frac{2n+1}{1+k_n} (\Delta C_{nm}(t) \cos m\lambda + \Delta S_{nm}(t) \sin m\lambda) \quad (2)$$

where $\Delta\sigma$ is the change in surface density (mass/area), ρ_w is the density of the water and k_n is the Love numbers [35]. The change of surface mass is usually expressed in meters of equivalent water thickness (EWH). All the mass anomalies derived from GRACE data were explicated as total water mass change.

3.2 Mascons and regional solutions

Other GRACE solutions can also be obtained by other research centers where different numerical approaches are used to reach temporal resolution of one day to one month in the form of SH coefficients (global approaches) or spatial grids (local or regional approaches). As alternative to the SH approach, which is based on frequency representation instead of pure spatial localization [36], other types of base functions are used to represent surface water mass densities, mass concentration elements or mascons. In this case, water mass anomalies are estimated in specified concentrated surfaces on the Earth's locations. The GRACE mascons have been proposed by several research groups such as Goddard Space Flight Center (GSFC) [37–41], Jet Propulsion Laboratory (JPL) [42, 43] and Center of Space Research (CSR) [44] at the University of Texas, Austin, where they are processed differently. As an instance, the 1° equatorial equivalent sampled mascons developed at CSR are computed by no temporal smoothing and regularization, as they are only based on GRACE information, whereas more recent mascons solutions are derived by using partial derivatives to relate KBRR observations to EWH to be determined [44]. In a second version, the mascons are related to the range rate or the range acceleration using SH that remain truncated at certain degrees and orders, as proposed by [38]. Mascons can also be estimated by post-processing of Level-2 GRACE SH solutions without a direct use of range rate observations (see examples in [44–47]). Global

grids of mascons solutions can be easily downloaded from [48, 49] for CSR and JPL Releases 06, respectively. Note that these latter solutions need to be scaled by a gain factor that varies geographically. A sequential Kalman Filtering (KF) approach for estimating regional maps of water mass changes by progressive integration of daily along-track GRACE geopotential anomalies has been recently proposed by [1, 50]. This iterative Kalman filter procedure has been successfully applied to determine $2^\circ \times 2^\circ$ surface water mass density solutions over continental regions instead of using the SH or mascons representation [51–53].

3.3 Spatial resolution and accuracy of the GRACE products on lands

The GRACE products contribute in continental hydrology research with a novel information: the terrestrial water storage or integrated water content, i.e. the sum of the water contained in the column from the different hydrological reservoirs: surface water, soil water, groundwater and snow cover. An early study showed an expected measurement accuracy of a few millimeters of EWH in terms of surface density for a reference water density of 1000 kg/m^3 , over areas of $400 \text{ km} \times 400 \text{ km}$, this work was based on Land Surface Models (LSM) outputs as soil moisture, evapotranspiration and run-off. It is expected that the presence of noise in the shorter wavelengths affects the TWS retrieval [34]. In addition, errors due to the spectra truncation increase as the area of the studied basin decrease. Based on LSM outputs and the expected accuracy of the GRACE land water solutions, it was proved that the changes in TWS could be detected by the GRACE system if they exceed 1.5 cm of EWH over an area of $200\,000 \text{ km}^2$ [54]. The accuracy of the GRACE land water solutions was expected to be about 0.7 cm of EWH for a drainage area of $400\,000 \text{ km}^2$ and 0.3 cm for a drainage basin of 4 million of km^2 [55].

Current GRACE Products have a spatial resolution of a few hundred kilometers (around 200 km for the mascons and for the regional solutions, and 330 km for the releases 03 and 05 for a typical degree of truncation of $n = 60\text{--}90$). Errors were estimated to be around 4 cm at the Equator, and decreasing to 1.5 cm in Polar regions due to denser GRACE satellite tracks coverage [56].

4. Continental hydrology assessment by GRACE observations

The GRACE mission has been observing mass changes in the Earth's body during 15 years, and since 2018 the new mission GRACE-FO continues this task. These satellite gravimetric missions have many applications as: to better understanding earthquake mechanism [57–60]; to quantify sea level rise [61, 62] and; to observe hydrological cycles [6, 63].

Analysis of the GRACE solutions consists of finding a set of time coefficients from SH or gridded solutions, so that the TWS anomalies for a given period can be decomposed into geographical coefficients:

$$\begin{aligned} \Delta\sigma(\lambda, \theta, t) = & A(\lambda, \theta) + B(\lambda, \theta)t + C_1(\lambda, \theta)\sin(\omega t) + C_2(\lambda, \theta)\cos(\omega t) \\ & + D_1(\lambda, \theta)\sin(\omega' t) + D_2(\lambda, \theta)\cos(\omega' t) \end{aligned} \quad (3)$$

With $\omega = 2\pi/T$ and $\omega' = 2\pi/T'$, considering $T = 1$ year and $T' = 1/2$ year, so that annual and semi-annual amplitudes C and D and phases φ and φ' are:

$$C = \sqrt{C_1^2 + C_2^2} \quad \text{and} \quad D = \sqrt{D_1^2 + D_2^2} \quad (4)$$

$$\varphi = \tan^{-1} \frac{C_1}{C_2} \text{ and } \varphi' = \tan^{-1} \frac{D_1}{D_2} \quad (5)$$

These model coefficients A, B, C₁, C₂, D₁ and D₂ for GRACE variations are usually adjusted following the least square minimum criteria and then represented regionally or globally. The residuals from this relatively simple Eq. 3 of water mass variations represent intermediate wavelengths, short-term variations of unmodeled phenomena and possibly errors of the a priori correcting models (see Section 3.1).

4.1 Long term water mass variations, climate changes and irrigation

In particular, the linear trend, or equivalently the $B(\lambda, \theta)$ term, that is expressed in mm of EWH per year, corresponds to the increase if positive (or decrease when negative) of the water mass storage, and it can be interpreted in terms of long-term mass balance on the considered multi-year period.

A relatively complete synthesis of works on the evolution of the water storage in several parts of the world for 2002–2017 have recently presented [64] (Figure 3). The most important losses of mass are located on the ice shelves of Greenland and Antarctica, where ice storage is drastically melting at the highest rates (more than 200 Gt/y) due to the global warming and this can contribute to half of the sea level rise of about 0.3 mm/y.

In earlier studies based on SH and recently mascons solutions [47], analyzing these GRACE data has shown a continuous acceleration of the Greenland ice shelf melting.

Regions of important loss of water are revealed by GRACE such as the drought lasting up to 2007 in the southeast of Australia [48], in the North of India [62] as well as California [65]. Besides, continental waters are accumulating in other regions like in the endoheric Okavango delta in Africa [63].

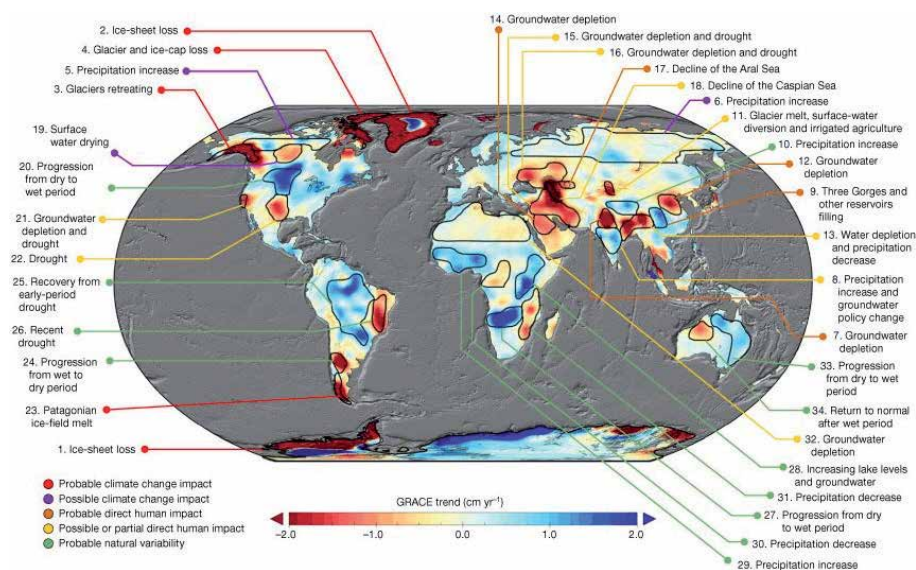


Figure 3. Global map of the TWS trends and their climatic causes sorted by colors according to [64].

The same authors have validated the constant decrease of deep water of the North Sahara aquifer sensed by GRACE with in situ water table records from wells. The Level-2 solutions need to be combined with radar altimetry data and/or model outputs in lower thus wetter latitudes, so that GRACE solutions have been used to isolate the long-term evolution of groundwater over the entire Amazon basin [66].

4.2 Seasonal cycles in major drainage river basins

The fluctuations of TWS at annual and semi-annual scales reflect the effects of climatic phenomena varying seasonally as: rainfalls, snow, temperature, evapotranspiration, river runoff, soil moisture, river discharge, groundwater and human activities. The knowledge of these periodical variations that are dominant in the large tropical basins is important to evaluate water resources. The seasonal signals estimated by GRACE are generally adjusted as described by C_1 , C_2 , D_1 and D_2 in Eq.

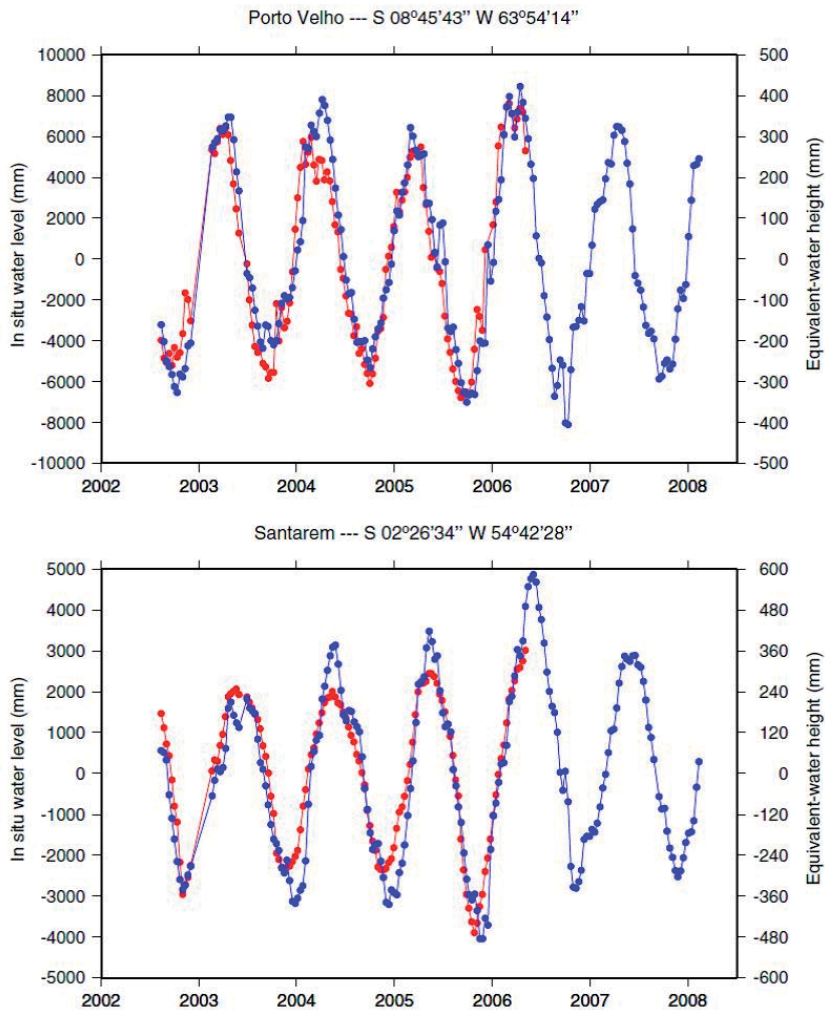


Figure 4. Times series of in-situ observations of Agência nacional del Agua (red) and GRACE observations (blue) at the stations of Porto Velho and Santarem in the Amazon basin [28]. We can notice the high correlation of these dominant annual amplitudes.

3. These amplitudes and phases determined from GRACE solutions (Eqs. 4 and 5) allow to improve the understanding of water cycle.

For example, GRACE-based annual signals over the Amazon basin show a predominant annual amplitude in fall and in spring of hundreds of EWH at the basin scale [3] driven essentially by the rainfall seasonality [67]. A comparison of GRACE observed signals and in-situ measured are shown in **Figure 4**. A detailed study of the major tributaries in the Amazon river basin demonstrates that the rainfall variations generated surface water fluxes delayed by two months due to transfer processes [53].

In the African continent, GRACE solutions show that the stronger seasonal amplitudes are located in the Sahel latitudinal band and in the tropical Congo basin (**Figure 5**). An extended study based on Principal Analysis Components reveals a biannual or quadrennial water mass variations related to the West African monsoon [63]. The use of GRACE products also helps to conclude that dry season processes, in particular, evapotranspiration and the presence of vegetation, have an important role in the modeling of soil moisture in the Sahel region [66].

GRACE solutions have also been useful to observe snow cover variations in high latitude regions [68]. For Antarctica, seasonal analysis shows very variable TWS amplitudes in coastal areas with important snow accumulation rates because of oceanic humidity [69].

In the tropical and equatorial regions, GRACE products reveal that seasonal precipitations precede land water storage with a temporal lag of 2 months, however, seasonal cycle of surface temperature is out of phase with respect to TWS, whereas in cold and temperate regions seasonal phenomena are due to more complex

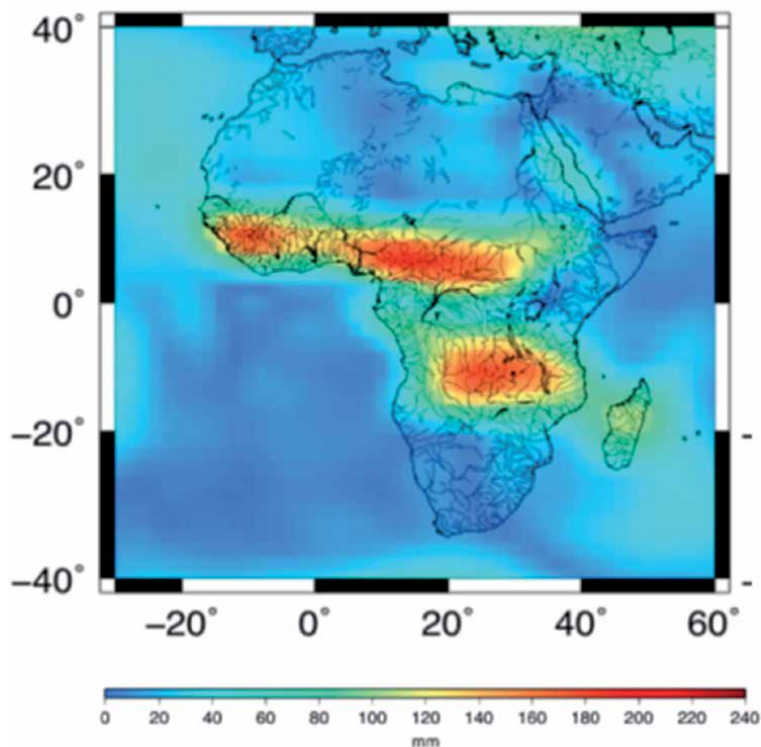


Figure 5. Map of the seasonal amplitudes of the water mass changes adjusted by least squares adjustment of pure annual sinusoids at grid cells $[C \sin(\omega t + \varphi)]$ using the 10-day regional solutions over Africa for the period 2003–2012 [70].

interactions [69]. There is also a significant contribution of river discharge in the spatial distribution of seasonal water storage with a dependency of climate [70].

Regional time variations of evapotranspiration rate - expressed in mm/yr. - can be also derived by integrating and solving the water mass balance equation, which relates TWS on land provided by GRACE, precipitation data from the Global Precipitation Climatology Centre, runoff given by a global land surface model and the unknown evapotranspiration to be determined [71].

4.3 Detection of extremes events

Gravimetric satellites missions also image the extreme climate events in the whole Earth system. Floods and droughts have been largely studied in different continents using the GRACE Level-2 products.

In the case of the Amazon basin, GRACE has revealed periods of extreme droughts and floods. During the 2005 drought, the TWS in the river and floodplains of the Amazon basin was 70% below its average for the 2003–2007 period [71]. However, in 2009 gravity measurements display an exceptional flood associated to La Niña event [26]. The maximum value of TWS in the entire Amazon basin was estimated at $\sim 624 \pm 32$ Gt with respect to the mean value.

New detection approaches based on GRACE data are developed to identify drought episodes and their severity [72]. Advances in GRACE data treatment

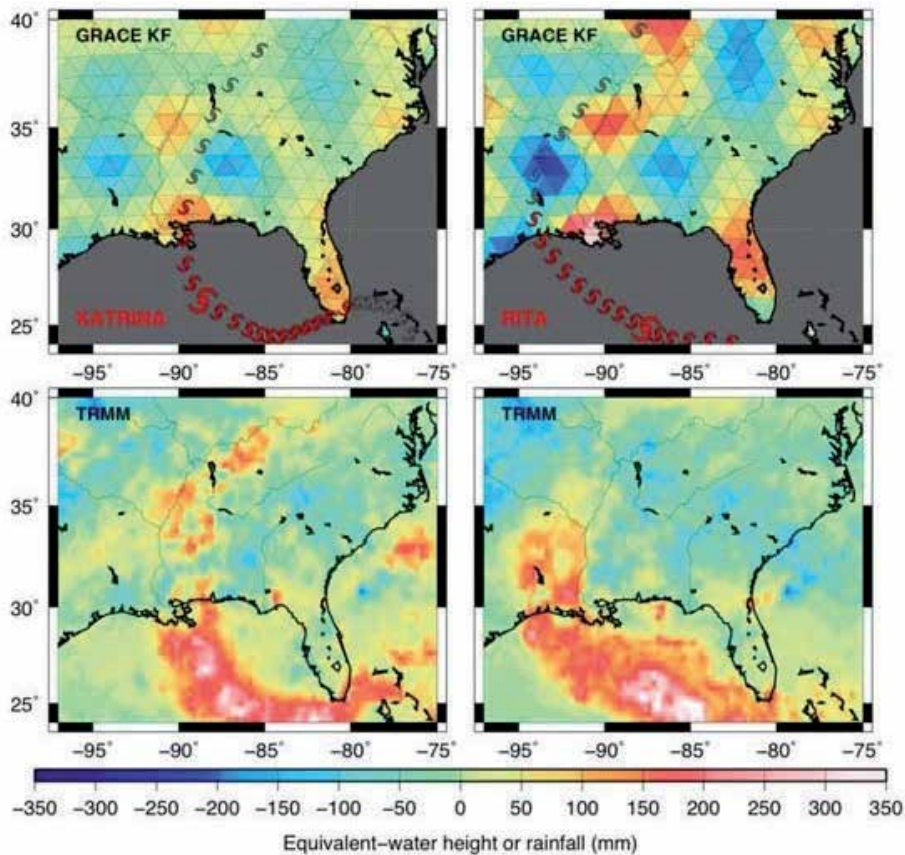


Figure 6. Differences of weekly-averaged of GRACE solutions derived by the Kalman filter approach as proposed by [73], before and during the Katrina and Rita episodes (top); and comparison with the anomalies of TRMM precipitation for the same periods (bottom).

have allowed to improve spatial and temporal resolution, then rapid extremes events of several days has been observed [73]. One example is the most powerful depressions in late summer 2005 during the cyclonic season in the Gulf of Mexico and Louisiana, better known under the name of “Katrina” (23–31/08/2005), and followed by “Rita” (17–26/09/2005). The direct consequences of the passage of these hurricanes caused important rainfalls along their tracks, thus the significant storage and accumulation of water falling on land could be observed as water mass variations in the range of a few days. As shown in **Figure 6** the important rainfalls of Katrina located in the south of the Great Plains have produced river floods, and thus an important water accumulation is revealed by GRACE in the coastal region of New Orleans (up to 300 mm of EWH).

5. Conclusion

During its sixteen years of operation, the GRACE mission provided a novel source of information on variations of water mass on lands at unprecedented spatial and temporal resolutions. This mission offered an exceptional dataset for studying large-scale water mass redistributions, and for the very first time, the opportunity to monitor water changes in all the hydrological compartments and from regional to global scales. While spherical harmonics solutions were firstly used, regional and local approaches have already demonstrated the possible access to spatial (better localization of structures by construction) and temporal (through daily updates using Kalman filter strategies, e.g. see [73]) scales that were higher than those that were offered by global SH solutions. Additional bibliographic resources and useful information about GRACE can be found on the GRACE Tellus web site [74]. The GRACE mission ended in 2017, and later on a partnership between NASA and the German Research Centre for Geosciences (GFZ) decided to schedule GRACE Follow-On (GRACE-FO) mission to launch in 2018 in order to ensure the continuity of GRACE-type space gravimetry. By using a similar twin satellite configuration of the low-Earth and nearly polar orbit at 300–500 km altitude, the GRACE-FO mission is following its successful predecessor [75]. Additionally, it carries a demonstrator of laser system to measure the inter-satellite distance and velocity, and hence for an improved precision. It is promising for providing new perspectives in hydrology studies, such as refined long-term mass balance estimates of surface water storage and ice sheets. These new data that offer continuity with the previous GRACE observations will be of first interest for hydrology of global hydrological model calibration to constrain their operations through assimilation techniques.

Acknowledgements

We would like to thank the anonymous reviewer for his helpful contribution for improving the quality of this chapter.

Author details

Guillaume Ramillien^{1*} and Lucía Seoane²

1 Centre National de la Recherche Scientifique (CNRS), Géosciences Environnement Toulouse (GET), Observatoire Midi-Pyrénées (OMP), Toulouse, France

2 Université Paul Sabatier Toulouse (UPS), Géosciences Environnement Toulouse (GET), Observatoire Midi-Pyrénées (OMP), Toulouse, France

*Address all correspondence to: guillaume.ramillien@get.omp.eu

IntechOpen

© 2021 The Author(s). Licensee IntechOpen. This chapter is distributed under the terms of the Creative Commons Attribution License (<http://creativecommons.org/licenses/by/3.0>), which permits unrestricted use, distribution, and reproduction in any medium, provided the original work is properly cited. 

References

- [1] Ramillien G, Biancale R, Gratton S, Vasseur X, Bourgoigne S. GRACE-derived surface water mass anomalies by energy integral approach: application to continental hydrology. *Journal of Geodesy* 2011;85:313-328. <https://doi.org/10.1007/s00190-010-0438-7>.
- [2] Dickey JO, Marcus SL, de Viron O, Fukumori I. Recent Earth oblateness variations: unraveling climate and postglacial rebound effects. *Science* 2002;298:1975-1977. <https://doi.org/10.1126/science.1077777>.
- [3] Wolff M. Direct measurements of the Earth's gravitational potential using a satellite pair. *Journal of Geophysical Research (1896-1977)* 1969;74:5295-300. <https://doi.org/10.1029/JB074i022p05295>.
- [4] Tapley BD, Bettadpur S, Watkins M, Reigber C. The gravity recovery and climate experiment: Mission overview and early results. *Geophysical Research Letters* 2004;31. <https://doi.org/10.1029/2004GL019920>.
- [5] Velicogna I, Mohajerani Y, A G, Landerer F, Mouginit J, Noel B, et al. Continuity of Ice Sheet Mass Loss in Greenland and Antarctica From the GRACE and GRACE Follow-On Missions. *Geophysical Research Letters* 2020;47:e2020GL087291. <https://doi.org/10.1029/2020GL087291>.
- [6] Schmidt R, Flechtner F, Meyer U, Neumayer K-H, Dahle Ch, König R, et al. Hydrological Signals Observed by the GRACE Satellites. *Surv Geophys* 2008;29:319-334. <https://doi.org/10.1007/s10712-008-9033-3>.
- [7] GRACE photojournal JPL NASA [Internet] 2020. Available from <https://photojournal.jpl.nasa.gov/catalog/PIA04235> (accessed December 18, 2020).
- [8] Integrated System Data Center 2018. Available from <https://isdc.gfz-potsdam.de/homepage/> (accessed December 18, 2020).
- [9] Physical Oceanography Distributive Active Data Center 2020. Available from <https://podaac.jpl.nasa.gov/> (accessed December 18, 2020).
- [10] Reigber C, Schmidt R, Flechtner F, König R, Meyer U, Neumayer K-H, et al. An Earth gravity field model complete to degree and order 150 from GRACE: EIGEN-GRACE02S. *Journal of Geodynamics* 2005;39:1-10. <https://doi.org/10.1016/j.jog.2004.07.001>.
- [11] Tapley B, Ries J, Bettadpur S, Chambers D, Cheng M, Condi F, et al. GGM02 – An improved Earth gravity field model from GRACE. *J Geodesy* 2005;79:467-478. <https://doi.org/10.1007/s00190-005-0480-z>.
- [12] Ramillien G, Frappart F, Seoane L. 6 - Space Gravimetry Using GRACE Satellite Mission: Basic Concepts. In: Baghdadi N, Zribi M, editors. *Microwave Remote Sensing of Land Surface*, Elsevier; 2016, p. 285-302. <https://doi.org/10.1016/B978-1-78548-159-8.50006-2>.
- [13] Hofmann-Wellenhof B, Moritz H. *Physical Geodesy*. 2nd ed. Wien: Springer-Verlag; 2006. <https://doi.org/10.1007/978-3-211-33545-1>.
- [14] Bettadpur S. UTCSR level-2 processing standards document for level-2 product release 0004, GRACE 327-742 (CSR-GR-03-03). Center for Space Research, The University of Texas at Austin, Austin. 2007.
- [15] Flechtner F. GFZ Level-2 Processing Standards Document for Product Release 0004. Rev.1.0, GRACE project documentation 327-743 2007.

- [16] Chambers DP, Bonin JA. Evaluation of Release-05 GRACE time-variable gravity coefficients over the ocean. *Ocean Sci* 2012;8:859-868. <https://doi.org/10.5194/os-8-859-2012>.
- [17] Dahle C, Flechtner F, Gruber C, König D, König R, Michalak G, et al. GFZ GRACE Level-2 Processing Standards Document for Level-2 Product Release 0005 : revised edition, January 2013 2013.
- [18] Vishwakarma DB, Devaraju B, Sneeuw N. What Is the Spatial Resolution of grace Satellite Products for Hydrology? *Remote Sensing* 2018;10. <https://doi.org/10.3390/rs10060852>.
- [19] Forootan E, Didova O, Schumacher M, Kusche J, Elsaka B. Comparisons of atmospheric mass variations derived from ECMWF reanalysis and operational fields, over 2003-2011. *Journal of Geodesy* 2014;88:503-514. <https://doi.org/10.1007/s00190-014-0696-x>.
- [20] Han S-C, Jekeli C, Shum CK. Time-variable aliasing effects of ocean tides, atmosphere, and continental water mass on monthly mean GRACE gravity field: TEMPORAL ALIASING ON GRACE GRAVITY FIELD. *J Geophys Res* 2004;109. <https://doi.org/10.1029/2003JB002501>.
- [21] Ray RD, Luthcke SB. Tide model errors and GRACE gravimetry: towards a more realistic assessment. *Geophysical Journal International* 2006;167:1055-1059. <https://doi.org/10.1111/j.1365-246X.2006.03229.x>.
- [22] Thompson PF, Bettadpur SV, Tapley BD. Impact of short period, non-tidal, temporal mass variability on GRACE gravity estimates: IMPACT OF SHORT PERIOD, NON-TIDAL, TEMPORAL MASS VARIABILITY ON GRACE GRAVITY ESTIMATES. *Geophys Res Lett* 2004;31:n/a-n/a. <https://doi.org/10.1029/2003GL019285>.
- [23] Swenson S, Wahr J. Post-processing removal of correlated errors in GRACE data. *Geophysical Research Letters* 2006;33. <https://doi.org/10.1029/2005GL025285>.
- [24] Swenson S, Wahr J. Monitoring the water balance of Lake Victoria, East Africa, from space. *Journal of Hydrology* 2009;370:163-176. <https://doi.org/10.1016/j.jhydrol.2009.03.008>.
- [25] Chambers DP, Wahr J, Nerem RS. Preliminary observations of global ocean mass variations with GRACE. *Geophysical Research Letters* 2004;31. <https://doi.org/10.1029/2004GL020461>.
- [26] Chen JL, Wilson CR, Tapley BD, Yang ZL, Niu GY. 2005 drought event in the Amazon River basin as measured by GRACE and estimated by climate models. *Journal of Geophysical Research: Solid Earth* 2009;114. <https://doi.org/10.1029/2008JB006056>.
- [27] Ramillien G, Frappart F, Cazenave A, Güntner A. Time variations of land water storage from an inversion of 2 years of GRACE geoids. *Earth and Planetary Science Letters* 2005;235:283-301. <https://doi.org/10.1016/j.epsl.2005.04.005>.
- [28] Ramillien G, Famiglietti JS, Wahr J. Detection of Continental Hydrology and Glaciology Signals from GRACE: A Review. *Surv Geophys* 2008;29:361-374. <https://doi.org/10.1007/s10712-008-9048-9>.
- [29] Swenson SC, Milly PCD. Climate model biases in seasonality of continental water storage revealed by satellite gravimetry. *Water Resources Research* 2006;42. <https://doi.org/10.1029/2005WR004628>.
- [30] Tamisiea ME, Leuliette EW, Davis JL, Mitrovica JX. Constraining hydrological and cryospheric mass flux in southeastern Alaska using

- space-based gravity measurements. *Geophysical Research Letters* 2005;32. <https://doi.org/10.1029/2005GL023961>.
- [31] Velicogna I, Wahr J. Greenland mass balance from GRACE. *Geophysical Research Letters* 2005;32. <https://doi.org/10.1029/2005GL023955>.
- [32] Wahr J, Swenson S, Zlotnicki V, Velicogna I. Time-variable gravity from GRACE: First results. *Geophysical Research Letters* 2004;31. <https://doi.org/10.1029/2004GL019779>.
- [33] Sakumura C, Bettadpur S, Bruinsma S. Ensemble prediction and intercomparison analysis of GRACE time-variable gravity field models. *Geophysical Research Letters* 2014;41:1389-1397. <https://doi.org/10.1002/2013GL058632>.
- [34] Wahr J, Molenaar M, Bryan F. Time variability of the Earth's gravity field: Hydrological and oceanic effects and their possible detection using GRACE. *Journal of Geophysical Research: Solid Earth* 1998;103:30205-30229. <https://doi.org/10.1029/98JB02844>.
- [35] Han D, Wahr J. The viscoelastic relaxation of a realistically stratified earth, and a further analysis of postglacial rebound. *Geophysical Journal International* 1995;120:287-311. <https://doi.org/10.1111/j.1365-246X.1995.tb01819.x>.
- [36] Freedman W, Schreiner M. *Spherical Functions of Mathematical Geosciences: A Scalar, Vectorial, and Tensorial Setup*. Berlin, Heidelberg: Springer Berlin Heidelberg; 2009. <https://doi.org/10.1007/978-3-540-85112-7>.
- [37] Luthcke SB, Zwally HJ, Abdalati W, Rowlands DD, Ray RD, Nerem RS, et al. Recent Greenland Ice Mass Loss by Drainage System from Satellite Gravity Observations. *Science* 2006;314:1286-1289. <https://doi.org/10.1126/science.1130776>.
- [38] Luthcke SB, Sabaka TJ, Loomis BD, Arendt AA, McCarthy JJ, Camp J. Antarctica, Greenland and Gulf of Alaska land-ice evolution from an iterated GRACE global mascon solution. *Journal of Glaciology* 2013;59:613-631. <https://doi.org/10.3189/2013JoG12J147>.
- [39] Rowlands DD, Luthcke SB, Klosko SM, Lemoine FGR, Chinn DS, McCarthy JJ, et al. Resolving mass flux at high spatial and temporal resolution using GRACE intersatellite measurements. *Geophysical Research Letters* 2005;32. <https://doi.org/10.1029/2004GL021908>.
- [40] Rowlands DD, Luthcke SB, McCarthy JJ, Klosko SM, Chinn DS, Lemoine FG, et al. Global mass flux solutions from GRACE: A comparison of parameter estimation strategies—Mass concentrations versus Stokes coefficients. *Journal of Geophysical Research: Solid Earth* 2010;115.
- [41] Watkins MM, Wiese DN, Yuan D-N, Boening C, Landerer FW. Improved methods for observing Earth's time variable mass distribution with GRACE using spherical cap mascons. *Journal of Geophysical Research: Solid Earth* 2015;120:2648-2671. <https://doi.org/10.1002/2014JB011547>.
- [42] Wiese DN, Landerer FW, Watkins MM. Quantifying and reducing leakage errors in the JPL RL05M GRACE mascon solution. *Water Resources Research* 2016;52:7490-7502. <https://doi.org/10.1002/2016WR019344>.
- [43] Wiese DN, Yuan D-N, Boening C, Landerer FW, Watkins MM. JPL GRACE Mascon Ocean, Ice, and Hydrology Equivalent Water Height Release 06 Coastal Resolution Improvement (CRI) Filtered Version 1.0 2018. <https://doi.org/10.5067/temsc-3mjc6>.
- [44] Save H, Bettadpur S, Tapley BD. High-resolution CSR GRACE RL05 mascons. *Journal of*

Geophysical Research: Solid Earth 2016;121:7547-7569. <https://doi.org/10.1002/2016JB013007>.

[45] Jacob T, Wahr J, Pfeffer WT, Swenson S. Recent contributions of glaciers and ice caps to sea level rise. *Nature* 2012;482:514-518. <https://doi.org/10.1038/nature10847>.

[46] Schrama EJO, Wouters B, Rietbroek R. A mascon approach to assess ice sheet and glacier mass balances and their uncertainties from GRACE data. *Journal of Geophysical Research: Solid Earth* 2014;119:6048-6066. <https://doi.org/10.1002/2013JB010923>.

[47] Velicogna I, Sutterley TC, van den Broeke MR. Regional acceleration in ice mass loss from Greenland and Antarctica using GRACE time-variable gravity data. *Geophysical Research Letters* 2014;41:8130-8137. <https://doi.org/10.1002/2014GL061052>.

[48] CSR GRACE/GRACE-FO RL06 Mascon Solutions [Internet] 2020. Available from http://www2.csr.utexas.edu/grace/RL06_mascons.html (accessed December 3, 2020).

[49] Monthly Mass Grids - Global mascons (JPL RL06_v02) [Internet] 2020. Available from https://grace.jpl.nasa.gov/data/get-data/jpl_global_mascons/ (accessed December 3, 2020).

[50] Ramillien GL, Frappart F, Gratton S, Vasseur X. Sequential estimation of surface water mass changes from daily satellite gravimetry data. *Journal of Geodesy* 2015;89:259-282. <https://doi.org/10.1007/s00190-014-0772-2>.

[51] Ramillien GL, Seoane L, Frappart F, Biancale R, Gratton S, Vasseur X, et al. Constrained Regional Recovery of Continental Water Mass Time-variations from GRACE-based Geopotential Anomalies over South

America. *Surveys in Geophysics* 2012;33:887-905. <https://doi.org/10.1007/s10712-012-9177-z>.

[52] Seoane L, Ramillien G, Frappart F, Leblanc M. Regional GRACE-based estimates of water mass variations over Australia: validation and interpretation. *Hydrology and Earth System Sciences* 2013;17:4925-4939. <https://doi.org/10.5194/hess-17-4925-2013>.

[53] Frappart F, Seoane L, Ramillien G. Validation of GRACE-derived terrestrial water storage from a regional approach over South America. *Remote Sensing of Environment* 2013;137:69-83. <https://doi.org/10.1016/j.rse.2013.06.008>.

[54] Rodell M, Famiglietti JS. Detectability of variations in continental water storage from satellite observations of the time dependent gravity field. *Water Resources Research* 1999;35:2705-2723. <https://doi.org/10.1029/1999WR900141>.

[55] Swenson S, Wahr J, Milly PCD. Estimated accuracies of regional water storage variations inferred from the Gravity Recovery and Climate Experiment (GRACE). *Water Resources Research* 2003;39. <https://doi.org/10.1029/2002WR001808>.

[56] Landerer FW, Swenson SC. Accuracy of scaled GRACE terrestrial water storage estimates. *Water Resources Research* 2012;48:n/a-n/a. <https://doi.org/10.1029/2011WR011453>.

[57] Han S-C, Shum CK, Bevis M, Ji C, Kuo C-Y. Crustal dilatation observed by GRACE after the 2004 Sumatra-Andaman earthquake. *Science* 2006;313:658-662. <https://doi.org/10.1126/science.1128661>.

[58] Han S-C, Sauber J, Luthcke S. Regional gravity decrease after the 2010 Maule (Chile) earthquake indicates large-scale mass redistribution.

Geophysical Research Letters 2010;37.
<https://doi.org/10.1029/2010GL045449>.

[59] Li J, Shen W-B. Monthly GRACE detection of coseismic gravity change associated with 2011 Tohoku-Oki earthquake using northern gradient approach. *Earth, Planets and Space* 2015;67:29. <https://doi.org/10.1186/s40623-015-0188-0>.

[60] Fatolazadeh F, Goita K, Javadi Azar R. Determination of earthquake epicentres based upon invariant quantities of GRACE strain gravity tensors. *Scientific Reports* 2020;10:7636. <https://doi.org/10.1038/s41598-020-64560-w>.

[61] Hsu C-W, Velicogna I. Detection of sea level fingerprints derived from GRACE gravity data. *Geophysical Research Letters* 2017;44:8953-8961. <https://doi.org/10.1002/2017GL074070>.

[62] Jeon T, Seo K-W, Youm K, Chen J, Wilson CR. Global sea level change signatures observed by GRACE satellite gravimetry. *Scientific Reports* 2018;8:13519. <https://doi.org/10.1038/s41598-018-31972-8>.

[63] Frappart F, Ramillien G, Leblanc M, Tweed SO, Bonnet M-P, Maisongrande P. An independent component analysis filtering approach for estimating continental hydrology in the GRACE gravity data. *Remote Sensing of Environment* 2011;115:187-204. <https://doi.org/10.1016/j.rse.2010.08.017>.

[64] Rodell M, Famiglietti JS, Wiese DN, Reager JT, Beaulieu HK, Landerer FW, et al. Emerging trends in global freshwater availability. *Nature* 2018;557:651-659. <https://doi.org/10.1038/s41586-018-0123-1>.

[65] Thomas BF, Famiglietti JS, Landerer FW, Wiese DN, Molotch NP, Argus DF. GRACE Groundwater Drought Index: Evaluation of California

Central Valley groundwater drought. *Remote Sensing of Environment* 2017;198:384-392. <https://doi.org/10.1016/j.rse.2017.06.026>.

[66] Frappart F, Papa F, Güntner A, Tomasella J, Pfeffer J, Ramillien G, et al. The spatio-temporal variability of groundwater storage in the Amazon River Basin. *Advances in Water Resources* 2019;124:41-52. <https://doi.org/10.1016/j.advwatres.2018.12.005>.

[67] Crowley JW, Mitrovica JX, Bailey RC, Tamisiea ME, Davis JL. Annual variations in water storage and precipitation in the Amazon Basin. *J Geod* 2008;82:9-13. <https://doi.org/10.1007/s00190-007-0153-1>.

[68] Frappart F, Ramillien G, Seoane L. 8 - Monitoring Water Mass Redistributions on Land and Polar Ice Sheets Using the GRACE Gravimetry from Space Mission. In: Baghdadi N, Zribi M, editors. *Land Surface Remote Sensing in Continental Hydrology*, Elsevier; 2016, p. 255-279. <https://doi.org/10.1016/B978-1-78548-104-8.50008-5>.

[69] Llubes M, Lemoine J-M, Rémy F. Antarctica seasonal mass variations detected by GRACE. *Earth and Planetary Science Letters* 2007;260:127-136. <https://doi.org/10.1016/j.epsl.2007.05.022>.

[70] Ramillien G, Frappart F, Seoane L. Application of the Regional Water Mass Variations from GRACE Satellite Gravimetry to Large-Scale Water Management in Africa. *Remote Sensing* 2014;6:7379-7405. <https://doi.org/10.3390/rs6087379>.

[71] Frappart F, Papa F, Silva JS da, Ramillien G, Prigent C, Seyler F, et al. Surface freshwater storage and dynamics in the Amazon basin during the 2005 exceptional drought. *Environ Res Lett* 2012;7:044010. <https://doi.org/10.1088/1748-9326/7/4/044010>.

[72] Thomas AC, Reager JT, Famiglietti JS, Rodell M. A GRACE-based water storage deficit approach for hydrological drought characterization. *Geophysical Research Letters* 2014;41:1537-1545. <https://doi.org/10.1002/2014GL059323>.

[73] Ramillien G, Seoane L, Schumacher M, Forootan E, Frappart F, Darrozes J. Recovery of Rapid Water Mass Changes (RWMC) by Kalman Filtering of GRACE Observations. *Remote Sensing* 2020;12:1299. <https://doi.org/10.3390/rs12081299>.

[74] GRACE Tellus [Internet] 2020. Available from <http://grace.jpl.nasa.gov> (accessed December 18, 2020).

[75] GRACE FO [Internet] 2020. Available from <https://gracefo.jpl.nasa.gov/> (accessed January 18, 2021).

Radar Satellite Altimetry in Geodesy - Theory, Applications and Recent Developments

Marijan Grgić and Tomislav Bašić

Abstract

Radar satellite altimetry has revolutionized our understanding of the Earth's sea-level shape and its change over time, monitoring of the natural and human-induced water cycle, marine gravity computations, seafloor relief (bathymetry) reconstruction, tectonics, water mass balance change monitoring, etc., thus providing significant impact in geodesy. Today satellite radar altimetry is critical for unifying the vertical height systems, regional and global geoid modeling, monitoring of the sea level rise impact, monitoring of the ice sheet melting, and others. This chapter gives an overview of the technology itself and the recent developments including the SAR (Synthetic Aperture Radar) altimetry, coastal altimetry retracking methods, and new satellite missions (e.g. Sentinel-6). Besides, the chapter presents recent applied studies utilizing the altimeter data for ice sheet monitoring, vertical land motion estimating, bathymetric computations, and marine geoid modeling.

Keywords: altimetry-derived bathymetry, coastal altimetry, geodesy, gravity modeling, radar satellite altimetry, sea level, sea topography

1. Introduction

Radar satellite altimetry provides global, frequent, and precise measurements of uniform accuracy of the sea level height related to a desired geodetic reference frame at different time epochs and from various altimeter sensors. Designed in 1969 at the Williamstown Conference on Solid Earth and Ocean Physics [1, 2], the technology was developed through the experimental missions Skylab (see [3]), Geodynamics Experimental Ocean Satellite 3 (GEOS-3, see [4]), and SEAFaring SATellite (SEASAT, see [5]). Since the early 1990s, different altimeter satellite missions provide reliable and solid information on the sea level thus enabling various applications in geodesy, oceanography, glaciology, climate research, atmosphere, wind, waves, biology, and navigation [6, 7]. To this day, more than 80,000 publications discuss or include altimeter data, technology, or products [8].

In geodesy, satellite altimetry is used to study Earth's shape and size, sea-level variability, Earth's gravity field over oceans and its change, tectonic plate motion, bathymetry, natural hazards, and inland water-related occurrences. The data acquired by the satellite altimeters are distributed at different levels of complexity and applicability; from source, non-processed measurements, which must be

corrected using various atmospheric and geophysical models and corrections, up to complete products ready to use in different applications. The measurements are distributed with different timeliness, most often in near real-time (e.g., in less than 3 hours after the acquisition).

This book chapter presents the theoretical background of the technology, basic principles and data processing procedures, current trends in technology, and different applications of the technology. The chapter gives an overview of the relevant literature and points towards more specific studies.

2. Radar altimetry technology and principles

This section gives the theoretical background on the altimeter principles and concepts, the development of the technology and the satellite missions, and current advances on altimeter data processing and product deriving.

2.1 Concepts of satellite altimetry

Conceptually, satellite altimeters measure the distance from the satellite to the sea-level surface, i.e., the range R , thus enabling deriving of the sea level surface referred to any desired geodetic reference frame such as the ellipsoid or the geoid. The altimeter transmits a short pulse of microwave radiation with known power towards the sea surface, where it interacts with the sea surface. The range is measured from a time taken for incident radiation of a signal to reflect back to the altimeter, which enables determining of the sea surface height. Eq. (1) presents the basic principle of satellite altimetry, i.e., the measuring of the range \hat{R} from the round-trip travel time, without refraction accounted for, based on the speed of light in vacuum c :

$$\hat{R} = \frac{ct}{2}. \quad (1)$$

After applying the corrections to the measurements, the basic equation can be modified to present corrected range R as [6, 9]:

$$R = \hat{R} - \sum_j \Delta R_j = \hat{R} - (\Delta R_{tropoD} + \Delta R_{tropoW} + \Delta R_{iono} + \Delta R_{od} + \dots) \quad (2)$$

where $\Delta R_j, j = 1, \dots$ is the sum of the atmospheric and technology corrections applied to the signal pulse, which encompasses dry and wet component of the tropospheric correction, R_{tropoD} and R_{tropoW} , ionospheric correction R_{iono} , the influences of the ocean dynamics R_{od} , and the other corrections [6]. Due to such influences, the propagation of the signal through the atmosphere is slowed down, meaning that the corrections of the R are positive values. The accuracy of the range is, naturally, directly correlated to the accuracy of the corrections applied to derive the sea surface height.

The basic principles of the technology integrated with the other related remote sensing systems are shown in **Figure 1**. The accuracy of determining the satellite altimeter position is critical for the measurements of the range. The accurate position of the satellite is ensured through the precise orbit computations in

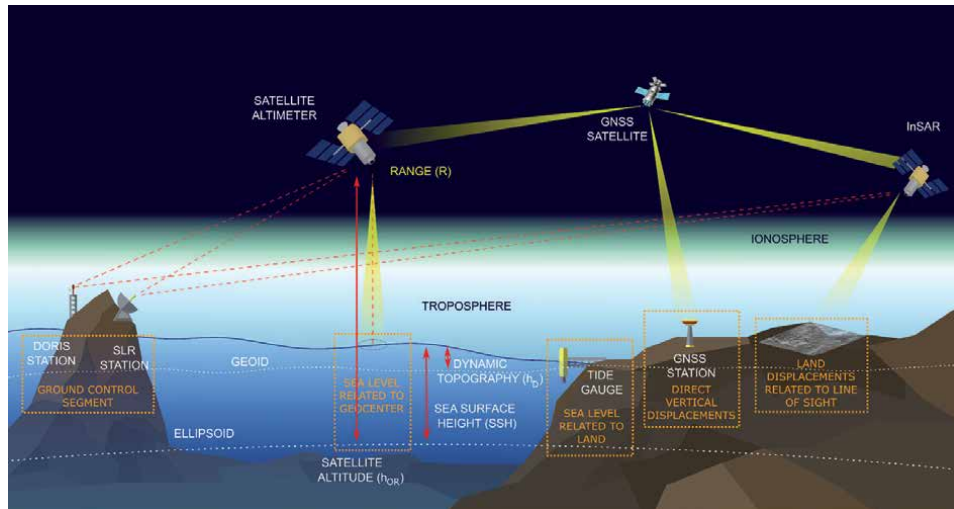


Figure 1. Satellite altimetry and related observation systems (tide gauge sea level measurements, interferometric synthetic aperture radar (InSAR), GNSS (global navigation satellite system), Doppler Orbitography and Radiopositioning integrated by satellite (DORIS) and satellite laser ranging (SLR)) shown in integrated observation systems of the earth (adapted from [10]).

combination with satellite and ground-based tracking systems. Satellite altimeters are usually equipped with GNSS and DORIS receivers to ensure onboard satellite tracking. Some of the altimeters are additionally equipped with star trackers, which give altitude and position information when GNSS is not available [11]. The ground tracking system is most often based on satellite laser ranging (SLR) tracking methods that provide satellite position from a global network of observation stations.

Besides the on-board navigation devices and retroreflectors for laser tracking, satellites carry microwave radiometers, which usually operate on two or more frequencies. A radiometer is an instrument that measures radiant energy reflected from the oceans and serves to estimate the surface water vapor (see e.g., [12]). The measurements depend on surface winds, ocean and near-ocean air temperature, salinity, foam, and the absorption by water vapor and clouds [7].

As shown in **Figure 1**, satellite altimeters are measuring ranges relative to the center of the Earth, i.e., to the reference ellipsoid. Satellites are flying in known pre-defined orbits h_{OR} that are computed with respect to the fixed coordinate system hence enabling straightforward deriving of the Sea Surface Height (SSH), which is related to a reference ellipsoid, from a measured range (Eq. (3)).

$$SSH = h_{OR} - R = h_{OR} - \hat{R} + \sum_j \Delta R_j. \quad (3)$$

The analyses of the shapes of signals returned from the sea surface are used for derivation of the Significant Wave Height (SWH) information. SWH is defined as four times the standard deviation of sea surface elevation and it corresponds to the average crest-to-trough height of 1/3 of the highest waves [6]. Therefore, it is often denoted as $h_{1/3}$. Also, the sea roughness, which is correlated with surface wind speed can be estimated from the power of the returned signal.

For more details, please see [6, 7].

2.2 Previous and current satellite altimeter missions

Overall, the development of the satellite altimetry can be divided into three phases – (1) experimental, (2) modern, and (3) future phase (following [6, 9]). **Figure 2** present the timeline overview of the altimeter satellite missions launched during all three phases along with the origin of the satellite missions and their period of orbit repeating. The modern (current) era can be defined from the launch of the ERS-1 and TOPEX/Poseidon missions in 1991 and 1992 onwards. European ERS-1 was launched on July 17, 1991, into a sun-synchronous polar orbit (Francis, 1984) with three setups of repetitivity: 3-day, 35-day (the most used), and 336-day repeat cycle. The mission lasted till March 2000, exceeding its expected lifespan by far. To support ERS-1, ESA (European Space Agency) developed a satellite-based tracking system within Precision Range and Range-Rate Equipment (PRARE) mission and widespread ground segment that enabled:

- calibration of the radar altimeter to 10 cm using the ground-based laser retroreflector,
- real-time data acquisition,
- data processing and generation of fast-delivery products [13].

Data were disseminated as low-rate fast-delivery products and high-rate products via the Broadband Data Dissemination Network. At the same time, the efforts by NASA (National Aeronautics and Space Administration) and CNES (French National Centre for Space Studies) resulted in TOPEX/Poseidon mission, being the product of 20 years of technological and engineering development [14]. That satellite mission has revolutionized satellite altimetry by introducing the second altimeter frequency (C-band, 5.3 GHz) and the third frequency on the microwave radiometer (18 GHz), which enabled computations of ionospheric delay corrections, and removing of the effects of wind speed on measurements, respectively [14]. The mission provided high measurement precision of measured data with an

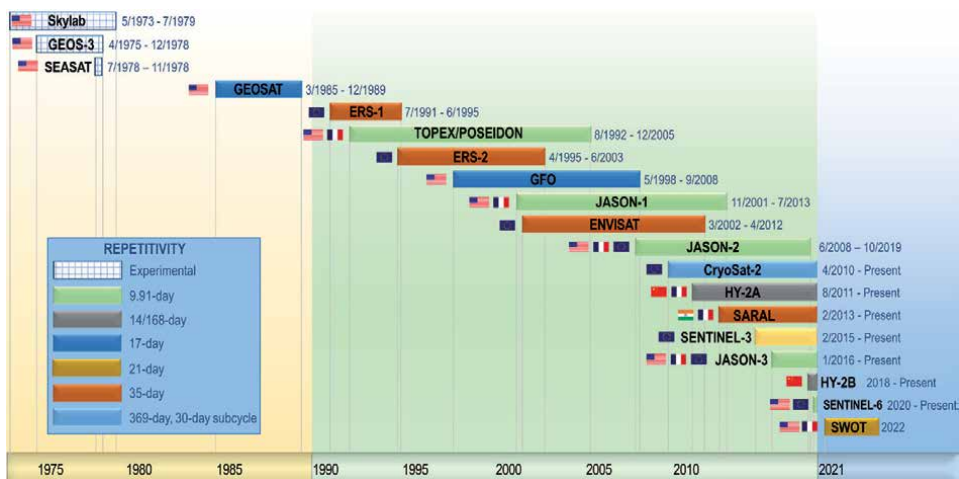


Figure 2. Altimeter satellite missions' timeline overview divided into an experimental era (yellow), modern era (green), and future altimetry era (blue) along with the missions' orbit reportativity and information about their countries of origin (following and updating from [9]).

RMSE (Root Mean Square Error) of 2 cm and orbit accuracy estimated at around 2.5 cm (see [6, 9]). Later improvements of the TOPEX/Poseidon data processing based on its dual-frequency altimeter estimates of sea-surface height resulted in an overall precision expressed with root-sum-of-squares (RMS) of about 4 cm [6], which today is an expected accuracy of altimeter data from different satellite missions and can get up to RMS of 2 cm for open ocean altimetry [9]. The advances in orbit determination were due to the development of the DORIS satellite tracking system. DORIS was developed by CNES to determine the satellite orbits with centimeter accuracy from a network of 60 ground stations settled worldwide [15].

At present, several satellites are providing measured altimeter data:

- Cryogenic Satellite (CryoSat)-2 designed and built by ESA and launched in 2010,
- Haiyang (HY)-2a approved and led by China National Space Administration (CNSA) launched in 2011,
- SARAL launched in 2013 as a cooperative mission between the Indian Space Research Organization (ISRO) and CNES,
- Sentinel-3 launched in 2015 by ESA and operated by EUMETSAT,
- Jason-3 designed in collaboration of the NASA and ESA as the successor of TOPEX/Poseidon and Jason 1/2,
- Haiyang (HY)-2b launched as the second in the series of Chinese Haiyang satellites in 2018,
- and Sentinel-6 Michael Freilich (previously referred to as Jason CS) launched in late 2020, which continues the EU Copernicus and NASA program and previous TOPEX/Poseidon and Jason 1/2/3 satellite missions.

Sentinel-6 satellite mission is currently in its commissioning phase, i.e., in the calibration/validation phase. **Figure 3** presents Sentinel-6 sea-level anomaly derived from ‘Short Time Critical Level 2 Low Resolution’ data, overlaid on a map showing similar products from the other Copernicus altimetry missions: Jason-3, Sentinel-3A, and Sentinel-3B (for details and original research, please see [17]). The background image is a map of sea-level anomalies from satellite altimeter data provided by the Copernicus Marine Environment Monitoring Service for 4 December 2020. The data for this image were taken from the Sentinel-6 products generated on 5 December 2020. Being in its commissioning phase, the measurements obtained by the Sentinel-6 are promising [17].

The characteristics of previous and current satellite missions are given in **Table 1**.

Surface Water Ocean Topography (SWOT) mission is planned to be launched primarily to enable terrestrial water monitoring. The mission is a joint project of NASA, CNES, the Canadian Space Agency, and the UK Space Agency. It is expected to operate in Ka-band with a 0.86 cm radar wavelength [18].

2.3 Advanced altimeter processing methods – retracking

Pulse-limited altimetry, often referred to as low resolution mode (LRM) altimetry, or traditional altimetry, is limited by the size of the radar surface footprint,

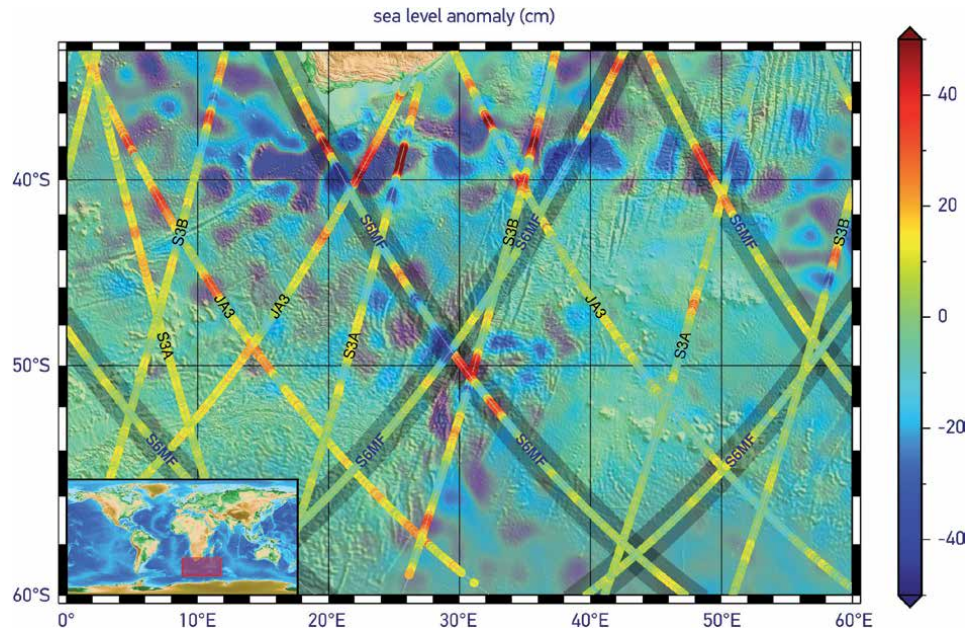


Figure 3. Early Sentinel-6 measurements validation comparing to Jason-3, sentinel-3A, and sentinel-3B [16].

Mission	Orbit height (km)	Inclination	Latitude coverage	Equator track distance (km)	Band	Frequency (GHz)
GEOSAT	785	108°	72°	163	Ku	13.5
ERS-1/2	785	98°	81°	80	Ku	13.8
TOPEX/POSEIDON Jason-1/2/3 Sentinel-6	1336	66°	66°	315	Ku/C	13.6/5.3
GFO	785	108°	72°	163	Ku	13.5
Envisat	785	98°	81°	163	Ku/S	13.6/3.2
CryoSat-2	717	92°	88°	7	Ku	13.6
HY-2A/2B	964	99°	60°	90	Ku/C	13.6/5.3
SARAL/ALTIKA	800	98°	81°	90	Ka	35

Table 1. An overview of the basic characteristics of satellite altimetry missions.

i.e., the size of the area illuminated by the radar from the satellite [6]. Depending on the SWH, the radius of the altimeter footprint can range from 1 km up to 7 km (e.g. for Jason missions), which enables high accuracy of the altimetry in open ocean areas, and on the other side, due to the contamination in the reflected radar altimeter signal caused by the land [19], lower accuracy in the coastal and inland areas (see e.g., [14]).

Significant efforts were done to overcome coastal altimetry issues through different projects, e.g., for the Mediterranean Sea projects were conducted such as ALBICOCCA (Altimeter-Based Investigations in Corsica, Capraia and Contiguous Areas), ALTICORE (Altimetry for Coastal Regions), COASTALT (Development of

Radar Altimetry Data Processing in the Coastal Zone), SAMOSA (SAR Altimetry Mode Studies and Applications), and the PISTACH (Coastal and Hydrology Altimetry product) [20]. The projects resulted in improvements of the onboard trackers and developments of the waveform retracker. On-board trackers are devices used for the prediction of surface measurements thus enabling outlier detection and easier surface tracking [21]. The waveform retracker work on the ground after the waveform data are downloaded from a satellite. The retracker most often attempt to fit the model or function to the measured waveform to provide as accurate as possible results [21]. The retracker integrate physical functions (such as the Brown ocean retractor) or empirical functions. Altimeter retracker are further discussed in [22–27].

Different retracker process different satellite mission data for different areas. For instance, ALES (Adaptive Leading Edge Subwaveform) is designed to be applied to Jason 1/2 and Envisat in both open ocean and coastal zones [27], X-TRACK retractor was designed particularly for coastal areas, ALES+ was later designed for the sea ice leads, coastal and inland waters [28], Goddard Space Flight Center (GSFC) designed several retracker for ice areas [29], etc. Such retracker nowadays enable utilizing of satellite altimetry in the coastal zones, and inland water areas. All the retracked data is available through the Coastal altimetry community [30].

2.4 Advanced altimeter processing methods – Delay-Doppler altimetry

One of the most significant recent developments in satellite altimetry technology was the introduction of the Delay-Doppler (DD) or SAR-mode altimetry that enables better observations of the small-scale features (below 50 km) and improved spatial resolution along the satellite track compared to conventional pulse-limited altimeters (see [31]). DD satellite altimeters employ the Doppler effect caused by the movement of the satellite in the along-track direction to improve the spatial resolution in the same direction [31] enabling the data sampling along-track e.g., up to 300 m for Sentinel-3. In other words, the altimeter footprint of the DD altimeters is reduced by an order of magnitude with respect to conventional altimeters – from a few kilometers up to a few hundreds of meters [32]. Hence, DD altimeters, such as those on the CryoSat-2 (SIRAL, SAR Interferometric Radar Altimeter), Sentinel-3 (SRAL, Synthetic Aperture Radar Altimeter), deliver more and/or improved data over the ocean, and, especially, in sea ice areas and coastal areas in general.

The SAR altimetry is based on the coherent processing of multiple echoes (e.g., 64 Ku-band pulses emitted by CryoSat-2 and Sentinel-3) within each altimeter burst (aperture duration of approx. 3.5 ms for CryoSat-2 and Sentinel-3), which enables resolving the reflected signals for along-track cells rather than the large footprints generated by the pulse limited altimeters. That naturally results in an improved resolution in the along-track (azimuth) direction of the satellite with the pulse-limited form that depends on the altimeter footprint maintained in the across-track direction (see [31, 32]).

Figure 4 presents the SAR technology and processing compared to the conventional satellite altimeters. The SAR processing includes counting for the along-track phase shift within each echo obtained from different radar burst, which depends on the geometry of the observation [31]. That produces the multiple echoes gathered at the same ground cell, which allows for the subsequent averaging (i.e., summing coherently) that increases the signal-to-noise ratio, i.e., it results in improved observations of the sea surface.

In [33] different studies on satellite radar altimetry pointed out that the SAR altimetry already performs better over the coastal zones than the conventional altimetry (see also [34]). They also emphasized the potential of the SAR technology

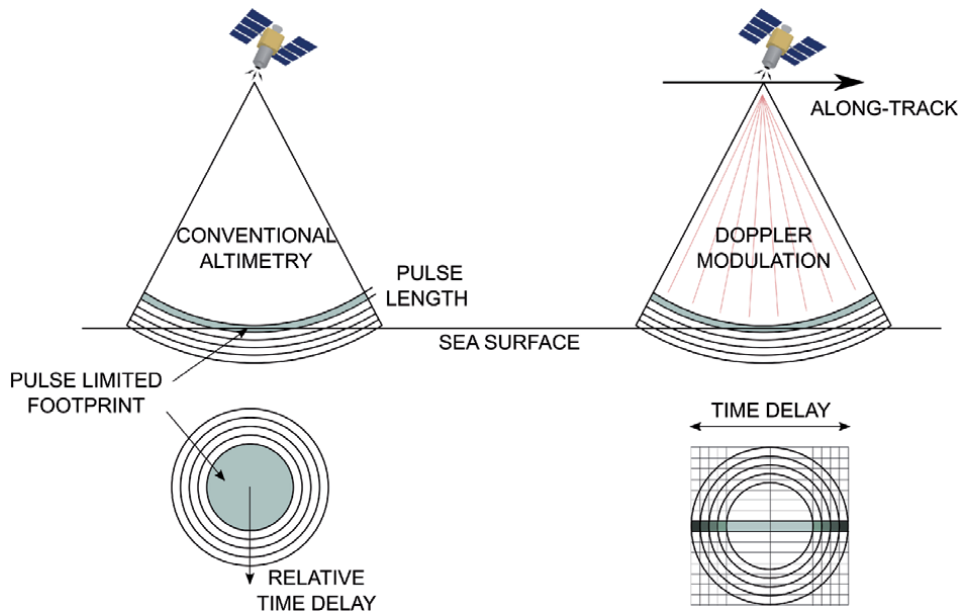


Figure 4. Comparison of the principles of the conventional and SAR altimetry (adapted from the [7]).

for applications to inland water monitoring as well as the applications in cryosphere studies, such as measuring the ice sheet elevation change and sea ice freeboard.

2.5 Altimeter data download and processing

Altimeter data are available at different levels of complexity through different platforms and for various purposes. AVISO (Archiving, Validation, and Interpretation of Satellite Oceanographic Data) for instance offers gridded and along-track multi-mission altimeter data products (not) corrected for the geophysical effects and for different purposes [35]. Besides, AVISO offers access to Basic Radar Altimetry Toolbox (BRAT) software as well as the tools such as Marine Geospatial Ecology Tools (MGET). On top of that, through the Live Access Server (LAS), AVISO offers on-the-fly data visualization, metadata access, and quick comparisons of the measurements. For geodetic purposes, AVISO's most valuable products are related to the SSH, often upgraded to show ocean variability or cryosphere changes.

Near-real-time along-track satellite altimeter data are available also through the Jet Propulsion Laboratory (JPL) PO.DAAC Drive system (Physical Oceanography Distributed Active Archive Center). The data are delivered as a map or digital data, focusing on the SSH, wind speed, wave heights, and geostrophic velocity vectors [36].

Different products are also available from Copernicus Marine Service [16], which offers complete studies on sea-related topics. That includes original measurements, sea-level-related maps, and sea-level forecasts.

Finally, all the georeferenced source altimeter measurements and many corrections for the measurements are available through the RADS (Radar Altimeter Database System) [37]. RADS provides harmonized, validated, and cross-calibrated sea level altimeter data for the desired area and period of the observations, and it is probably the best place to start with the altimetry for the geodetic studies. Also, RADS offers data preprocessing and processing steps integrated within the system and available through the additional tools.

3. Altimeter products and study cases

A wide variety of satellite altimetry products cover many research fields. In the following section, we focus on presenting the application of altimetry in geodesy.

3.1 Sea-level change

Sea level change is studied as the global and local phenomena (**Figure 5**). Today, the global sea-level change is routinely computed from the altimetry for the period from 1992 onwards by AVISO, Commonwealth Scientific and Industrial Research Organization (CSIRO), University of Colorado Boulder (CU), NASA - Goddard Space Flight Center (GSFC), The National Oceanic and Atmospheric Administration (NOAA), and others. All the global research studies agree on the current sea level linear trend of approx. 3.2 mm/yr. although the processing methods could differ slightly. The estimates on the global sea-level change trends from satellite altimetry are regularly reported within the IPCC (The Intergovernmental Panel on Climate Change) reports that provide policymakers with regular scientific assessments on climate change. Several studies reported on the regional and local sea-level change, e.g., [39] consolidated the trends and expected sea-level change globally and for the ocean regions, [40] reported on the projections of the regional sea level for the 21st century, [41, 42] recomputed all satellite altimeter data to get more pronounced sea-level change estimates and a better perspective on the impact of future sea-level rise.

The satellite altimetry enabled finer detection of the current acceleration of global and regional sea-level rise. E.g., [38] reported on the climate-change-driven acceleration in sea level rise over the altimeter era, [43] investigated the regional sea-level rise during the altimeter era with previous studies done on uncovering the anthropogenic influence on the sea level rise in some regions [44]. With the climate change acceleration, monitoring of the sea-level change and its variation is going to be even more important. A future perspective on gauging the sea-level change and the needed improvements, both for the satellite observations and the terrestrial (tide gauge and other) measurements, is summarized in [45].

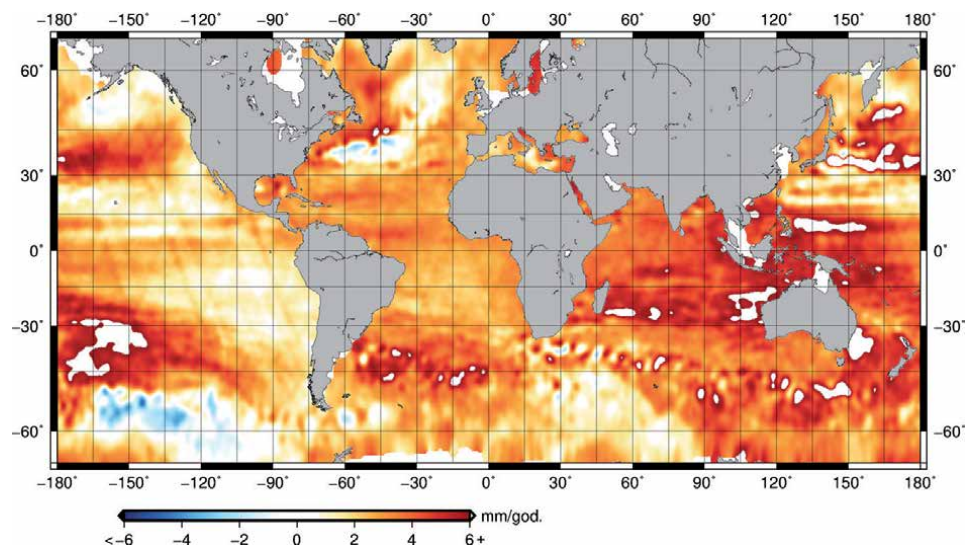


Figure 5.
Global Sea level trends (data downloaded from [38]).

The mean sea surface and its change are one of the bases for vertical height system modeling and implementation. A wide initiative on unifying the vertical height reference systems (for details see [46–48]) most usually encompasses absolute sea-level modeling from satellite altimetry extended for the tide gauge measurements at the coast (see e.g., [49]) along with the extensive analysis of vertical land movements, GNSS measurements, gravity estimations, etc. For such purposes, further progress in coastal altimetry and altimetry, in general, is crucial.

3.2 Gravity models

One of the basic geodetic tasks is determining the Earth’s shape and size. The satellite altimetry gave an insight into the topography of the oceans, which later enabled the reconstruction of the Earth’s gravity field over the oceans through gravity recovery. Gravity recovery stands for the geodetic operations and procedures of fitting the (altimeter) data to a gravity field that allows for the determination of the gravity information at any location [6]. Three standard procedures can be used to compute the gravity field from the altimetry: (1) employing the least-squares collocation on the altimeter measurements with the computed slopes of the sea surfaces along the satellite tracks or (2) along with the computed deflections of the vertical (e.g. [50, 51]), and (3) using the Vening Meinesz formula for the computations of the gravity field from the deflections of the vertical derived from satellite altimetry [52] (Figure 6).

Today, the global gravity field models are usually derived from gravity satellite mission(s) only or from combined observations (both ground and satellite data). When using combined data, satellite altimetry is most often included in

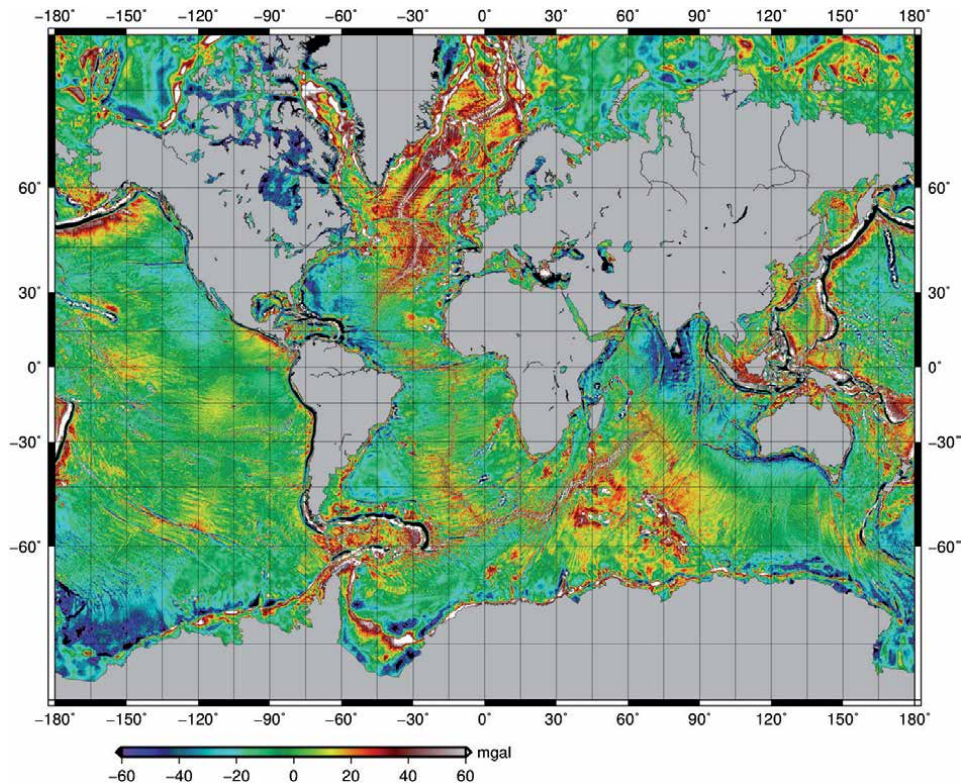


Figure 6. Altimetry-derived global ocean gravity map (data downloaded from [53]).

modeling. Such combined models are, e.g., XGM2019e_2159 [54], GAO2012 [55], EIGEN-6C4 [56], and EGM2008 [57]. Models derived from altimetry only are given in, e.g., [53, 58].

3.3 Bathymetry

Due to the expenses of the traditional bathymetric measuring methods (e.g., weighted lines/poles), the information about the water depths and topography of the seafloor remained mainly unexplored over the open ocean until the utilization of satellite altimetry. Today, with the global and uniform coverage, satellite altimetry is crucial in computations of the global bathymetric models fulfilling the in-situ data gaps.

Predicting the bathymetry from the altimetry relies on the method developed in 1983 by [59], who have shown the potential of such modeling using the Seasat altimetry data. Over the years, the methods were further developed (e.g., [58]). Today most of the bathymetric models integrate the same altimetry-derived bathymetry. **Table 2** presents some of the most common global bathymetric models starting from the most recently updated: (1) GEBCO_2019 (The General Bathymetric Chart of the Oceans) [60], (2) SRTM15+ (Shuttle Radar Topography Mission: Global Bathymetry and Topography at 15 arcseconds) [61], (3) EMODnet (European Marine Observation and Data Network) [62], (4) SRTM30_PLUS [63], (5) S&S V19.1 (Smith & Sandwell) [59], (6) DTU10BAT (Technical University of Denmark) [57], and (7) ETOPO1 (National Oceanic and Atmospheric Administration's dataset) [64, 65].

Bathymetric models derived from satellite altimetry are not reliable enough for underwater navigation, construction works, or similar, as the errors of the bathymetric estimates sometimes exceeds 100 m but do offer general insight onto the seafloor topography and make the best available bathymetric data for many areas (see e.g., [60, 66]). **Figure 7** presents an example of the global bathymetric model.

3.4 Altimeter data with the other technologies and potential studies

As mentioned above, the satellite altimeter data for geodetic purposes can be integrated with tide gauges when estimating the sea-level change, with shipborne bathymetry obtained by echo sounders when modeling the bathymetry, and with discrete gravity measurements or satellite gravity when computing Earth's gravitational field. Furthermore, the satellite altimetry can be used to access the vertical land motion over the coastal area by comparing the sea level change trends from

Name	Year of issue/update	Resolution
GEBCO_2019	2019	15"
SRTM15 + V2.1	2019	15"
EMODnet	2018	1/16"
SRTM30_PLUS	2014	30"
S&S V19.1	2014	1'
DTU10BAT	2010	1'-2' (Equator)
ETOPO1	2008	1'

Table 2.
Basic details on the most common global bathymetric models derived from satellite altimetry and shipborne data.

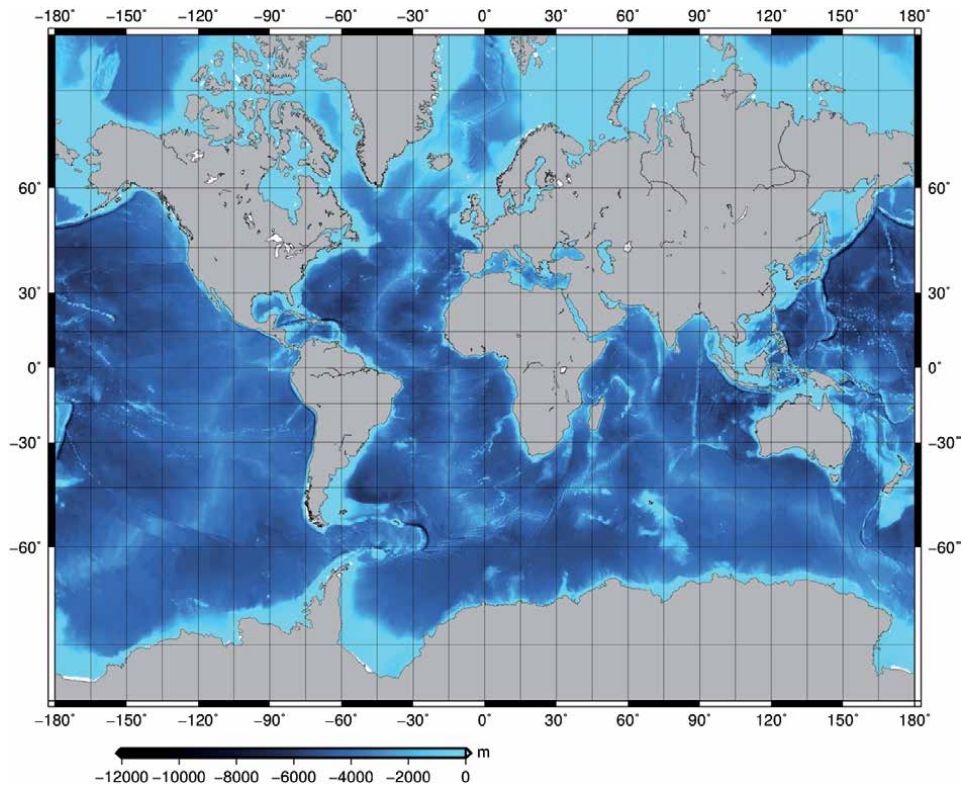


Figure 7.
Altimetry-derived global ocean bathymetric map (data downloaded from [53]).

satellite altimetry and from tide gauges where the latter obtain the trend accounted for the vertical land change (e.g., [10, 67, 68]). The altimetry can further be employed in multidiscipline-based early warning systems such as those forecasting the floods [69], or tsunamis [70], and the other climate-related forecasting systems that lead towards the operational oceanography, i.e., to the forecasting system of the sea-related variables such as sea level, temperature, and currents, based on the long-term routine measurements and real-time observations of the oceans and atmosphere (see e.g., [71]).

4. Conclusion

Satellite altimetry has proven over the years to be a reliable source of the information on the oceans. Many of the applications of the technology are related to the geodetic tasks, out of which some are almost exclusively reserved for geodesy (such as the gravity field modeling), and some are taking a great part in multidisciplinary research (e.g., as in the climate-related studies). The overview given in this book chapter summarized the theoretical basis of the technology, its evolution, and current developments with insight on the availability of different altimetry data and the ready-to-use altimeter products. The chapter could be a good starting point for diving into the geodetic or related research and practical studies on satellite altimetry.

Author details

Marijan Grgić* and Tomislav Bašić
University of Zagreb Faculty of Geodesy, Zagreb, Croatia

*Address all correspondence to: mgrgic@geof.unizg.hr

IntechOpen

© 2021 The Author(s). Licensee IntechOpen. This chapter is distributed under the terms of the Creative Commons Attribution License (<http://creativecommons.org/licenses/by/3.0>), which permits unrestricted use, distribution, and reproduction in any medium, provided the original work is properly cited. 

References

- [1] Kaula W M. The terrestrial environment. [Washington]: National Aeronautics and Space Administration; for sale by the Clearinghouse for Federal Scientific and Technical Information, Springfield, Va; 1970.
- [2] Shum C, Tapley B, Ries J. Satellite altimetry: Its applications and accuracy assessment. *Advances in Space Research*. 1993;13(11):315-324. DOI: 10.1016/0273-1177(93)90234-3
- [3] McGoogan J, Miller L, Brown G, Hayne G. The S-193 radar altimeter experiment. *Proceedings of the IEEE*. 1974;62(6):793-803.
- [4] Stanley H. The Geos 3 Project. *Journal of Geophysical Research*. 1979;84(B8):3779. DOI: 10.1029/JB084iB08p03779
- [5] Tapley B, Born G, Parke M. The SEASAT altimeter data and its accuracy assessment. *Journal of Geophysical Research*. 1982;87(C5):3179. DOI: 10.1029/JC087iC05p03179
- [6] Fu L L, Cazenave A. *Satellite Altimetry and Earth Sciences: A Handbook of Techniques and Applications (International geophysics series ; v. 69)*. Academic Press; 2001.
- [7] Rosmorduc V, Benveniste J, Bronner E, Dinardo S, Lauret O, Maheu C et al. *Radar Altimetry Tutorial*. European Space Agency; 2018.357 p.
- [8] Google Scholar. Search on 'satellite altimetr'. 2021. Available from: [https://scholar.google.hr/scholar?hl=hr&as_sdt=0%2C5&q=satellite+altimetry&btnG=\[Accessed: 2021-01-10\]](https://scholar.google.hr/scholar?hl=hr&as_sdt=0%2C5&q=satellite+altimetry&btnG=[Accessed: 2021-01-10])
- [9] Grgić M, Jukić S, Nerem R S, Bašić T. *Satellite Altimetry: The Technology and its Application in Geodesy (in Croatian)*. *Geodetski list*. 2017;4:307-326.
- [10] Grgić M, Bender J, Bašić T. *Estimating Vertical Land Motion from Remote Sensing and In-Situ Observations in the Dubrovnik Area (Croatia): A Multi-Method Case Study*. *Remote Sensing*. 2020;12(21):3543. DOI: 10.3390/rs12213543
- [11] Liebe C. Accuracy performance of star trackers - a tutorial. *IEEE Transactions on Aerospace and Electronic Systems*. 2002;38(2):587-599.
- [12] Ruf C, Keihm S, Janssen M. TOPEX/Poseidon Microwave Radiometer (TMR). I. Instrument description and antenna temperature calibration. *IEEE Transactions on Geoscience and Remote Sensing*. 1995;33(1):125-137. DOI: 10.1109/36.368215
- [13] Strawbridge F, Laxon S. ERS-1 altimeter fast delivery data quality flagging over land surfaces. *Geophysical Research Letters*. 1994;21(18):1995-1998. DOI: 10.1029/94GL01730
- [14] Vignudelli S, Cipollini P, Kostianoy A, Benveniste J. *Coastal Altimetry*. Springer Science & Business Media; 2011.
- [15] Barlier F. The DORIS system: a fully operational tracking system to get orbit determination at centimeter accuracy in support of Earth observations. *Comptes Rendus Geoscience*. 2005;337(14):1223-1224. DOI: 10.1016/j.crte.2005.07.007
- [16] CMEMS (Copernicus Marine Service) [Internet]. http://www.esa.int/Applications/Observing_the_Earth/Copernicus/Sentinel-6/Sea-level_monitoring_satellite_first_results_surpass_expectations/
- [17] *Sea-level monitoring satellite first results surpass expectations* [Internet]. ESA Observing the Earth. 2021 [cited 20

January 2021]. Available from: http://www.esa.int/Applications/Observing_the_Earth/Copernicus/Sentinel-6/Sea-level_monitoring_satellite_first_results_surpass_expectations

[18] Fu L, Alsdorf D, Rodriguez E, Morrow R, Mognard N, Lambin J et al. The SWOT (Surface Water and Ocean Topography) mission: spaceborne radar interferometry for oceanographic and hydrological applications. *OCEANOBS*. 2009; 2009. p. 21-25.

[19] Dufau C, Martin-Puig C, Moreno L. User requirements in the coastal ocean for satellite altimetry. *Coastal Altimetry*. 2011;51-60 p.

[20] Benveniste J. Radar altimetry: past, present and future. *Coastal Altimetry*. 2011;1-17 p.

[21] Gommenginger C, Thibaut P, Fenoglio-Marc L, Quartly G, Deng X, Gomez-Enri J, Gao Y. A review of retracking methods and some applications to coastal waveforms. *Coastal Altimetry*. 2011;61-101 p.

[22] Martin T, Zwally H, Brenner A, Bindenschadler R. Analysis and retracking of continental ice sheet radar altimeter waveforms. *Journal of Geophysical Research*. 1983;88(C3):1608. DOI: 10.1029/jc088ic03p01608

[23] Rodríguez E, Martin J. Assessment of the TOPEX altimeter performance using waveform retracking. *Journal of Geophysical Research*. 1994;99(C12): 24957. DOI: 10.1029/94jc02030

[24] Davis C. A robust threshold retracking algorithm for measuring ice-sheet surface elevation change from satellite radar altimeters. *IEEE Transactions on Geoscience and Remote Sensing*. 1997;35(4):974-979. DOI: 10.1109/36.602540

[25] Sandwell D, Smith W. Retracking ERS-1 altimeter waveforms for optimal

gravity field recovery. *Geophysical Journal International*. 2005;163(1): 79-89. DOI: 10.1111/j.1365-246x.2005.02724.x

[26] Bao L, Lu Y, Wang Y. Improved retracking algorithm for oceanic altimeter waveforms. *Progress in Natural Science*. 2009;19(2):195-203. DOI: 10.1016/j.pnsc.2008.06.017

[27] Passaro M, Cipollini P, Vignudelli S, Quartly G, Snaith H. ALES: A multi-mission adaptive subwaveform retracker for coastal and open ocean altimetry. *Remote Sensing of Environment*. 2014;145:173-189. DOI: 10.1016/j.rse.2014.02.008

[28] Passaro M, Rose S, Andersen O, Boergens E, Calafat F, Dettmering D et al. ALES+: Adapting a homogenous ocean retracker for satellite altimetry to sea ice leads, coastal and inland waters. *Remote Sensing of Environment*. 2018;211:456-471. DOI: 10.1016/j.rse.2018.02.074

[29] Zwally H J, Brenner A C, Major J A, Bindenschadler R A, Marsh J G. Growth of the Southern Greenland Ice Sheet. *Science*. 1998;281(5381):1249o-1249. DOI: 10.1126/science.281.5381.1249o

[30] International Coastal Altimetry Community | www.coastalt.eu [Internet]. [Coastalt.eu](http://www.coastalt.eu). 2021 [cited 16 January 2021]. Available from: <http://www.coastalt.eu/>

[31] Santos-Ferreira A, da Silva J, Srokosz M. SAR-Mode Altimetry Observations of Internal Solitary Waves in the Tropical Ocean Part 2: A Method of Detection. *Remote Sensing*. 2019;11(11):1339. DOI: 10.3390/rs11111339

[32] Egado A, Smith W. Fully Focused SAR Altimetry: Theory and Applications. *IEEE Transactions on Geoscience and Remote Sensing*. 2017;55(1):392-406. DOI: 10.1109/tgrs.2016.2607122

- [33] Maggioni V, Massari C. *Extreme Hydroclimatic Events and Multivariate Hazards in a Changing Climate*. San Diego: Elsevier; 2019.
- [34] Dinardo S, Fenoglio-Marc L, Buchhaupt C, Becker M, Scharroo R, Joana Fernandes M et al. Coastal SAR and PLRM altimetry in German Bight and West Baltic Sea. *Advances in Space Research*. 2018;62(6):1371-1404. DOI: 10.1016/j.asr.2017.12.018
- [35] Aviso+ [Internet]. Aviso.altimetry.fr. 2021 [cited 22 January 2021]. Available from: <https://www.aviso.altimetry.fr/en/home.html>
- [36] Ocean Surface Topography from Space [Internet]. Ocean Surface Topography from Space. 2021 [cited 18 January 2021]. Available from: <https://sealevel.jpl.nasa.gov/data/>
- [37] Scharroo R, Leuliette E, Lillibridge J, Byrne D, Naeije M, Mitchum G. RADS: Consistent multi-mission products. 20 Years of Progress in Radar Altimetry. Venice-Lido: ESA; 2013.
- [38] Nerem R, Beckley B, Fasullo J, Hamlington B, Masters D, Mitchum G. Climate-change-driven accelerated sea-level rise detected in the altimeter era. *Proceedings of the National Academy of Sciences*. 2018;115(9):2022-2025. DOI: 10.1073/pnas.1717312115
- [39] Wang J, Church J, Zhang X, Chen X. Reconciling global mean and regional sea level change in projections and observations. *Nature Communications*. 2021;12(1). DOI: 10.1038/s41467-021-21265-6
- [40] Slangen A, Carson M, Katsman C, van de Wal R, Köhl A, Vermeersen L et al. Projecting twenty-first century regional sea-level changes. *Climatic Change*. 2014;124(1-2):317-332. DOI: 10.1007/s10712-019-09575-3
- [41] Ablain M, Cazenave A, Larnicol G, Balmaseda M, Cipollini P, Faugère Y et al. Improved sea level record over the satellite altimetry era (1993-2010) from the Climate Change Initiative project. *Ocean Science*. 2015;11(1):67-82. DOI: 10.5194/os-11-67-2015
- [42] Ablain M, Legeais J, Prandi P, Marcos M, Fenoglio-Marc L, Dieng H et al. Satellite Altimetry-Based Sea Level at Global and Regional Scales. *Surveys in Geophysics*. 2016;38(1):7-31. DOI: 10.1007/s10712-016-9389-8
- [43] Hamlington B, Frederikse T, Nerem R, Fasullo J, Adhikari S. Investigating the Acceleration of Regional Sea Level Rise During the Satellite Altimeter Era. *Geophysical Research Letters*. 2020;47(5). DOI: 10.1029/2019GL086528
- [44] Hamlington B, Strassburg M, Leben R, Han W, Nerem R, Kim K. Uncovering an anthropogenic sea-level rise signal in the Pacific Ocean. *Nature Climate Change*. 2014;4(9):782-785. DOI: 10.1038/nclimate2307
- [45] Cazenave A, Palanisamy H, Ablain M. Contemporary sea level changes from satellite altimetry: What have we learned? What are the new challenges?. *Advances in Space Research*. 2018;62(7):1639-1653. DOI: 10.1016/j.asr.2018.07.017
- [46] Rülke A, Liebsch G, Sacher M, Schäfer U, Schirmer U, Ihde J. Unification of European height system realizations. *Journal of Geodetic Science*. 2012;2(4):343-354. DOI: 10.2478/v10156-011-0048-1
- [47] Woodworth P, Hughes C, Bingham R, Gruber T. Towards worldwide height system unification using ocean information. *Journal of Geodetic Science*. 2012;2(4):302-318. DOI: 10.2478/v10156-012-0004-8

- [48] Sánchez L, Sideris M. Vertical datum unification for the International Height Reference System (IHRs). *Geophysical Journal International*. 2017;:ggx025. DOI: 10.1093/gji/ggx025
- [49] Grgić M, Nerem R, Bašić T. Absolute Sea Level Surface Modeling for the Mediterranean from Satellite Altimeter and Tide Gauge Measurements. *Marine Geodesy*. 2017;40(4):239-258. DOI: 10.1080/01490419.2017.1342726
- [50] Rapp R, Bašić T. Oceanwide gravity anomalies from GEOS-3, Seasat and Geosat altimeter data. *Geophysical Research Letters*. 1992;19(19):1979-1982. DOI: 10.1029/92GL02247
- [51] Knudsen P. Simultaneous Estimation of the Gravity Field and Sea Surface Topography From Satellite Altimeter Data By Least-Squares Collocation. *Geophysical Journal International*. 1991;104(2):307-317. DOI: 10.1111/j.1365-246X.1991.tb02513.x
- [52] Hwang C, Hsu H, Jang R. Global mean sea surface and marine gravity anomaly from multi-satellite altimetry: applications of deflection-geoid and inverse Vening Meinesz formulae. *Journal of Geodesy*. 2002;76(8):407-418. DOI: 10.1007/s00190-002-0265-6
- [53] Andersen O, Knudsen P, Kenyon S, Factor J, Holmes S. Global gravity field from recent satellites (DTU15) — Arctic improvements. *First Break*. 2017;35(12). DOI: 10.3997/1365-2397.2017022
- [54] The combined global gravity field model XGM2019e. *Journal of Geodesy*. 2020;94:66(2020). DOI: 10.1007/s00190-020-01398-0
- [55] Demianov G, Sermyagin R, Tsybankov I. Global Gravity Field Model GAO2012. DOI: 10.5281/zenodo.814573
- [56] Förste C, Bruinsma S L, Abrikosov O, Lemoine J, Marty J C, Flechtner F, Balmino G, Barthelmes F, Biancale R. EIGEN-6C4 The latest combined global gravity field model including GOCE data up to degree and order 2190 of GFZ Potsdam and GRGS Toulouse. GFZ Data Services. DOI: 10.5880/ICGEM.2015.1
- [57] Pavlis N K, Holmes S A, Kenyon S C, Factor J K. The development and evaluation of the Earth Gravitational Model 2008 (EGM2008). *Journal of Geophysical Research: Solid Earth*. 2012;117:B04406. DOI: 10.1029/2011JB008916
- [58] Smith W, Sandwell D. Global Sea Floor Topography from Satellite Altimetry and Ship Depth Soundings. *Science*. 1997;277(5334):1956-1962. DOI: 10.1126/science.277.5334.1956
- [59] Dixon T, Naraghi M, McNutt M, Smith S. Bathymetric prediction from SEASAT altimeter data. *Journal of Geophysical Research*. 1983;88(C3):1563. DOI: 10.1029/jc088ic03p01563
- [60] Mayer L, Jakobsson M, Allen G, Dorschel B, Falconer R, Ferrini V et al. The Nippon Foundation—GEBCO Seabed 2030 Project: The Quest to See the World's Oceans Completely Mapped by 2030. *Geosciences*. 2018;8(2):63. DOI: 10.3390/geosciences8020063
- [61] Tozer B, Sandwell D, Smith W, Olson C, Beale J, Wessel P. Global Bathymetry and Topography at 15 Arc Sec: SRTM15+. *Earth and Space Science*. 2019;6(10):1847-1864. DOI: 10.1029/2019EA000658
- [62] Calewaert J B, Weaver P, Gunn V, Gorringer P, Novellino A. The European Marine Data and Observation Network (EMODnet): your gateway to european marine and coastal data. *Quantitative Monitoring of the Underwater Environment*, Springer, Cham. 2016;31-46. DOI: 10.3389/fmars.2019.00313

- [63] Becker J, Sandwell D, Smith W, Braud J, Binder B, Depner J et al. Global Bathymetry and Elevation Data at 30 Arc Seconds Resolution: SRTM30_PLUS. *Marine Geodesy*. 2009;32(4):355-371. DOI: 10.1080/01490410903297766
- [64] Ramillien G, Cazenave A. Global bathymetry derived from altimeter data of the ERS-1 geodetic mission. *Journal of Geodynamics*. 1997;23(2):129-149. DOI: 10.1016/s0264-3707(96)00026-9
- [65] Amante C, Eakins B W. ETOPO1 arc-minute global relief model: procedures, data sources and analysis. National Oceanic and Atmospheric Administration, Boulder, Colorado. 2009.
- [66] Smith W. On the accuracy of digital bathymetric data. *Journal of Geophysical Research*. 1993;98(B6):9591. DOI: 10.1029/93JB00716
- [67] Santamaría-Gómez A, Gravelle M, Wöppelmann G. Long-term vertical land motion from double-differenced tide gauge and satellite altimetry data. *Journal of Geodesy*. 2013;88(3):207-222. DOI: 10.1007/s00190-013-0677-5
- [68] Fenoglio-Marc L, Dietz C, Groten E. Vertical Land Motion in the Mediterranean Sea from Altimetry and Tide Gauge Stations. *Marine Geodesy*. 2004;27(3-4):683-701. DOI: 10.1080/01490410490883441
- [69] Chang C, Lee H, Hossain F, Basnayake S, Jayasinghe S, Chishtie F et al. A model-aided satellite-altimetry-based flood forecasting system for the Mekong River. *Environmental Modelling & Software*. 2019;112:112-127. DOI: 10.1016/j.envsoft.2018.11.017
- [70] Sepúlveda I, Tozer B, Haase J, Liu P, Grigoriu M. Modeling Uncertainties of Bathymetry Predicted With Satellite Altimetry Data and Application to Tsunami Hazard Assessments. *Journal of Geophysical Research: Solid Earth*. 2020;125(9). DOI: 10.1029/2020JB019735
- [71] Flather R. Existing operational oceanography. *Coastal Engineering*. 2000;41(1-3):13-40. DOI: 10.1016/s0378-3839(00)00025-9

Coastal Sea Level Trends from a Joint Use of Satellite Radar Altimetry, GPS and Tide Gauges: Case Study of the Northern Adriatic Sea

Stefano Vignudelli and Francesco De Biasio

Abstract

For the last century, tide gauges have been used to measure sea level change along the world's coastline. However, tide gauges are heterogeneously distributed and sparse in coverage. The measured sea level changes are also affected by solid-Earth geophysics. Since 1992, satellite radar altimetry technique made possible to measure heights at sea independent of land changes. Recently various efforts started to improve the sea level record reprocessing past altimetry missions to create an almost 30 year-long combined record for sea level research studies. Moreover, coastal altimetry, i.e. the extension of altimetry into the oceanic coastal zone and its exploitation for looking at climate-scale variations of sea level, has had a steady progress in recent years and has become a recognized mission target for present and future satellite altimeters. Global sea level rise is today well acknowledged. On the opposite, the regional and local patterns are much more complicated to observe and explain. Sea level falls in some places and rises in others, as a consequence of natural cycles and anthropogenic causes. As relative sea level height continues to increase, many coastal cities can have the local elevation closer to the flooding line. It is evident that at land-sea interface a single technique is not enough to de-couple land and sea level changes. Satellite radar altimetry and tide gauges would coincide at coast if land had no vertical motion. By noting this fact, the difference of the two independent measurements is a proxy of land motion. In this chapter, we review recent advances in open ocean and coastal altimetry to measure sea level changes close to the coasts over the satellite radar altimetry era. The various methods to measure sea level trends are discussed, with focus on a more robust inverse method that has been tested in the Northern Adriatic Sea, where Global Positioning System (GPS) data are available to conduct a realistic assessment of uncertainties. The results show that the classical approach of estimating Vertical Land Motion (VLM) provides values that are almost half of those provided by the new Linear Inverse Problem With Constraints (LIPWC) method, in a new formulation which makes use of a change of variable (LIPWC_{COV}). Moreover, the accuracy of the new VLM estimates is lower when compared to the VLM estimated from GPS measurements. The experimental Sea Level Climate Change Initiative (SLCCI) data set (high resolution along track) coastal sea level product (developed within Climate Change Initiative (CCI) project) that has been also assessed in the Gulf of Trieste show that the trends calculated with the gridded and along track

datasets exhibit some differences, probably due to the different methodologies used in the generation of the products.

Keywords: Satellite radar altimetry, Tide gauges, GPS, Sea level, Adriatic Sea

1. Introduction

Sea level rise is primarily an issue at the boundary line with land. It represents a potential threat to infrastructures and population living in low-elevation coastal areas [1]. The land disappears not only because the rising sea changes the coastline, but also because at a place there could be the land moving up or down, therefore contrasting or accelerating sea level rise [2]. Sea level can change significantly from one coastal location to another, as a result of a number of ocean, atmospheric and land processes that occur at various spatial and temporal scales [3].

In a global change scenario, as speculated in Li et al. [4], a slow rise of the sea level of few cm associated to climate change would make a difference to the coastline. It would not retreat from land, making it permanent. The flooding line of transient events (e.g., storm surges, tsunamis, etc.) would also uplift, increasing the risk of more frequent land inundation and more inland propagation [5]. An example is the City of Venice that has long been vulnerable to short duration flooding during winter [6]. The problem was so important that a system of 78 storm gates, known as MOSE [7] has been constructed to protect the city when high water is expected in Venice [8]. Long-term rising sea levels will represent additional challenges in the future [8].

Understanding the climate-related contribution to the sea level change and how much it will likely affect coastal regions is a major challenge, as it also requires local-scale measurements of the land effects. In this chapter, we review the sea level trend measuring system involving the integration of recent satellite-based observations from radar altimeters and Global Positioning System (GPS) receivers with historical data from tide gauge stations. The latest advances in open ocean and coastal altimetry to measure sea level changes close to the coasts over the satellite radar altimetry era are also summarized. A more robust inverse method to estimate sea level trends is also presented. It has been tested in the Northern Adriatic Sea, where GPS data are available to conduct a realistic assessment of uncertainties.

2. Techniques for measuring sea levels

Since Roman period, sea level has been measured nearby land just sticking a graduated pole within protected piscinae [9]. Since the 19th Century, tide gauges have been used in some coastal places around the world to measure the local change in sea level relative to the adjacent land [10, 11]. The baseline for measuring sea level over time is typically a mean sea level computed by averaging all the measurements over a period of years at each location. This relative sea level that will rise if ocean levels rise and/or land levels fall is the net change in the sea level and is the quantity of interest to the local coastal community in the real-time monitoring.

However, understanding the future coastal sea level changes and their relative significance requires to remove the effect of waves, tides, and other short-term fluctuations. But tide gauges alone cannot determine whether the sea level is rising, the land is sinking, or both. Sea level can rise or retreat in the long-term in response to the natural processes that alter the volume of water, including the climate-related contribution. The land level changing over time (the so-called vertical land motion, VLM or subsidence/uplift) can rise or fall due to natural processes (e.g., tectonic

shifts; sediment loading, glacial isostatic adjustment, etc.) but also as a consequence of man-made factors (e.g., ground water extraction; oil and gas pumping, etc.).

There are various techniques for measuring VLM, e.g., geotechnical investigations using spirit levels and borehole extensometers [12]; geodetic surveying with Global Positioning System (GPS) satellite technology [13]; satellite remote sensing observations that use a technique called interferometric synthetic aperture radar (InSAR) [14]. The advantage of satellites is that they ensure almost global coverage in a repeatable manner and consistency of the measuring system over long time periods that is an important requirement for the detection of slow changes over time.

The quantification of VLM before the modern satellite era is difficult due to the poor coverage of geotechnical investigations. The advent of GPS receivers and their co-location with tide gauges made possible to continuously measure land elevation changes with simultaneous sea level reading at the same location [15]. GPS sensors return vertical and horizontal positions. The vertical position is a measure of the elevation of the land surface relative to the center of Earth, also referred as absolute. It is generally two to three times less precise than the horizontal components. The present picture is that, while there are many tide gauges around the world, not all have permanent GPS receivers co-located or near them [16].

The InSAR tool uses repeating multiple satellite radar imagery to create a time profile of land elevation change. The advantage respect to the GPS technology is the much higher density of VLM measuring points in the imaged area. The technique to provide statistically significant results requires a sufficient number of images and reduced scattering over time for the area of interest. The availability of images from the first satellites (e.g., ERS and Envisat) can be very irregular both in time and space [17]. Only the recent Sentinel-1 constellation provides global coverage and more frequent revisiting. Other satellite missions (e.g., COSMO-SkyMed, RADARSAT, etc.) only provide imagery on demand.

Sea level can be also measured with satellites using radar altimeters. These instruments send microwave pulses down along the satellite's ground track and measure their echoes, revisiting the same place every 10 days or more depending on the mission. The time their echoes take to bounce back allows the system to measure the satellite's altitude above the sea surface (the so-called range). It can be then corrected for instrumental and environmental effects. Knowing the satellite orbit with respect to Earth's center of mass, the absolute, not relative, sea level can be thus calculated, and its change tracked over time.

Routine sea level observations began in 1992 with the TOPEX/Poseidon spacecraft on a 10-day repeat cycle, and this has subsequently been followed up by the Jason 1/2/3 series and the recent Sentinel-6 mission, providing a near-global fully consistent along track data set of sea level to understand how sea levels have changed over the past nearly three decades. Over the years, various satellite missions with different orbital configurations and other scientific objectives were launched, e.g., ERS-1/2, Envisat, Sentinel-3, SARAL, CryoSat-2 and HY-2A/B.

But single satellites have limitations. The sea level is tracked along paths whose distance is relatively large. A satellite alone could not fly in the region of interest, as it is for example the case of Venice for the T/P-Jason-Sentinel-6 family. Moreover, it has been difficult to retrieve data near coast where both the presence of land and more complex ocean surface scattering make the standard processing problematic [18].

3. Coastal sea level from satellite radar altimetry – a review

The satellite radar altimetry system has been initially conceived for usage in open ocean. The processing of radar echoes and the development of corrections is

now at mature stage in this domain, with the various datasets routinely used for global sea level studies. However, data were normally flagged as bad and therefore rejected in the coastal zone. But the situation rapidly changed in the last ten years for two reasons: (1) the prospect of recovering a valuable long-term sea level data around the global coastline; (2) the improved suitability of the new and future altimeters (like those on CryoSat-2, AltiKa, Sentinel-3, Sentinel-6, Crystal). Therefore, a new domain “coastal altimetry”, i.e. the extension of altimetry into the oceanic coastal zone has been emerging, with a community around it developing a set of coastal altimetry techniques in order to get more and better sea level data closer to the coast.

The analyses of radar echoes revealed that pulse-limited missions, if reprocessed with dedicated models, could provide reliable range measurements to few km from the coastline. An example is the Adaptive Leading Edge Subwaveform (ALES) retracking algorithm, that has been validated and applied successfully to sea level research, demonstrating the ability to increase the quality and the quantity of sea level retrievals in coastal areas [19].

In addition, it was noted that geophysical corrections that must be applied to altimeter range data have a significant impact in coastal altimetry and therefore their constant improvement is crucial. There have been noticeable developments to improve the tropospheric delay [20], the tidal sea level where global models have still large errors [21] and the mean sea surface models, suitable for the observation of the coastal sea level [22]. There have been also improvements in procedures to avoid aliasing of major tidal signals and short-period ocean response to meteorological forcing aliases onto low frequency signals [23].

The wet tropospheric correction is the major source of uncertainty in altimetry budget error, due to its large spatial and temporal variability: this is reason why a multi-channel passive microwave radiometer is on the same platform as the altimeter. Unfortunately, this estimate gets quickly corrupted as soon as land enters the radiometer footprint, i.e. 20–50 Km from the coast. Alternative corrections have been devised and appear to be successful at least in some particular conditions [24]. A very promising approach was the one attempting to estimate the wet tropospheric path delay from GPS measurements known as GPD (GNSS-derived Path Delay), and its latest version called GPD+ (Plus) [25].

The classical data editing used in open ocean was also considered excessively restrictive and revisited with novel editing/re-interpolation approaches (e.g., [26]). The new data from the various reprocessing efforts are now bringing altimetry around the global coastline, with a higher spatial resolution and precision that was previously not available in coastal and shelf sea areas, while constant improvement [18] and validation [27] are still ongoing. The new coastal altimetry datasets open a new opportunity to study sea level change from open ocean to coast and differences in trend and variability at various distances from the coast, also nearby tide gauges [28].

4. A new sea level record from satellite radar altimetry for climate studies

Several radar altimetry missions have been in operation since the first launch in 1973 (see **Figure 1**). The TOPEX/Poseidon and Jason series (with the addition of the just launched Sentinel-6) is the reference mission for long-term sea level studies, as it is ensured the continuity in the same orbit [29]. However, a single altimeter only provides measurement along a track from open ocean closer to coast. There is always a trade-off between temporal sampling and ground-track spatial coverage.

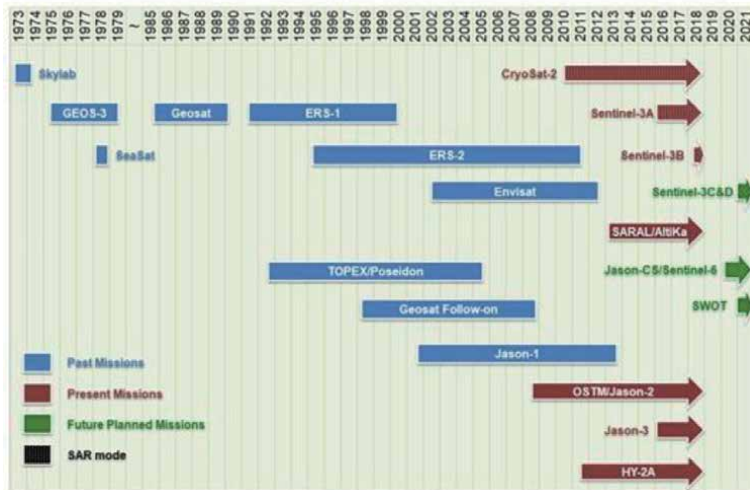


Figure 1.
 Main characteristics of satellite altimetry missions operating until now and planned for the future.

A single altimeter always leaves gaps along the coast between neighboring tracks: tenths to hundred km are not covered, so that the vast majority of the worldwide coast is not sampled. The coverage can be augmented with additional existing altimeters.

Data from the various altimeter missions were used to create several datasets. Examples include RADS [30], X-TRACK [28], etc. that also provide sea level estimates. Since 1992, at least two altimeter satellites have been operating simultaneously, and during some periods, even more than two. Such data can be combined in a single product to provide a consistent long-term sea level data set, globally with sufficient spatial coverage over almost three decades. However, altimeter missions need to be accurately homogenized and cross-calibrated to reduce biases and uncertainties [31].

A satellite-based sea level data set to analyze long-term trends that uses the available historic observations from the various radar altimeters is key requirement for the climate community [32]. A recent reprocessing within the European Space Agency (ESA) Sea Level Climate Change Initiative (SLCCI) has produced a gridded altimetry product with a spatial resolution of 0.25° (which is around 25 km resolution) from 1993 to 2015 [33, 34], thus permitting a more detailed view of sea-level change around the world coastlines.

The sea level Environment Climate Variable (ECV) (at global and regional scales) is now operationally produced by the Copernicus Climate Change Service (C3S) [35] by applying the altimetry processing standards developed in the SLCCI initiative. The C3S product ensures a stable number of two altimeters since the beginning and the reference field used to compute sea level anomalies (SLA) is a homogeneous mean sea surface for all missions. The C3S record is a regional product, gridded at 0.125° in the Mediterranean Sea, starting in 1993 and offering ongoing coverage [36]. Both the SLCCI and the C3S datasets are state-of-the-art products designed to be a reference for climate-related sea level studies.

In the case-study illustrated in the chapter, the SLCCI and C3S datasets are used to assess their maturity as state-of-the-art altimetry datasets in climatological studies. The multi-mission gridded products have not still tuned for last 10 km from the coast, where the amount of valid data might decrease. The ESA CCI + Sea Level

project, started in 2017, is extending the processing to the coastal zone, and an experimental coastal sea level product is going to be released to the public, in six selected regions: Northern Europe, Mediterranean Sea, Western Africa, North Indian Ocean, Southeast Asia and Australia [37]. This product is along-track and combines the enhanced spatial resolution provided by high-rate data (20-Hz), the post-processing strategy of X-TRACK and the advantage of the ALES retracker [38]. The product relies on the GPD+ wet tropospheric correction [39] and the FES2014 tidal corrections [40]. The X-TRACK/ALES SLCCI 20 Hz along-track dataset will be indicated with SLCCI-AT hereinafter.

5. Methods of estimating sea level trends

The trend is an indicator describing how sea level has changed over long time. It provides a simple predictive scenario if what observed in the past might be representative in the near future. The classical approach is to calculate a straight line through sea level data using a linear regression. The most used method for fitting data is least squares. However, other methods based on more complex models exist to estimate trends from sea level time series [41]. The trend estimation is sensitive to the length of the record and start/end periods. There might be variability at different inter-annual to decadal timescales occurring within the data. Moreover, in addition to the linear trend, there might be autocorrelation of the noise in the data [42].

A single tide gauge cannot explain to what extent the observed trend is related to ocean and/or land changes, without any nearby GPS. With the advent of satellite radar altimetry and the possibility to use altimeter passages nearby tide gauges a new method was proposed by Cazenave et al. [43]. It assumes that both the tide gauge and altimetry system measure the same ocean signal and the difference is a measure of VLM at the gauge: hereinafter we refer to this method as the “direct” or “classical” method. Another assumption is that there are no instrumental errors introducing significant drifts. This direct method provides VLM at the selected tide gauge station only.

Different implementations of the basic idea were successively proposed involving more tide gauges, more rigorous error analysis with mitigation of the uncertainties introduced by the assumptions and taking advantage of longer and improved altimeter-derived time series available at that time (e.g., [44–47] and others).

An advanced method to estimate VLM that includes supplementary constraints from adjacent tide gauges has been proposed by Kuo et al. [48]. Its solution is based on the inversion of a linear system, formed mixing differences of altimetry- and tide gauge-derived trends, and differences of trends from neighboring tide gauges only, introduced in the linear system through Lagrange multipliers. As the solution of such a system requires its inversion, the method is referred to as Linear Inverse Problem with Constraints (LIPWC), or shortly “inverse” method. The new method optimally combines short-term altimetry records with long-term tide gauge observations. It assumes that absolute sea level change at tide gauges over a long time span is the same. The advantage of the method is that long (>40 years) tide gauge records contribute to reduce the error in the final VLM solution, and random and systematic errors in one or more time series trend are shared among all the other, cutting down the impact on the originating one. The disadvantage is that the method cannot be applied if the absolute sea level change is different from place to place. Nevertheless, this method can be useful in closed and semi-enclosed basins and could be adapted to work also in case a GPS at the coast is used instead of a tide gauge.

Kuo et al. [48] applied the inverse method within a semi-enclosed sea (Baltic Sea region of Fennoscandia). The results showed a significant reduction of uncertainties

compared with those from conventional approaches, which are limited to the overlapping periods between altimetry and tide gauges. An extension of the method has been applied to Great Lakes and in open ocean regions, such as Alaskan coast [49]. It has been also extended along the coasts of southern Europe [50] with constraints between pairs of tide gauges based on correlation and overlapping periods. The same method has been extended to open ocean in New Zealand straddles, the Tasman Sea and Pacific Ocean [51]. All studies confirmed the superiority of the inverse method to the classical direct approach.

A new variant of the inverse method considers to difference sea level trends between pairs of tide gauge records and pairs of altimetry records [52]. Another study proposed different mathematical and statistical models, which enable simultaneous estimation of absolute and relative sea level trends and VLM at a tide gauge station merging altimetry and tide gauge records without the aid of geological information or GPS measurements [53].

6. A revisited linear inverse model to estimate sea level trends

The linear inverse model proposed by Kuo et al. [48, 49], and then by Wöppelmann and Marcos [50], assumes that the absolute sea level change rates are similar at all the tide gauge (TG) sites. This assumption is particularly important for the successful inversion. The explanation will be provided in this section.

The difference between the absolute sea level rise (ASLR) and the relative sea level rise (RSLR) rates, i.e. the velocities at which the sea level vertical motion is observed by satellite altimeters and TGs, denoted respectively with \dot{g} and \dot{s} , is an estimate of the vertical velocity at which the land beneath TGs is moving. Such vertical crustal velocity, as previously stated, is named vertical land motion (VLM) and indicated by \dot{u} . A subscript i is added to denote that the quantities \dot{g} , \dot{s} and \dot{u} refer to the i -th TG of a group of N :

$$\dot{u}_i = \dot{g}_i - \dot{s}_i \quad i = 1, \dots, N \quad (1)$$

Eq. (1) is sufficient to obtain good estimates of the VLM rates at each TG, provided that all the variables in the equation refer to the same period and to coherent geophysical processes and have negligible inherent drifts and errors. Eq. (1) can be expressed in vector–matrix notation:

$$G\dot{u} = d; G = I_N \quad (2)$$

where \dot{u} is the column vector of the unknown VLMs $\dot{u} = (\dot{u}_1, \dots, \dot{u}_N)$, and d is the column vector whose elements are formed by the right-hand side of Eq. (1): $d = (\dot{g}_1 - \dot{s}_1, \dots, \dot{g}_N - \dot{s}_N)$. In this picture all the unknown VLMs are mutually independent, and the linear system is easily inverted, offering the solution component by component. However, the solution is affected by large errors, as the period during which Eq. (1) is valid corresponds to the overlap period of TG and satellite altimetry observations, and thus no more back in time than 1992. In fact, the current time span of satellite altimetry data is less than 30 years. Such a short time span hinders the derivation of accurate trends from altimeter-gauge time series, as they are affected by inter-annual and decadal sea level signals, in particular by the 18.6-year lunar nodal tide, leading to uncertainties of the order of 1–2 mm yr⁻¹ [47, 54, 55]. For this reason, Kuo et al. [48] proposed a more elaborate linear system, in which constraints formed by the differenced time series of TGs over longer time periods (>40 yr) pose strong limits to the magnitude of the final errors thanks to the length

of the time series. Such constraints are formed imposing that the rate of relative vertical motion between two TGs must equal the difference of their VLMs:

$$r\dot{u}_{ij} = (\dot{g}_i - \dot{s}_i) - (\dot{g}_j - \dot{s}_j). \quad (3)$$

At this stage, the constraints still contain explicitly the ASLR at sites i, j , which are not known back in time beyond the beginning of the altimetry era. But if each couple of TGs in Eq. (3) are observing the same ASLR for some reason, for example they can be inside a lake or a semi-enclosed basin, Eq. (3) simplifies to:

$$r\dot{u}_{ij} = (\dot{s}_j - \dot{s}_i), \quad (4)$$

leaving out any reference to the ASLRs. Containing only the differences of the RSLR, Eq. (4) can be extended to the whole period of overlapping observations of the two TGs, which usually are longer and affected by lower errors. To distinguish the RSLR observed at the TG in the altimetry era from that observed in the common, longer period of observations of TGs i, j , we rewrite Eq. (4) as:

$$r\dot{u}_{ij} = \dot{\zeta}_j - \dot{\zeta}_i \quad (5)$$

where we used the Greek letter ζ to indicate that the TG RSLR difference is calculated over the complete overlapping time span of the two tide gauges, even before the altimetry era.

The two linear systems for the Eqs. (2) and (5) are written in vector-matrix form as:

$$G\dot{u} = d; \quad \dot{u} = \begin{pmatrix} \dot{u}_1 \\ \vdots \\ \dot{u}_N \end{pmatrix}; \quad d = \begin{pmatrix} \dot{g}_1 - \dot{s}_1 \\ \vdots \\ \dot{g}_N - \dot{s}_N \end{pmatrix}; \quad G = I_N, \quad (6)$$

$$F\dot{u} = h; \quad h = -F \begin{pmatrix} \dot{\zeta}_1 \\ \vdots \\ \dot{\zeta}_N \end{pmatrix}; \quad F = \begin{pmatrix} 1 & -1 & 0 & 0 & \dots & 0 \\ 0 & 1 & -1 & 0 & \dots & 0 \\ \dots & \dots & \dots & \dots & \dots & \dots \\ 0 & 0 & 0 & \dots & 1 & -1 \end{pmatrix}. \quad (7)$$

The matrix F is the design matrix by which the constraints are formed and introduced in the linear system. The constraints can be chosen arbitrarily, but they must be linearly independent so that the rank of matrix F is $L \leq N - 1$. For the system to admit an OLS solution, L , the rank of the matrix F , must be $< N$, so that one degree of freedom is left in the linear system for the OLS procedure to perform the unknowns estimate. Without such degree of freedom, the system would become even-determined, and the N constraints $r\dot{u}_{ij} = \dot{\zeta}_j - \dot{\zeta}_i$ would automatically determine the solutions for the unknown \dot{u}_i , and there would be no need for an OLS estimation.

Not always assumption $\dot{g}_i - \dot{g}_j = 0$ is valid for every couple of TGs paired in a constraint. In such case independent linear systems are to be considered for each group of homogeneous TGs. Wöppelmann and Marcos [50] for example, applying this method to the seas of the southern Europe, treated separately the sites inside the Mediterranean Sea from those on the Atlantic coast of the Iberian Peninsula, as the oceanographic behaviors of the two sets of TG sites were observed to be markedly different. In this case the two linear system are totally independent and there cannot be a connection between the two groups.

A unique linear system incorporating the constraints (7) in the system (6) is formed recurring to the Lagrange multipliers technique: the inverse linear problem with constraints [56] (LIPWC). It stems from the minimization of the expression $\Phi(\dot{u}) = e^T e + 2\lambda^T (F\dot{u} - h)$, obtained as the sum of the L_2 norm of the prediction error $e = G\dot{u} - d$ and the inner product of the constraint equations $F\dot{u} - h = 0$ by the Lagrange multipliers λ^T . The resulting ordinary least squares (OLS) equation in matrix form is:

$$\begin{pmatrix} I & F^T \\ F & 0 \end{pmatrix} \begin{pmatrix} \dot{u} \\ \lambda \end{pmatrix} = \begin{pmatrix} d \\ h \end{pmatrix} \quad (8)$$

which is a linear system of the form $A \cdot X = Y$, with $A = \begin{pmatrix} I & F^T \\ F & 0 \end{pmatrix}$. Such system is solved by direct inversion, provided the inverse of matrix A exists:

$$X = \begin{pmatrix} \dot{u} \\ \lambda \end{pmatrix} = A^{-1}Y; \quad Y = \begin{pmatrix} d \\ h \end{pmatrix} \quad (9)$$

The standard errors of the \dot{u} are estimated as the diagonal elements of the covariance matrix $A^{-1}\Omega (A^{-1})^T$, with Ω given by

$$\Omega = \begin{pmatrix} \sigma_1^2 & 0 & \dots & 0 \\ 0 & \sigma_2^2 & \dots & 0 \\ \vdots & \vdots & \ddots & \vdots \\ 0 & 0 & \dots & \sigma_{N+L}^2 \end{pmatrix} \quad (10)$$

where N and L are respectively the number of parameters \dot{u}_{ij} and constraints $r\dot{u}_{ij}$. The previous expression for Ω holds assuming no autocorrelation and heteroscedasticity of the regression residuals. The resultant errors of the OLS estimators are generally referred to as heteroscedasticity-consistent standard errors or White–Huber robust standard errors [57]. Finally, the estimated parameters are given by $X_i \pm \delta X_i$:

$$X = A^{-1}Y; \quad X_i = \begin{cases} \dot{u}_i & \text{if } 0 \leq i \leq N \\ \lambda_i & \text{if } N + 1 \leq i \leq N + L \end{cases}$$

$$\delta X_i = \text{diag} \left(A^{-1}\Omega (A^{-1})^T \right)_i \quad (11)$$

A possible attenuation of the condition that $\dot{g}_i - \dot{g}_j = 0$, for each pairs of TGs involved in a constrain, arises from the observation that if $r\dot{u}_{ij} = (\dot{g}_i - \dot{s}_i) - (\dot{g}_j - \dot{s}_j)$ can be rewritten as $r\dot{u}_{ij} = (-\dot{s}'_i) - (-\dot{s}'_j)$, then the reference to the ASLR has disappeared. Such situation can be achieved by a change of variable, as proposed by De Biasio et al. [58]:

$$\begin{aligned} \dot{g}_i &\rightarrow \dot{g}'_i = \dot{g}_i - \dot{g}_i = 0 \\ \dot{s}_i &\rightarrow \dot{s}'_i = \dot{s}_i - \dot{g}_i \\ \dot{\zeta}_i &\rightarrow \dot{\zeta}'_i = \dot{\zeta}_i - \dot{g}_i \end{aligned}$$

$$\dot{u}_i = \dot{g}_i - \dot{s}_i = \dot{g}_i - \dot{g}_i + \dot{g}_i - \dot{s}_i = \dot{g}'_i - \dot{s}'_i. \quad (12)$$

In other words, we overcome the limitation of equal ASLR at all TGs by removing from both, the TG time series and the altimetry time series associated with the TG, a linear trend equal to that measured by the altimeter. Such change of variables (COV) does not alter the statistical properties of the TG and altimetry time series but eliminates any difference in relative sea level changes due to different absolute sea level changes. For it to work two assumptions are necessary:

1. All the time series have a linear trend in every period in which they are considered.
2. The absolute sea level rates observed by satellite altimetry in its era can be extended backward in time to cover the timespan of the associated TG relative sea level time series.

While the first assumption can be easily verified by visual inspection or with more precise statistical methods, as the goodness-of-fit R^2 test [59], the second assumption, needed to permit the third change of variable in Eq. (12), can be more difficult to assess. In general, the linearity of a TG's RSLR trend can partly corroborate the validity of the second assumption, as the probability that two different, non-linear trends of the local ASLR and VLM perfectly combine by chance, to give an overall linear trend, is obviously low.

7. Case-study of Venice and Adriatic Sea

The method of derivation of VLM described in the previous section will now be applied to a real case. To this end we have chosen the Adriatic Sea for its complexity and for the interest in this area. Indeed, several historical heritage cities and commercial/productive sites lie in the coastal area of the region, not to mention the number of people leaving along the Adriatic Sea coast, which at the end of last century was already higher than 3.5 million [60]. First, we will derive the VLM values in the Adriatic Sea using the classical LIPWC technique. After that, the LIPWC method will be applied to the same data using the change of variable presented in Eq. (12), and the results of the two strategies compared.

The TG in the Adriatic Sea for which long time series of monthly sea level are available are few. **Table 1** reports their name, position, and data availability. The records of the TGs have been formed in some case from different sources,

Location	TG Name	Lat (° N)	Long (° E)	Data (%)	Time Span (Years)	Record Length (Years)
Venice	VENEZIA *	45°25'51.45"	12°20'13.39"	97	1872–2018	147
Venice off-shore	VEPTF	45°18'51.29"	12°30'29.69"	100	1974–2018	45
Trieste	TRIESTE *	45°38'50.00"	13°45'33.90"	89	1875–2018	145
Rovinj	ROVINJ	45°05'01.18"	13°37'44.86"	99	1955–2018	64
Split	SPLIT *	43°30'23.88"	16°26'18.44"	100	1952–2018	67
Dubrovnik	DUBROVNIK	42°39'28.40"	18°03'38.84"	99	1956–2018	63

Table 1. Principal characteristics of tide gauges considered in Adriatic Sea. Some of the tide gauge records have been formed by collating partial records from different sources. Such situation is marked by an asterisk after the tide gauge name.

principally the Permanent Service for Mean Sea Level (PSMSL) [61], the Venice Tide Forecast and Early Warning Center (Centro Previsioni e Segnalazioni Maree, CPSM) of Venice Municipality, the Istituto Superiore per la Protezione e la Ricerca Ambientale (Italian Institute for Environmental Protection and Research (ISPRA)) and the Institute of Marine Sciences of the National Research Council of Italy (CNR-ISMAR).

Figure 2 shows the position of the TGs on the map of the Adriatic Sea region. Some of the TG records have been formed by collating partial records from different sources. Such TGs are marked by an asterisk. The individual positions of the TGs with respect to the twelve closest nodes of the

C3S altimetry grid are shown in **Figure 3**: note that some of the grid nodes are represented over land. This is an artifact of the gridding procedure that partially extrapolates over land the SLA field [36].

VEPTF is the shortest record in the set, as it started sea level recordings only in 1974. Nonetheless, its length is almost double that of the altimetry era, and abundantly double the period of the lunar nodal tide. To treat evenly all the TG records, we consider in situ sea level data from 1974 up to 2018 for all the TGs.

Plots of the in situ, as well as of the altimetry sea level anomaly monthly means observed at the six locations in the Adriatic Sea are reported in **Figure 4**: the seasonal and tidal signals have been removed from both the in situ and the altimetry datasets. The altimetry grid node associated to the TG time series has been chosen as the one whose time series has the higher correlation coefficient with the sea level time series of the TG, among the twelve grid nodes closest to the latter. All the sea level trend errors have been calculated considering serial correlation and are given with a 95% confidence interval.

The altimetry dataset used to represent sea level anomaly in **Figure 4** is C3S. The in situ and the remotely sensed sea level records are in good agreement, as the lowest Pearson's correlation coefficient between altimetry and TG sea level time series is 0.82 at the Rovinj station, while all the others reach values larger than 0.91.

However, in some period a marked difference between in situ and altimetry SLA are seen, as for example in VENEZIA during 2012–2019 (TG sea level higher than altimetry), which is also confirmed by the nearby TG of VEPTF and seems to interest in a lesser extent also TRIESTE and DUBROVNIK, and for ROVINJ in

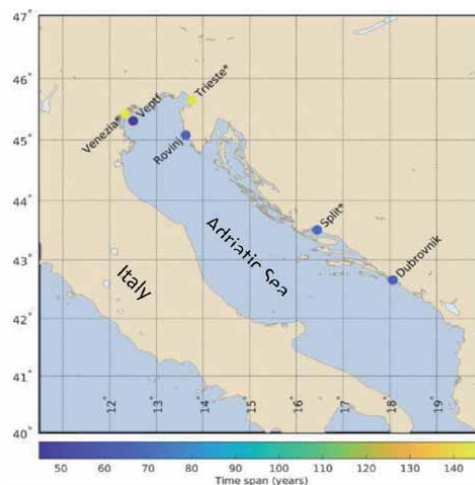


Figure 2. Positions of six tide gauges in Adriatic Sea. Color bar indicates length of available time series of sea level at tide gauges; shortest time series is about 50 years.

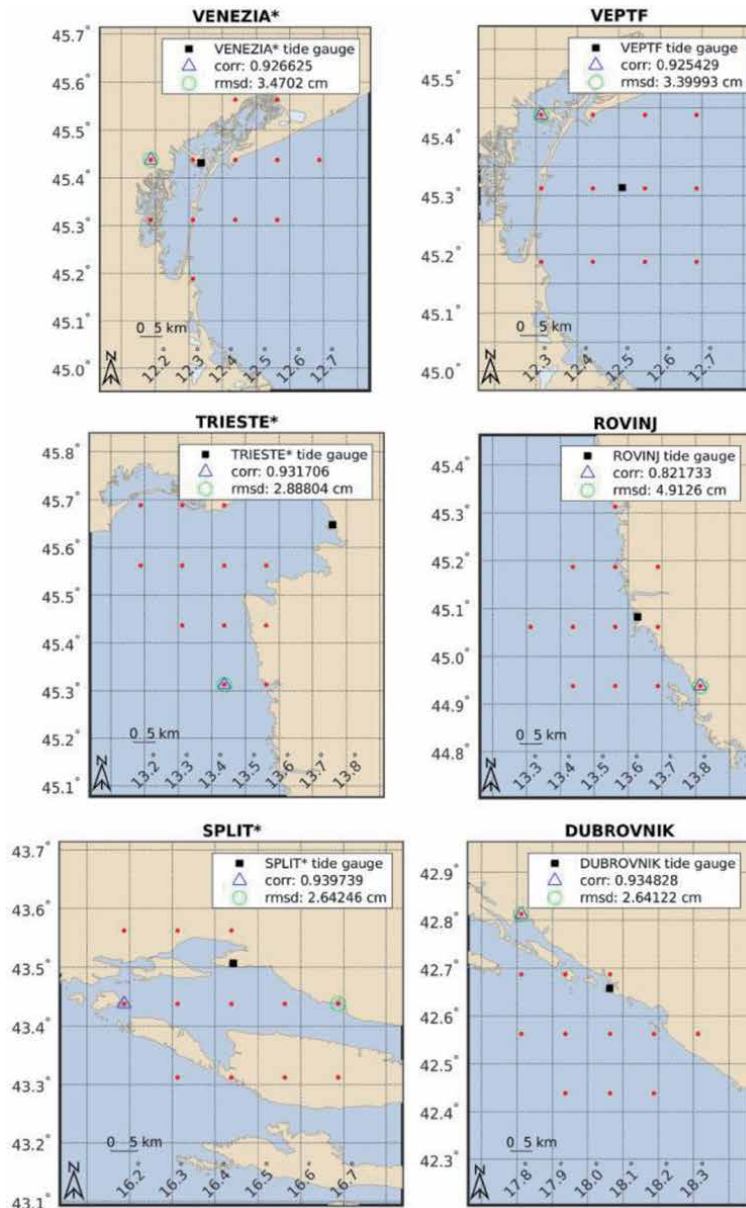


Figure 3. Geographical location of the six tide gauges and position of the twelve nearest grid points of C3S altimetry SLA. Tide gauges are marked by black squares. Altimetry grid nodes are red dots. Blue triangle marks the grid node with best correlation match. Also shown (green circle) the lowest root mean square difference of the TG and altimetry monthly time series.

2014–2015 (TG sea level lower than altimetry), and also SPLIT in 2002–2005 (TG higher than altimetry). On the other hand, common patterns are identified in all the records throughout the observation period.

Global positioning system (GPS) observations are synergistically included in our analysis. Several sources of GPS data, at different elaboration levels, are currently available online for geocentric surface velocity data and trends from continuous GPS (CGPS) stations at selected locations, in particular near TGs: Système d’Observation du Niveau des Eaux Littorales (SONEL)/Université La Rochelle (ULR) [62], Nevada Geodetic Laboratory (NGL, University of Nevada) [63]. Other

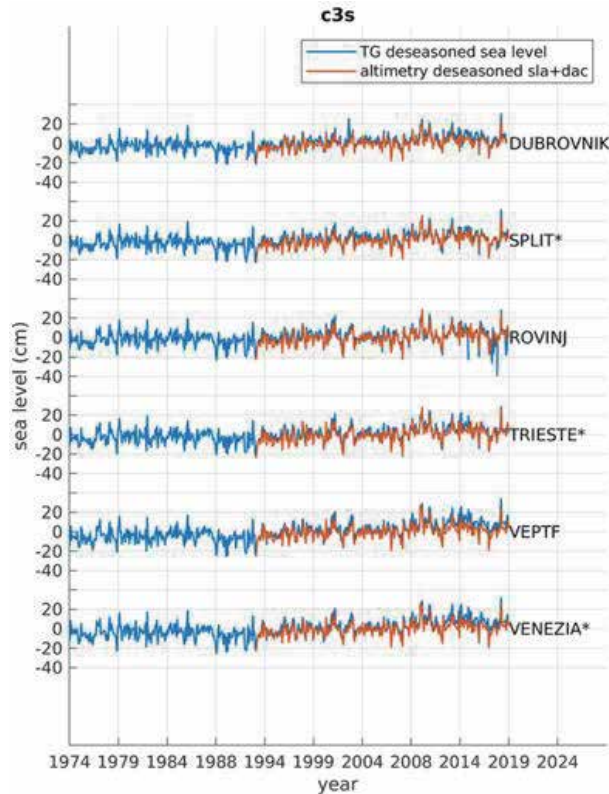


Figure 4. Plots of the sea level anomalies registered by tide gauges (1974–2018, in blue) and observed by the satellite altimetry (1993–2018, C3S dataset, in orange).

sources of information are available from local and national public agencies: in this study we used for the VENEZIA TG station also data acquired and processed by ISPRA at the PSAL tide gauge [64], which provides a relevant part of the VENEZIA sea level record. **Table 2** reports the vertical velocities registered at five of the six tide gauges considered in this study, with their time span and the values provided by one or more centers for the same TG by one or more GPS stations nearby.

GPS station	NGL (mm y ⁻¹) Span (yr)	SONEL (mm y ⁻¹) Span (yr)	ISPRA (mm y ⁻¹) Span (yr)	Distance from TG (Km)	Pooled Mean (mm y ⁻¹)
PSAL VENEZIA	-1.70 ± 0.80 2014–2020	—	-1.46 ± 0.09 2010–2015	0.01	-1.59 ± 0.65 2014–2020
TRIE TRIESTE	-0.52 ± 0.45 2003–2020	0.20 ± 0.26 2003–2013	—	6.97	-0.25 ± 0.52 2003–2020
PORE ROVINJ	-1.51 ± 1.03 2011–2021	—	—	16.62	-1.51 ± 1.03 2011–2021
SPLT SPLIT	0.45 ± 0.68 2004–2012	-0.25 ± 0.34 2004–2012	—	< 4.00	0.10 ± 0.64 2004–2012
DUBR+DUB2 DUBROVNIK	-1.83 ± 0.70 2000–2020	—	—	4.15	-1.83 ± 0.70 2000–2020

Table 2. Geocentric surface vertical velocities at three locations in the Adriatic Sea from GPS stations.

PSAL is almost co-located with the VENEZIA PUNTA DELLA SALUTE TG. For SPLIT, data from the CGPS station of SPLT were acquired. It is worth mentioning that SPLT is, with PSAL in VENEZIA, among the few CGPS co-located with TGs in the Adriatic Sea. The TRIE CGPS station is the nearest to the TRIESTE TG, but 6.9 km far from it, over a hill north-west of Trieste: for this reason, TRIE CGPS station cannot be considered co-located with the TRIESTE TG. Neither can the PORE CGPS station for ROVINJ be considered as such, and the DUBR and DUB2 CGPS stations in DUBROVNIK: PORE is located 16 km north of Rovinj along the coast, while DUBR and DUB2 are located 4 km away and 400 m in height.

With the data described so far, the VLM can be derived with the classical method, i.e. subtracting the TG RSLR from the ASLR observed by altimetry at the associated grid point. This approach, described in [43], allows to estimate the VLM separately at each location for which RSL and ASL records are available. The error associated to these estimates is drastically reduced when the linear trend of VLM is calculated by differencing the time series of the ASL and RSL, instead of combining the two errors of ASLR and RSLR as they were two independent measurements. From here on, all the errors on the sea level change rate are calculated according to this convention. The results of such approach are shown in **Table 3**: in column 1 appear the TG locations, in column 2 the ASLR derived by altimetry, in column 3 the RSLR derived by the TG, and in column 4 the VLM ($\dot{u}_i = \dot{g}_i - \dot{s}_i$) derived by differencing the time series of ASL and RSL monthly time series.

First of all we note that the error of the VLM estimates in the fourth column, obtained as standard error of the trend of the differenced time series (ASL-RSL) are much lower than that provided by the error propagation formula for the difference of the trend estimates of two statistically-independent time series, as in this case the error propagation formula would provide $\sigma_{gs} = \sqrt{\sigma_g^2 + \sigma_s^2}$, and in the VENEZIA case, for example, it would determine a standard error of 2.26 mm y^{-1} instead of the 0.65 mm y^{-1} resulting by calculating the trend and the standard deviation of the differentiated time series.

A second aspect worth to note is the independence of each VLM determination from all the others. That means if one of the VLM estimates is affected by large errors or relies on data of bad quality (RSL and/or ASL), it does not influence the evaluation of the others.

The third observation about the numbers reported in **Table 3** is that while the ASLR is almost constant at all sites of the Adriatic Sea considered in this study, the RSLR observed at the TGs are much more varied, determining VLM estimates going from -2.12 to $+2.30 \text{ mm y}^{-1}$. From one side, this means that the vertical velocity

Location	\dot{g} (mm y ⁻¹)	\dot{s} (mm y ⁻¹)	$(\dot{g} - \dot{s})$ (mm y ⁻¹)
VENEZIA	3.36 ± 1.45	5.15 ± 1.73	-1.79 ± 0.65
VEPTF	3.38 ± 1.46	5.50 ± 1.73	-2.12 ± 0.67
TRIESTE	3.75 ± 1.58	3.56 ± 1.66	0.18 ± 0.60
ROVINJ	3.33 ± 1.58	1.03 ± 1.85	2.30 ± 1.06
SPLIT	3.60 ± 1.36	2.92 ± 1.65	0.68 ± 0.63
DUBROVNIK	3.34 ± 1.22	3.79 ± 1.48	-0.45 ± 0.55

Table 3. Results of calculations using C3S altimetry dataset (1993–2018). Column 1 reports the TG location; columns 2 and 3 the absolute and relative sea level rates in the altimetry era; column 4 the VLM calculated with the classical approach (ALT-TG). All data are in mm y⁻¹.

field applicable to the Adriatic area is not constant, potentially revealing that different processes could be at the base of the observed crustal motions. From the other side, such numbers reveal also that the VLM is an essential parameter in sea level studies conducted mainly from tide gauge data. Thus, every methodology able to estimate the VLM at the TG is of extreme interest to correct the RSL observed at the TGs themselves, in particular where no geodetic measurements are available to estimate the VLM.

To conclude this section about the classical approach to VLM estimate from sea level data, we report a comparison of the two gridded altimetry datasets: C3S and SLCCI. To provide a fair comparison, both datasets have been limited to the same common period of temporal coverage: 1993–2015. The results of the classical approach to VLM estimate are given in **Table 4**.

Column 4 of **Table 4** reports the RSLR, which is common to both ways to calculate VLM, the classical and the LIPWC.. In columns 2 and 3, differences can be seen in the ASLR measured by C3S and SLCCI: the most notable refers to TRIESTE, which appears to observe an ASLR of 4.51 mm y^{-1} in the C3S dataset, and 3.42 mm y^{-1} in the SLCCI dataset: these numbers differ by more than 1 mm y^{-1} . The difference in ASLR for TRIESTE is reflected in the final VLM rate. Regardless the marked difference for TRIESTE, the other rates appear in good agreement between the two datasets, even if in general C3S supplies lower errors.

So far, we have shown the results of the classical approach to VLM determination from altimetry and tide gauge. From now on we present and analyze the results of the linear inverse problem with constraints, in the modified version which exploit a change of variable to disentangle the contribution of the ASLR from the system. To do so we examine only the results relative to the C3S dataset, for three reasons: first of all, the final results do not differ much between the two datasets; second, the C3S gridded product has an enhanced resolution in the Mediterranean Sea, and an appropriate regional processing; third, the C3S dataset has a time span longer than SLCCI, and most important, it is intended to be continuously updated in the future. VLM results derived with the LIPWC-COV approach are shown in **Table 5**, together with the values of the ASLR and RSLR values used for the calculation, and the VLM derived with the classical approach for ease of comparison.

The difference between the results obtained in the classical approach and the LIPWC-COV approach is evident; while the classical approach range of VLMs is $[-2.12 \text{ } 2.30] \text{ mm y}^{-1}$, that provided by LIPWC-COV is almost half as wide: $[-1.41 \text{ } 0.93]$. This is to the result of the introduction of the constraints in Eq. (7), which enter the linear system, propagating the structure and values of the relative vertical motion between the TGs in the solution. The effect of the constraints is best seen in

Location	\dot{g} C3S (mm y^{-1})	\dot{g} SLCCI (mm y^{-1})	\dot{s} (mm y^{-1})	$(\dot{g} - \dot{s})$ C3S (mm y^{-1})	$(\dot{g} - \dot{s})$ SLCCI (mm y^{-1})
VENEZIA	4.16 ± 1.71	4.47 ± 2.07	6.08 ± 2.08	-1.93 ± 0.79	-1.61 ± 0.91
VEPTF	4.17 ± 1.73	4.47 ± 2.07	6.44 ± 2.07	-2.27 ± 0.81	-1.97 ± 0.93
TRIESTE	4.51 ± 1.84	3.42 ± 1.78	4.49 ± 1.98	0.02 ± 0.71	-1.07 ± 0.74
ROVINJ	4.09 ± 1.85	4.37 ± 1.86	1.91 ± 2.04	2.18 ± 1.17	2.46 ± 1.04
SPLIT	4.44 ± 1.57	4.15 ± 1.48	4.15 ± 1.87	0.29 ± 0.70	0.00 ± 0.76
DUBROVNIK	4.01 ± 1.42	3.98 ± 1.45	4.67 ± 1.70	-0.66 ± 0.62	-0.69 ± 0.70

Table 4.
 VLM estimates from in situ RSL and remotely observed C3S and SLCCI ASL 1993-2015.

Location	\dot{g} (mm y ⁻¹)	\dot{s} (mm y ⁻¹)	$\dot{\xi}$ (mm y ⁻¹)	$(\dot{g} - \dot{s})$ (mm y ⁻¹)	LIPWC-COV (mm y ⁻¹)	GPS (mm y ⁻¹)
VENEZIA	3.36 ± 1.45	5.15 ± 1.73	3.26 ± 0.73	-1.79 ± 0.65	-0.93 ± 0.39	-1.59 ± 0.65
VEPTF	3.38 ± 1.46	5.50 ± 1.73	3.78 ± 0.73	-2.12 ± 0.67	-1.41 ± 0.47	—
TRIESTE	3.75 ± 1.58	3.56 ± 1.66	2.30 ± 0.67	0.18 ± 0.60	0.42 ± 0.33	-0.25 ± 0.52
ROVINJ	3.33 ± 1.58	1.03 ± 1.85	1.36 ± 0.71	2.30 ± 1.06	0.93 ± 0.37	-1.51 ± 1.03
SPLIT	3.60 ± 1.36	2.92 ± 1.65	2.20 ± 0.66	0.68 ± 0.63	0.37 ± 0.33	0.10 ± 0.64
DUBROVNIK	3.34 ± 1.22	3.79 ± 1.48	2.69 ± 0.58	-0.45 ± 0.55	-0.41 ± 0.46	-1.83 ± 0.70

Table 5.

VLM results using C₃S altimetry dataset (1993–2018). Location in column 1; ASLR in column 2; RSLR in the altimetry era (1993–2018) in column 3; RSLR 1974–2018 in column 4; VLM calculated with the classical approach in column 5, as in column 4 of Table 3, and with the LIPWC-COV in column 6. Column 7 reports the VLM values directly detected by the GPS stations associated with three TGs.

Figure 5, where the plot of the LIPWC-COV solution follows the general form of the classical solution, but with a reduced spread.

In Figure 5 are reported also the VLM values measured by the CGPS stations of PSAL (VENEZIA), TRIE (TRIESTE) and SPLT (SPLIT), and the values of VLM estimated by Wöppelmann and Marcos [50] with the LIPWC technique without the change of variable.

In the classical approach, as there is no optimization of errors as in the LIPWC technique, we see a wide spread of the VLM values. This is particularly evident for ROVINJ TG, whose $(\dot{g} - \dot{s})$ estimates reach more than 2 mm y⁻¹, while the LIPWC-COV approach calculates it as less than 1 mm y⁻¹. The LIPWC solution proposed by Wöppelmann and Marcos [50] presents much lower standard errors than LIPWC-COV solution described in this study. We presume that such low standard errors

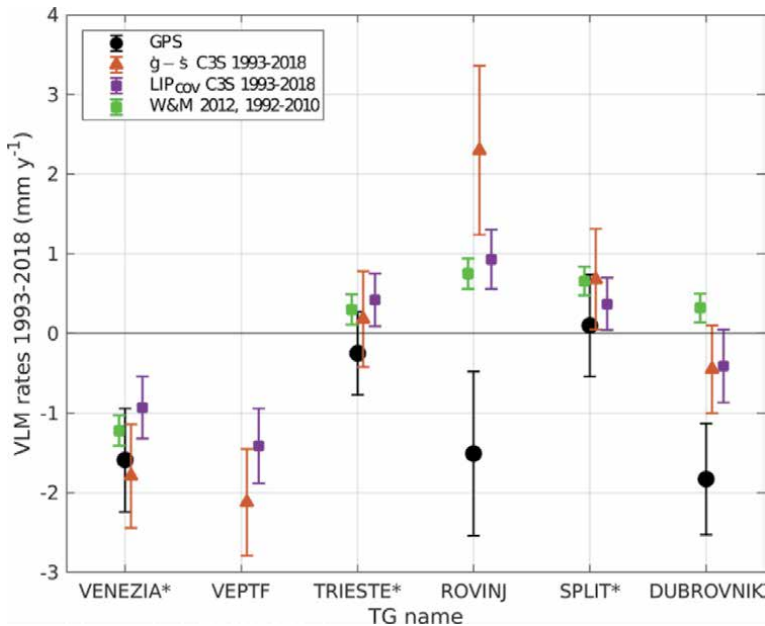


Figure 5.

Scatterplots of VLM values derived with the classical $(\dot{g} - \dot{s})$ and the LIPWC-COV approaches using the C₃S altimetry dataset (period 1993–2018). GPS estimates (in black) are also reported. Results from the study of Wöppelmann and Marcos (W&M) for the period 1992–2010 are shown in green for comparison. The zero level is drawn in black. (adapted from [58]).

were attained by a different methodology in calculating the rates of absolute and relative sea level change rates and their formal errors. Moreover, in the years following 2010 the VLM rates at the five common TG locations have remained substantially unmodified with respect to the Wöppelmann and Marcos' results. As a final step regarding VLM, we have calculated the root mean square difference (RMSD) of the VLM calculated with GPS and those calculated with the classical and the new (LIPWC-COV) approaches and found that the second one is lower: Classic approach: 1.84 mm y^{-1} ; LIPWC-COV approach: 1.34 mm y^{-1} .

The discrepancy observed between this study and that of Wöppelmann and Marcos can largely be ascribed to the different periods covered by the altimetry datasets (C3S and SLCCI datasets cover time periods respectively 44% and 23% longer than the study of Wöppelmann and Marcos). Other factors that may contribute to explain the difference between the results of the two studies are the processing of the altimetry data and the inclusion of the VEPTF TG in this study. The rates of absolute sea level change at the TGs, calculated as the sum of relative sea level change and VLMs derived in this study with the LIPWC-COV approach, for the whole period covered by the TG record, are reported in **Table 6**.

The uncertainty of the sample mean (last row of **Table 6**) was obtained as standard error of the sample mean, considering the rates as random and independent variables. The absolute sea level change rates vary in a very narrow interval, 2.33–2.71, with a sample mean of 2.43 mm y^{-1} . The standard deviation of the sample is much lower than the precision of each individual determination of SL change rate at the TGs. As pointed out by Wöppelmann and Marcos [50], such a low dispersion is unlikely to be determined from estimates of independent random variables: it is instead the evidence of the high performance of LIPWC method for determining accurate VLM rates from TG and altimetry differenced time series. The ASLR rates calculated by altimetry in 1993–2018 and through the LIPWC-COV technique (1974–2018) are shown in **Figure 6**.

Clearly, the ASLR values calculated for the longer period are smaller than those calculated in the shorter one, but the modulation of the rate from TG to TG is apparently reflected in the LIPWC-COV approach. As already noted, the errors associated to the ASLR rates derived in the LIPWC-COV are also smaller, thanks to the introduction of the constraints on the relative vertical land motion between paired TGs. The mean value of the ASLR calculated for the Adriatic Sea with the LIPWC-COV approach, is in general agreement with both regional studies on the Mediterranean Sea ($0.7 \pm 0.2 \text{ mm y}^{-1}$ (1945–2000) [65]; $1.60 \pm 0.35 \text{ mm y}^{-1}$ (1992–2010) [50]; $2.44 \pm 0.5 \text{ mm y}^{-1}$ (1993–2012) [66]; $2.87 \pm 0.33 \text{ mm y}^{-1}$ (1992–2016) [67]),

Location	$\xi\text{-VLM}_{LIPWC-COV}$
VENEZIA	2.33 ± 0.83
VEPTF	2.37 ± 0.86
TRIESTE	2.71 ± 0.75
ROVINJ	2.29 ± 0.80
SPLIT	2.57 ± 0.74
DUBROVNIK	2.28 ± 0.74
Pooled mean	2.43 ± 0.80
Sample mean	2.43 ± 0.18

Table 6. ASLR from TG records over whole period 1974–2018, corrected for VLM estimated with the LIPWC-COV approach. All data are in mm y^{-1} .

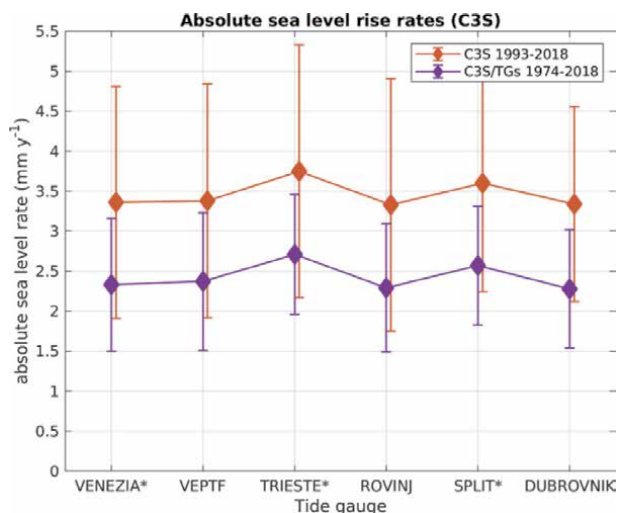


Figure 6.

Absolute sea level change rates as calculated by altimetry 1993–2018, and by the LIPWC-COV approach integrating data from TGs in 1974–2018.

and at global scale ($2.0 \pm 0.3 \text{ mm y}^{-1}$ (1971–2010) [68]; $3.0 \pm 0.7 \text{ mm y}^{-1}$ (1993–2010) [69]; $2.8 \pm 0.5 \text{ mm y}^{-1}$ (1993–2010) [68]; 3.1 mm y^{-1} (1992–2018) [32]).

Among the ASLR altimetry rates associated with the six TGs in the Adriatic Sea, those for TRIESTE are very different in the C3S and SLCCI dataset. In order to investigate such a large difference ($0.02 \pm 0.71 \text{ mm y}^{-1}$ SLCCI; $-1.07 \pm 0.74 \text{ mm y}^{-1}$ C3S; see **Table 4**) the SLCCI-AT X-TRACK/ALES 20 Hz along-track coastal altimetry dataset has been used.

The analysis focuses on the descending track 196 of the Jason-1 (2001–2013) and Jason-2 (2008–2019) altimetry missions and covers the period 2002–2016 with 532 cycles (from 22 Jan 2002 to 23 Jun 2016 at 350 m resolution along-track) with MSSH computed using cycles from 1 to 517. The position of the track 196 and the geographical setting are shown in **Figure 7**.

Altimetry data at the 71 observation points of track 196 are compared to 10' interval RSL observations of the TRIESTE TG. The TG time series did not undergo any filtering or processing, and the astronomical tide and Dynamic Atmospheric Correction (DAC) corrections are not applied to the altimetry time series.

The goal of the investigation is to explore the possible causes of the different ASLR rates obtained by the two gridded altimetry datasets near Trieste, to look for clues directly into the original along track data from the Jason missions, reprocessed with advanced and coastal specific re-tracking (ALES) and improved coastal processing (X-TRACK). We also want to ascertain the suitability of the new SLCCI-AT record in long term coastal sea level monitoring. We concentrated on the altimeter track 196 of the SLCCI-AT dataset, which first crosses Marano Lagoon and a 0.5 km wide sandbar before entering the Gulf of Trieste from north, near Grado, and then flies over Umag and the full extent of the Istria peninsula. The retrieval is particularly problematic in the gulf area due to the complex morphology of the land. Moreover, some data loss could be due to sea-to-land and land-to-sea crossings that might influence the behavior of the on-board tracker. Operational altimetry products do not provide data over this section of the Gulf of Trieste, while the SLCCI-AT dataset provides 71 points along track, most of which yield over 70% of valid data (blue box in **Figure 8**). The most improvement is near the Istrian peninsula with more than 90% of data recovered. The valid data percentages decrease abruptly over a distance ranging 5 km from the coast. The reduced performance over the

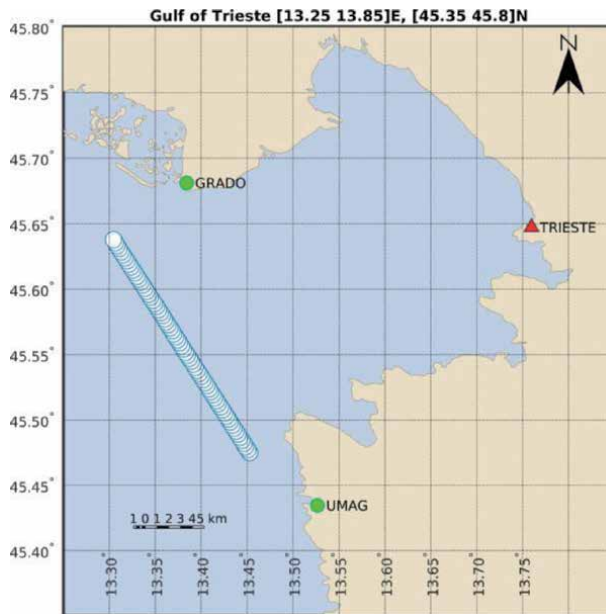


Figure 7. Gulf of Trieste. The positions of the SLCCI along-track 20 Hz altimetric product version 1.0 samples of the descending track 196 (white circles), and the TRIESTE TG stations (red triangle). Umag in Croatia and Grado in Italy are also shown (green circles).

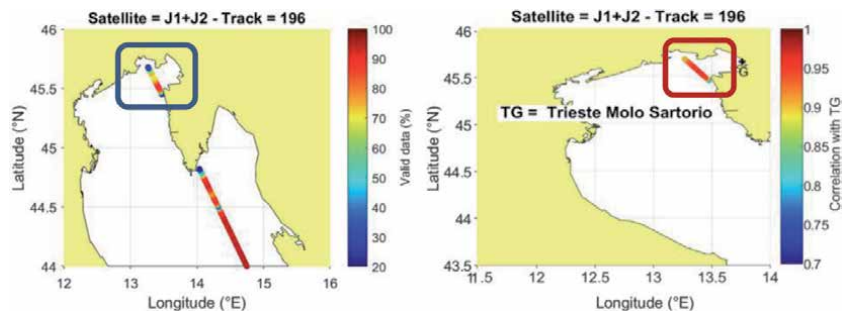


Figure 8. J1 + J2 track 196 geographical settings. Left: Percentage of valid data along the track. Right: Correlation with TRIESTE tide gauge. Adapted from the coastal sea level project of the ESA climate change initiative (SL_CCI bridging phase) document "Part II: Validation Results" (http://www.esa-sealevel-cci.org/webfm_send/588).

lagoon and islet (almost all data have been rejected) is probably related to the data corruption in the land-sea-transition. Note that at 1 Hz, any coastal altimetry along track product would give no more than 3–4 points along this 24 km long stretch of track 196.

The data accuracy can be assessed in more detail comparing the altimeter-derived 20-Hz SLA with corresponding tide gauge sea level measurements. It should be noted that the TRIESTE TG is located in the harbor, and therefore it does not measure exactly the same ocean dynamics as the altimeter flying offshore. Nonetheless, the Pearson's linear correlation coefficient of most of the 71 points along the section of track 196 facing the Trieste harbor exceeds 0.9 (red box in **Figure 8**). The RMS difference between altimetry observations and tide gauge measurements of instantaneous sea level is almost constant along the track 196 section in the Gulf of Trieste, and around 10 cm (not shown).

From the time series of SLCCI-AT SLA at each data point of the track 196 facing Trieste, we have calculated the slopes of the fitting lines, gradually growing the confidence interval from 68–95%, and performed Mann-Kendall statistical significance tests [70, 71] modified for autocorrelated data [72] on all the 71 fitting lines. The Mann-Kendall test is commonly employed to detect monotonic trends in time series. The null hypothesis is that the data come from a population with independent realizations and are identically distributed. The alternative hypothesis is that the data follow a monotonic trend. In **Figure 9** the results of such calculation are reported for a preliminary version of the SLCCI-AT dataset at 20 Hz. The black diamonds mark the acceptance or rejection of the null hypothesis following this scheme:

- 1 - the null hypothesis “the sample has no trend” is rejected.
- 0 - the null hypothesis “the sample has no trend” cannot be rejected.

Already with a 68% confidence interval the null hypothesis (the trend is not statistically significant) is rejected in less than 24% of the data points. With a 95% confidence interval only for four fitting lines out of 71 the null hypothesis is rejected. In both cases the errors associated to the slopes are higher than the slopes themselves.

A similar analysis replicated on the final version of the SLCCI-AT dataset, published at the end of the SLCCI project, gave better results. **Figure 10** reports the representation of the statistical characteristics of the slopes derived from the last version of the data of the SLCCI-AT X-TRACK/ALES SLA 20 Hz, with 95% confidence interval. The left panel shows slopes and associated errors at every data point latitude (low latitudes are near Umag, high latitudes near Grado); different colors indicate the statistical significance of the Mann-Kendall test (blue: significant; orange: not significant). The right panel shows the box and whisker plots of the two distributions (left: not significant; right: significant). The number of statistically significant slopes is much higher in the final version of the dataset, even if the variability is still rather high and difficult to explain because of the limited spatial variability along the track. Slopes are higher towards north (Grado), and lower near Umag. Considering only the statistically significant slopes in the SLCCI-AT dataset, their sample mean and standard deviation result to be $3.40 \pm 1.01 \text{ mm yr}^{-1}$ (Feb-2002 – Jun-2016) which is not far from the trends we have found in the Adriatic Sea at all the tide gauges. We recalculated the altimetry trends near TRIESTE in the

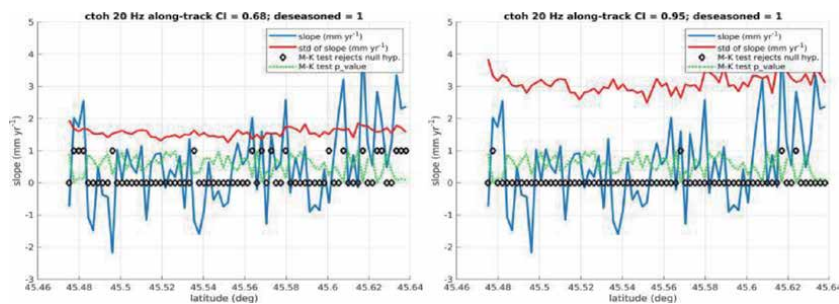


Figure 9. Slopes and slope errors of the lines fitting the time series of along track SLA at every data point of track 196 near Trieste. Also plotted the Mann-Kendall test results. Black diamonds: 1 - rejection of the null hypothesis (the sample has no trend); 0 - no rejection. Green line: p -value. Adapted from the coastal sea level project of the ESA climate change initiative (SL_CCI bridging phase) document “Part II: Validation Results” (http://www.esa-sea-level-cci.org/webfm_send/588).

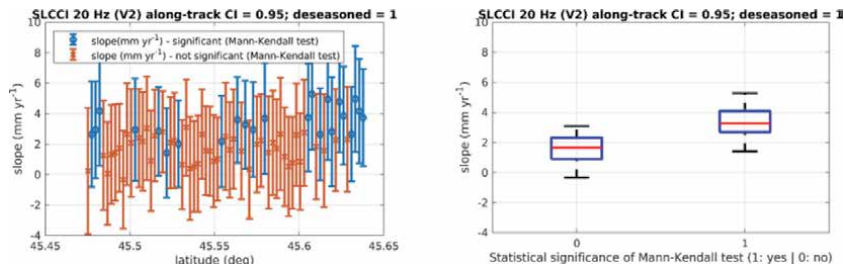


Figure 10. SLCCI SLA 20 Hz. Left: Slopes and slope errors of the lines fitting every data point of the track 196 in the Gulf of Trieste. Blue: Statistically significant slopes according to the Mann-Kendall test. Orange: Slopes not significant. Right: Box and whisker plots for the statistically significant and non-significant slopes. Red: Median value. Box: Upper and lower quartiles. Whiskers: Highest and lowest observations. Adapted from the coastal sea level project of the ESA climate change initiative (SL_CCI bridging phase) document “Part II: Validation Results” (http://www.esa-sealevel-cci.org/webfm_send/588).

ġ TRIESTE 2002–2016		
SLCCI-AT (mm y ⁻¹)	SLCCI (mm y ⁻¹)	C3S (mm y ⁻¹)
3.40 ± 1.01	3.66 ± 3.97	5.07 ± 3.64

Table 7. Trends for Trieste in February 2002 – June 2016 from SLCCI project and C3S altimetry. Column 1: SLCCI-AT along track 20 Hz product. Column 2: SLCCI gridded product. Column 3: C3S gridded product.

SLCCI and C3S gridded products. The altimetry ASLR trends found so far in the analysis are summarized in **Table 7**.

The trends calculated with the SLCCI dataset (along track and gridded) are in good agreement, apart from the different errors affecting the two results, due to the different methods used to calculate them. The C3S trend is instead higher than the other two. We believe that the difference between the results is to be ascribed to the different methodologies used in the two products. In any case the difference between the SLCCI and the C3S results is not yet explained by this further analysis, and the Gulf of Trieste remains a controversial place for the derivation of climatologically relevant oceanic variables from altimetry, because of the proximity of the land and the geometry of the surrounding coastline, and the very short time coverage of the altimetric datasets.

8. Summary and prospects

The sea level is a key variable of the climate system. Tide gauges measuring sea level variability are in operation since the 1900s. Satellite-based observations of sea level changes are more recent. Nevertheless, they play a crucial role in understanding the future coastal sea level changes. Advance in the processing of satellite radar altimetry have expanded the utility of this data set for climate-related studies and extended the potential exploitation in the coastal zone. The joint usage of the two different measuring systems (in situ and satellite) has two challenges. First how the two data sets can be consistently and systematically used in synergy to address that objective of estimating robust coastal sea level trends. Second how using high-rate (i.e. 20 Hz) altimeter measurements with a coastal-oriented processing could improve the satellite-based trend estimates with respect to the standard (1 Hz) data, especially near coast.

In this chapter, a more robust inverse method (called LIPWC-COV) has been proposed and tested in the Northern Adriatic Sea, where GPS data are available to conduct a realistic assessment of uncertainties. The results show that the classical approach of estimating VLMs provides less accurate trends than the LIPWC-COV method, and with lower errors. Moreover, the LIPWC-COV has demonstrated to compare better than the classic method with GPS derived VLMs.

In this chapter, the experimental SLCCI data set (high resolution along track) coastal sea level product (developed within SLCCI project) has been also assessed in the Gulf of Trieste, as it was possible only at that site. The retrieval is particularly problematic in the gulf area due to the complex morphology of the land. The trends calculated with the gridded and along track datasets show some differences, probably due to the different methodologies used in the generation of the products.

This study offers a more consolidated and improved understanding of the sea level trend variability in the Northern Adriatic Sea. The next step is to extend the application of the new methodology to the Mediterranean Sea.

Acknowledgements

The authors want to thank the European Space Agency, which propelled the Climate Change Initiative to produce a climate quality record of sea level from satellite altimetry. Likewise, the authors express gratitude to the European Union for making available the satellite altimetry data record through the Copernicus Earth Observation Programme Services. The authors also want to acknowledge Centro Previsioni e Segnalazioni Maree (CPSM) and Alvisè Papa for providing tide gauge data under the CNR-ISP/CPSM technical–scientific collaboration agreement 2019–2022; the CNES distribution service AVISO+ for the dynamic atmospheric correction data; the Italian Institute for Environmental Protection and Research (ISPRA) for providing tide gauge and GPS data; CNR-ISMAR and Fabio Raicich for the time series of the Trieste tide gauge; PSMSL, national Oceanographic Centre, Liverpool, UK, for making available the tide gauge global record. The authors thank the SONEL Data Centre and the Nevada Geodetic Laboratory (NGL) for processing and making available the GPS trend global record. Finally, we acknowledge CPSM for funding the “Vento da Satellite+” project on the development of satellite data in storm surge forecasting; ESA who funded the “HYDROCOASTAL” project (ESA contract No. 4000129872/20/I-DT), and the “SL_CCI Bridging Phase” project (ESA contract No. 4000109872/13/I-NB), from which some of the images in this chapter were adapted.

Author details

Stefano Vignudelli^{1*} and Francesco De Biasio²

1 National Research Council of Italy, Institute of Biophysics, Pisa, Italy

2 National Research Council of Italy, Institute of Polar Sciences and Ca' Foscari University, Venice, Italy

*Address all correspondence to: stefano.vignudelli@pi.ibf.cnr.it

IntechOpen

© 2021 The Author(s). Licensee IntechOpen. This chapter is distributed under the terms of the Creative Commons Attribution License (<http://creativecommons.org/licenses/by/3.0>), which permits unrestricted use, distribution, and reproduction in any medium, provided the original work is properly cited. 

References

- [1] IPCC, 2019. IPCC Special Report on the Ocean and Cryosphere in a Changing Climate [H.-O. Pörtner, D.C. Roberts, V. Masson-Delmotte, P. Zhai, M. Tignor, E. Poloczanska, K. Mintenbeck, A. Alegría, M. Nicolai, A. Okem, J. Petzold, B. Rama, N.M. Weyer (eds.), available online at <https://www.ipcc.ch/srocc/download-report/>
- [2] Herrera-García, G., Ezquerro, P., Tomás, R., Béjar-Pizarro, M., López-Vinielles, J., Rossi, M., ... and Ye, S. (2021). Mapping the global threat of land subsidence. *Science*, 371 (6524), 34-36, doi: 10.1126/science.abb8549.
- [3] Frederikse, T., Landerer, F., Caron, L., Adhikari, S., Parkes, D., Humphrey, V. W., ... and Wu, Y. H. (2020). The causes of sea-level rise since 1900. *Nature*, 584(7821), 393-397.
- [4] Li, L., Switzer, A. D., Wang, Y., Chan, C. H., Qiu, Q., and Weiss, R. (2018). A modest 0.5-m rise in sea level will double the tsunami hazard in Macau. *Science advances*, 4(8), eaat1180. doi: 10.1126/sciadv.aat1180
- [5] Taherkhani, M., Vitousek, S., Barnard, P. L., Frazer, N., Anderson, T. R., and Fletcher, C. H. (2020). Sea-level rise exponentially increases coastal flood frequency. *Nature Scientific reports*, 10, 6466, doi:10.1038/s41598-020-62188-4
- [6] Cavaleri, L., Bajo, M., Barbariol, F., Bastianini, M., Benetazzo, A., Bertotti, L., Chiggiato, J., Ferrarin, C., Trincardi, F., Umgiesser, G. (2020). The 2019 flooding of Venice and its implications for future predictions. *Oceanography*, 33(1), 42-49, doi:10.2307/26897834
- [7] Fice, J. L., and Scotti, A. (1990). The flood-prevention scheme of Venice: Experimental module. *Water and Environment Journal*, 4(1), 70-77, doi: 10.1111/j.1747-6593.1990.tb01559.x
- [8] Umgiesser, G. (2020). The impact of operating the mobile barriers in Venice (MOSE) under climate change. *Journal for Nature Conservation*, 54, 125783, doi: 10.1016/j.jnc.2019.125783
- [9] Lambeck, K., Anzidei, M., Antonioli, F., Benini, A., & Esposito, A. (2004). Sea level in Roman time in the Central Mediterranean and implications for recent change. *Earth and Planetary Science Letters*, 224(3-4), 563-575.
- [10] Marcos, M, Puyol, B, Amores, A, Pérez Gómez, B, Fraile, MÁ, Talke, SA. Historical tide gauge sea-level observations in Alicante and Santander (Spain) since the 19th century. *Geosci Data J.* 2021; 00: 000– 000. <https://doi.org/10.1002/gdj.3.112>
- [11] Stefan A. Talke and David A. Jay "Nineteenth Century North American and Pacific Tidal Data: Lost or Just Forgotten?," *Journal of Coastal Research* 29(6a), 118-127, (1 November 2013). <https://doi.org/10.2112/JCOASTRES-D-12-00181.1>
- [12] Riley, F. S. (1986). *Developments of borehole extensometry in Johnson. AI, Carbognin, Laura, and Ubertini, L., eds., Land subsidence: International Association of Hydrological Sciences Publication, (151), 939.*
- [13] Wang, G., & Soler, T. (2015). Measuring land subsidence using GPS: Ellipsoid height versus orthometric height. *Journal of surveying engineering*, 141(2), 05014004.
- [14] Ferretti, A., Colombo, D., Fumagalli, A., Novali, F., & Rucci, A. (2015). InSAR data for monitoring land subsidence: Time to think big. *Proceedings of the International Association of Hydrological Sciences*, 372, 331-334.
- [15] Wöppelmann, G., Miguez, B. M., Bouin, M. N., and Altamimi, Z. (2007).

Geocentric Sea-level trend estimates from GPS analyses at relevant tide gauges world-wide. *Global and Planetary Change*, 57(3–4), 396–406.

[16] Woodworth, P. L., Wöppelmann, G., Marcos, M., Gravelle, M., and Bingley, R. M. (2017). Why we must tie satellite positioning to tide gauge data. *Eos*, 98(4), 13–15.

[17] Crosetto, M., Monserrat, O., Cuevas-González, M., Devanthy, N., and Crippa, B. (2016). Persistent scatterer interferometry: A review. *ISPRS Journal of Photogrammetry and Remote Sensing*, 115, 78–89.

[18] Vignudelli, S., Birol, F., Benveniste, J., Fu, L. L., Picot, N., Raynal, M., and Roinard, H. (2019). Satellite altimetry measurements of sea level in the coastal zone. *Surveys in geophysics*, 40(6), 1319–1349, doi: 10.1007/s10712-019-09569-1.

[19] Passaro, Marcello & Cipollini, Paolo & Vignudelli, S. & Quartly, Graham & Snaith, Helen. (2014). ALES: A multi-mission adaptive subwaveform retracker for coastal and open ocean altimetry. *Remote Sensing of Environment*. 145. 173–189. 10.1016/j.rse.2014.02.008.

[20] Fernandes, M. J., Lázaro, C., and Vieira, T. (2020) On the role of the troposphere in satellite altimetry. *Remote Sensing of Environment*, 252, 112149, doi:10.1016/j.rse.2020.112149.

[21] Stammer, D., Ray, R. D., Andersen, O. B., Arbic, B. K., Bosch, W., Carrère, L., ... & Yi, Y. (2014). Accuracy assessment of global barotropic ocean tide models. *Reviews of Geophysics*, 52(3), 243–282.

[22] Andersen, O. B., Zhang, S., Sandwell, D. T., Dibarboure, G., Smith, W. H., & Abulaitjiang, A. (2021). The unique role of the Jason geodetic missions for high resolution gravity field

and mean sea surface modelling. *Remote Sensing*, 13(4), 646.

[23] Carrere, L., Faugère, Y., & Ablain, M. (2016). Major improvement of altimetry sea level estimations using pressure-derived corrections based on ERA-interim atmospheric reanalysis. *Ocean Science*, 12(3), 825–842.

[24] Fernandes, M. J., Brown, S., Obligis, E., Lazaro, C., and Nunes, A. L. (2013). An inter-comparison between algorithms for wet path delay retrieval in the coastal regions. *ESASP*, 710, 58.

[25] Lázaro, C., Fernandes, M. J., Vieira, T., and Vieira, E. (2019). A coastally improved global dataset of wet tropospheric corrections for satellite altimetry. *Earth System Science Data Discussions*, 1–31, doi 10.5194/essd-2019-171.

[26] Roblou, L., Lamouroux J., Bouffard J., Lyard F., Le Hénaff M., Lombard A., Marsaleix P., De Mey P., and Birol F. (2010). Post-processing altimeter data toward coastal applications and integration into coastal models, in *Coastal Altimetry* (Editors Vignudelli S., Cipollini P., Kostianoy A., Benveniste J.) pp. 217–246, Springer, Berlin, doi:10.1007/978-3-642-12796-0_5.

[27] Gómez-Enri, J., Vignudelli, S., Cipollini, P., Coca, J., and González, C. J. (2018). Validation of CryoSat-2 SIRAL Sea level data in the eastern continental shelf of the Gulf of Cadiz (Spain). *Advances in Space Research*, 62(6), 1405–1420, doi: 10.1016/j.asr.2017.10.042

[28] Birol F., Fuller N., Lyard F., Cancet M., Nino F., Delebecque C., Fleury S., Toublanc F., Melet A., Saraceno M., Léger F. (2017). Coastal applications from nadir altimetry: Example of the X-TRACK regional products. *Adv Space Res* 59(4):936–953, doi: 10.1016/j.asr.2016.11.005

- [29] Scharroo, R., Bonekamp, H., Ponsard, C., Parisot, F., von Engeln, A., Tahtadjiev, M., ... and Montagner, F. (2016). Jason continuity of services: Continuing the Jason altimeter data records as Copernicus Sentinel-6. *Ocean Science*, 12(2), 471-479, doi: 10.5194/os-12-471-2016
- [30] Scharroo, R., Leuliette, E. W., Lillibridge, J. L., Byrne, D., Naeije, M. C. and Mitchum, G. T. (2013). RADS: Consistent multi-mission products. In proceedings of the symposium on 20 years of Progress in radar altimetry, Venice, 20–28 September 2012. European Space Agency special publication, SP-710, 1–4.
- [31] Prandi, P., Meyssignac, B., Ablain, M., Spada, G., Ribes, A., and Benveniste, J. (2021) Local sea level trends, accelerations and uncertainties over 1993–2019. *Scientific Data*, 8(1), 1-12, doi: doi.org/10.6084/m9.figshare.13297757
- [32] Cazenave, A., Hamlington, B., Horwath, M., Barletta, V. R., Benveniste, J., Chambers, D., Döll, P., Hogg, A. E., Legeais, J. F., Merrifield, M., Meyssignac, B., Mitchum, G., Nerem, S., Pail, R., Palanisamy, H., Paul, F., von Schuckmann, K., and Thompson, P. (2019). Observational requirements for long-term monitoring of the global mean sea level and its components over the altimetry era. *Frontiers in Marine Science*, 6, 582. <https://doi.org/10.3389/fmars.2019.00582>.
- [33] Legeais, J.F., Ablain, M., Zawadzki, L., Zuo, H., Johannessen, J.A., Scharffenberg, M.G., Fenoglio-Marc, L., Fernandes, M.J., Andersen, O.B., Rudenko, S. and Cipollini, P., 2018. An improved and homogeneous altimeter sea level record from the ESA climate change initiative. *Earth System Science Data*, 10(1), 281-301, doi:10.5194/essd-10-281-2018.
- [34] SLCCI Project consortium, (2016). Time series of Gridded Sea level anomalies (SLA) v2.0, European Space Agency, Rome, Italy, doi:10.5270/esa-sea_level_cci-MSLA-1993_2015-v_2.0-201612.
- [35] Bell, B., Hersbach, H., Berrisford, P., Horányi, A., Muñoz-Sabater, J., Nicolas, J., ... and Soci, C. (2020). Satellite observations in support of the Copernicus Climate Change Service. In *Space, Satellites, and Sustainability* (Vol. 11527, p. 115270C). International Society for Optics and Photonics, doi: 10.1117/12.2576497.
- [36] Mertz, F., Legeais, J.-F., (2020). Product User Guide and Specification Sea Level v1.2, ECMWF, Shinfield Park, UK, 2020, p. 31.
- [37] Benveniste, J., Birol, F., Calafat F., Cazenave A., Dieng H., Gouzenes Y., Legeais J. F., Léger F., Niño F., Passaro M., Schwatke C., and Shaw A. (2020). Coastal Sea level anomalies and associated trends from Jason satellite altimetry over 2002–2018. *Sci Data* 7, 357 (2020). <https://doi.org/10.1038/s41597-020-00694-w>
- [38] Birol, F., Léger, F., Passaro, M., Cazenave, A., Niño, F., Calafat, F., Shaw, A., Legeais, J.F., Gouzenes, Y., Schwatke, C. J., and Benveniste J. (2021). The X-TRACK/ALES multi-mission processing system: New advances in altimetry towards the coast. *Advances in Space Research*, 67 (8), 2398-2415, doi:10.1016/j.asr.2021.01.049.
- [39] Fernandes, M., and Lázaro, C. (2016). GPD+ wet tropospheric corrections for CryoSat-2 and GFO altimetry missions. *Remote Sensing*, 8 (10), 851. MDPI AG. Retrieved from <http://dx.doi.org/10.3390/rs8100851>.
- [40] Lyard, F. H., Allain, D. J., Cancet, M., Carrère, L., and Picot, N. (2020). FES2014 global ocean tides atlas: Design and performances, *Ocean Sci. Discuss.* [preprint], <https://doi.org/10.5194/os-2020-96>, in review.

- [41] Visser, H., Dangendorf, S., and Petersen, A. C. (2015). A review of trend models applied to sea level data with reference to the “acceleration-deceleration debate”. *Journal of Geophysical Research: Oceans*, 120(6), 3873–3895.
- [42] Weatherhead, E. C., Reinsel, G. C., Tiao, G. C., Meng, X. L., Choi, D., Cheang, W. K., Keller, T., DeLuisi, J., Wuebbles, D. J., Kerr, J. B., Miller, A. J., Oltmans, S. J., and Frederick, J. E. (1998). Factors affecting the detection of trends: Statistical considerations and applications to environmental data, *J. Geophys. Res.* 103, 17149–17161, doi: 10.1029/98JD00995
- [43] Cazenave, A., Dominh, K., Ponchaut, F., Soudarin, L., Cretaux, J. F., and Le Provost, C. (1999). Sea level changes from Topex-Poseidon altimetry and tide gauges, and vertical crustal motions from DORIS. *Geophysical Research Letters*, 26(14), 2077–2080. <https://doi.org/10.1029/1999GL900472>.
- [44] Fenoglio-Marc, L., Dietz, C., and Groten, E. (2004). Vertical land motion in the Mediterranean Sea from altimetry and tide gauge stations. *Marine Geodesy*, 27(3–4), 683–701, doi: 10.1080/01490410490883441
- [45] Kleinherenbrink, M., Riva, R., and Frederikse, T. (2018). A comparison of methods to estimate vertical land motion trends from GNSS and altimetry at tide gauge stations. *Ocean Science*, 14(2), 187–204, 10.5194/os-14-187-2018
- [46] Nerem, R. S., and Mitchum, G. T. (2002). Estimates of vertical crustal motion derived from differences of TOPEX/POSEIDON and tide gauge sea level measurements. *Geophysical Research Letters*, 29(19), 40–41, doi: 10.1029/2002GL015037
- [47] Ray, R. D., Beckley, B. D., and Lemoine, F. G. (2010). Vertical crustal motion derived from satellite altimetry and tide gauges, and comparisons with DORIS measurements. *Advances in Space Research*, 45(12), 1510–1522, doi: 10.1016/j.asr.2010.02.020
- [48] Kuo, C. Y., Shum, C. K., Braun, A., and Mitrovica, J. X. (2004). Vertical crustal motion determined by satellite altimetry and tide gauge data in Fennoscandia. *Geophysical Research Letters*, 31, L01608, doi:10.1029/2003GL019106
- [49] Kuo, C. Y., C. K. Shum, A. Braun, K. C. Cheng, and Y. Yi (2008), Vertical motion determined using satellite altimetry and tide gauges, *Terr. Atmos. Ocean. Sci.*, 1(2), 21–35, 10.3319/TAO.2008.19.1-2.21(SA)
- [50] Wöppelmann, G., and Marcos, M. (2012). Coastal Sea level rise in southern Europe and the nonclimate contribution of vertical land motion. *Journal of Geophysical Research*, 117, C01007, doi: 10.1029/2011JC007469
- [51] Fadil, A., Denys, P., Tenzer, R., Grenfell, H. R., and Willis, P. (2013). New Zealand 20th century sea level rise: Resolving the vertical land motion using space geodetic and geological data. *Journal of Geophysical Research*, 118, 6076–6091, doi:10.1002/2013JC008867
- [52] Santamaría-Gómez, A., Gravelle, M., and Wöppelmann, G. (2014). Long-term vertical land motion from double-differenced tide gauge and satellite altimetry data. *Journal of Geodesy*, 88(3), 207–222, doi: 10.1007/s00190-013-0677-5
- [53] Iz, H. B., Shum, C. K., and Yang, T. Y. (2020). Conflation of satellite altimetry and tide gauge records at coast. *Journal of Geodetic Science*, 10(1), 62–68, doi:10.1515/jogs-2020-0113
- [54] Trupin, A., and Wahr, J. (1990). Spectroscopic analysis of global tide gauge sea level data. *Geophysical Journal International*, 100(3), 441–453., doi: 10.1111/j.1365-246X.1990.tb00697.x

- [55] Woodworth, P. L. (2012). A note on the nodal tide in sea level records. *Journal of Coastal Research*, 280, 316–323, doi: 10.2112/JCOASTRES-D-11A-00023.1
- [56] Menke, W. (1989). *Geophysical Data Analysis: Discrete Inverse Theory* (1st Ed., Vol. 45). Academic Press, Inc.
- [57] White, H. (1980). A Heteroskedasticity-consistent covariance matrix estimator and direct test for Heteroskedasticity. *Econometrica*, 48, 817–838, doi:10.2307/1912934
- [58] De Biasio, F., Baldin, G., and Vignudelli, S. (2020). Revisiting vertical land motion and sea level trends in the Northeastern Adriatic Sea using satellite altimetry and tide gauge data. *Journal of Marine Science and Engineering*, 8(11), 949. <https://doi.org/10.3390/jmse8110949>.
- [59] Lewis-Beck, M. S. (1980). *Applied Regression. An Introduction*. Newbury Park: Sage Publications.
- [60] Sekulić, B., Sondi, I., (1997). Koliko je Jadran doista opterećen antropogenim i prirodnim unosom tvari? [to what extent is the Adriatic Sea actually burdened with man-induced and natural inflow of substances]. *Hrvatski Geografski Glasnik* (in Croatian). Croatian geographic society. 59 (1). ISSN 1331-5854
- [61] Holgate, S.J.; Matthews, A.; Woodworth, P.L.; Rickards, L.J.; Tamisiea, M.E.; Bradshaw, E.; Foden, P. R.; Gordon, K.M.; Jevrejeva, S.; Pugh, J., (2013). New data systems and products at the permanent Service for Mean sea Level. *J. Coast. Res.*, 29, 493–504, doi: 10.2112/JCOASTRES-D-12-00175.1
- [62] Sonel, Université La Rochelle. (n. d.). GPS portal Sonel. Retrieved July 28, 2020, from <https://www.sonel.org/-GPS-.html>.
- [63] Blewitt, G.; Hammond, W.; Kreemer, C., (2018). Harnessing the GPS data explosion for interdisciplinary science. *Eos*, 99, doi:10.1029/2018EO104623.
- [64] Baldin, G.; Crosato, F. (2017). *L'innalzamento del Livello Medio del Mare a Venezia: Eustatismo e Subsidenza; Quaderni—Ricerca Marina; ISPRA—Istituto Superiore per la Protezione e la Ricerca Ambientale*: Rome, Italy, 2017.
- [65] Calafat, F. M., and Gomis, D. (2009). Reconstruction of Mediterranean Sea level fields for the period 1945–2000. *Global and Planetary Change*, 66(3–4), 225–234. <https://doi.org/10.1016/j.gloplacha.2008.12.015>.
- [66] Bonaduce, A., Pinardi, N., Oddo, P., Spada, G., and Larnicol, G. (2016). Sea-level variability in the Mediterranean Sea from altimetry and tide gauges. *Climate Dynamics*, 47(9), 2851–2866. <https://doi.org/10.1007/s00382-016-3001-2>.
- [67] Grgić, M., Nerem, R. S., and Bašić, T. (2017). Absolute sea level surface Modeling for the Mediterranean from satellite altimeter and tide gauge measurements. *Marine Geodesy*, 40(4), 239–258. <https://doi.org/10.1080/01490419.2017.1342726>.
- [68] Church, J. A., and White, N. J. (2011). Sea-level rise from the late 19th to the early 21st century. *Surveys in Geophysics*, 32(4–5), 585–602. <https://doi.org/10.1007/s10712-011-9119-1>.
- [69] Hay, C. C., Morrow, E., Kopp, R. E., and Mitrovica, J. X. (2015). Probabilistic reanalysis of twentieth-century sea-level rise. *Nature*, 517(7535), 481–484. <https://doi.org/10.1038/nature14093>.
- [70] Kendall, M. G. (1975) - *Rank Correlation Methods*, 4th ed. Charles Griffin, London.
- [71] Mann, H. B. (1945) - *Nonparametric tests against trend*. *Econometrica*:

Journal of the Econometric Society,
245–259.

[72] Khaled H. Hamed, A. Ramachandra Rao, (1998). A modified Mann-Kendall trend test for autocorrelated data, *Journal of Hydrology*, 204, 1–4, 182-196, DOI: 10.1016/S0022-1694(97)00125-X.

Beyond Mapping Functions and Gradients

Jean-Pierre Barriot and Peng Feng

Abstract

Mapping functions and gradients in GNSS and VLBI applications were introduced in the sixties and seventies to model the microwave propagation delays in the troposphere, and they were proven to be the perfect tools for these applications. In this work, we revisit the physical and mathematical basis of these tools in the context of meteorology and climate applications and propose an alternative approach for the wet delay part. This alternative approach is based on perturbation theory, where the base case is an exponential decay of the wet refractivity with altitude. The perturbation is modeled as a set of orthogonal functions in space and time, with the ability to separate eddy-scale variations of the wet refractivity.

Keywords: GNSS meteorology, positioning, VLBI, deep space tracking, neutral delays, mapping functions, gradients

1. Introduction

The effect of the Earth atmosphere on the propagation of light was noticed just after the invention of the telescope by Galileo Galilei, and tables of atmospheric refraction (bending of ray lights) were already available in the XVII century. After the advent of VLBI observations in the fifties and the launch of the first Earth satellite in the sixties, the modeling of the time delays caused by the neutral atmosphere became a necessity.

The current mathematical structure of the modeling of the propagation time delays, used in almost all GNSS software is given by [1].

$$\begin{aligned} \delta L(e_0) = m_h(e_0) [L_z^h + \cot g(e_0)(G_N^h \cos(\varnothing) + G_E^h \sin(\varnothing))] \\ + m_w(e_0) [L_z^w + \cot g(e_0)(G_N^w \cos(\varnothing) + G_E^w \sin(\varnothing))] \end{aligned} \quad (1)$$

where δL is the slant (extra) delay with respect to propagation in vacuum along the bended ray, L_z^h and L_z^w are the hydrostatic and wet zenith delays, e_0 and \varnothing are the satellite elevation and azimuth angles as seen from the station, respectively; G_N^h and G_N^w , G_E^h and G_E^w are the north and east components of the hydrostatic and wet delays gradients; m_h and m_w are the hydrostatic and wet mapping functions. Eq. (1) is used in precise GNSS processing software through the modeling of the phase signal [2–4].

The mapping functions “map” the so-called slant neutral atmosphere (extra) delay δL (i.e. the delay along the bended ray from the observer to the emitter) to two “zenithal delays”, named hydrostatic delay (very often improperly called “dry”

delay) L_z^h and wet delay L_z^w , essentially caused by the water vapor. The mapping functions are usually written [5] in the form of continuous fractions, that were introduced by Marini [6, 7] and normalized by Herring [8] in the form

$$m(e_0) = \frac{1 + \frac{a}{1 + \frac{b}{1+c}}}{\sin(e_0) + \frac{a}{\sin(e_0) + \frac{b}{\sin(e_0)+c}}} \quad (2)$$

Other (simplified) forms of the mapping functions can be found in the literature [9], but the mainstream form is always Eq. (2). The gradients themselves, noted by the upper case letter G in Eq. (1) were introduced to compensate azimuthal anisotropic effects [10–12].

For the last thirty years, the improvements on these formulas mainly focused on better and better determinations of the coefficients a , b , c , by comparisons of these formulas with ray tracing. The literature acknowledges as “best” models the VMF1 and VMF3 families, with some seasonally adjusted coefficients constrained from ray-tracing results with respect to Numerical Weather Models (NWM) [13, 14].

The role of the water vapor in the neutral delay is important, as it can be up to 20% (about 45 cm of the zenithal delay L_z^w), with respect to the total zenithal delay $L_z^h + L_z^w$ (about 2.3 m). The other gases, including carbon dioxide, have a negligible role in the neutral delay [9, 15], thus cannot be detected through GNSS processing.

Water is present in its three phases on Earth atmosphere, hydrosphere and continents: solid, liquid and water vapor, with important latent heats between phases. Water vapor in the atmosphere has large sources (evaporation, evapotranspiration) and sinks (rain, snow). Water vapor is also the most important greenhouse gas (beyond carbon dioxide) and the driver of cloud coverage. To describe the water cycle [16] is therefore of the uttermost importance, as evidenced by the so-called Energy Balance models [17, 18] that can be written

$$C_1 S_0 (1 - \alpha) = C_2 \frac{dT}{dt} + C_3 T^4 (1 - \beta) \quad (3)$$

Where S_0 is the solar constant (1360 W/m^2), T is the mean temperature on the Earth surface in Kelvin, t is the time. C_1 , C_2 and C_3 are constants.

The coefficients α and β are albedos, respectively in the visible and infrared wavelengths, both mainly driven by the water vapor contents of the Earth atmosphere [19]. The coefficient α reflects the cloud coverage, typically today at the 30% level, and the coefficient β is an infrared albedo, keeping our planet warm at around 15°C . Without the greenhouse gases, our planet will be at a freezing mean temperature of -18°C . They have antagonist effects, an increase of α means a cooling of Earth surface, and an increase of β means a warming, with a lot of intricacies between the positive and negative feedbacks related to the water vapor cycle of the climate models [20]. The ultimate goal of global long-term climate models [21] is to predict which effect will prevail (this is the dT/dt term in the right side of Eq. (3)).

The study [22] highlights the difficulty of measuring atmospheric water vapor with sufficient spatial and temporal resolution, and with sufficient accuracy, to provide observational constraints. GNSS processing is not the only source of water vapor data in the atmosphere. Remote sensing by satellites is the main provider [23], but the resolution of their data sets is limited by the distance between the satellites and the Earth and their orbital cycles. Besides, satellites are expensive. GNSS receivers, even precise ones, are a lot cheaper, and can provide long-term time series with high temporal resolution. Other ground-based instruments are

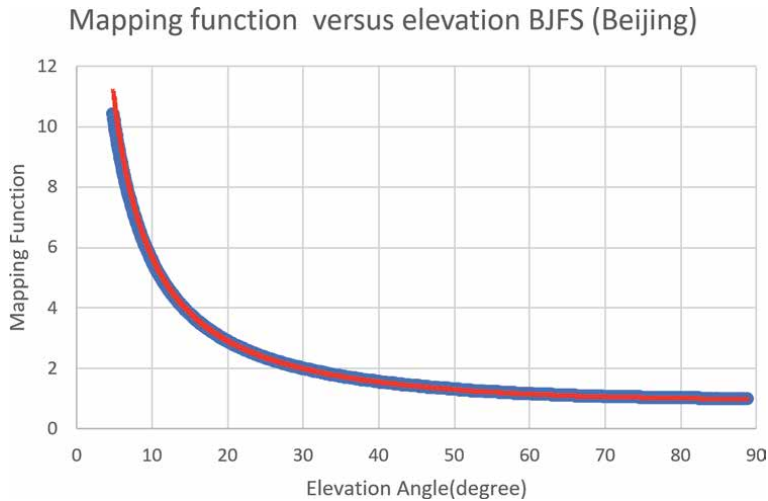


Figure 1. The mapping functions m_h (blue) and m_w (red) plotted against each other for a typical GNSS station in Beijing (latitude: 39.6086° N, longitude: 115.8922° E), winter time on January 16th, 2012, with the VMF1 model [13], parameterized by inputting data from the ECMWF numerical weather model EAR-40 [31].

mainly lidars [24], photometers [25], and water vapor radiometers [26]. The only source providing *in situ* meteorological data are the radiosondes [27], launched twice per day in a limited amount of worldwide sites. Many studies have been devoted to the causal relationship between water vapor and rain [28, 29], including extreme events [30].

It is therefore important to separate the water vapor modeling coefficients L_z^w , G_N^w and G_E^h from the hydrostatic coefficients L_z^h , G_N^h and G_E^h in Eq. (1). But this is easier said than done, as the functions $m_h(e_0)$ and $m_w(e_0)$ in Eq. (1) have almost the same dependence on the elevation angle e_0 (see **Figure 1**).

2. Basic assumptions at the core of the definition of mapping functions and gradients

Mapping functions, as they were introduced by Marini [6, 32] are based on the assumption of a totally layered atmosphere. This means that the refractivity n is only a function of height (the exact meaning of the word height is related to the definition of geoid). The ray equation of radio waves (including light) obeys, in the spherical approximation and again for a totally layered atmosphere (dependence on geocentric radius r of the refractivity n), the prime integral relation

$$n(r) r \cos(e) = n(r_0)r_0 \cos(e_0) \quad (4)$$

where r is the geocentric radius, r_0 is the geocentric radius at the receiver location, $n(r)$ is the refractivity at geocentric radius r , e is the angle between the tangent to the bended ray and the local horizon (the plane perpendicular to the direction of r at height r). e_0 is the elevation angle of the tangent of the bended ray at the receiver location.

The details of the computation of the ray path can be found in [6, 33, 34]. The refractivity of the atmosphere is a function of pressure, temperature and water vapor contents. A formula widely used is the Smith and Weintraub formula [35], derived for laboratory conditions (air perfectly mixed), as

$$(n - 1) = K_1 \frac{P_d}{T} + K_2 \frac{e}{T} + K_3 \frac{e}{T^2} \quad (5)$$

where P_d is the partial pressure of dry air in millibars, T is the temperature in Kelvin, e is the partial pressure of water vapor. K_1, K_2 and K_3 are constants. The P_d term corresponds to the “dry” part of the refractivity, the e terms correspond to the “wet” part of the refractivity. Many authors have improved the coefficients K_1, K_2 and K_3 year after year [15, 36, 37].

This formula can be easily rewritten as

$$(n - 1) = K'_1 \frac{P}{T} + K'_2 \frac{e}{T} + K_3 \frac{e}{T^2} \quad (6)$$

Where $P = P_d + e$. This rewriting, where the first term is denominated as the hydrostatic component of the refractivity, was proposed by Davis et al. [7] and then has been widely accepted, but led to a track of confusion in the literature between the meaning of “hydrostatic” and “dry”. The word “hydrostatic” has specifically no meaning in Eq. (6), other than indicating that the total pressure is used instead of the partial pressure of the non-wet (dry) air, as in Eq. (5). The word “hydrostatic” has a precise meaning in numerical weather models [38], where it indicates that the equilibrium of an air column is a balance between the vertical pressure gradient and the buoyancy forces, neglecting convective processes [39] as a simplification of the Navier–Stokes primitive Equations [40]. This is also the assumption made in the Saastamoinen model of the atmosphere propagation delays [41], with the total pressure P at ground level taken as a parameter (and with also the assumption of an atmosphere “at rest”).

To a good degree of approximation, the refractivity of air obeys a twofold exponential formula [42].

$$n(r) = 1. + \delta n_h + \delta n_w = 1. + N_h \exp\left(\frac{r - r_0}{H_h}\right) + N_w \exp\left(\frac{r - r_0}{H_w}\right) \quad (7)$$

The terms N_h, H_h and N_w, H_w have, respectively, a value of $250 \cdot 10^{-6}$, 8.7 km, $128 \cdot 10^{-6}$ and 2.7 km for the location of our geodesy observatory in Tahiti (from the fit of radiosounding data over a typical year). The scale height H_w varies from 1.5 km to up to 8 km from place to place and according to a seasonal cycle [43]. For all practical GNSS purposes, one can consider that the water vapor is concentrated in the troposphere (from 8 km over the poles to 18 km at the Equator [44, 45], and that the atmosphere extends up to 100 km [46, 47]. The International Union of Telecommunications [48] recommends the use, for radio-link purposes, on a worldwide basis and for altitudes taken from sea level, of the formula (7), with $N_h = 315 \cdot 10^{-6}$, $H_h = 7.35$ km, the wet part being omitted (it is in fact included as a worldwide average in N_h and H_h).

The prime integral (4) allows two things: 1/the computation of the path, 2/the computation of the time delay along the path as

$$L = \int_{path} n ds \quad (8)$$

The extra delay (in equivalent length) caused by the atmosphere is

$$\delta L = \int_{path} (n - 1) ds \quad (9)$$

By inserting Eq. (6) into Eq. (9) we get the separation of δL into additive “hydrostatic” δL_h and “wet” δL_w delays. The ratios of δL_h and δL_w with respect to the corresponding values taken along a vertical path are by definition (as in Eq. (1)) the hydrostatic (m_h) and wet (m_w) mapping functions that only depend on the elevation angle e_0 of the tangent of the bended ray at the receiver location.

Davis et al. [10] pushed the physical analysis of Eq. (9) a little bit further by introducing the notion of gradients. This notion is also based on the basic assumption of a main dependence of the refractivity with respect to height, with the refractivity in the neighborhood of the receiver written as

$$n = n_V(r) + \text{small lateral terms} \quad (10)$$

where r is taken along the local vertical of the receiver, and n_V is the variation of n along the vertical of the observation site (the value of n at the receiver station is $n(r_0) = n_V(r_0)$). One can note that this writing violates, on a pure mathematical ground the dependence of n on only the geocentric radius, that was assumed for the computation of the path in Eq. (4) (i.e. no small lateral terms should be present). If we define a local frame with units vector (\hat{x}, \hat{y}) in the tangent plane perpendicular to the vertical direction of the station (usually defined by the North and East directions as in Eq. (1), we get, with also the assumption of a “flat Earth”, the approximation

$$n(r; x, y) \simeq n_V(r) + \left(\frac{\partial n}{\partial x}\right)_{(r)} x + \left(\frac{\partial n}{\partial y}\right)_{(r)} y \quad (11)$$

This is nothing else than a Taylor series, meaning that x and y are assumed to be small, and the subscript (r) emphasizes that the partial derivatives of n are varying with the height r (i.e. they are not taken at $r = r_0$). For low elevation angles of the path, x and y are by no means “small”, and can reach up to several hundreds of kilometers. We can define Eq. (11) as a “cylindrical” expansion of the refractivity.

If we insert this in Eq. (9), we get

$$\delta L(e_0) = \int_{\text{path}} (n_V - 1) ds + \int_{\text{path}} \left(\frac{\partial n}{\partial x}\right)_{(r)} x ds + \int_{\text{path}} \left(\frac{\partial n}{\partial y}\right)_{(r)} y ds \quad (12)$$

If we now divide the first right term of Eq. (12) by

$$\delta L(e_0) = \int_{\text{vertical}} (n_V - 1) ds \quad (13)$$

We get

$$\delta L(e_0) = m(e_0) \int_{\text{vertical}} (n_V - 1) ds + \int_{\text{path}} \left(\frac{\partial n}{\partial x}\right)_{(r)} x ds + \int_{\text{path}} \left(\frac{\partial n}{\partial y}\right)_{(r)} y ds \quad (14)$$

where $m(e_0) \approx \frac{1}{\sin e_0}$ is by definition the mapping function. The value $\frac{1}{\sin e_0}$ is obtained by setting all the coefficients $a, b, c \dots$ to 0 in Eq. (2).

By writing $R^2 = x^2 + y^2$, $x = R \cos \phi$, $y = R \sin \phi$, and taking advantage of the fact that the path is nearly a straight line, as n is close to 1 at a 10^{-3} level, we can write, for the two integrals involving the derivatives of n , $R = r \cotg(e_0)$ and $ds = \frac{dr}{\sin(e_0)}$. This is permissible, because physically these derivatives, as well as x and y are assumed to be small quantities. We obtain for the integral relative to the partial derivative $\left(\frac{\partial n}{\partial x}\right)$

$$\int_{path} \left(\frac{\partial n}{\partial x} \right)_{(r)} x ds = m(e_0) \cot e_0 \cos \phi \int_{r=r_0}^{r_{top}} \left(\frac{\partial n}{\partial x} \right)_{(r)} r dr \quad (15)$$

where r_{top} is the top of the atmosphere with respect to the geocentric radius (around 100 km), and a similar expression in $\sin \phi$ for the partial derivative $\left(\frac{\partial n}{\partial y} \right)$.

The precise details of the mathematical machinery linking Eq. (11) to Eq. (1) can be found in Davis et al. [10]. The important fact, from a physical point-of-view is that, if we split the refractivity into a “hydrostatic” and a “wet” part, we get the “hydrostatic” and “wet” gradients of Eq. (1) as

$$G_N^h = \int_{r=r_0}^{r_{top}} \left(\frac{\partial n_h}{\partial x} \right)_{(r)} r dr, G_E^h = \int_{r=r_0}^{r_{top}} \left(\frac{\partial n_h}{\partial y} \right)_{(r)} r dr \quad (16)$$

$$G_N^w = \int_{r=r_0}^{r_{top}} \left(\frac{\partial n_w}{\partial x} \right)_{(r)} r dr, G_E^w = \int_{r=r_0}^{r_{top}} \left(\frac{\partial n_w}{\partial y} \right)_{(r)} r dr \quad (17)$$

The significations of the gradients are therefore the integration, along the altitude, weighted by the altitude, of the North and East directional derivatives of the “hydrostatic” and “wet” parts of the refractivity, evaluated along the vertical of the receiver location. It is in fact an integration along the geometrical line-of-sight.

3. Physical meaning of zenithal delays and gradients

The modeling of the extra-delays caused by the atmosphere by the combination of mapping functions and gradients of Eq. (1) has proved very effective since Davis introduced his formula 30 years ago [49–51]. But what is the real meaning of effective?

We have to remember that this model was primarily introduced to model atmospheric delays in VLBI, then to improve positioning estimates from GNSS data, and it is now battle-proven for these two applications. But another application, being known today as GNSS meteorology, emerged during the nineties, first with the modeling of the integrated water vapor contents along the vertical of the GNSS receiver (i.e. no gradients), known as “precipitable water” (or PW), that used the L_z^w zenithal delay converted to PW through a multiplicative constant, known as the Π constant introduced by Bevis et al. [52]. Because the wet and dry mapping functions cannot be separated, for any practical purposes, in Eq. (1), the separation between the sum $L_z^d + L_z^w$ and L_z^w must be done by introducing an “external hydrostatic estimate” L_z^h , the model of choice being the so-called Saastamoinen model [41]. By its own inception, a PW time series is relative to a particular GNSS station, and does not provide any information about the lateral gradients of the water vapor contents of the atmosphere for this site. But a dense network of GNSS receivers do. An even more powerful way to grasp the 3D and even 4D (with the inclusion of time) variations of the water vapor contents of the atmosphere is the tomography, first promoted by [1, 53, 54]. In the approach of tomography, Eq. (1) is just seen as an intermediate tool, the data inputted in the tomography software being the reconstructed δL^w (the “wet” part of Eq. (1)). The tomography approach needs a dense network of GNSS receivers over a limited area, and take advantage of a multiple crossing paths between the receivers and the satellites of the GNSS constellations to invert the intrinsically ill-posed correspondence between the δL^w and the 3D atmospheric water vapor refractivity field over the area.

All the tomography software treat, to obtain a tractable problem, the rays as straight lines. This means that low-elevation slant delays cannot be considered.

Some authors [51, 55, 56] tried to assess the physical meaning of tropospheric gradients, but their effort were limited to qualitative assessments and correlations studies. Up to our knowledge [57], nobody is using gradients as data to constraint operational NWMs, albeit efforts having made to extract gradients from NWM numerical simulations [14] or make comparisons with NWMs outputs [58], or even to propose the use of slant delays for such a use [59]. The only GNSS data products that are currently inputted (assimilated) in NWMs are total zenithal delays (i.e. the sum $L_z^d + L_z^w$), as for example in the latest Météo-France AROME model [60].

This is clearly sending the message that the meteorology community does not yet consider gradients as a usable data set. We think that the main reason for this is the underlying assumption of the cylindrical Taylor's expansion [Eq. (11)], at the basis of the notion of gradients, where a strict separation between vertical variations and lateral variations is assumed, and supposed valid over all the troposphere (at least as seen from the receiver location). This assumption is closely related to the hydrostatic assumption, itself closely linked to the highly non-linear Navier–Stokes equations, which admit as solutions a combination of laminar and turbulent/convective flows. At scales larger than a few tens of kilometers, the atmospheric flows are mostly horizontal [61]. This corresponds to the highest resolution available for typical MNW models, built around the hydrostatic assumption [62]. The atmospheric turbulence [63] itself is organized as “vortices”, or eddies, with scales varying over several orders of magnitude, from a few meters to several hundreds of kilometers [64, 65]. A combination of laminar and turbulence is also possible, and it is known as “frozen flow”, where “frozen turbulence” is carried by laminar flow [66]. This is illustrated for the layman by clouds driven by the wind. Atmospheric turbulence/convection is modeled through statistical tools, the structure functions [67], that obeys an exponential decay with altitude (i.e. turbulence is “higher” in the boundary layer) [68]. The definition of gradients by Davis et al. [10] is simply too crude from a “meteorological” point-of-view.

4. Beyond zenithal delays and gradients

Therefore, what can be the future of the modeling of neutral delays in GNSS meteorology? Applications in GNSS positioning and VLBI clearly show that Eq. (1) is sufficient for these applications, because what is of interest to these users are the integrated delays, not directly the variations of refractivity in the atmosphere. Eq. (1) is sufficient by itself to model these slant (extra) delays, as evidenced by tomography applications and the statistical analysis of these delays [69]. The zenithal total delays have proven to have a physical meaning, as they are related to the modeling of PW through an a priori model of the “dry” atmosphere and a proportional correspondence to zenithal wet delays. They are also feeding the current medium resolution NWM models. The gradients themselves are more questionable. They are merely *ad hoc*, empirical corrections introduced for positioning and VLBI applications.

Can the definition of gradients be improved? From a physical point-of-view, we do not think so. The main assumption to derive the delay gradients in Davis et al. formula (Eqs. (16) and (17)) is an integration, along the line-of-sight receiver-satellite, of the gradients of the refractivity. Even with a better “geometrical definition” of the gradients, taking into account the curvature of Earth, the bending of the rays, etc. ... , the main problem is that a line-of-sight station-satellite usually cross – and average– many eddies. According to [70], the shape and size of the eddies

depend on the altitude. Close to the ground (0–2 km of altitude), the eddies are assumed to be small and not far from isotropic, while the irregularities at higher altitudes are highly anisotropic, i.e., the eddies become more flattened laterally. Along the vertical, the refractivity variation is mainly dominated by an exponential decay [71], but this is not the case along the horizontal direction. Besides, the repartition of the lines-of-sight in the sky can be scarce or uneven. For example, the GPS constellation, the most used one because of the high quality of its orbit modeling, offer quasi-repeating repeating tracks where only a few satellites (4 to 12) are visible from a particular location (**Figure 2**). This means that only a few lines-of-sight can be used at any time, and that there is, from a practitioner point of view, not enough data to constraint a better representation of the slant delays than the six-parameters Eq. (1).

Hopefully, Augmented Constellations and Low-Earth-Orbits constellations (LEO) will become soon a reality [72–74], thanks to the ever-decreasing size and costs of satellites, as well as the availability of miniaturized atomic clocks [75]. LEO constellations are particularly interesting for GNSS meteorology, as their satellites will cross the sky in a few minutes instead of hours, with a boost by one order of magnitude, or even two, of the available line-of-sight geometries. Our proposal to keep the separation of the refractivity into a “hydrostatic” and “wet” part, with the “hydrostatic” slant part evaluated separately from proven models like the Saastamoinen [41] model and subtracted from the total slant delay, then to represent the wet refractivity field based on a mean exponential decay of the wet refractivity as

$$\delta n_w(r) = N_w \exp\left(\frac{r - r_0}{H_w}\right) (1. + \varepsilon_w(x, y, z, t)) \quad (18)$$

where the ε_w terms represent the departure of the wet refractivity field from the exponential local decay law and x, y, z, t are local coordinates with respect to a frame linked with the local GNSS receiver and t is time. As the wet scale height can vary by a factor of four, it must be provided from external sources (for example from the ECMWF-ERA series of climate models, see [76]). An estimate of H_w can also be determined from the slant wet delays themselves, but only if a reliable estimate of the wet refractivity is available, as the integral over the geometrical path between the GNSS satellite and the receiver is proportional to $N_w H_w$ for a pure exponential decay of the wet refractivity. Empirical relations also exist between the ground value of the refractivity and scale height for example [77], but they are probably out-of-date. H_w is by itself a very important parameter, as [71] demonstrated that

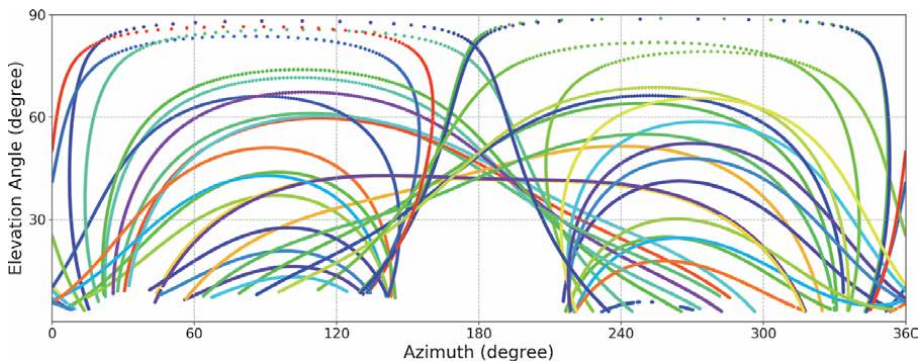


Figure 2. The sky-tracks (in elevation and azimuth) of the GPS satellites (one color per satellite) visible from the THTI station (latitude: 17.5769° S, longitude: 149.6063° W), in the wet season on January 10th, 2018.

this scale height is related to the rate at which the PW decorrelates with horizontal separation.

On the contrary of Davis et al. [10], we fully represent the term $\epsilon_w(x, y, z, t)$ as a 3D (or 4D if the time is present) series expansion

$$\epsilon_n(x, y, z, t) = \sum_n \lambda_n \Phi_n(x, y, z, t) \quad (19)$$

where the $\Phi_n(x, y, z, t)$ are a set of suitably chosen orthogonal functions in the atmospheric lens comprised between the local horizon of the station and the local tropopause. The λ_n are the coefficients of the expansion. If the shape of the tropopause boundary is known [78], the Φ_n functions can be defined as empirical orthogonal functions (EOF) [79] or as a pre-defined set of orthogonal functions renormalized according to the Gram-Schmidt scheme [80].

A preliminary attempt with a small data set was made by [81] with the assumption of a constant altitude tropopause (see **Figure 3**), where the Φ_n orthogonal functions are a subset of Zernike functions [82]. The line-of-sight are assumed to be straight-lines to obtain tractable equations, as it is the case for tomography [83, 84] and the statistical analysis of the slant delays [85, 86]. This implies that low-elevation rays cannot be taken into account.

The integral relation to be solved with respect to ϵ_w is therefore

$$\delta L_w(e_0) = N_w \int_{\text{path}} \text{geometrical} \exp\left(\frac{r-r_0}{H_w}\right) (1 + \epsilon_w(x, y, z, t)) ds \quad (20)$$

This integral relationship is averaging the wet refractivity field along the lines-of-sight (fan-beam tomography [87, 88]), and the inversion in terms of λ_n coefficients must be regularized. By construction, the ϵ_w correction must be small, so we can use a truncated Singular Value decomposition (the EOF approach) or a Tikhonov approach [89] to enforce this smallness with respect to 1. The use of a priori refractivity values along the vertical for sites collocated with radiosoundings can also be envisaged [90] (in preparation). The Tikhonov approach, and its ability to model local variations of the refractivity field has been investigated in the framework of radar tomography [87, 91, 92].

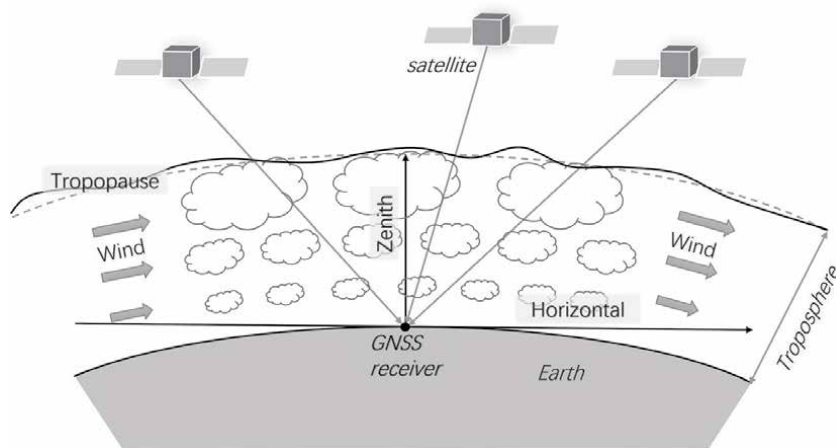


Figure 3. The geometry of the inversion of the wet delays, with the representation of eddies in the troposphere, flattened with altitude and pushed by the wind [62, 63].

The only case where the hypothesis of a small ϵ_w can be violated occurs during inversion episodes, where atmospheric temperature increases when altitude increases. The warm inversion layer then acts as a cap and stops atmospheric mixing [93] causing a large deviation of the refractivity with respect to the exponential decay.

The end-product for the meteorology community of the inversion of Eq. (19) cannot only be the set of H_w and λ_n coefficients, that are too difficult to handle. We propose, in addition, to give the results in the form of records over a grid the resolution of which is in agreement with the maximum degree of the expansion in Eq. (19), with respect to a suitable ellipsoid (like WGS84), and with these fields:

Observation Time, Latitude, Longitude, Geometrical height, total refractivity, wet refractivity.

The refractivity fields can then be converted, if needed, to water vapor levels according to Eq. (6) with suitable temperature profiles over the troposphere and/or feed high resolution NWM taking natively into account turbulent/convective processes [94]. Xia et al. [95] tried to derive the refractivity field from slant delays by substituting Eq. (6) into Eq. (9), but the underlying hypothesis is an atmosphere at rest, in a similar fashion of the neutral delay model of Saastamoinen [41, 96].

Is the approach developed in this article directly implementable in GNSS software, as a replacement of the usual approach of Eq. (1)? The response is a careful yes [69]. Strictly speaking, a mapping function defines, from the point of view of differential geometry, a time-evolving coordinate chart that is a non-orthogonal system of coordinates made of the refracted elevation at ground level, the length along the bended ray, and the azimuth. We think that such an implementation in GNSS software implies at least the use of a constant (i.e., not evolving with time) system of coordinates (i.e., a constant mapping function), that therefore must be computed with respect to some standard model of the atmosphere, carefully designed and normalized [97]. For this purpose, it should be noted that the variation of the propagation delay caused by the bending is of second order with respect to the integration of the refractivity along the path [98].

Finally, the modeling of the wet refractivity field through an expansion series in time and space (Eq. (19)) can be also used to model tropospheric delays, in a correlated way, between uplink and downlink signals to planetary space crafts, where the uplink and downlink separation in time can reach tens of minutes or even hours [99].

5. Conclusion

We discussed in this brief paper the pros and cons of the standard approach mapping functions + gradients to model the neutral delays of the atmosphere, and more specifically the wet delays caused by the presence of water vapor in the troposphere. If this standard approach is almost perfect for people doing positioning, deformation and VLBI studies, as they see the neutral delays as “noise”, it is not so well adapted to people looking at these delays as signals to study atmospheric processes. In particular, the standard definition of gradients is too crude, and does not permit to have access to the horizontal turbulence/convection scales, that are key parameters to model these processes in high resolution NWM models. We therefore propose an alternative way to model the wet tropospheric delays, through a representation of the wet refractivity field as a perturbation over an exponential decay with altitude with a locally adjusted scale height and a time/space series expansion over a suitable basis of orthogonal functions. Our approach is computationally expensive, and maybe not suited for real-time applications, but its

end-product are records of the total and wet refractivity values with high-resolution in time (minute-scale) and distance (sub km-scale), in accordance with the needs of future numerical weather models [38], the emerging field of the modeling of atmospheric rivers [100, 101] and besides does not require the additional step of water vapor tomography, with lower cost, better mobility and simpler operation [102].

Acknowledgements

This research was funded by a DAR grant from the French Space Agency (CNES) to the Geodesy Observatory of Tahiti. Feng Peng did this research in the framework of his Ph.D., with a 14-months stay at the Observatory of Tahiti funded through the Cai Yuanpei program.

Conflict of interest

The authors declare no conflict of interest.

Author details

Jean-Pierre Barriot^{1*} and Peng Feng²

¹ University of French Polynesia, French Polynesia

² LIESMARS State Key Laboratory, Wuhan University, China

*Address all correspondence to: jean-pierre.barriot@upf.pf

IntechOpen

© 2021 The Author(s). Licensee IntechOpen. This chapter is distributed under the terms of the Creative Commons Attribution License (<http://creativecommons.org/licenses/by/3.0>), which permits unrestricted use, distribution, and reproduction in any medium, provided the original work is properly cited. 

References

- [1] Flores A, Ruffini G, Rius A. 4D tropospheric tomography using GPS slant wet delays. *Ann Geophys.* 2000;18(2):223–34.
- [2] Webb FH, Zumberge JF. An introduction to GIPSY/OASIS-II precision software for the analysis of data from the Global Positioning System. Pasadena, California; 1995.
- [3] Dach, R., S. Lutz, P. Walser PF (Eds). Bernese GNSS Software Version 5.2. Vol. 2, Astronomical Institute, University of Bern. Bern, Switzerland: University of Bern, Bern Open Publishing; 2015. 826 p.
- [4] O’Driscoll Cillian. Carrier phase and its measurement for GNSS. *GNSS Insider* [Internet]. 2010 [cited 2021 Jan 16]; Available from: www.insidegnss.com
- [5] Nikolaidou T, Balidakis K, Nievinski F, Santos M, Schuh H. Impact of different NWM-derived mapping functions on VLBI and GPS analysis. *Earth, Planets Sp.* 2018 Dec 1;70(1):1–16.
- [6] Marini JW. Correction of Satellite Tracking Data for an Arbitrary Tropospheric Profile. *Radio Sci.* 1972 Feb 1;7(2):223–31.
- [7] Davis JL, Herring TA, Shapiro II, Rogers AEE, Elgered G. Geodesy by radio interferometry: Effects of atmospheric modeling errors on estimates of baseline length. *Radio Sci.* 1985 Nov 1;20(6):1593–607.
- [8] Herring TA. Modeling Atmospheric Delays in the Analysis of Space Geodetic Data. In: *Symposium on Refraction of Transatmospheric Signals in Geodesy*, 19–22 May 1992. Delft, Netherlands: Netherlands Geodetic Commission Publications on Geodesy; 1992. p. 157–64.
- [9] Nilsson T, Böhm J, Wijaya DD, Tresch A, Nafisi V, Schuh H. Path Delays in the Neutral Atmosphere. In: *Atmospheric Effects in Space Geodesy*. Springer, Berlin, Heidelberg; 2013. p. 73–136.
- [10] Davis JL, Elgered G, Niell AE, Kuehn CE. Ground-based measurement of gradients in the “wet” radio refractivity of air. *Radio Sci.* 1993;28(6):1003–18.
- [11] MacMillan DS. Atmospheric gradients from very long baseline interferometry observations. *Geophys Res Lett.* 1995;22(9):1041–4.
- [12] Chen G, Herring TA. Effects of atmospheric azimuthal asymmetry on the analysis of space geodetic data. *J Geophys Res Solid Earth.* 1997;102(B9): 20489–502.
- [13] Boehm J, Werl B, Schuh H. Troposphere mapping functions for GPS and very long baseline interferometry from European Centre for Medium-Range Weather Forecasts operational analysis data. *J Geophys Res Solid Earth.* 2006;111(2):1–9.
- [14] Landskron D, Böhm J. VMF3/GPT3: refined discrete and empirical troposphere mapping functions. *J Geod.* 2018;92(4):349–60.
- [15] Rüeger JM. Refractive Index Formulae for Radio Waves. In: *FIG Technical Program*. Washington, D.C. USA: FIG XXII International Congress; 2002. p. 1–13.
- [16] Stevens B, Brogniez H, Kiemle C, Lacour J-L, Crevoisier C, Kiliani J. Structure and Dynamical Influence of Water Vapor in the Lower Tropical Troposphere. In *Springer, Cham*; 2017. p. 199–225.
- [17] McGuffie K, Henderson-Sellers A. *A Climate Modelling Primer*. Chichester, UK: John Wiley & Sons, Ltd; 2005. 1–280 p.

- [18] Stocker T. Model Hierarchy and Simplified Climate Models. In: *Introduction to Climate Modelling*. Springer-Verlag Berlin Heidelberg; 2011. p. 25–51.
- [19] Dessler AE, Sherwood SC. A matter of humidity. *Science* (80-). 2009;323(5917):1020–1.
- [20] Schmidt GA, Ruedy RA, Miller RL, Lacis AA. Attribution of the present-day total greenhouse effect. *J Geophys Res Atmos*. 2010 Oct 27;115(20).
- [21] Hansen J, Sato M, Ruedy R, Kharecha P, Lacis A, Miller R, et al. Dangerous human-made interference with climate: a GISS modelE study. *Atmos Chem Phys*. 2007 May 7;7(9):2287–312.
- [22] Elliott WP, Gaffen DJ. Chapman Conference Probes Water Vapor in the Climate System. In: *Eos, Transactions American Geophysical Union*. John Wiley & Sons, Ltd; 1995. p. 67–67.
- [23] King MD, Kaufman YJ, Menzel WP, Tanré D. Remote Sensing of Cloud, Aerosol, and Water Vapor Properties from the Moderate Resolution Imaging Spectrometer (MODIS). *IEEE Trans Geosci Remote Sens*. 1992;30(1):2–27.
- [24] Whiteman DN, Melfi SH, Ferrare RA. Raman lidar system for the measurement of water vapor and aerosols in the Earth's atmosphere. *Appl Opt*. 1992 Jun 1;31(16):3068.
- [25] Halthore RN, Eck TF, Holben BN, Markham BL. Sun photometric measurements of atmospheric water vapor column abundance in the 940-nm band. *J Geophys Res Atmos*. 1997 Feb 27;102(4):4343–52.
- [26] Cimini D, Campos E, Ware R, Albers S, Giuliani G, Orearuno J, et al. Thermodynamic atmospheric profiling during the 2010 winter olympics using ground-based microwave radiometry. *IEEE Trans Geosci Remote Sens*. 2011 Dec;49(12 PART 2):4959–69.
- [27] Durre I, Vose RS, Wuertz DB. Overview of the integrated global radiosonde archive. *J Clim*. 2006 Jan 15;19(1):53–68.
- [28] Van Baelen J, Reverdy M, Tridon F, Labbouz L, Dick G, Bender M, et al. On the relationship between water vapour field evolution and the life cycle of precipitation systems. *Q J R Meteorol Soc*. 2011 Jan 1;137(S1):204–23.
- [29] Koulali A, Ouazar D, Bock O, Fadil A. Study of seasonal-scale atmospheric water cycle with ground-based GPS receivers, radiosondes and NWP models over Morocco. *Atmos Res*. 2012 Feb 1;104–105:273–91.
- [30] Brenot H, Ducrocq V, Walpersdorf A, Champollion C, Caumont O. GPS zenith delay sensitivity evaluated from high-resolution numerical weather prediction simulations of the 8–9 September 2002 flash flood over southeastern France. *J Geophys Res*. 2006 Aug 16;111(D15):D15105.
- [31] Uppala SM, Kållberg PW, Simmons AJ, Andrae U, da Costa Bechtold V, Fiorino M, et al. The ERA-40 re-analysis. *Q J R Meteorol Soc*. 2005 Oct 1;131(612):2961–3012.
- [32] Marini JW, Murray CW. Correction of laser range tracking data for atmospheric refraction at elevations above 10 degrees. Goddard Space Flight Center, Greenbelt, Maryland: NASA Technical Report; 1973.
- [33] Thayer GD. A Rapid and Accurate Ray Tracing Algorithm for a Horizontally Stratified Atmosphere. *Radio Sci*. 1967;2(2):249–52.
- [34] Thompson DA, Pepin TJ, Simon FW. Ray Tracing in Refracting Spherically Symmetric Atmosphere. *J Opt Soc Am*. 1982;72(11):1498–501.

- [35] Smith EK, Weintraub S. The Constants in the Equation for Atmospheric Refractive Index at Radio Frequencies. *Proc IRE*. 1953;41(8):1035–7.
- [36] Boudouris G. On the index of refraction of air, the absorption and dispersion of centimeterwaves by gases. *J Res Natl Bur Stand Sect D Radio Propag*. 1963;67D(6):631.
- [37] Bevis M. GPS meteorology: mapping zenith wet delays onto precipitable water. Vol. 33, *Journal of Applied Meteorology*. 1994. p. 379–86.
- [38] Bauer P, Thorpe A, Brunet G. The quiet revolution of numerical weather prediction. Vol. 525, *Nature*. Nature Publishing Group; 2015. p. 47–55.
- [39] Stevens B. Atmospheric moist convection. Vol. 33, *Annual Review of Earth and Planetary Sciences*. Annual Reviews; 2005. p. 605–43.
- [40] Steppeler J, Hess R, Schättler U, Bonaventura L. Review of numerical methods for nonhydrostatic weather prediction models. *Meteorol Atmos Phys*. 2003 Jan;82(1–4):287–301.
- [41] Saastamoinen J. Atmospheric Correction for the Troposphere and Stratosphere in Radio Ranging Satellites. In: *Geophysical Monograph Series*. 1972. p. 247–51.
- [42] Butler B. Precipitable water at KP 1993–1998, MMA MEMO 238 [Internet]. 1998 [cited 2021 Jan 14]. Available from: <https://library.nrao.edu/public/memos/ama/main/memo238.pdf>
- [43] Zhang B, Yao Y, Xu C. Global empirical model for estimating water vapor scale height. *Cehui Xuebao/Acta Geod Cartogr Sin*. 2015 Oct 1;44(10):1085.
- [44] Reid GC, Gage KS. On the annual variation in height of the tropical tropopause. *J Atmos Sci*. 1981 Sep 1;38(9):1928–38.
- [45] Tomikawa Y, Nishimura Y, Yamanouchi T. Characteristics of Tropopause and Tropopause Inversion Layer in the Polar Region. *SOLA*. 2009;5(1):141–4.
- [46] Minzner RA, Reber CA, Jacchia LG, Huang FT, Cole AE, Kantor AJ, et al. Defining Constants, Equations, and Abbreviated Tables of the 1975 U.S. Standard Atmosphere. NASA Technical Report R-459; 1976.
- [47] Fleming EL, Chandra S, Barnett JJ, Corney M. Zonal mean temperature, pressure, zonal wind and geopotential height as functions of latitude. *Adv Sp Res*. 1990;
- [48] ITU-R. The radio refractive index : its formula and refractivity data. Vol. P.453–11, Radiocommunication Sector of IUT. 2015.
- [49] Bar-Sever YE, Kroger PM, Borjesson JA. Estimating horizontal gradients of tropospheric path delay with a single GPS receiver. *J Geophys Res Solid Earth*. 1998 Mar 10;103(B3):5019–35.
- [50] MacMillan DS, Ma C. Atmospheric gradients and the VLBI terrestrial and celestial reference frames. *Geophys Res Lett*. 1997;24(4):453–6.
- [51] Graffigna V, Hernández-Pajares M, Gende M, Azpilicueta F, Antico P. Interpretation of the Tropospheric Gradients Estimated With GPS During Hurricane Harvey. *Earth Sp Sci*. 2019;6(8):1348–65.
- [52] Bevis M, Businger S, Herring TA, Rocken C, Anthes RA, Ware RH. GPS meteorology: remote sensing of atmospheric water vapor using the global positioning system. *J Geophys Res*. 1992;97(D14):15787.
- [53] Hirahara K. Local GPS tropospheric tomography. *Earth, Planets Sp*. 2000;52(11):935–9.

- [54] de Haan S, van der Marel H. Observing three dimensional water vapour using a surface network of GPS receivers. *Atmos Chem Phys Discuss.* 2008 Sep 11;8(5):17193–235.
- [55] Morel L, Pottiaux E, Durand F, Fund F, Boniface K, De Oliveira PS, et al. Validity and behaviour of tropospheric gradients estimated by GPS in Corsica. *Adv Sp Res.* 2015;55(1): 135–49.
- [56] Nahmani S, Bock O, Guichard F. Sensitivity of GPS tropospheric estimates to mesoscale convective systems in West Africa. *Atmos Chem Phys.* 2019;19(14):9541–61.
- [57] Guerova G, Jones J, Douša J, Dick G, De Haan S, Pottiaux E, et al. Review of the state of the art and future prospects of the ground-based GNSS meteorology in Europe. *Atmos Meas Tech.* 2016;9(11):5385–406.
- [58] Douša J, Dick G, Kačmařík M, Bro Řková R, Zus F, Brenot H, et al. Benchmark campaign and case study episode in central Europe for development and assessment of advanced GNSS tropospheric models and products. *Atmos Meas Tech.* 2016 Jul 14;9(7):2989–3008.
- [59] Järvinen H, Eresmaa R, Vedel H, Salonen K, Niemelä S, de Vries J. A variational data assimilation system for ground-based GPS slant delays. *Q J R Meteorol Soc.* 2007 Apr 1;133(625):969–80.
- [60] Hdidou FZ, Mordane S, Moll P, Mahfouf J-F, Erraji H, Dahmane Z. Impact of the variational assimilation of ground-based GNSS zenith total delay into AROME-Morocco model. *Tellus A Dyn Meteorol Oceanogr.* 2020 Jan 1;72(1):1–13.
- [61] Haynes PH. Transport and Mixing in the Atmosphere. In: *Mechanics of the 21st Century.* Dordrecht: Springer; 2005. p. 139–52.
- [62] Holton JR, Hakim GJ. An introduction to dynamic meteorology: Fifth edition. Vol. 9780123848. Academic Press; 2012. 1–552 p.
- [63] Foken T. 50 years of the Monin-Obukhov similarity theory. Vol. 119, *Boundary-Layer Meteorology.* Springer; 2006. p. 431–47.
- [64] Xue H, Feingold G. Large-eddy simulations of trade wind cumuli: Investigation of aerosol indirect effects. *J Atmos Sci.* 2006;63(6):1605–22.
- [65] Neggers RAJ, Jonker HJJ, Siebesma AP. Size statistics of cumulus cloud populations in large-eddy simulations. *J Atmos Sci.* 2003;60(8): 1060–74.
- [66] Schöck M, Spillar EJ. Method for a quantitative investigation of the frozen flow hypothesis. *J Opt Soc Am A.* 2000; 17(9):1650.
- [67] Schulz-DuBois EO, Rehberg I. Structure function in lieu of correlation function. *Appl Phys.* 1981 Apr;24(4): 323–9.
- [68] Bobak JP, Ruf CS. A new model for the structure function of integrated water vapor in turbulence. *Radio Sci.* 1999 Nov 1;34(6):1461–73.
- [69] Zhang F, Barriot J, Xu G, Hopuare M. Modeling the Slant Wet Delays From One GPS Receiver as a Series Expansion With Respect to Time and Space: Theory and an Example of Application for the Tahiti Island. *IEEE Trans Geosci Remote Sens.* 2020;1–13.
- [70] Halsig S, Artz T, Iddink A, Nothnagel A. Using an atmospheric turbulence model for the stochastic model of geodetic VLBI data analysis 6. *Geodesy. Earth, Planets Sp.* 2016 Dec 1; 68(1):1–14.
- [71] Ruf CS, Beus SE. Retrieval of tropospheric water vapor scale height

- from horizontal turbulence structure. *IEEE Trans Geosci Remote Sens.* 1997;35(2):203–11.
- [72] Li X, Li X, Ma F, Yuan Y, Zhang K, Zhou F, et al. Improved PPP Ambiguity Resolution with the Assistance of Multiple LEO Constellations and Signals. *Remote Sens.* 2019 Feb 17;11(4):408.
- [73] Li X, Zus F, Lu C, Ning T, Dick G, Ge M, et al. Retrieving high-resolution tropospheric gradients from multiconstellation GNSS observations. *Geophys Res Lett.* 2015;42(10):4173–81.
- [74] Wei H, Li J, Zhang S, Xu X. Cycle Slip Detection and Repair for Dual-Frequency LEO Satellite GPS Carrier Phase Observations with Orbit Dynamic Model Information. *Remote Sens.* 2019 May 29;11(11):1273.
- [75] Ely TA, Burt EA, Prestage JD, Seubert JM, Tjoelker RL. Using the Deep Space Atomic Clock for Navigation and Science. *IEEE Trans Ultrason Ferroelectr Freq Control.* 2018 Jun 1;65(6):950–61.
- [76] Kennett EJ, Toumi R. Temperature dependence of atmospheric moisture lifetime. *Geophys Res Lett.* 2005 Oct 16;32(19):1–4.
- [77] Bean BR, Thayer GD. Models of the Atmospheric Radio Refractive Index. *Proc IRE.* 1959;47(5):740–55.
- [78] Hoerling MP, Schaack TK, Lenzen AJ. Global objective tropopause analysis. *Mon Weather Rev.* 1991 Aug 1;119(8):1816–31.
- [79] Zhang Z, Moore JC. *Mathematical and Physical Fundamentals of Climate Change.* Elsevier; 2015. 1–494 p.
- [80] Arfken G, Romain JE. 9.3 Gram-Schmidt Orthogonalization. In: *Mathematical Methods for Physicists* 3rd Edition. Academic Press; 1985. p. 516–20.
- [81] Barriot J-P, Serafini J, Sichoix L. Estimating the 3D Time Variable Water Vapor Contents of the Troposphere from a Single GNSS Receiver. In: *International Conference on Earth Observations & Societal Impact.* Tainan, Taiwan: Taiwan group on Earth Observations; 2013. arXiv: 2102.01858.
- [82] Mathar RJ. Zernike basis to Cartesian transformations. *Serbian Astron J.* 2009;179(179):107–20.
- [83] Flores A, Gradinarsky LP, Elósegui P, Elgered G, Davis JL, Rius A. Sensing atmospheric structure: Tropospheric tomographic results of the small-scale GPS campaign at the Onsala Space Observatory. *Earth, Planets Sp.* 2000;52(11):941–5.
- [84] Bender M, Stosius R, Zus F, Dick G, Wickert J, Raabe A. GNSS water vapour tomography - Expected improvements by combining GPS, GLONASS and Galileo observations. *Adv Sp Res.* 2011; 47(5):886–97.
- [85] Wheelon AD. *Electromagnetic scintillation. Volume 1, Geometrical optics.* Cambridge University Press; 2001. 455 p.
- [86] Schön S, Brunner FK. Atmospheric turbulence theory applied to GPS carrier-phase data. *J Geod.* 2008 Jan;82(1):47–57.
- [87] Barriot JP, Kofman W, Herique A, Leblanc S, Portal A. A two dimensional simulation of the CONSERT Experiment (radio tomography of comet Wirtanen). *Adv Sp Res.* 1999 Jan 1;24(9):1127–38.
- [88] Peng H, Stark H. Direct Fourier Reconstruction in Fan-Beam Tomography. *IEEE Trans Med Imaging.* 1987 Sep;6(3):209–19.
- [89] Menke W. *Geophysical data analysis: Discrete inverse theory.* Academic Press; 2012. 1–352 p.
- [90] Feng P, Zhang F, Li F, Yan J, Barriot J-P. Line of Sight Wet

Refractivity from a single GNSS Receiver (in preparation). 2021.

[91] Benna M, Barriot JP, Kofman W. A priori information required for a two or three dimensional reconstruction of the internal structure of a comet nucleus (CONSERT experiment). *Adv Sp Res*. 2002 Mar 1;29(5):715–24.

[92] Benna M, Piot A, Barriot JP, Kofman W. Data set generation and inversion simulation of radio waves propagating through a two-dimensional comet nucleus (CONSERT experiment). *Radio Sci*. 2002;37(6):3–1–3–16.

[93] Wallace JM, Hobbs P V. *Atmospheric Science: An Introductory Survey: Second Edition*. Atmospheric Science: An Introductory Survey: Second Edition. Elsevier Inc.; 2006. 1–488 p.

[94] Hanna N, Trzcina E, Möller G, Rohm W, Weber R. Assimilation of GNSS tomography products into the Weather Research and Forecasting model using radio occultation data assimilation operator. *Atmos Meas Tech*. 2019 Sep 10;12(9):4829–48.

[95] Xia P, Ye S, Guo M, Jiang W, Xu C. Retrieval of Tropospheric Refractivity Profiles Using Slant Tropospheric Delays Derived From a Single Ground-Based Global Navigation Satellite System Station. *Earth Sp Sci*. 2019 Jul 1; 6(7):1081–97.

[96] Saastamoinen J. Contributions to the theory of atmospheric refraction - Part II. Refraction corrections in satellite geodesy. *Bull Géodésique*. 1973;47(1): 428.

[97] Minzner RA. The 1976 Standard Atmosphere and its relationship to earlier standards. *Rev Geophys*. 1977;15 (3):375–84.

[98] Zernov N, Lundborg B. The statistical theory of wave propagation

and HF propagation in the ionosphere with local inhomogeneities. Swedish Institute of Space Physics; 1993.

[99] Thornton CL, Border JS. *Radiometric Tracking Techniques for Deep Space Navigation*. Border: Wiley; 2003.

[100] Payne AE, Demory M-E, Leung LR, Ramos AM, Shields CA, Rutz JJ, et al. Responses and impacts of atmospheric rivers to climate change. *Nat Rev Earth Environ*. 2020 Mar 9;1 (3):143–57.

[101] Lavers DA, Ralph FM, Richardson DS, Pappenberger F. Improved forecasts of atmospheric rivers through systematic reconnaissance, better modelling, and insights on conversion of rain to flooding. *Commun Earth Environ*. 2020 Dec 28;1(1):1–7.

[102] Lin L, Zhao Z, Zhu Q, Zhang Y. Profiling tropospheric refractivity in real time, based on a relevance vector machine and single ground-based GPS receiver. *Int J Remote Sens*. 2012;33(13): 4044–58.

GNSS Networks for Geodynamics in the Caribbean, Northwestern South America, and Central America

Héctor Mora-Páez and Franck Audemard

Abstract

For several years, under the framework of national and international projects, the number of GNSS geodetic stations has been increasing in countries located in the area comprised by the Caribbean, northwestern South America and Central America. Data from these geodetic stations have made it possible not only to meet the needs for geospatial information in each of the countries, but also to get a better understanding about the geodynamic interaction of the Caribbean, South American, Nazca and Cocos plates, as well as tectonic blocks wedged in between these plates. This article presents a brief description of the tectonic framework, the existing geodetic networks and the results obtained using data from some stations in the study area.

Keywords: GNSS, Plate tectonics, North Andean Block, Caribbean region, South America plate

1. Introduction

Tectonic and volcanic activities are intimately related to the interaction of different lithospheric plates and crustal blocks. In the study region of this paper, the tectonics and volcanic activity are directly related to the interaction of the Caribbean, South America, Nazca and Cocos plates, with the smaller North Andean, Maracaibo, Choco and Panama blocks wedged in between, as has been pointed out by various authors [1–13]. This highly complex tectono-dynamic configuration of intense intraplate deformation is manifested in a high density of faults, most of which are considered active or potentially active over northwestern South America and southeastern Central America. In addition, seismicity is spread over a broad area across the wide plate boundary in northwestern South America, Central America, and southwestern Caribbean. Also, several countries in this region present intense volcanic activity, such as Guatemala, Nicaragua, Costa Rica, Colombia and Ecuador, as well as on many of the islands of the Lesser Antilles.

There is no doubt that space geodesy has contributed significantly to the study of the kinematics of the Earth's crust, allowing to improve the understanding of the tectonics complexity at a global, regional and local level. The analysis and comprehension of the Earth's crust strain in several places of the world, with a variety of different characteristics and tectonic styles, has gradually been supported by the

results obtained from the geodetic networks, initially composed of field stations of data gathering under episodic campaigns type, and later by continuously operating reference stations (cGPS). Several authors have pointed out the extensive applications of space geodesy for scientific purposes, e.g. [14–16], among others. In the study area, despite the restrictions due to the limited coverage of the national GNSS/GPS networks, its impact is already being observed in studies of the Earth dynamics. The data from the stations have allowed the generation of high precision products such as geodetic time series, velocity fields and estimation of tectonic plate motion rates, seismic cycle analysis, estimation of the magnitude and spatial variability of the plate coupling, among other aspects. In addition to tectonic studies, its use has been extended to the volcano deformation monitoring in several countries (Colombia, Costa Rica, Ecuador, Nicaragua), subsidence studies; the use of data for ionosphere and troposphere studies as well as its inclusion, still in its initial state, in tsunami warning systems. Progress has also been made in the conception of multi-parameter stations, based on the joint installation in the same site of diverse equipment such as geodetic, seismological, strong motion and meteorological instruments, among others. It is also important to note that there is a good data availability, although not from all stations due to particular restrictions, that allows its use for various scientific purposes. However, in some cases, through agreements or by formal request of data to national institutions, these can be obtained.

2. Tectonic setting

Gathering of geologic, tectonic, seismologic and geodetic data through the last decades has led to a better understanding of the Caribbean plate, its margins and adjacent regions, progressively bringing in more complexity to the once drawn “drawer-like” Caribbean plate model [17]. In fact, the Caribbean plate borders are actually “plate boundary zones”, PBZ, in the sense of [18], “wide deformation zones” in the sense of [19], particularly transpressional along the southern Caribbean PBZ, or “wide plate margins” in the sense of [10]. These margins amalgamate tectonic blocks of diverse size, composition, origin and geometry (**Figure 1**), somehow surrounding the Caribbean Sea, cored by the Caribbean Large Igneous Province (CLIP) or plateau.

The recognition of such tectonic blocks started first along the southern Caribbean margin and northwestern South America corner, because being poorly defined by a disperse infrequent and moderate-in-magnitude (instrumental) seismicity, as well as by a poor surface/sea-bottom expression of the active tectonic features in comparison with the other Caribbean PBZs (**Figure 2**).

The study of this very complex but subtly expressed southern PBZ was enhanced by the fact that a large portion of the features are on land (**Figure 1**). Conversely, the northern Caribbean plate boundary became a natural laboratory for numerous space geodesy studies due to its apparent structural simplicity, although the first of all GPS studies worldwide, GPS CASA (Central And South America) Project was carried out in the complex southern Caribbean PBZ between 1988 and 1998 [10, 20]. Not as expected, GPS networks have not fully resolved the posed kinematic questions along this northern Caribbean PBZ, since the networks are mostly installed in rather small islands that are within the plate margin themselves that also resulted to be a complex PBZ with several active features lying offshore (**Figure 3**). As a matter of fact, the larger islands, such as Jamaica and Hispaniola, exist as a proof of such PBZ compressional or transpressional processes. A similar situation happens along the eastern border of the Caribbean plate, where the Atlantic plate subducts beneath an arc of active volcanic islands sitting on the

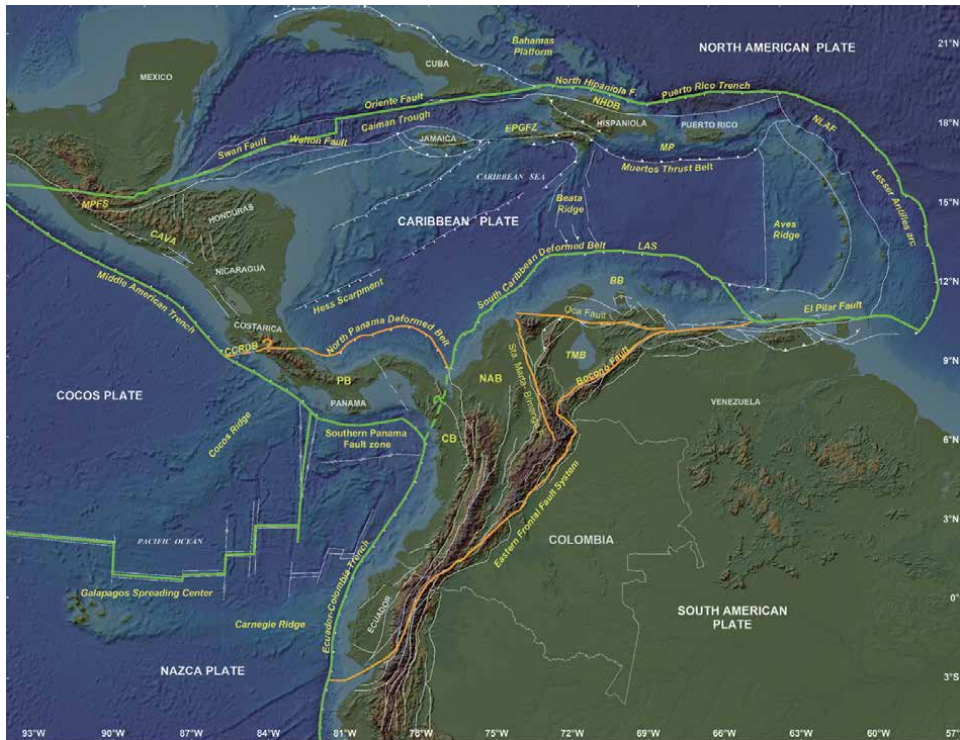


Figure 1. Tectonic frame. Tectonic blocks: PB (Panama B.), CB (Chocó B.), NAB (North Andean B.), TMB (Triangular Maracaibo B.), BB (Bonaire B.). Other features: CAVA (Central America Volcanic Arc); CCRDB (Central Costa Rica Deformed Belt), EPGFZ (Enriquillo-Plantain Garden Fault Zone), LAS (Leeward Antilles Subduction), MP (Mona Passage), MPFS (Motagua-Polochic Fault System), NHDB (North Hispaniola Deformed Belt), NLAF (Northern Lesser Antilles Forearc). Modified from [13].

Caribbean plate. Stable GPS stations inside the Caribbean, such as on San Andrés and Providencia islands and Serranilla Cay (Colombia), and Aves Island (Venezuela), will provide a reliable answer as to the relative motion between the Caribbean and surrounding plates. In addition, longer time span comparisons between these internal sites to the plate should confirm any internal deformation or fragmentation of the Caribbean plate itself, as proposed by [13].

Besides, strain partitioning at different scales is common to the four Caribbean plate PBZs (**Figure 1**). In Central America, a coastal sliver, bounded by the Central America trench on the southwest and the active Central America volcanic arc (CAVA) on the northeast, escapes to the north-west (NW), taking advantage of the weakening of the continental crust by the CAVA volcanic activity [21–24]. A similar situation is reported in the northern Lesser Antilles arc, where the forearc in this region, limited by the active arc on the west-southwest (WSW) and the Atlantic trench on the north-northeast (ENE), moves northward with respect to the arc [25, 26]. Along the northern Caribbean PBZ, the northernmost sliver of the Hispaniola Island, bounded by North Hispaniola and Septentrional faults on the north and south respectively, displaces west faster than most of the island. In the southern Caribbean PBZ, the Bonaire block as well as the block containing the Caribbean nappes overridden onto South America along northern Venezuela (outcropping in the Coastal and Interior ranges), accommodate shortening while slipping dextrally along the large west–east (W-E) trending Oca-Ancón, San Sebastián and El Pilar fault system (**Figure 1**).

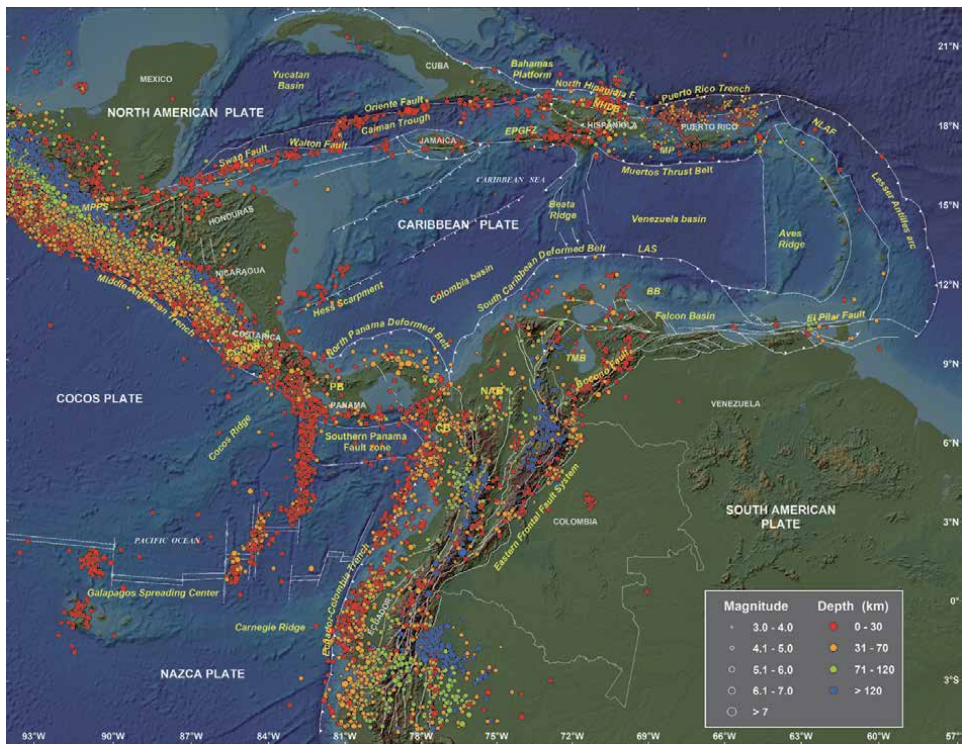


Figure 2. Seismicity. Earthquake epicenters larger than 3 of magnitude recorded in the study area by the National Earthquake Information Center (NEIC) of the USGS and the National Seismic Network operated by the Geological Survey of Colombia for the period of time 2000–2020.

In addition, block indentation and extrusion, and occasional induced oceanic subduction processes at the opposite side of indenters, are also present and rather common to the Caribbean PBZs. Indentation (collision) by submarine relieves or ridges (e.g. Carnegie and Cocos), as engine of tectonic block escape, has been invoked along the Pacific border of South America against the Nazca plate, as for the Pacific coastal sliver of Central America extending between Costa Rica and Guatemala, respectively. In other cases, such strain partitioning has been attributed to the oblique convergence of the subducting plate beneath the overriding one, such as along the northern sector of the Lesser Antilles arc and northernmost block of Hispaniola Island. So has the Ecuadorian-Colombian trench at the southern tip of the North Andes Block –NAB- [27], in the sense of [3]. However, the best regional example of indentation-extrusion is the collision and latter northward-prograding suturing of the Chocó block (originally a constitutive piece of the Cenozoic Panamá arc) against the north–south trending western coast of South America. Some authors as early as early 90’s, e.g. [28–30], propose that such collision and diachronic suturing process induces the NNE-directed tectonic escape of a large portion of northwestern South America, extending from the Guayaquil Gulf-Tumbes basin –GGTB- in SW Ecuador to the Dutch Leeward Antilles (Aruba, Bonaire, Curaçao islands lying north of Venezuela, in the southern Caribbean), and incorporating most of Ecuador territory, the 3 main mountain chains (Western, Central and Eastern) of Colombia and all western mountainous Venezuela. This escape takes place along a major plate boundary named as the Eastern Frontal Fault System –EFFF- by [3]. Much precision has been gathered through the years as to the geometry of that NAB southeastern boundary (e.g., [31–35], among many others). This tectonic escape is probably young in age, starting in the late Miocene

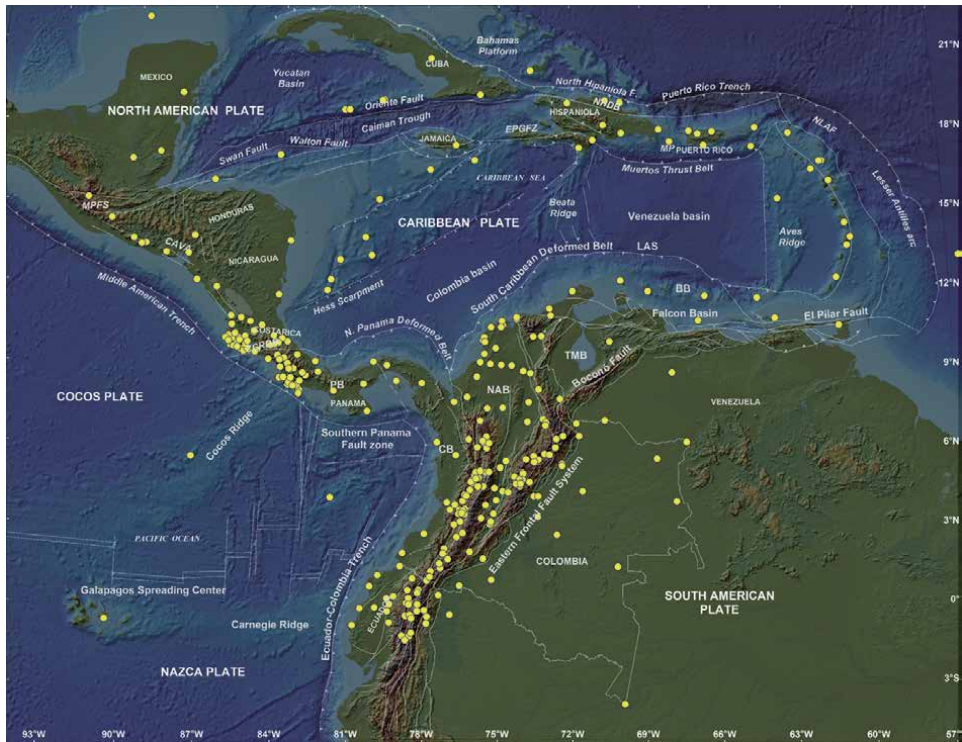


Figure 3. cGPS stations located on the study zone. **Table 1** lists the cGPS stations by country.

(e.g., [12, 36]), with a tectonic paroxysm in the Pliocene (last 5–3 Ma, [21]), when most of the Eastern Cordillera of Colombia [37] and Mérida Andes of Venezuela [12] have actually started elevating to their present heights. A significant fraction of the time delay for the effective coupling (suturing) of the Chocó block against South America, besides the obliquity between the confronting plates, may be explained by the low rigidity exhibited by the Panamá arc at the latitudes of Panamá, which is intensely deformed internally by oroclinal bending and NW-SE trending en-echelon left-lateral faulting (e.g. [13, 24, 38]). The effective collision/accretion of the Chocó block drives the extrusion of NAB (in the sense of [3]), which in the sense of [39] already comprises several NE-escaping blocks, such as Chocó, Maracaibo and Bonaire and others; NAB for this author was already an amalgamation of tectonic blocks. The subduction along which Caribbean plateau floor disappeared into the mantle and drove this indentation-extrusion process, is today partly fossilized between the Chocó block and South America, in association with or running near to the Romeral fault system. This collision has surface expression down to latitude 4°N in Colombia, up to an ENE-WSW-trending alignment of surface tectonic features running across the three Colombian chains at the latitude of Santa Fé de Bogotá, such as Garrapatas, Río Verde and Ibagué faults, and the change of structural style of the front of the Llanos foothills of the Eastern Cordillera, where a dominant dextral strike-slip style on the south (e.g. Algeciras fault) shifts to a much more compressional style on the north (e.g. Guaicáramo, Cusiana and Yopal faults. [39]). Also, the latter author underlines that the Eastern Cordillera becomes much wider across, north of this imaginary line. [40] proposes a broken indenter model for the Panamá-Chocó arc, in which the Chocó arc has been recently accreted to the NAB, resulting in a rapid decrease in shortening in the Eastern Cordillera. At depth,

such a change of structural style roughly coincides with the Caldas tear, as described by [41]. In fact, it is not a plate tear but the confrontation of two different oceanic slabs [13]. On the north, the oceanic-plateau-affinity Caribbean plate sinks to the ESE, as a flat slab lying under the Triangular Maracaibo block and Mérida Andes and reaching depths of almost 700 km further east. This subducted piece of Caribbean plate was the one carrying the Panamá arc on its trailing edge and its consumption into the mantle conducted to the collision of the Panamá arc against South America. Meanwhile on the south, the Nazca plate which is a typical oceanic plate at these latitude, subducts under western South America. [42] propose that buoyant Caribbean crust has been amagmatically subducting under the North Andes for 75 Ma.

Finally, the Caribbean plate itself can be considered as a single unit, at least at the current resolution level of the GPS results in the order of 2–3 mm/a [43]. However, the Hess escarpment is seismically active towards its southwestern end [13] and is moving left-laterally in that order of magnitude. In addition, this major submarine tectonic feature juxtaposes two very different Caribbean entities at naked eye. And it lies in the southern prolongation of an imaginary northeast-southwest (NE–SW) striking line passing over the southern tip of the Bahamas platform, where transpression north of it is dominant, building up the Island of Hispaniola. This author proposes that such accident may have played a major role in the faster eastward migration of the Southern Caribbean, the one carrying the LIP or oceanic plateau, in the late and middle Miocene. This author further indicates that a modern reactivation could be starting in the recent geologic time, also with dominant sinistral and subordinate normal components, but this time related to the push of the floating Cocos ridge when being subducted.

3. Regional and national geodetic networks

In the study area, it is observed that the number of installed cGPS stations has gradually increased, some of them as part of global networks as well as international networks as a benefic consequence of catastrophic natural events, and others that correspond to different countries to meet the needs of geospatial information and definition of national reference frames in some countries, as well as to carry out studies with various purposes such as tectonic, volcanic, subsidence, among others. cGPS stations established in North America, Central America and the Caribbean are described by [44]. For this paper, a survey of the cGPS stations currently in operation is made, including those of some national networks, which allows establishing that there are about 307 stations with data availability; the location of these stations is displayed in **Figure 3**. Twelve of the stations are part of the International GNSS Service (IGS) global network, installed in 10 countries, three of them in Ecuador.

On January 12, 2010, a magnitude 7.0 earthquake struck Haiti, causing more than 316,000 people dead or missing, 300,000 injured and more than 1.3 million homeless [45]. Due to this disaster, with the purpose of advancing in the knowledge of the geodynamics of the Caribbean plate and strengthening national and regional capacities for the hazards identification and risk mitigation of geophysical and meteorological origin, the National Science Foundation (NSF) of USA sponsored the establishment of the Continuously Operating Caribbean GPS Observational Network (COCONet) project, operated by UNAVCO, conceived as the appropriate strategy to complement existing national geodetic networks [46]. The COCONet network reached a number of 135 stations, incorporating stations owned by several national networks. **Figure 3** shows the location of 54 of these stations corresponding to 22 countries. We have only used these stations in order to have a wide spatial

coverage, and because some stations have experienced problems in their operation, limiting the continuous availability of data.

In Colombia, the Geological Survey began in 2007 the development of GeoRED, a research and development project based on space geodesy technology that relied on a multifaceted approach to cataloging and defining the geodynamics of north-western South America [47]. GeoRED is a Spanish acronym for *Geodesia: Red de Estudios de Deformación*. The general purpose of the GeoRED Project is to improve the technical, scientific and operational capabilities in Colombia for analysis, interpretation and policy formulation regarding phenomena related to crustal deformation in Colombia, using GNSS satellite technology. The GNSS GeoRED project is being executed under the operations framework of the Space Geodesy Research Group-SGRG of the Geohazards Directorate [48]. The current cGPS network has 153 stations installed as December 2020. Among these stations, 117 are GeoRED stations, 5 GNSS stations as part of the COCONet Project, and the Bogotá IGS GNSS station. Under a collaborative partnership with local Colombian institutions, thirteen stations have been installed with the Geographical Institute under a joint initiative named GNSS Colombia; eight with the Sugar Cane Research Institute (CENICAÑA); seven with the Bogota City Water Supply Company; and two stations installed with the Universidad Nacional and the Universidad Distrital, respectively. These stations have been fixed to the ground, following mainly UNAVCO's directions for the installation of permanent stations for the study of crustal deformation. Additionally, the Geological Survey of Colombia –GSC- has deployed another geodetic network composed of 70 permanent stations installed in three volcanic regions for the surveillance of the active volcanoes of the country, where the monitoring is carried out from three volcanological and seismological observatories.

In Ecuador, The Geophysical Institute of the National Polytechnical School of Quito began installing in 2006 a network of GPS stations on the edifices of the most active volcanoes in the country. At the end of 2008, it started to implement a country-wide CGPS network of 70 stations [49]. At present, RENGEO (Spanish acronym for *Red Nacional de Geodesia*) is a geodetic network composed of 85 permanent stations, of which 30 are located in potentially active volcanoes [50]. The GPS receivers acquire data at different data tracking intervals, of 15 seconds and 1 second for volcanoes, and 30 seconds, 1 second and 0.2 seconds for tectonic studies, which are transmitted to the Monitoring Center in Quito through different ways such as radio links, internet, microwaves and satellite system. After the occurrence of the 2016 Pedernales earthquake, in order to improve the capacity of monitoring and generation of early warning information, especially due to tsunami hazards, a geodetic cGPS network in the province of Esmeraldas was implemented in real time. The data from this network are integrated with the seismic data to improve the rapid determination of the magnitudes and better characterize the source of the rupture.

The deployment of the GPS geodetic network in Costa Rica has been the result of actions carried out by institutions such as the OVSICORI, Spanish acronym for *Observatorio Vulcanológico y Sismológico de Costa Rica* (Volcanological and Seismological Observatory of Costa Rica), an institute that belongs to the Universidad Nacional, in coordination with foreign entities and researchers (UNAVCO, universities of South Florida, Central Washington, Georgia Tech, among others), as well as the contribution of National real estate institution. For geodynamic purposes, by the end of 2009, 19 cGPS stations had been established in the Nicoya Peninsula [51]. At present, the geodetic network of Costa Rica is composed of 55 cGPS stations [52].

In Venezuela, [53] points out that there are currently six cGPS stations that are part of COCONet (**Figure 3**), and two stations of the VENCREEP project funded by

COUNTRY	N° of Stations	COUNTRY	N° of Stations	COUNTRY	N° of Stations
Anguilla	1	El Salvador	4	Montserrat (Antilles)	1
Antigua & Barbuda	2	Grenada	1	Netherlands Antilles	1
Aruba	1	Guadeloupe	1	Nicaragua	4
Belize	1	Guatemala	3	Panama	12
British Virgin Is.	1	Haiti	1	Puerto Rico	4
Cayman Is.	4	Honduras	4	Dominican Republic	8
Colombia	141	Jamaica	3	St. Lucia	3
Costa Rica	55	Las Bahamas	1	Trinidad & Tobago	1
Cuba	2	Martinique	1	Venezuela	6
Ecuador	37	Mexico	2	Virgin Islands	1

Table 1. Number of cGPS stations discriminated by country in the study region and depicted in **Figure 3**.

the French National Research Agency. Initial efforts by FUNVISIS since 2003 have focused on the installation of 2 local campaign networks (western and eastern Venezuela) of more than 70 benchmarks. These data is complementary for tectonic studies.

Table 1 indicates the number of stations installed in each country that are part of the study area, which are represented in **Figure 3**. It is possible that there are additional stations in some countries, but we have considered that these stations will improve, in a short-term, the understanding of the geodynamics of the study region.

In terms of instrumentation, **Figure 3** depicts that cGPS station distribution is rather homogenous throughout the Caribbean region and adjacent areas, except for 3 countries (Colombia, Costa Rica and Ecuador). Such homogeneity is a result from the COCONet project implementation, trying to reduce large gaps of data availability. Conversely, the concentration of stations in the 3 abovementioned countries responds to national policies, as already mentioned (Nicoya experiment in Costa Rica, post-Pedernales 2016 earthquake instrumentation in Ecuador and GeoRED project in Colombia).

4. Data processing and velocity field

The Geological Survey of Colombia received a grant to host a Regional Data Center headquartered in Bogotá that serves the entire circum-Caribbean community and functions as a mirror for COCONet data and metadata [54]. From the existing stations in the study area and displayed in **Figure 3**, the International Geodesy Lab of GeoRED currently processes 214 stations located on the Caribbean, South America, Nazca and Cocos tectonic plates across many country borders (**Figure 4**).

All GPS data obtained in the own format of each receiver are converted to RINEX format using the TEQC (Translating, Editing, Quality Check) tool developed by UNAVCO [55]. GPS data processing is carried out using the scientific software GIPSY-X/RTGx v 1.3 developed by JPL-CALTECH-NASA [56], and made

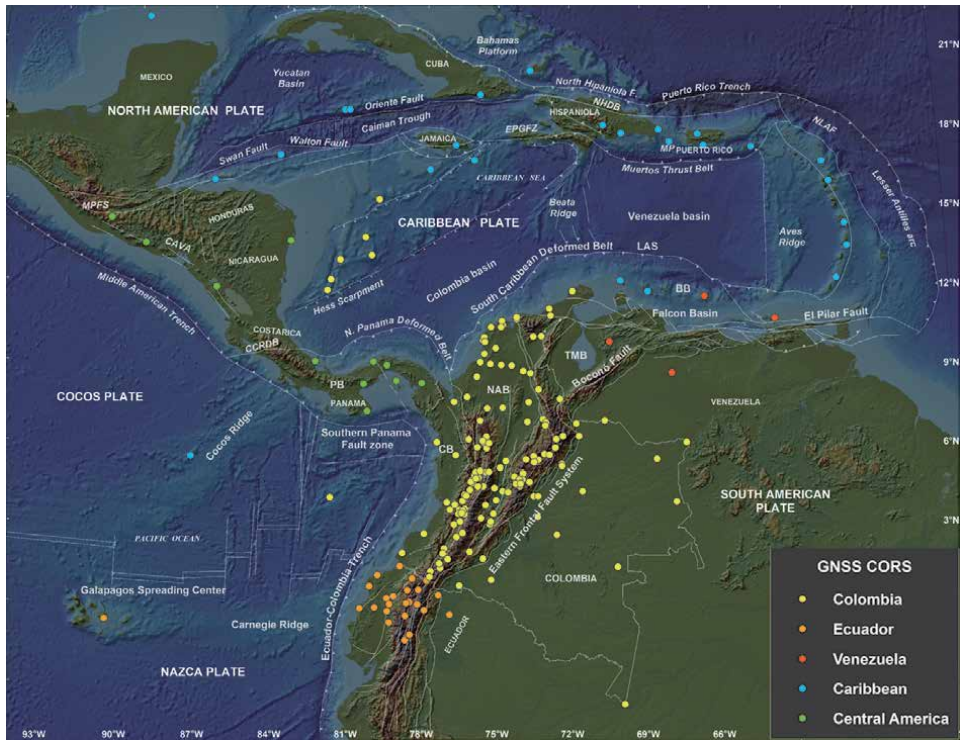


Figure 4.
cGPS stations processed at GeoRED-GSC.

available to GeoRED under a cooperation agreement. Final orbits are used in the processing, which include satellite orbits of the GNSS constellations, satellite clock and Earth orientation parameters that are provided in the appropriate format for Gipsy-X by JPL-NASA as contribution to the International GNSS Service (IGS). For the estimation of the tropospheric delay of the GNSS signals, the numerical model known as the Vienna Mapping Function (VMF1) is used, which is an update of the previous model known as VMF [57]. The ocean loading corrections are obtained from the Onsala Space Observatory, and are applied to eliminate the land and ocean tides. The amplitudes and phases of the main oceanic tidal loading terms are estimated by applying the FES2014b model [58]. The processing includes ionospheric models generated regularly by the IGS.

GIPSY-X/RTGx v 1.3 software uses the Precise Point Positioning (PPP) data processing strategy which is based on obtaining precise reference satellite orbit and clock products using the IGS GNSS global network.

Site coordinates for each day are computed in the non-fiducial frame and transformed to the ITRF2014 frame using a 7-parameter Helmert transformation [59]. The ECEF coordinates have been transformed into topocentric coordinates, which allow daily changes in the coordinates to be expressed in terms of local displacements in the North, East and Up (NEU) components with respect to a position in an initial epoch.

GPS time series have been generated using the HECTOR software v 1.7.2 [60] developed by SEGAL (Space & Earth Geodetic Analysis Laboratory), a center formed by the cooperation between the University of the Interior of Beira (UBI) and the Geophysical Institute Infante D. Luiz (IDL) from Portugal. HECTOR is a specialized software for the study of geodetic time series, which allows estimating

the time series trend with temporal noise correlations. It is a dynamic software that only accepts stationary noise with constant noise properties, which allows fast matrix operations, benefiting the reduction in processing time.

For the estimation of geodetic velocities, GeoRED has adopted the recommendation of [61], who consider that the period of time of data required to estimate a trend in geodetic stations should be at least 2.5 years, in order to avoid that the estimated motion rate can be affected by various types of noise, including seasonal noise. Thus, the period of observations used in the processing extends to the time range from 2.5 to 20 years. January 1, 2010 is used as the reference epoch for all velocities estimation rather than the midpoint of each individual time series. For the time series estimation, it was used a combined model of power law plus white noise, and power spectrum predicted and observed plots were generated, to verify that the appropriate noise model has been used.

We present a new horizontal velocity field using data from 105 cGPS stations located in the study region. **Figure 5** shows the velocities with respect to ITRF2014. **Figure 6** shows the velocities with respect to the South American plate (SOAM), **Table 2**, following the procedure described by [40], who determined the velocity field using only 60 cGPS stations. These new velocity vectors allow observing the strain partitioning at different scales at the four PBZs of the Caribbean plate.

The ISCO station, Costa Rica, located on the Cocos plate, subducts beneath Central America, and shows the highest velocity in the study area, 86 mm/yr. wrt SOAM; similar value was obtained by [40] in ITRF2008. The importance of continuous geodetic instrumentation for the seismic cycle monitoring in this zone is indicated by [62] analyzing the occurrence of the Mw 7.6 September 5, 2012, Costa Rica earthquake, recorded in the network installed in the Nicoya Peninsula [51].

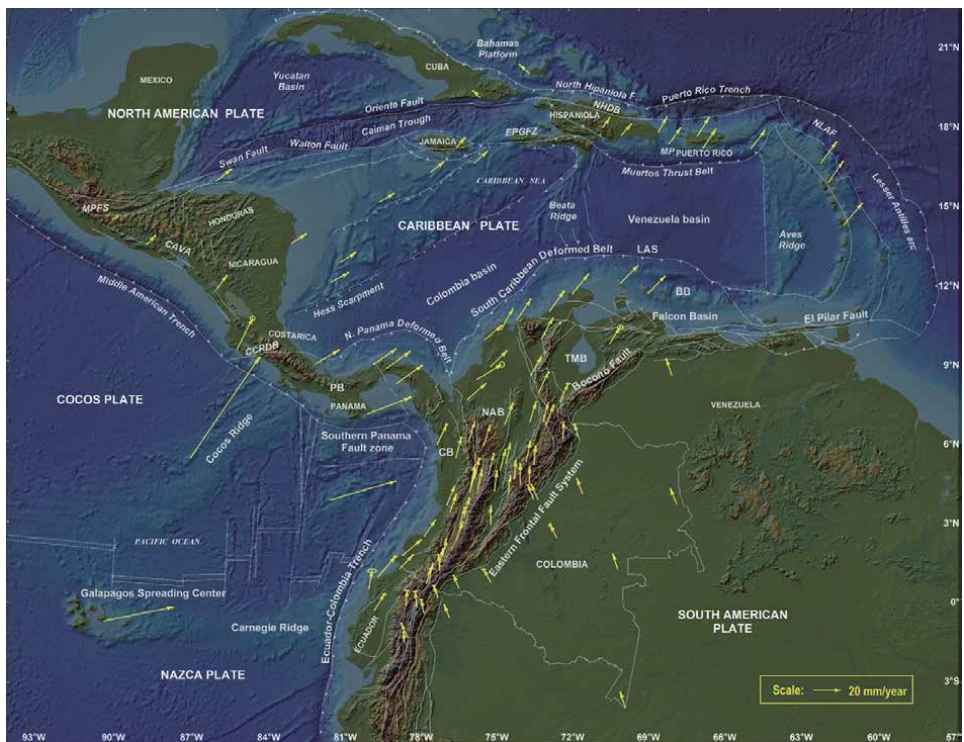


Figure 5.
GPS horizontal velocity field wrt to ITRF 2014.

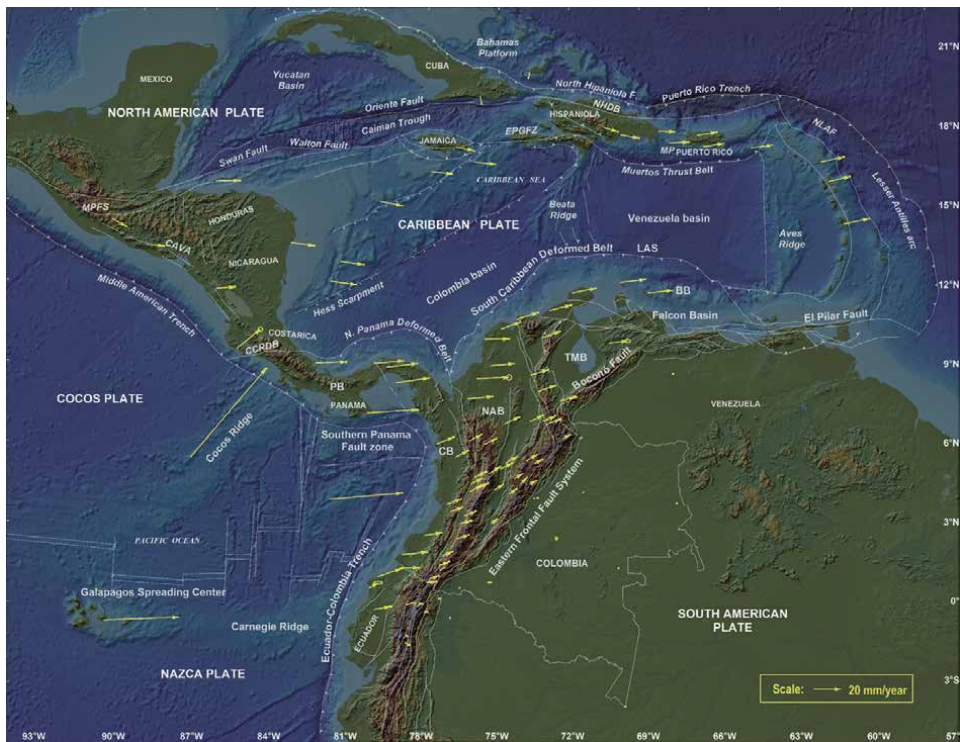


Figure 6. GPS horizontal velocity field wrt to SOAM, ITRF2014. **Table 2** provides the actual values of all GPS site velocities depicted here.

The ISCO station, installed in 2011, is the only place that allows estimating the motion of the Cocos plate using GNSS geodetic instruments [63]; these authors estimated the Cocos-Caribbean convergence by comparing the baseline between ISCO and the SANO station, located on the island of San Andrés on the Caribbean plate, obtaining a value of 78 ± 1 mm/yr expressed in ITRF2008. We have made the same comparison, but expressed in ITRF2014, obtaining a value of 76.8 ± 0.5 mm/yr. This result is in agreement with the MORVEL estimate of [43] mentioned by [63] of 76.4 ± 2.5 mm/yr.

Six stations, located on islands in the western sector of the Caribbean plate, show an east-southeast general direction of motion, in a range of 96° to 101° of azimuth, and velocities with respect to SOAM of 18.7 ± 0.3 mm/yr (SANO), 17.1 ± 0.3 mm/yr (CN35), 16.7 ± 0.5 mm/yr (CAYS), 15.9 ± 0.4 mm/yr (CN11), 15.3 ± 0.3 mm/yr (CN10), and 12.9 ± 0.3 mm/yr (CN12). On the other hand, three stations located on the eastern side of the Caribbean plate on islands of the Lesser Antilles, show velocity values with respect to SOAM about 17.1 ± 0.7 mm/yr (CN01), 16.6 ± 0.5 mm/yr (AMBF) and 18.9 ± 0.4 mm/yr (LMMF), in a general east-northeast direction, with azimuth values in the range of 76° to 78° .

MALO (Malpelo Island) and GLPS (Galapagos Island) stations confirm the rapid motion of the Nazca plate wrt to SOAM. The estimated velocity values in ITRF2014 are not so different from those estimated by [40] in ITRF2008. The ITRF2014 velocities are 53.2 ± 0.5 mm/yr with an azimuth of 87.8° for MALO, and 54.9 ± 0.2 mm/yr and azimuth 87.8° for GLPS.

The GPS stations located on the Colombian coast of the Pacific Ocean show similar values to those obtained by [40], increasing the velocity to the south. However, the ESMR station, located in Ecuadorean coast shows variation in the

ID	LON	LAT	VelE	VelN	SigE	SigN	ID	LON	LAT	VelE	VelN	SigE	SigN
ABCH	-73.722	4.638	4.8	2.7	0.3	0.2	INTO	-76.043	4.642	8.1	4.2	0.4	0.2
ABMF	-61.528	16.262	16.1	3.9	0.3	0.3	INVE	-74.232	11.188	15.7	4.9	0.4	0.1
ACHO	-80.173	7.415	36.7	2.4	0.9	0.4	ISCO	-87.056	5.544	55.4	65.1	0.7	0.4
ACPI	-79.950	9.371	22.0	2.0	0.2	0.2	LMMF	-60.996	14.595	18.5	3.9	0.4	0.2
ACP6	-79.408	9.238	22.1	2.6	0.2	0.2	LUMB	-77.328	0.137	1.1	-1.0	0.7	0.3
AJCM	-74.885	5.210	8.7	4.7	0.3	0.2	MALO	-81.606	4.003	53.0	4.5	0.5	0.3
ALPA	-72.918	11.528	15.9	4.0	0.5	0.5	MANA	-86.249	12.149	13.2	1.0	0.4	0.3
ANCH	-76.870	3.535	9.3	3.2	0.3	0.3	MECE	-73.712	7.107	9.7	4.6	0.3	0.2
AOPR	-66.754	18.347	14.4	2.4	0.3	0.2	MIPR	-66.527	17.886	15.0	2.6	0.2	0.1
AUCA	-76.883	-0.641	0.5	-0.9	0.4	0.2	MITU	-70.232	1.261	0.5	0.7	0.2	0.1
BA3E	-75.234	0.742	-1.2	-0.5	1.2	0.2	MOME	-80.047	0.492	6.6	3.8	2.6	0.9
BAAP	-73.554	4.072	0.4	-0.1	0.3	0.1	MOPR	-67.931	18.077	14.3	0.9	0.4	0.2
BAEZ	-77.887	-0.459	2.3	-0.1	0.8	0.3	MORA	-73.683	8.959	13.1	4.0	0.3	0.3
BAME	-74.565	4.236	6.1	3.7	0.3	0.3	OCEL	-71.616	4.271	0.4	0.6	0.4	0.1
BAPA	-74.658	5.466	8.0	4.5	0.2	0.2	OVSC	-77.257	1.210	3.3	2.1	0.3	0.2
BASO	-77.393	6.203	12.0	5.1	0.8	0.4	PAL2	-73.184	7.131	9.0	3.7	0.3	0.3
BIEC	-78.502	-1.447	-1.2	0.8	0.4	0.5	PASI	-76.499	0.513	0.2	-0.3	0.5	0.2
BOBG	-73.358	8.312	12.3	4.4	0.4	0.2	PLTR	-75.332	5.044	8.4	4.8	0.4	0.4
BOGT	-74.081	4.640	4.6	4.8	0.3	0.2	POVA	-76.615	2.449	9.2	2.9	0.4	0.2
BUGT	-76.996	3.826	10.6	4.1	0.3	0.2	PUIN	-67.903	3.851	-0.1	0.1	0.3	0.2
CAYS	-79.846	15.795	16.4	-3.3	0.5	0.2	QSEC	-85.357	9.840	17.0	13.9	1.4	1.3
CCAN	-76.300	3.360	8.3	3.6	0.4	0.4	QUIL	-77.291	1.394	7.3	2.9	0.5	0.3

ID	LON	LAT	VelE	VelN	SigE	SigN	ID	LON	LAT	VelE	VelN	SigE	SigN
CCPA	-76.085	4.325	8.5	4.8	1.0	0.5	RSDS	-69.911	18.461	13.4	-2.5	0.4	0.3
CCSQ	-76.474	3.063	8.2	1.9	0.8	0.3	RIOP	-78.651	-1.651	3.2	-2.0	0.5	0.5
CIOH	-75.534	10.391	17.8	0.2	0.8	0.2	ROA0	-86.527	16.318	17.6	0.0	0.7	0.2
CN01	-61.765	17.048	16.7	3.8	0.5	0.4	SALF	-78.155	-0.233	2.7	1.9	1.3	0.2
CN05	-68.359	18.564	12.1	-0.2	0.2	0.2	SANO	-81.716	12.580	18.5	-2.5	0.2	0.2
CN06	-70.656	18.790	11.0	-3.4	0.4	0.3	SCUB	-75.762	20.012	1.0	-5.4	0.2	0.2
CN10	-75.971	17.415	15.2	-1.5	0.3	0.2	SEL1	-75.529	6.191	9.3	4.6	0.3	0.2
CN11	-77.784	17.021	15.8	-1.9	0.3	0.2	SGCG	-73.064	6.992	10.5	4.0	0.3	0.7
CN12	-76.749	18.004	12.7	-2.5	0.5	0.3	SNLR	-78.847	1.293	14.0	0.2	0.5	0.2
CN14	-73.678	20.975	-1.2	-4.2	0.3	0.3	SSIA	-89.117	13.697	12.7	-1.4	0.4	0.4
CN19	-70.049	12.612	18.4	2.2	0.2	0.2	TEAT	-73.539	5.422	5.9	3.4	0.5	0.3
CN20	-82.256	9.352	22.5	0.8	0.6	0.5	TICU	-69.939	-4.187	0.2	0.0	0.4	0.2
CN28	-79.034	8.625	23.9	3.5	0.4	0.3	TONE	-76.139	6.324	9.6	5.2	0.2	0.2
CN29	-83.375	14.049	16.9	-2.4	0.5	0.4	TUCO	-78.748	1.815	18.4	1.9	0.4	0.2
CN35	-81.363	13.376	16.9	-2.4	0.6	0.3	URRO	-76.210	8.012	18.8	1.7	0.3	0.3
CN36	-75.821	8.820	23.6	0.9	1.4	1.7	UWAS	-72.391	6.451	5.4	2.3	0.3	0.2
CN38	-71.988	12.222	17.1	3.4	0.5	0.2	VBUV	-73.859	5.533	8.0	4.8	0.4	0.2
CN39	-70.524	10.206	13.3	1.7	1.8	1.1	VDPR	-73.248	10.436	14.0	4.9	0.2	0.2
CN40	-68.958	12.180	18.1	1.9	0.2	0.2	VEDE	-75.765	4.460	7.6	3.9	0.4	0.3
CN41	-68.042	8.943	0.9	0.6	0.4	0.3	VMER	-77.153	1.785	7.4	3.0	0.2	0.2
COEC	-77.787	0.716	7.1	0.9	0.6	0.2	VNEI	-75.255	3.062	4.7	3.4	0.3	0.3
CORO	-75.288	9.328	17.5	1.5	0.3	0.2	VORI	-77.672	0.863	6.8	2.2	0.3	0.3

ID	LON	LAT	VelE	VelN	SigE	SigN	ID	LON	LAT	VelE	VelN	SigE	SigN
CRO1	-64.584	17.757	16.1	2.1	0.3	0.1	VOTU	-74.710	7.019	11.0	5.2	0.4	0.3
CUC1	-72.513	7.932	11.2	2.9	1.2	0.4	VPIJ	-75.107	4.397	6.4	4.2	0.3	0.1
ESMR	-79.724	0.935	17.6	6.2	1.1	0.3	VPOL	-74.861	10.794	14.0	5.2	0.4	0.2
FLFR	-79.843	-0.357	11.7	2.2	1.2	0.3	VPOM	-73.382	4.068	-0.3	0.4	0.5	0.2
GGPA	-78.594	-0.180	5.1	1.5	1.4	0.2	VQUI	-76.642	5.692	9.0	4.8	0.5	0.2
GLPS	-90.304	-0.743	54.8	2.1	0.2	0.2	VROS	-74.323	4.847	6.0	3.6	0.2	0.2
GUAP	-77.895	2.574	13.0	2.2	0.3	0.2	VJSG	-72.639	2.533	-0.4	-1.1	0.7	0.9
GUAT	-90.520	14.590	10.5	-5.7	0.4	0.2	VTAM	-71.753	6.452	1.6	0.2	0.7	0.2
INRI	-75.897	4.909	8.3	4.0	0.6	0.4							

Table 2.
GPS site velocities (mm/yr) relative to SOAM in ITRF2014.

northern component of velocity, which can be attributed to the effect of the 2016 Pedernales earthquake [64, 65]. It is important to note that the velocity field of [40] is estimated based on data until March 2016, prior to the aforementioned earthquake. The new velocity field contains the offsets associated to the coseismic displacements for the generation of the respective time series and velocity estimation.

At regional scale, wrt to SOAM, we can clearly see how NAB (in the sense of [3]) is detached from SOAM, and is moving at around from few mm/yr to a ten of mm/yr in the ENE-NE direction. In a general manner, slip rates within NAB tend to decrease from west to east, from the Pacific border towards inland, and from south to north, implying coupling at the over-riding plate-slab interface (e.g. [27]). Meanwhile, the Caribbean plate seems to exhibit a more similar (more homogeneous) slip rate across the plate, trending E-ESE. The herein obtained values across the Caribbean plate tend to confirm the ≈ 20 mm/yr of eastward motion of this thickened oceanic plate already known per years now. However, it is very clear now that the Panamá block probably is not part of the Caribbean plate, because exhibiting a higher slip rate to the E-ENE than the rest of the Caribbean plate (e.g. [12, 39, 40]). It appears that such higher slip rate is transferred to NAB located to the east, confirming the indentation-extrusion mechanism responsible for the tectonic escape of NAB, as a consequence of collision and later suturing of the Chocó block against SA (and directly to NAB; e.g. [13, 28–30, 39, 40]).

5. Conclusions

A new horizontal geodetic velocity field wrt SOAM is presented, expressed in ITRF2014. With respect to the previous estimate, the spatial coverage of the study area has been increased, as well as the number of stations and the observation time at each station used in the solution.

The precision of the ISCO motion estimation, located on the Cocos plate, has been improved with respect to previous estimation, using data from 7.6 years of observation.

Although there are no substantial differences in the station velocities processed in this study, located on islands both west and east of the Caribbean plate, except for that shown by one station, it can be concluded that the Caribbean plate probably does not behave uniformly as a unit, as one might conclude from the difference between the directions, about 21° , changing in the general direction from east-southeast to east-northeast.

The study region shows examples of the importance of GNSS geodetic instrumentation for the study of the seismic cycle.

Acknowledgements

To the Geological Survey of Colombia for supporting the Space Geodesy Research Group which has allowed the implementation and development of the GeoRED project, first between 2007 and 2016, funded by the grant 0043000220000 from the National Planning Department, and second, 2018–2021 funded under the institutional code 1000810 as part of the Research, Monitoring and Evaluation of Geological Hazards in the national territory. TO UNAVCO for its permanent support and for facilitating our participation in the COCONet project as well as the installation of stations in several countries, including in our countries of Colombia and Venezuela; also for the grant that permitted the implementation of the Regional Data Center in Bogotá, Colombia. To the Geophysical Institute of the

Polytechnic School of Quito, Ecuador, for cooperation and joint work, as well as the exchange of data with the GSC. To JPL-NASA for the license to use the GIPSY-X software, and to SEGAL for providing the HECTOR software. To the members of the SGRG for all their support to advance the GeoRED project.

Author details

Héctor Mora-Páez^{1*} and Franck Audemard²

1 Geological Survey of Colombia, Bogotá, Colombia

2 Central University of Venezuela, Caracas, Venezuela

*Address all correspondence to: hmora@sgc.gov.co

IntechOpen

© 2021 The Author(s). Licensee IntechOpen. This chapter is distributed under the terms of the Creative Commons Attribution License (<http://creativecommons.org/licenses/by/3.0>), which permits unrestricted use, distribution, and reproduction in any medium, provided the original work is properly cited. 

References

- [1] Case J. E., Durán L., López A., Moore W. Tectonic investigations in western Colombia and eastern Panama. *Bulletin Geological Society of America*. 1971: 82 (10): 2685-2712. DOI: 10.1130/0016-7606(1971)82[2685:TIWCA]2.0.CO;2
- [2] Dewey, J. Seismicity and tectonics of western Venezuela. *Bulletin Seismological Society of America*. 1972: 62 (6): 1711-1751.
- [3] Pennington W. D. Subduction of the Eastern Panama Basin and Seismotectonics of Northwestern South America. *Journal of Geophysical Research*. 1981: 86 (B11): 10753-10770. DOI: 10.1029/JB086iB11p10753
- [4] Kellogg J., Bonini W. Subduction of the Caribbean Plate and basement uplifts in the overriding South-American plate. *Tectonics*. 1982:1: 251-276. DOI: 10.1029/TC001i003p00251
- [5] Freymueller J. T., Kellogg J. N., Vega V. Plate motions in the north Andean region. *Journal of Geophysical Research*. 1993: 98: 21853-21863. DOI: 10.1029/GL017i003p00207
- [6] van der Hilst R., Mann P. Tectonic implications of tomographic images subducted lithosphere beneath northwestern South America, *Geology*. 1994: 22:451-454. DOI: 10.1130/0091-7613(1994)022<0451:TIOTIO>2.3.CO;2
- [7] Kellogg J.N., Vega V., Stallings T.C., Aiken, C.L.V. Tectonic development of Panama, Costa Rica, and the Colombian Andes: Constraints from Global Positioning System geodetic studies and gravity. In: Mann P. (editor), *Geologic and tectonic development of the Caribbean Plate boundary in Southern Central America*. Geological Society of America, Special Paper 295, 1995: 75-90. DOI: 10.1130/SPE295-p75
- [8] Pindell J. L., Higgs R., Dewey J. Cenozoic palinspatic reconstruction, paleogeographic evolution and hydrocarbon setting of the northern margin of South America. In: Pindell, J. and Drake, C. (eds) *Paleogeographic Evolution and Non-glacial Eustasy, Northern South America*. Society for Sedimentary Geology, Special Publications. 1998:58: 45-85. DOI: 10.2110/pec.98.58.0045
- [9] Taboada A., Rivera L.A., Fuenzalida A., Cisternas A., Hervé P., Harmen B., Olaya J., Rivera C. Geodynamics of the northern Andes: subductions and intracontinental deformation (Colombia). *Tectonics*. 2000: 19: 787-813.
- [10] Trenkamp R., Kellogg J. N., Freymueller J. T., Mora, H. Wide plate margin deformation, southern Central America and northwestern South America, CASA GPS observations. *J. South Am. Earth Sci.* 2002:15, 157-171, DOI: 10.1016/S0895-9811(02)00018-4.
- [11] Cediel F., Shaw R. P., Cáceres C. Tectonic assembly of the Northern Andean Block, in *The Circum-Gulf of Mexico and the Caribbean: Hydrocarbon habitats, basin formation, and plate tectonics* Bartolini C., Buffler R. T., Blickwede J., (editors) AAPG Memoir 2003: 79, 815-848.
- [12] Audemard F. E., Audemard F. A. Structure of the Mérida Andes, Venezuela: relations with the South America-Caribbean geodynamic interaction. *Tectonophysics*. 2002: 345: 299-327. DOI: 10.1016/S0040-1951(01)00218-9
- [13] Audemard F. A. Active block tectonics in and around the Caribbean: A Review. In: Schmitz M., Audemard F. A., Urbani F. (Eds): *El Límite Noreste de la Placa Suramericana - Estructuras Litosféricas de la Superficie al Manto*

- (The Northeastern Limit of the South American Plate - Lithospheric Structures from Surface to the Mantle) Editorial Innovación Tecnológica, Facultad de Ingeniería-Universidad Central de Venezuela/FUNVISIS. 2014: 29-77
- [14] Davis J. L., Fialko Y., Holt W. E., Miller M. M., Owen S. E., Pritchard M. E. (Eds.) A Foundation for Innovation: Grand Challenges in Geodesy, Report from the Long-Range Science Goals for Geodesy Community Workshop. 2012: UNAVCO, Boulder, Colorado, 79 pp.
- [15] Bock Y, Melgar D. Physical applications of GPS geodesy: a review. *Rep Prog Phys.* 2016: 79 (10):106801. DOI: 10.1088/0034-4885/79/10/106801.
- [16] Teunissen P. J. G., Montenbruck O., (eds) Springer Handbook of Global Navigation Satellite Systems, Springer International Publishing. 2017: 1327 p. DOI: 10.1007/978-3-319-42928-1
- [17] Hess H. History of Ocean Basins. In: Engel, A. E. J., James, H. L. and Leonard B. F. (eds.): *Petrologic studies: a volume in honor of A. F. Buddington.* Geological Society of America. 1962: 599-620. New York
- [18] Mann P., Burke K., Matumoto T. Neotectonics of Hispaniola: Plate motion, sedimentation, and seismicity at a restraining bend. *Earth Planet. Sci. Lett.* 1984:70: 311-324. DOI: 10.1016/0012-821X(84)90016-5
- [19] Audemard F. A. Quaternary tectonics and stress tensor of the northern inverted Falcón Basin, northwestern Venezuela. *Journal of Structural Geology, Special Memorial Issue to Paul Hancock.* 2001: 23(2-3): 431-453. DOI: 10.1016/S0191-8141(00)00116-4
- [20] Kellogg J. N., Dixon T. H. Central and South America GPS Geodesy - CASA UNO. *Geophys. Res. Lett.* 1990: 17 (3): 195-198, DOI:10.1029/GL017i003 p00195.
- [21] Lyon-Caen H., Barrier E., Lasserre C., Franco A., Arzu I., Chiquin M., Chiquin L.M., Duquesnoy T., Flores O., Galicia O., Luna J., Molina E., Porras O., Requena J., Robles V., Romero J., Wolf R. Kinematics of the North American-Caribbean-Cocos plates in Central America from new GPS measurements across the Polochic-Motagua fault system: *Geophysical Research Letters* 2006: 33 p. L19309, DOI: 10.1029/2006GL027694.
- [22] LaFemina P.C., Dixon T.H., Govers R., Norabuena E., Turner H., Saballos A., Mattioli G., Protti M., Strauch W. Forearc motion and Cocos Ridge collision in Central America: *Geochemistry Geophysics Geosystems* G3, 2009:Q05S14, DOI: 10.1029/2008GC002181.
- [23] Alvarado D., DeMets C., Tikoff B., Hernández D., Wawrzyniec, T.F., Pullinger C., Mattioli G., Turner H.L., Rodríguez M., Correa-Mora F. Forearc motion and deformation between El Salvador and Nicaragua: GPS, seismic, structural, and paleomagnetic observations. *Lithosphere* 2011: 3(1): 3-21.
- [24] Kobayashi D., LaFemina P., Geirsson H., Chichaco E., Abrego A., Mora H., Camacho E. Kinematics of the western Caribbean: Collision of the Cocos Ridge and upper plate deformation, *Geochem. Geophys. Geosyst.* 2014:15, 1671-1683, DOI: 10.1002/2014GC005234.
- [25] López A. M., Stein S., Dixon T., Sella G., Calais E., Jansma P., Weber J., LaFemina P. Is there a northern Lesser Antilles forearc block?, *Geophys. Res. Lett.* 2006:33. DOI: 10.1029/2005GL025293
- [26] Feuillet N., Manighetti I., Tapponnier P. Jacques E. Arc parallel extension and localization of volcanic

- complexes in Guadeloupe, Lesser Antilles, *J. Geophys. Res.* 2002:107. DOI: 10.1029/2001JB000308.
- [27] Sagiya T., Mora-Páez H. Interplate coupling along the Nazca subduction zone on the Pacific coast of Colombia deduced from GeoRED GPS observation data. In: Gómez-Tapias, J. & Pinilla-Pachón, A.O. (editors), *The Geology of Colombia, Volume 4 Quaternary*. Servicio Geológico Colombiano, Publicaciones Geológicas Especiales 2020: 38, 499-513. Bogotá. DOI: 10.32685/pub.esp.38.2019.15
- [28] Audemard F. A. Néotectonique, Sismotectonique et Aléa Sismique du Nord-ouest du Vénézuéla (Système de failles d'Oca-Ancón). PhD thesis, Université Montpellier II, France 1993: 369 pp + appendix
- [29] Audemard, F. A. Evolution Géodynamique de la Façade Nord Sud-américaine: Nouveaux apports de l'Histoire Géologique du Bassin de Falcón, Vénézuéla. *Proceedings XIV Caribbean Geological Conference, Trinidad, 1998*: 2, 327-340.
- [30] Audemard, F. A. Key issues on the post-Mesozoic southern Caribbean plate boundary. In: James K. H., Lorente M. A., Pindell, J., (eds). *Origin and Evolution of the Caribbean Plate*, Geological Society, London, Special Publications. 2009: 328: 567-584. DOI: 10.1144/SP328.23
- [31] Schubert C. Neotectonics of Boconó Fault, western Venezuela. *Tectonophysics* 1982: 85: 205-220.
- [32] Soulas J.-P. Neotectónica y tectónica activa en Venezuela y regiones vecinas. *Proceedings of VI Congreso Geológico Venezolano* 1986:10: 6639-6656.
- [33] Velandia F., Acosta J., Terraza R., Villegas H. The current tectonic motion of the Northern Andes along the Algeciras Fault System in SW Colombia. *Tectonophysics* 2005: 399: 313-329. DOI: 10.1016/j.tecto.2004.12.028.
- [34] Alvarado A., Audin L., Nocquet J. M., Jaillard E., Mothes P., Jarrín P., Segovia M., Rolandone F., Cisneros D. Partitioning of oblique convergence in the Northern Andes subduction zone: Migration history and the present-day boundary of the North Andean Sliver in Ecuador, *Tectonics* 2016: 35: 1048-1065. DOI:10.1002/2016TC004117.
- [35] Diederix H., Bohórquez O. P., Mora-Páez H., Peláez J. R., Cardona L., Corchuelo Y., Ramírez J., Díaz-Mila F. The Algeciras Fault System of the Upper Magdalena Valley, Huila Department. In: Gómez-Tapias, J. & Pinilla-Pachón, A. O. (eds.): *The Geology of Colombia, Volume 4 Quaternary*. Servicio Geológico Colombiano, Publicaciones Geológicas Especiales 2020:38: 423-452, DOI: 10.32685/pub.esp.38.2019.12.
- [36] Bermúdez M. A., Kohn B. P., van der Beek P. A., Bernet M., O'Sullivan P. B., Shagam R. Spatial and temporal patterns of exhumation across the Venezuelan Andes: Implications for Cenozoic Caribbean geodynamics. *Tectonics* 2010:29, TC5009, DOI: 10.1029/2009TC002635
- [37] Mora-Páez H., Mencin D. J., Molnar P., Diederix H., Cardona-Piedrahita L., Peláez-Gaviria J.-R., Corchuelo-Cuervo Y. GPS velocities and the construction of the Eastern Cordillera of the Colombian Andes, *Geophys. Res. Lett.* 2016: 43, 8407-8416, DOI:10.1002/2016GL069795.
- [38] Rockwell T. K., Gath E., González T., Madden C., Verdugo D., Lippincott C., Dawson T., Owen L. A., Fuchs M., Cadena A., Williams P., Weldon E., Franceschi, P. Neotectonics and paleoseismology of the Limón and Pedro Miguel faults in Panamá: Earthquake hazard to the Panamá Canal. *Bull. Seismol. Soc. Am.* 2010:100(6): 3097-3129. DOI: 10.1785/0120090342.

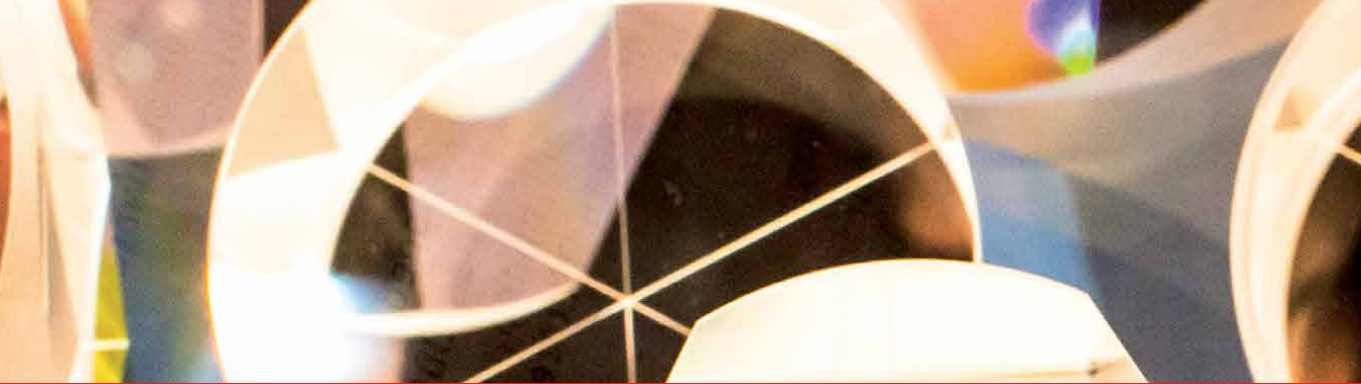
- [39] Audemard, F. A. Ruptura de los grandes sismos históricos venezolanos de los siglos XIX y XX, revelados por la sismicidad instrumental contemporánea. XI Congreso Venezolano de Geofísica, Caracas, Venezuela, Nov. 17-20, 2002, (8 pp, Extended Abstract in CD).
- [40] Mora-Páez H., Kellogg, Freymueller J., Mencin D. Fernandes R., Diederix H., LaFemina P., Cardona-Piedrahita L., Lizarazo S., Peláez-Gaviria J-R, Díaz-Mila F., Bohórquez-Orozco O., Giraldo-Londoño L., Corchuelo-Cuervo Y. Crustal Deformation in the Northern Andes – Space Geodesy Velocity Field, *J. South American Earth Sciences* 2019: 89 (76-91), 10.1016/j.jsames.2018.11.002
- [41] Vargas C. A., Mann P. Tearing and Breaking Off of Subducted Slabs as the Result of Collision of the Panama Arc-Indenter with Northwestern South America. *Bulletin Seismological Society of America*. 2013;103(3): 2025-2046. DOI: 10.1785/0120120328
- [42] Kellogg J. N., Franco G. B., Mora-Páez H. Cenozoic tectonic evolution of the North Andes with constraints from volcanic ages, seismic reflection, and satellite geodesy, Chapter 4, In: *Andean Tectonics Book*, B. K Horton and A. Folguera (Eds), Elsevier, ISBN: 978-0-12-816009, 2019: 711 p. DOI: 10.1016/B978-0-12-816009-1.00006-X
- [43] DeMets C., Gordon R. G., Argus D. F. Geologically current plate motions. *Geophys. J. Int.* 2010;181: 1-80. DOI: 10.1111/j.1365-246X.2009.04491.x.
- [44] Murray J. R., Bartlow N., Bock Y., Brooks B. A., Foster J., Freymueller J., Hammond W. C., Hodgkinson K., Johanson I., López-Venegas A., Mann D., Mattioli G. S., Melbourne T., Mencin D., Montgomery-Brown E., Murray M. H., Smalley R., Thomas V. Regional Global Navigation Satellite System Networks for Crustal Deformation Monitoring. *Seismological Res. Lett.* 2019: 91 (2A): 552–572. DOI: 10.1785/0220190113
- [45] DesRoches R., Comerio M., Eberhard M., Mooney W., Rix G. J. Overview of the 2010 Haiti Earthquake. *Earthquake Spectra*. 2011: 27 (S1), S1-S21. DOI: 10.1193/1.3630129
- [46] Braun J., Mattioli G., Calais E., Carlson D., Dixon T. H., Jackson M., Kursinski R., Mora-Páez H., Miller M., Pandya R. Robertson R., Wang G. Focused Study of Interweaving Hazards Across the Caribbean. *Eos* 2012: 93 (9): 89-90. DOI: 10.1029/2012EO090001
- [47] Mora-Páez H., (2006). National GPS Network for Geodynamics Research, BPIN document and supplementary information, Project Proposal, (in Spanish), submitted to the National Planning Department, Colombia, INGEOMINAS, 63 p. + 5 modules
- [48] Mora-Páez H., Peláez-Gaviria J. R., Diederix H., Bohórquez-Orozco O., Cardona-Piedrahita L., Corchuelo-Cuervo Y., Ramírez-Cadena J., Díaz-Mila F. Space geodesy infrastructure in Colombia for geodynamics research. *Seismological Research Letters*, 2018: 89 (2A): 446–451. DOI: 10.1785/0220170185
- [49] Mothes P. A., Nocquet J. M., Jarrin P. Continuous GPS network operating throughout Ecuador. *Eos, Transactions American Geophysical Union*. 2013: 94(26), 229-231. DOI: 10.1002/2013EO260002
- [50] Alvarado A., Ruiz M., Mothes P., Yepes H., Segovia M., Vaca M., Ramos C., Enríquez W., Ponce G., Jarrín P., Aguilar J., Acero W., Vaca S., Singaicho J.C., Pacheco D., Córdova A. Seismic, Volcanic, and Geodetic Networks in Ecuador: Building Capacity for Monitoring and Research. *Seism. Res. Lett.* 2018;89 (2A): 432–439. DOI: <https://doi.org/10.1785/0220170229>

- [51] Outerbridge K. C., Dixon T. H., Schwartz S. Y., Walter J. I., Protti M., Gonzalez V., Biggs J., Thorwart M., Rabbel W. A tremor and slip event on the Cocos-Caribbean subduction zone as measured by a global positioning system (GPS) and seismic network on the Nicoya Peninsula, Costa Rica, *J. Geophys. Res.* 2010:115, B10408, DOI: 10.1029/2009JB006845.
- [52] Muller C., pers. comm. 2021
- [53] Audemard F.A., Reinoza C., López R, Feaux K., Jouanne F. Instalación de estaciones geodésicas de monitoreo continuo para fines geocientíficos en el margen caribe sureste. *Boletín de Geología* 2020: 42(2), 15-30. DOI: 10.18273/revbol.v42n2-2020001.
- [54] Mora-Páez H., Kellogg J.N., Freymueller, J.T. Contributions of space geodesy for geodynamic studies in Colombia: 1988 to 2017. In: Gómez, J. & Pinilla-Pachon, A.O. (editors), *The Geology of Colombia, Volume 4 Quaternary*. Servicio Geológico Colombiano, Publicaciones Geológicas Especiales 2020: 38, 479–498. Bogotá. DOI:10.32685/pub.esp.38.2019.14
- [55] Estey L. H., Meertens C. M. TEQC: The Multi-Purpose Toolkit for GPS/GLONASS Data, *GPS Solutions*. 1999: 3 (1) 42-49, John Wiley & Sons. DOI: 10.1007/PL00012778
- [56] Bertiger W., Bar-Sever Y., Dorsey A., Haines B., Harvey N., Hemberger D., Heflin M., Lu W., Miller M., Moore A.W., Murphy D., Ries P., Romans L., Sibois A., Sibthorpe A., Szilagyi, Valisneri M., Willis P. GipsyX/RTGx, A New Tool Set for Space Geodetic Operations and Research, *Advances in Space Research*. 2020: 66(3), 469-752, DOI: 10.1016/j.asr.2020.04.015
- [57] Boehm J., Werl B., Schuh H. Troposphere mapping functions for GPS and very long baseline interferometry from European Centre for Medium-Range Weather Forecasts operational analysis data, *J. Geophys. Res.* 2006: 111, B02406, DOI: 10.1029/2005JB003629.
- [58] Carrere L., Lyard F., Cancet M., Guillot A., Picot N. Finite Element Solution FES2014, a new tidal model. Validation results and perspectives for improvements, presentation to ESA Living Planet Conference, Prague 2016.
- [59] Altamimi Z., Rebischung P., Métivier L., Collilioux. ITRF2014: A new release of the International Terrestrial Reference Frame modeling nonlinear station motions, *J. Geophys. Res. Solid Earth* . 2016:121, 6109–6131. DOI: 10.1002/2016JB013098.
- [60] Bos M. S., Fernandes R. M. S., Williams S. D. P., Bastos L. Fast Error Analysis of Continuous GNSS Observations with Missing Data. *J. Geod.* 2013:87(4), 351–360, DOI: 10.1007/s00190-012-0605-0.
- [61] Blewitt G., Lavallée D. Bias in geodetic site velocity due to annual signals: theory and assessment. In: *Ádám J., Schwarz K.P. (Eds.), Vistas for Geodesy in the New Millennium*. International Association of Geodesy Symposia 2002: 125. Springer, Berlin, Heidelberg.
- [62] Yue H., Lay T., Schwartz S. Y., Rivera L., Protti M., Dixon T. H., Owen S., Newman A. V. The 5 September 2012 Nicoya, Costa Rica Mw 7.6 earthquake rupture process from joint inversion of high-rate GPS, strong-motion, and teleseismic P wave data and its relationship to adjacent plate boundary interface properties, *J. Geophys. Res. Solid Earth*. 2013:118, 5453-5466, doi:10.1002/jgrb.50379
- [63] Protti M., González V., Freymueller J., Doelger S. Isla del Coco, on Cocos Plate, converges with Isla de San Andrés, on the Caribbean Plate, at

78mm/yr. *Revista de Biología Tropical*, 2012): 60(3) 33-41.

[64] Nocquet J.M., Jarrin P., Vallée M., Mothes P. A., Grandin R., Rolandone F., Delouis B., Yepes H., Font Y. C., Fuentes D., Régnier M., Laurendeau A., Cisneros D., Hernandez S., Sladen A., Singaicho J. C., Mora H., Gomez J., Monte L., Charvis P. Supercycle at the Ecuadorian subduction zone revealed after the 2016 Pedernales earthquake. *Nature Geoscience*. 2017:10, 145–149. DOI: 10.1038/ngeo2864.

[65] Mothes P. A., Rolandone F., Nocquet J.-M., Jarrin P., Alvarado A. P., Ruiz M. C., Cisneros D., Mora-Páez H., Segovia M. Coseismic Surface Slip Recorded by Continuous and High Rate GPS during the 2016 Pedernales Mw 7.8 Earthquake, Northern Andes, Ecuador-Colombia, *Seismological Research Letters* 2018: 89(2A), 534-541, DOI: 10.1785/0220170243



Edited by Bihter Erol and Serdar Erol

Advances in space-borne technologies lead to improvements in observations and have a notable impact on geodesy and its applications. As a consequence of these improvements in data accuracies, spatial and temporal resolutions, as well as the developments in the methodologies, more detailed analyses of the Earth and a deeper understanding of its state and dynamic processes are possible today. From this perspective, this book is a collection of the selected reviews and case-study articles that report the advances in methodology and applications in geodesy. The chapters in the book are mainly dedicated to the Earth's gravity field theory and applications, sea level monitoring and analysis, navigation satellite systems data and applications, and monitoring networks for tectonic deformations. This collection is a current state analysis of the geodetic research in theory and applications in today's modern world.

Published in London, UK

© 2021 IntechOpen
© devteev / iStock

IntechOpen

ISBN 978-1-83962-768-2

